THE UNIVERSITY *of* EDINBURGH

THE UNIVERSITY *of* EDINBURGH

An exploration of Structure – Property Relationships in Nitropyrazole-based Energetic Materials Using Co-crystallisation and High Pressure

THE UNIVERSITY *of* EDINBURGH

Nurunnisa ATCEKEN

University of Edinburgh

Submitted for the Degree of Doctor of Philosophy

November 2021

Abstract

Energetic materials are chemical compositions that can rapidly release large amounts of energy when suitably triggered by impact, shock, spark or friction. Key properties of energetic materials include detonation velocity, oxygen balance, thermal and chemical stability, and sensitivity to initiation by external stimuli. To develop strategies for the design of energetic materials with desirable properties usually refer high energetic performance and low sensitivity, reliable structure-property relationships should be established. Therefore, the main objective of this thesis is to characterise a variety of energetic materials and correlate their structures with their energetic properties.

Nitropyrazole-based energetic materials were chosen as the subject of this study due to growing interest in their potential as replacements for existing energetic materials. Among the pyrazole family of energetic compounds, 3,4,5-TNP (3,4,5-trinitropyrazole) is of particular interest due to its superior detonation performance and low sensitivity to impact, friction and spark. To better understand the properties of 3,4,5-TNP, Chapter 3 explores the high pressure behaviour of 3,4,5-TNP. Energetic materials experience elevated pressures under operational conditions and this can alter the crystal structures and form novel polymorphs. The first part of the study focused on a high-pressure investigation of 3,4,5-TNP using a combination of Raman spectroscopy, neutron powder diffraction (NPD), and single crystal X-ray diffraction (SXRD). On compression up to 7.3 GPa, three new high-pressure phases of 3,4,5-TNP were identified and characterised. Form II was observed at 0.7 GPa and is characterised by an abrupt shortening of hydrogen-bonding interactions. Form III was observed at 2.2 GPa and is characterised by an abrupt conformational change affecting all of the NO_2 torsional angles in the asymmetric unit of 3,4,5-TNP. Form IV was observed at 5.3 GPa *via* a single crystal to single crystal transition. The structure of Form IV was solved and refined from single crystal X-ray diffraction data – it adopts the monoclinic crystal system with space group *Cc.* The neutron powder diffraction patterns recorded for a polycrystalline sample are consistent with Form IV at pressures above 5.3 GPa. Form IV appears to be more sensitive to initiation as demonstrated by its spontaneous initiation at elevated pressures during both neutron experiments. This increased impact sensitivity of Form IV compared to Form I was rationalised using a computational technique based-on a vibrational up-pumping

model. This work, therefore, highlights that pressure-induced polymorphism has a high probability of significantly altering the sensitivity of energetic materials.

Chapters 4 and 5 explore the use of co-crystal/salt-formation to tune the energetic properties of a variety of nitropyrazole-based energetic materials. Co-crystallisation/salt formation is a useful branch of crystal engineering that can be used for modifying key energetic properties such as sensitivity, thermal/chemical stabilities, processability, and energetic performance. The main motivation of multicomponent crystallisation studies was to establish structure-property relationships of novel co-crystals and salts of nitropyrazoles and to understand the extent to which these techniques are applicable for tailoring the properties of nitropyrazoles. As a result of broad co-former investigation, pyridine, substituted pyridines, and morpholine were found to be suitable co-formers for nitropyrazoles. 1,3-dinitropyrazole (1,3-DNP), 3,5-dinitropyrazole (3,5-DNP) and 3,4,5-trinitropyrazole (3,4,5-TNP) were crystallised with a selection of co-formers including pyridine, substituted pyridines, and morpholine resulting in 9 salts and 3 co-crystals. Structural characterisation of these compounds was performed using SXRD and NPD. The energetic parameters of the co-crystals/salts including detonation velocity, detonation pressure and oxygen balance were predicted using the EXPLO5 program. The thermal behaviour of the energetic salts and co-crystals were determined using differential scanning calorimetry. The thermal properties, impact sensitivities and energetic performance parameters were found to be altered upon co-crystallisation/salt formation. These material properties were attempted to correlate with structural features including crystal density, crystal-packing motif and intermolecular interactions. Non-covalent interactions were analysed in detail and hydrogen bonding appeared as the main factor increasing the stabilities of these salts and co-crystals. In Chapter 5, six halogen containing salts and co-crystals were investigated in the same group for highlighting the importance of halogen bonding in influencing energetic properties of materials. It is demonstrated that in addition to hydrogen bonding, halogen bonding contributes to the stability of these multicomponent structures and increase their crystal densities. In summary, it is seen that co-crystallisation/salt formation is demonstrated to be an efficient technique to tailor the energetic properties of nitropyrazole-based energetic materials.

Lay summary

Energetic materials are chemical compositions that can rapidly release large amounts of energy when suitably triggered by impact, shock, spark or friction. Key properties of energetic materials include ‘explosive power’, oxygen concentration, thermal and chemical stability, safety and tendency to initiation by external stimuli. To develop strategies for the design of energetic materials with desirable properties, reliable structure-property relationships should be established. Therefore, the main objective of this thesis is to characterise a variety of energetic materials and correlate their structures with their energetic properties.

Nitropyrazole-based compounds are five membered rings (two adjacent nitrogen atoms and three carbon atoms) with nitro (NO_2) group/groups attachment. They were chosen as the subject of this study due to growing interest in their potential as replacements for existing energetic materials. Among the pyrazole family of energetic compounds, 3,4,5-TNP (3,4,5-trinitropyrazole: three nitro groups attached to three C atoms) is of particular interest due to its superior explosive power and low sensitivity to impact, friction and spark. To better understand the properties of 3,4,5-TNP, Chapter 3 explores the high pressure behaviour of 3,4,5-TNP. Energetic materials experience elevated pressures under operational conditions and this can alter the crystal structures and form novel polymorphs (Polymorphs have the same chemical composition, but different arrangements of molecules in their crystal structures). The first part of the study focused on a high-pressure investigation of 3,4,5-TNP using a combination of different characterisation techniques (Raman spectroscopy, neutron powder diffraction and single crystal X-ray diffraction). On compression up to 7.3 GPa, three new high-pressure phases of 3,4,5-TNP were identified and characterised. Form II was observed at 0.7 GPa and is characterised by an abrupt shortening of hydrogen-bonding (type of intermolecular interaction) interactions. Form III was observed at 2.2 GPa and is characterised by an abrupt change affecting all of the angles formed between NO_2 groups and pyrazole rings. Form IV was observed at 5.3 GPa as a new polymorph of 3,4,5-TNP. The structure of Form IV was determined using single crystal X-ray diffraction data. The neutron powder diffraction data was also found to be consistent with single crystal X-ray diffraction data for Form IV at pressures above 5.3 GPa. Form IV appears to be more sensitive to initiation as demonstrated by its spontaneous initiation at elevated pressures during both neutron experiments. This increased impact sensitivity of Form IV compared to Form I was

rationalised using a computational technique based-on vibrational structure of molecules. This work, therefore, highlights that pressure-induced polymorphism has a high probability of significantly altering the sensitivity of energetic materials.

Co-crystallisation/salt formation is a technique in which two or more chemicals are crystallised into one crystal structure. Chapters 4 and 5 explore the use of co-crystal/salt-formation to tune the energetic performance of a variety of nitropyrazole-based energetic materials. These techniques can be used for modifying key energetic properties such as sensitivity, thermal/chemical stabilities, processability, and energetic performance. The main motivation of co-crystallisation/salt formation studies was to establish structure-property relationships of novel co-crystals and salts of nitropyrazoles and to understand the extent to which these techniques are applicable for tailoring the properties of nitropyrazoles. As a result of broad co-former investigation, pyridine, substituted pyridines, and morpholine were found to be suitable co-formers for nitropyrazoles. 1,3-dinitropyrazole (1,3-DNP), 3,5-dinitropyrazole (3,5-DNP) and 3,4,5-trinitropyrazole (3,4,5-TNP) were crystallised with a selection of co-formers including pyridine, substituted pyridines, and morpholine resulting in 9 salts and 3 co-crystals. Structural characterisation of these compounds was performed using SXRD and NPD. The energetic parameters which reflects 'the power' of the co-crystals/salts were predicted using a suitable program (EXPLO 5). The co-crystals and salts were exposed to heat and their thermal properties (melting and decomposition temperatures and behaviours) were observed. The thermal properties, impact sensitivities and energetic performance parameters were found to be altered upon co-crystallisation/salt formation. These material properties were attempted to correlate with structural features including crystal density, crystal-packing motif and intermolecular interactions. Intermolecular interactions were analysed in detail and hydrogen bonding appeared as the main factor increasing the stabilities of these salts and co-crystals. In Chapter 5, six halogen (Group 7A of the periodic table are the halogens) containing salts and co-crystals were investigated in the same group for highlighting the importance of halogen bonding in influencing energetic properties of materials. It is demonstrated that in addition to hydrogen bonding, halogen bonding contributes to the stability of these multicomponent structures and increase their crystal densities. In summary, it is seen that co-crystallisation/salt formation is demonstrated to be an efficient technique to tailor the energetic properties of nitropyrazole-based energetic materials.

Declaration

I declare that this thesis was written by myself and that the work detailed in this thesis is my own, or I have contributed substantially to such work, except where specific reference is made to the work of another.

Nurunnisa ATCEKEN

Acknowledgements

I would like to thank to everyone who helped and supported me in the course of this PhD. My biggest thanks to Prof. Colin Pulham for broadening my perspective in science and being a very supportive, motivating and diligent supervisor. Except all, I feel so lucky to have him as a good host and guide for this special time of my life in Scotland.

My other chance over the period of my PhD was to have Prof. Carole Morrison as my second supervisor. I would like to thank to her for being a good role model, introducing me computational chemistry, and for her sincere conversations full of science and motivation. Thanks to Dr. Craig Bull for his kind helps with neutron experiments at ISIS along with Dr. Nick Funnel. Also thanks to Dr. Xiaojiao Liu for conducting high-pressure X-ray diffraction experiments and for her friendship, everyday walks with 'What's for dinner?' chats. I thank to Dr. Gary Nichol for collecting single crystal X-ray data. Also, I would like to thank to Morrison group for the computational studies they conducted in this thesis, particularly, Jack Hemingway for phonon calculations and Imogen Christopher for heat of formation calculations. I also thank to Dr. Adam Michalchuck for his helps about computational part and answering my weird science questions without complain.

I would like to thank to Turkish Ministry of National Education for funding my school and living expenses during my PhD.

I want to say a big thank you to the Pulham Group including the current and previous members for their invaluable companionship and for sharing great memories during the conferences we attended all around the world. Hayleigh Lloyd, Xiaojiao Liu, Nilgun Sen (for being a sister), Angela Fong, Hannah Logan, Emily Goddard, Karl Hope, Rowan Clark, Akachai Khumsri, Sumit Konar, Oleg Nerushev and Stuart Kennedy, thank you! I want to thank office B11 mates: Nicola Kennedy and Chris Jones for making a fun writing environment and their friendships. Ellie Barber, thank you for being a fabulous flatmate, office mate and thesis writing buddy at the same time. Also many thanks to my Turkish friends for their friendship during this challenging global pandemic days: Selin, Meltem, Buse, Kadir and Murat, thank you.

Finally, my the most special thanks to my precious parents, grandmother (I believe she watches me), sister and nephews who always love and support me unconditionally.

This thesis is dedicated to my family who are my endless source of love, encouragement and motivation.

“Somewhere, something incredible is waiting to be known.”

— Carl Sagan

Contents

Abbreviations

1,3-DNP	1,3-dinitropyrazole
3,5-DNP	3,5-dinitropyrazole
3,4,5-TNP	3,4,5-trinitropyrazole
NMR	Nuclear Magnetic Resonance
SXRD	Single Crystal X-Ray Diffraction
NPD	Neutron Powder Diffraction
EoS	Equation of State
DSC	Differential Scanning Calorimetry
TGA	Thermogravimetric Analysis
BKW	Becker-Kistiakowsky-Wilson
Pyr	Pyridine
AmPyr	4-aminopyridine
AmPic	2-amino-6-picoline
DMAP	4-dimethylaminopyridine
Morph	Morpholine
AmClPyr	3-amino-2-chloropyridine
FPyr	3-fluoropyridine
BrPyr	3-bromopyridine
IPyr	3-iodopyridine

Chapter 1 Introduction

1.1 Energetic Materials

Definition

Energetic materials are chemical compositions that can react rapidly, when suitably triggered by impact, shock, spark or friction, to release large amounts of energy and heat as a result of exothermic decomposition reactions. Applications are broad and include military and civilian use, e.g. munitions, mining, quarrying, construction, demolition, space research and entertainment. [1]

Key properties of many energetic materials include C/H/N ratio, detonation velocity, oxygen balance, heat of formation, crystal morphology, density, defects, thermal and chemical stability, melting point and sensitivities to impact, friction, spark and shock. Detonation velocity refers to the shock wave that moves through an explosive upon detonation and is a critical parameter related to the energetic performance of the material. Both oxygen balance and gravimetric density are the main factors influencing the detonation velocity and detonation pressure of explosives. The oxygen balance represents the degree to which an explosive can be oxidised. If there is an amount of oxygen left unreacted after the oxidation, the energetic compound has a 'positive' oxygen balance. However, if the oxygen is completely used and excess fuel remains, the compound have a 'negative' oxygen balance. Molecules that have zero or a positive oxygen balance are more likely to be more powerful explosives. Sensitivity to initiation is seen as an important and challenging issue for energetic materials due to safety concerns. Factors that influence sensitivity include chemical structure, crystal packing, particle size and intra- and inter-molecular interactions. [2]

Classification

High-energy materials are classified according to their utilisation and performance. Taking into account their chemical nature, they can broadly be classified as three types; primary, and secondary explosives and propellants. Primary explosives are very sensitive materials and easily detonate by the application of heat, electrical spark, impact or friction. Their detonation velocities typically lie in the range of 3500-5500 ms^{-1}. They are used in small quantities within initiating devices, detonators and

percussion caps. Typical primary explosives include lead azide, lead styphnate, mercury fulminate, silver azide, and tetrazene hydrate. [3,1] Chemical structures of these compounds are given in Figure 1.1.

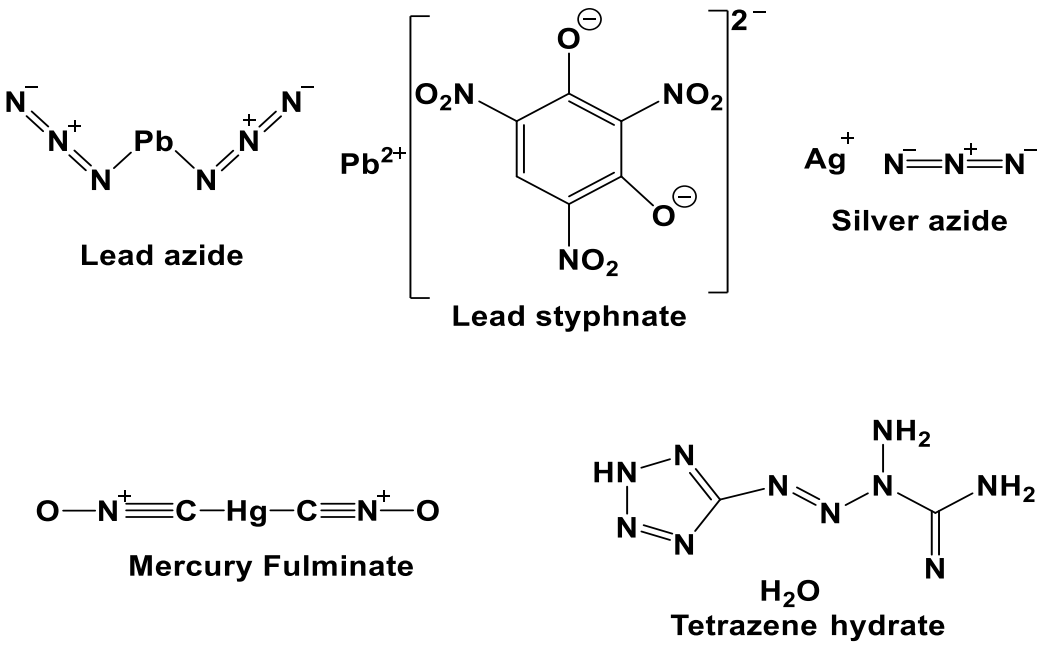

Figure 1.1 Molecular structures of typical primary explosives

Secondary explosives are materials that are mechanically and thermally less sensitive than primary explosives. However, their energetic performance is better than primary explosives, with detonation velocities in the range 5500-9000 ms^{-1}. Initiation of a secondary explosive usually requires energy to be released by a primary explosive. Whereas primary explosives can be initiated by heat, secondary explosives generally need shock waves or impact for initiation. TNT (2,4,6-trinitrotoluene), HMX (octahydro-1,3,5,7-tetranitro-1,3,5,7-tetrazocine), RDX (1,3,5-trinitroperhydro-1,3,5-triazine), NTO (3,5-nitrotriazolone) and CL-20 (Hexanitrohexaazaisowurtzitane), shown in Figure 1.2, are some of the commonly used secondary explosives.[4]

Propellants (sometimes known as low explosives) do not detonate quickly, but instead they exhibit sub-sonic burning. This group of materials often deflagrate and release large amounts of hot gas which accelerate projectiles, such as rockets, bullets, shells and missiles. On account of to these properties, they are used as an ingredient for

rocket fuels and as gun propellants.[5] Typical examples include hydroxylammonium nitrate, nitrocellulose, nitroglycerin, liquid hydrogen, hydrazine and its derivatives.

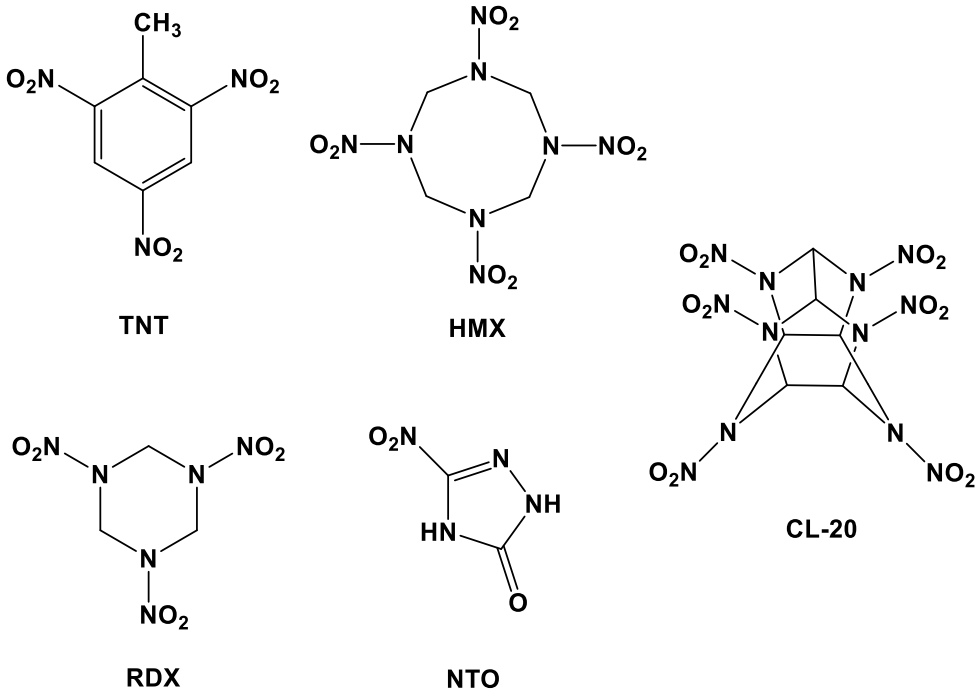

Figure 1.2 Molecular structures of some secondary explosives

As an example, initial decomposition reaction mechanism of nitroglycerin is given in Figure 1.3. The decomposition mechanisms of nitroglycerin at varying temperatures (2500, 2750, 3000, 3250 and 3500 K) are simulated using a computational technique by Zeng et al.[6] As a result, the initial decomposition mechanisms of nitroglycerin are mainly found to be O-NO_2 bond dissociation and the hydrogen capture reaction of NO_2. The main thermal decomposition products are NO_2, NO, HNO, CO_2, N_2, and H_2O. CO_2, N_2, and H_2O are determined as the final products.

Pyrotechnics are known as another class of energetic materials. Their formulations generally include metals and inorganic compounds that can be burnt when suitably initiated. This group of energetic compounds are used to produce special effects for entertainment or other specific aims such as to protect aircraft from heat-seeking missiles. [7]

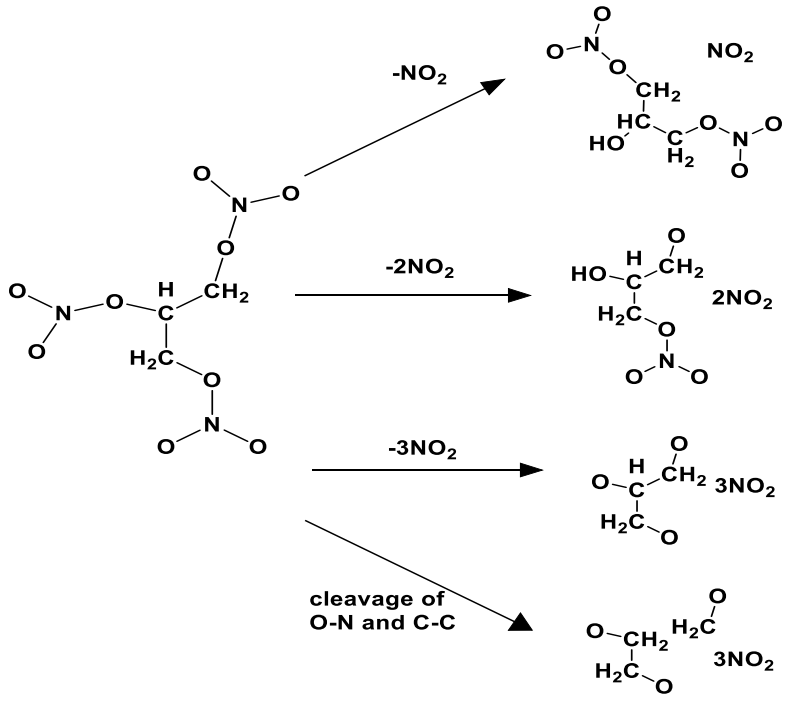

Figure 1.3 Initial decomposition mechanism of nitroglycerin (taken from ref [6] and modified)

1.1.1 Sensitivity of Energetic Materials

Due to their high chemical energy content, energetic materials represent a potential danger during their manufacture, storage and transport. The sensitivity of an energetic material determines its deployment susceptibility to initiation upon a mechanical, thermal or electrostatic stimulus. [8] Hence, sensitivity is commonly classified depending on the type of the stimulus which initiate the detonation such as impact, friction, electrostatic and heat sensitivity.

Impact and friction sensitivities represent the ease with which an energetic material can be initiated by mechanical stimuli. [8] Another prevalent reason for unintended initiations of energetic materials is electrostatic discharge. Sensitivity to spark is named as electrostatic sensitivity and is determined using capacitors charged with different amounts of electrical energies. [9,10] The application of heat can also initiate explosives if they are particularly thermally sensitive. An explosion can be initiated if heat generated from a decomposition reaction is greater than the loss of heat. [11]

Recent developments of novel explosive materials have focused on reducing the sensitivity of the explosive materials to accidental initiation by external stimuli.

Explosive materials that have reduced sensitivity are called Insensitive Munitions, (IM). Although these explosive materials are insensitive to accidental initiation they still perform very well when suitably initiated.[1] The United Nations has published a regulation which groups the energetic materials according to their sensitivities, see Table 1.1.

Table 1.1 United nations regulation for the transportation of dangerous goods [10]

	Sensitivity to impact (J)	**Sensitivity to friction (N or J m^{-1})**
Insensitive	> 40	> 360
Less sensitive	35-40	*ca.* 360
Sensitive	4-35	80-360
Very sensitive	< 4	10-80
Extremely sensitive		< 10

1.1.2 Thermal Stability of Energetic Materials

The thermal stability of energetic materials represents the stability of a compound to decomposition when exposed to heat. The thermal behaviour of energetic compounds is usually investigated by differential scanning calorimetry or accelerating rate calorimetry techniques. [11] Some essential thermal data such as onset temperature of melting or decomposition, type of a reaction (endothermic, exothermic) can be extracted by using these techniques. Another useful parameter to assess thermal stability and reactivity of an energetic material is bond dissociation energy. [12] The dissociation energy of the weakest bond, which is often the first bond to be broken in a molecule, has a big effect on thermal stability. Moreover, the elucidation of thermal decomposition mechanisms allows predictions to be made about the stabilities of energetic compounds. [13]

Melting (T_m) and decomposition (T_d) temperatures are important properties affecting application areas of energetic materials. Melt-casting is a commonly used method for loading energetic materials into a munition with advantages such as avoiding void space in the munition and allowing high processing efficiency. In order to apply this method efficiently, “melt-castable energetic materials” should be used. Distinctive characteristics of melt-castable materials are high - densities, low - melting point, and a large gap in between the onset temperature of decomposition and melting. An ideal melt-castable material should possess a high density, a low melting temperature

(typically 70 to 120ºC), and have a large temperature gap before the onset of decomposition. [14]

For energetic materials, a low T_m can be desirable to facilitate melt-casting, a process whereby the molten energetic materials is extruded into a closed cavity. On the other hand, a high T_m can be favourable for producing munitions that can withstand deformation prior to detonation.[14] On the other hand, a high T_d promotes a higher detonation temperature which in turn enhances the energetic performance of an explosive, allowing deeper penetration into a target. [15]

1.1.3 Structure – Property Relationships in Energetic Materials

Key properties of energetic materials are governed by their chemical composition and crystal structure. For example, detonation velocity and detonation pressure are usually proportional to crystal density. [16] The enthalpy of formation of an EM is also a key factor that influences detonation performance. [17] Using software such as EXPLO5, detonation parameters can be estimated. [18] However, due to complex mechanisms of initiation, correlations between the structure and sensitivity to initiation have not been fully explained. It is known that sensitivity of EMs is governed by the crystal packing motif and intermolecular interactions such as hydrogen bonding, halogen bonding and π-π interactions formed within structures. [19] Several studies have identified that a layered crystal packing motif was found to be useful for reducing impact sensitivity. This has been rationalised as follows. When an EM is exposed to an impact, shear stress is produced initially and this induces hot-spot formation with time and increasing temperature, ending up with decomposition and detonation of an energetic material. [20,21] The shear-sliding characteristic present in layered structures has a strong effect on impact sensitivity mechanism of an energetic compound. On account of strong π-interactions, the parallel layered structures act to dissipate the mechanical energy introduced from shock initiation through delocalised phonon vibrations, thus mitigating against the formation of hot-spots in the material and thus reducing mechanical sensitivity. [22-23] Vibrational up-pumping theory which explains how external mechanical impact is transferred via vibrational modes is given with more details in section 3.4.6.

Molecular properties have also been shown to correlate with energetic properties. Electrostatic potentials [24], vibrational properties [25], bond dissociation energies, NMR

shifts [26] and HOMO-LUMO gaps have been found to be important parameters affecting the impact sensitivities of energetic materials.

1.1.4 Prediction of Impact Sensitivity

Due to safety concerns and technical challenges, property testing of energetic materials is not always straightforward. Computational methods have, therefore, been developed to predict energetic properties to circumvent these difficulties in application. The fact that vibrational properties of energetic compounds are of great importance on impact sensitivity [27,25,28] and this lead to the "Vibrational Up-pumping Theory", first proposed by Coffey and Toton. [29] The theory was developed later by Dlott and Fayer,[30] and explains the changes in vibrational energy in a system after a shock applied, including the excitations occuring upon mechanical stimuli. More theoretical and technical details of this model are provided in Chapter 3 (Section 3.4.6). This model has been used as a means to predict the impact sensitivities of energetic materials. In a study performed by Michalchuk *et al*., relative impact sensitivities of a group of energetic material: HNB (hexanitrobenzene), *β*-HMX (1,3,5,7-tetranitro-1,3,5,7-tetrazoctane), α-FOX-7 (1,1-dinitro-2,2-diaminoethene), α-NTO (nitrotriazolone), TATB (1,3,5-triamino-2,4,6-trinitrobenzene), ε-CL-20 (hexanitrohexaaza-isowurtzitane) and o-TNT (orthorhombic 2,4,6-trinitrotoluene) were predicted successfully using up-pumping theory calculations based on phonon density of states simulated for each energetic compound. [31]

1.2 Nitropyrazole Family Energetic Materials

Nitrogen-rich chemical compounds are promising candidates to replace conventional explosives, as they generally have positive heats of formation, good thermal stabilities, low friction and impact sensitivities, and high energetic performance. [32] Pyrazole and its nitro derivatives (Figure 1.4) have a significant role in azole-based EMs. The presence of adjacent nitrogen atoms in the pyrazole ring that release dinitrogen gas on decomposition are the main reason behind of the high energy content. [33] Another advantage of such materials is that they release a large amount of dinitrogen gas as a detonation product which is neither toxic nor environmentally harmful, unlike most traditional explosives. [34] They produce less carbon monoxide, soot and other oxidised toxic explosive residues (NO, etc.). [35] They have a large

number of N-N and C-N bonds and therefore exhibit large positive heats of formation. Moreover, oxygen balance, density, detonation velocity and thermal stability of these compounds can be enhanced by adding nitro-groups to the pyrazole ring. A distinctive property of pyrazoles that distinguishes them from other NH-azole groups is that they are able to produce stable, endocyclic N-substituted nitro compounds. Highly nitrated pyrazoles are expected to be powerful explosives, but also useful ingredients for rocket propellants. However, due to their strong acidic characteristics, they can form very sensitive metal salts.

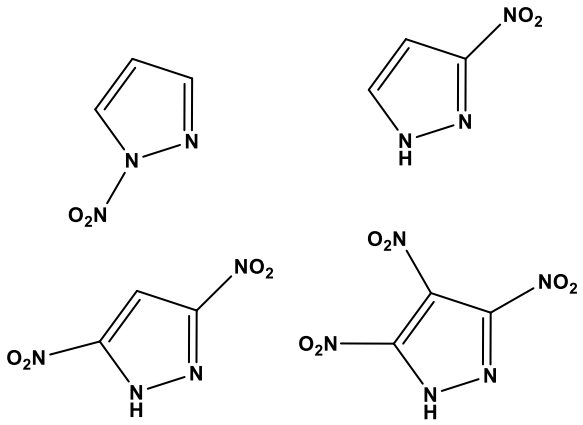

Figure 1.4 Selected nitropyrazole group compounds

1.2.1 Dinitropyrazoles (DNPs)

There has been great interest in dinitropyrazoles in applications such as energetic materials, efficient intermediates for synthesis of pharmaceuticals and ingredients of dye compounds. [36,37] They exhibit high crystal densities (3,4-DNP and 3,5-DNP have densities of 1.76 and 1.79 g cm^{-3} [38]) and thus display better energetic performance than mononitropyrazoles. In addition to their powerful detonation performance, they can be classified as melt-castable materials due to their favorable thermal properties. For example, 3,4-dinitropyrazole possesses low sensitivity and hygroscopicity, and moderate detonation performance with a detonation velocity of 8.24 km s^{-1} and detonation pressure of 28.8 GPa. Moreover, on account of its low melting point (86°C), it has been considered as a melt-castable replacement for TNT.[14] The dinitropyrazole compounds synthesised and used as co-formers of the salts and co-crystals investigated in this thesis were 1,3-dinitropyrazole (1,3-DNP) and 3,5-dinitropyrazole (3,5-DNP). These pyrazole-based compounds have high enthalpies of formation (ΔH_f

). For example, the estimated ΔH_f value for 1,3-DNP is 180 kJ mol^{-1} [39] and the experimental value for 3,5-DNP is 128.5 kJ mol^{-1}. [40] 3,5-dinitropyrazole is an attractive energetic compound with its high thermal and chemical stability among pyrazoles. Dinitropyrazoles are usually synthesised from pyrazoles using sequential nitration steps, and are useful to be precursors for trinitropyrazoles. More details are given in the experimental chapter of this thesis. In order to improve their performance, stability and practical use as energetic materials, N-amination, N-methylation, C-substitution and salt or co-crystal formation have been suggested as possible solutions. [41] For example, LLM-116 (4-amino-3,5-dinitropyrazole) is an insensitive and powerful explosive which has an energy output equal to 90% of HMX. [42]

1.2.2 Trinitropyrazoles (TNPs)

Trinitropyrazoles (3,4,5-TNP, 1,3,4-TNP) with their high densities and enthalpies of formation have attracted significant attention as they can be used as green replacements for conventional powerful explosives. Trinitropyrazoles are usually synthesised either by direct nitration of dinitropyrazoles as in this study [43] or from aminopyrazoles through oxidation. [44] Three nitro groups promote higher detonation velocities and pressures together with good oxygen balance. Among all-carbon-nitrated azoles, 3,4,5-trinitropyrazole is particularly attractive as it exhibits very favourable chemical and thermal stability, e.g. stable up to 200°C, can be stored for 3-4 months at 0-5°C compared to fully nitrated aromatic compounds based on furazanes, furoxanes and polynitroarylenes.[45] However, due to the multi-step synthetic route required for their preparation under harsh conditions with low yield, their practical use is not widespread. However, with different synthetic techniques, this could be improved. For instance, nitration of different pyrazoles can be performed using montmorillonite K-10 impregnated with bismuth nitrate with high yields. [46] The energetic properties of 3,4,5-TNP including detonation performance and sensitivities are provided with more details in Chapter 3.

1.3 Crystal Engineering

Crystal engineering can be described as the understanding of intermolecular interactions and their exploitation for the design of molecular solids with particular

physical and chemical characteristics. [47] It is a relatively new field in chemistry and has its origins in organic solid-state chemistry and in physical chemistry. As a consequence of the advances in X-ray crystallography, structure analysis has become less expensive and more readily available. The enhanced understanding of 3D structures of molecular solids has lead to the development of supramolecular chemistry and has broadened the applications of crystal engineering. The term "crystal engineering" was first coined by Raymond Pepinsky at the meeting of the American Physical Society in 1955. [48] Simultaneously, G. M. J. Schmidt (1950–1970) made significant contributions to this field with his studies in solid-state photochemistry and emphasised that chemical and physical properties of solids are highly influenced by their crystalline structures, such as distributions of molecules in the lattice and intermolecular interactions between them. [49] Crystal engineering seeks to establish meaningful relationships between molecular and supramolecular structures in terms of crystal packing motifs and non-covalent interactions. Supramolecular synthons, which are described by Desiraju as "spatial arrangements of intermolecular interactions" play an important role in the design of compounds with favourable properties using non-covalent interactions.[50] These methods typically rely on hydrogen bonding, on account of the abundance and strength. However, these interactions has recently been extended to encompass other types of interactions, such as halogen bonds and π–π interactions. [51] Therefore, crystal engineering can be seen as an alternative synthetic route for developing functional materials using intermolecular forces rather than covalent bonds. [50]

1.3.1 Hydrogen Bonding

The hydrogen bond is an efficient and well investigated interaction among different types of non-covalent interactions. Although it has been described in many different ways so far, it is defined comprehensively by IUPAC as '*an attractive interaction between a hydrogen atom from a molecule or a molecular fragment X–H in which X is more electronegative than H, and an atom or a group of atoms in the same or a different molecule, in which there is evidence of bond formation*'.[52] The donor-acceptor relationship behind hydrogen bonding can be symbolised simply by X-H···Y-Z, where three dots denote hydrogen bond interaction, X-H is hydrogen bond donor and Y-Z is hydrogen bond acceptor. Whereas hydrogen-bond acceptors possess a lone pair of electrons or high electron density centre like transition metals, alkenes,

etc., hydrogen-bond donors are able to remove electron density from the hydrogen atom by creating a positive charged region. Some typical examples of hydrogen-bond donors and acceptors are given in Table 1.2. Illustrations of some representative hydrogen bonding synthons are shown in Figure 1.5.

Table 1.2 Examples for hydrogen bond donors and acceptors

Donors	**Acceptors**
C-H	C=C, arenes
N-H	N
P-H	P
O-H	O
S-H	S
F-H	F
Cl-H	Cl
Br-H	Br
I-H	I

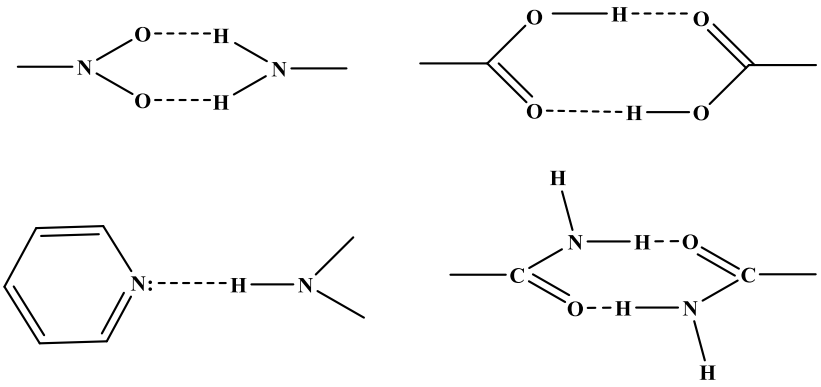

Figure 1.5 Some typical examples for hydrogen bonding synthons

One of the distinctive properties of the hydrogen bond is its directionality. Strong hydrogen bond tends to form linearly between molecules. However, weaker hydrogen bonds may be affected by other interactions and the bond angle (θ) may vary between 110° and 180°. The other important aspect is the length of the bond, which changes depending on its strength. When both molecules that form hydrogen bonds are neutral, the bond energy lies in the region 10 - 65 kJ mol^{-1}. This value can reach up to 190 kJ mol^{-1}, if one of the components is charged.[53] The strength of hydrogen bonds is dependent on the electronegativities of the atoms involved in hydrogen bonding. Hydrogen bonds are mostly classified based on the interaction strength, illustrated in

Table 1.3. In weak hydrogen bonds, either donor or acceptor or both of the moieties possess moderate to low electronegativities. Most of the hydrogen bonds in nature exhibit moderate strength. Hydrogen bonds formed between water molecules, proteins or nucleic acids are examples of interactions with moderate strength. Finally, strong hydrogen bonds are mostly observed between molecular ions. [54]

Table 1.3 Classification of hydrogen bond in a D-H···A system

	Strong	**Moderate**	**Weak**
Interaction type	Mostly covalent	Mostly electronic	Electrostatic
H…A (Å)	1.2-1.5	1.5-2.2	2.2-3.2
D…A (Å)	2.2-2.5	2.5-3.2	3.2-4.0
Bond angles (°)	175-180	130-180	90-150
Bond length relations	D–H ≈ H···A	D–H < H···A	D–H << H···A
Examples	F^-···HF, Cl···H_2O	Acids, alcohols, amines	X-H···π, H-F···N_2, C-H···O

1.3.2 Halogen Bonding

The halogen bond is defined by IUPAC as follows: *"A halogen bond occurs when there is evidence of a net attractive interaction between an electrophilic region associated with a halogen atom in a molecular entity and a nucleophilic region in another, or the same, molecular entity"*. [55] It is driven by the interaction between a Lewis acid represented by a halogen atom and a Lewis base.[56] The schematic illustration of a halogen bond is R-X···Y, and illustrated in Figure 1.6. The electron density of a halogen atom is anisotropically distributed when the atom is covalently bound to one atom, to a group or to multiple groups. Hence, an electrostatic interaction occurs between the partial electrophilic region of a halogen atom (X), termed a σ-hole and a nucleophile (Y), similar to a hydrogen bond. The strength of the halogen bond varies from 5 to 180 kJ mol^{-1} and increases as the electronegativity of X decreases, and the electron-withdrawing ability of R increases. [55]

Figure 1.6 Schematic illustration of a halogen bond

Whilst hydrogen bonding interactions have been the focus for many crystal engineering studies, the focus has recently expanded towards the halogen bonding motif as a crystal engineering tool, especially when studying molecules that lack hydrogen bond donor or acceptor moieties. [57] Due to its high directionality and adjustable interaction strength, halogen bonding may be used as an important tool for producing materials with improved response to optical fields and for building photoresponsive supramolecular complexes. [58,59]

1.3.3 π-π Interactions

π - π interactions are formed between π-orbitals that exist in aromatic rings. These interactions occur when π - σ attractions overcome unfavourable interactions such as π -electron or π - π repulsions. Although the stacking of aromatic rings can be perfectly aligned (see Figure 1.7a), often there is an off-set of alignment between molecules (see Figure 1.7b). There are some different conformations: (a) face-to-face, (b) edge-to-face and (c) T-shaped (Fig 1.7). The T-shaped conformations are observed when C-H···π interaction formed. Stacking distance varies over the range of 3.3-3.8 Å when the parallel alignment exists between two aromatic rings. [60]

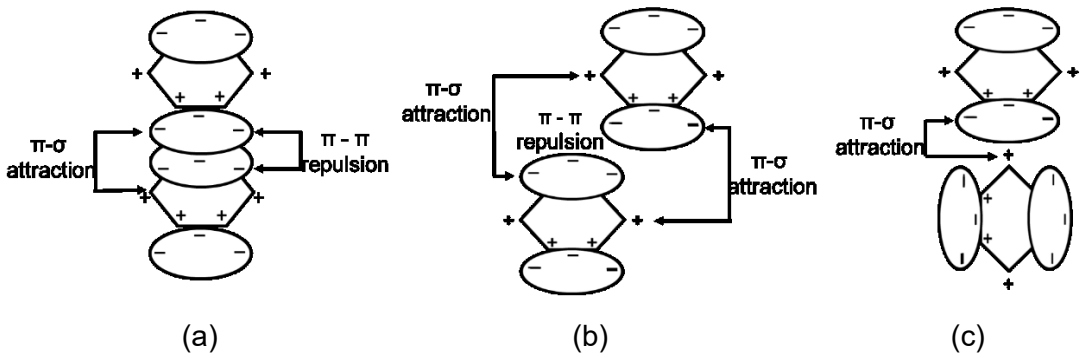

Figure 1.7 Different conformations of π-π stacking (a) face-to-face, (b) edge-to-face and (c) T-shaped

1.4 Co-crystallisation and Salt Formation

Co-crystallisation is a supramolecular technique in which two or more different neutral compounds (often termed co-formers) are combined with certain stoichiometric ratios in a crystalline lattice through intermolecular interactions. In salt formation, as distinct

from co-crystallisation, proton transfer is observed between co-formers, see Figure 1.8. Examples for a co-crystal and a salt are given in Figure 1.8. [61] The acid ionisation constant, pK_a, is commonly used to estimate molecular ionisation states. There is a rule called "ΔpK_a rule" see scheme 1.1. which is commonly exploited in the design of pharmaceutical co-crystals. According to the rule, a pair of compounds that have a ΔpK_a value lower than -1 ($\Delta pK_a < -1$) will form a co-crystal and higher than 4 ($\Delta pK_a > 4$) will form a salt. There will be undefined result (salt or co-crystal) for the ΔpK_a value between -1 and 4. [62]

There are some aspects that should be considered while seeking co-formers which are able to form co-crystals or salts.

Scheme 1.1 Equations for ΔpK_a

$$HA + H_2O \rightleftharpoons H_3O^+_{(aq)} + A^-_{(aq)} \qquad K_a = [H^+][A^-]/[HA]$$

$$B + H_2O \rightleftharpoons BH^+_{(aq)} + OH^-_{(aq)} \qquad K_b = [OH^-][HA]/[A^-]$$

$$pK_a = -\log_{10}K_a$$
$$pK_b = -\log_{10}K_b$$

ΔpK_a = pK_a (of conjugate acid) – pK_a

ΔpK_a is the difference in pK_a between **the pK_a of the conjugate acid** of the base (14-pK_b of base) and **pK_a** of the acid.

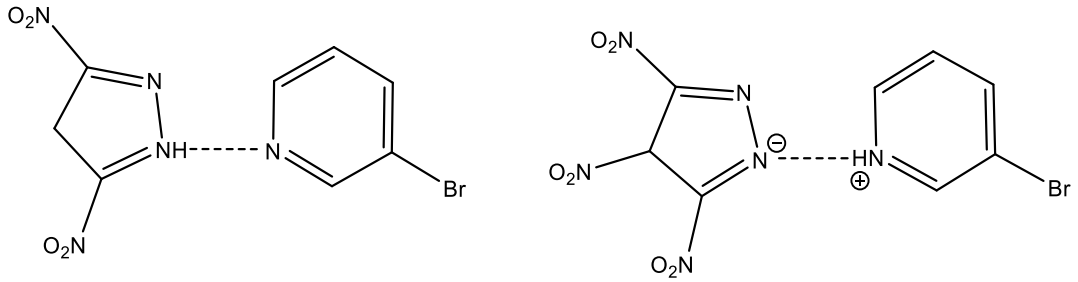

(a) Co-crystal (b) Salt

Figure 1.8 Example of a salt and a co-crystal

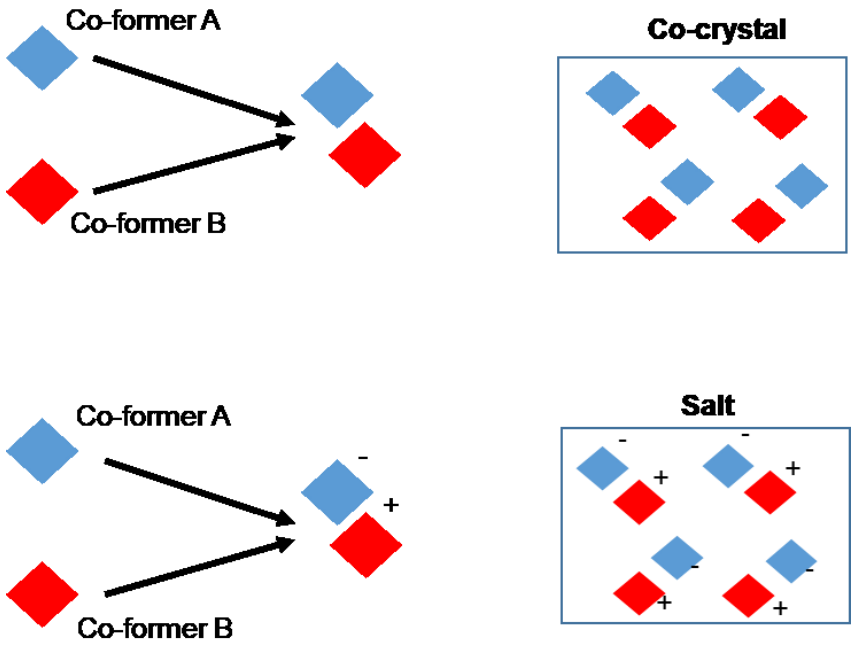

Figure 1.9 Scheme describing the basic principle of co-crystallisation and salt formation

The physicochemical properties of materials, such as melting point, conductivity, solubility, density *etc*. can be changed via multi-component molecular crystal formation techniques without changing their intrinsic chemical structures. Co-crystallisation and salt formation are therefore useful approaches for the development of the compounds with enhanced and targeted characteristics. These techniques found applications in the pharmaceutical industry, e.g. as a means to improve the solubility and processing of drug compounds. [61,63]

1.5 Co-crystals and Salts in Energetic Materials

Although co-crystals and salts of the pharmaceutical compounds have been well studied and applied in the pharmaceutical industry, it remains relatively new, but rapidly evolving technique in the field of energetic materials field. It has readily been introducing solutions to modify the physicochemical properties of energetic materials, by influencing oxygen balance, detonation pressure, velocity and sensitivity (to impact, friction and electrostatic discharge) as well as altering thermal chemical stability. [64,65] As the development of new energetic materials requires high levels of safety and performance requirements, only a limited number of potential energetic materials can be used practically in civilian or military technologies. [66] It is therefore

highly attractive to explore co-crystal formulations of known energetic materials as a route to modifying energetic properties and performance.

TNT, being a traditional explosive with moderate energetic performance and low sensitivity, has been subject of many co-crystallisation studies. 17 co-crystals of TNT with a group of polycyclic aromatic hydrocarbons were explored and investigated by Landenberger and Matzger in 2010. They highlighted the importance of the strong π-π interactions present in co-crystals of TNT and explained structure-property relationships in these examples. It was also observed that combining TNT with non-energetic compounds lowered the energetic performance of TNT. [67] Hence, co-crystals containing two energetic components are seen as attractive route to prevent the reduction in detonation velocity and pressure. For example, Bolton and Matzger combined TNT and CL-20 in a 1:1 ratio. The resulting co-crystal exhibited a better sensitivity without compromise of its detonation performance. The enhancement of the sensitivity was attributed to higher thermodynamic stability of the co-crystal compared to its co-formers. [68] Another explosive which has attracted great interest is CL-20, on account of it being most powerful energetic compound in use. However, the high sensitivity of CL-20 limits its practical use and so there is a drive to "tame" this energetic compound. In addition to the TNT/CL-20 co-crystal, a 2:1 co-crystal of the highly sensitive CL-20 with less sensitive HMX has been shown to be successful example, whereby the resulting co-crystal exhibited a lower impact sensitivity similar to β-HMX, thus eliminating safety concerns and broadening the potential application areas for CL-20. The reduced sensitivity reported for the CL-20/HMX co-crystal has been attributed to an increase in hydrogen bonding relative to the crystal structures of pure CL-20 and HMX. [69]

The other efficient technique for modifying materials is salt formation which is particularly useful for dealing with the acidity problem of some energetic materials. Salts are usually advantageous since they have high positive heats of formation and better chemical stabilities compared to their non-ionic analogues. They also possess low vapour pressures, which prevents the risk of exposure through inhalation.[70] Therefore, it becomes a useful tool for developing energetic formulations with favourable characteristics. For example, the hydroxylammonium salt of 3-dinitromethyl-1,2,4-triazolone was prepared and characterised by Zhang *et* al. This energetic salt, which possesses strong hydrogen bonding, π- π stacking and high nitrogen content, exhibited better impact and friction sensitivities, higher thermal

stability and detonation performance compared to the parent energetic compound. [71] Ammonium dinitramide (ADN) is another well-known example of an energetic salt that is an environmentally benign compound and exhibits outstanding performance as a rocket propellant. [72]

1.6 Co-crystals and Salts of Nitropyrazoles

Nitropyrazoles characterised by a 5-membered heterocycle ring with high nitrogen content take a significant place in azole-based family of energetic materials. They have been involved in many multi-component self-assembled structure investigation since they provide variety of synthons promoting non-covalent interaction formation. In addition to be an aromatic ring allowing the strong π-π interactions, nitropyrazoles possess suitable synthons that can act as hydrogen bond donors and acceptors. The variety of synthons can be increased with the suitable substitution of functional groups such as methyl, amino, or halogen, etc. An energetic-energetic co-crystal between 1-methyl-3,4,5-trinitropyrazole and CL-20 was reported by Ma et al. [73] The resulting co-crystal has an improved sensitivity compared to CL-20, outstanding energetic performance with a detonation velocity of 9347 m s^{-1} and a detonation pressure of 40.5 GPa. Another pyrazole-based energetic co-crystal was formed between 4-amino-3,5-dinitropyrazole and 3,4-diaminofurazan (DAF) which exhibited melt-castable behavior with an increased energetic performance comparing to DAF. [74]

There are also numerous salts of nitropyrazole-based energetic materials that have been investigated. Due its high density (1.90 g cm^{-3}) and acidic nature, 4-amino-3,5-dinitropyrazole has been useful tool as an anion source. Fifteen salts of 4-amino-3,5-dinitropyrazole with different bases (including ammonia, bicarbonate, a group of triazoles, aminoguanidinium sulfate) were prepared and characterised by Zhang *et* al. [75] The salts were found to have low sensitivities, acceptable thermal stabilities and energetic performance. The salts formed with carbohydrazinium (32.55 GPa, 8743 m s^{-1}) and diaminoguanidinium (28.85 GPa, 8751 m s^{-1}) appeared to be powerful explosives exhibiting a high performance close to known powerful explosives such as 1,3,5-triamino-2,4,6-trinitrobenzene (TATB, 31.15 GPa, 8114 m s^{-1}). In another study performed by Zhang *et* al., 14 different salts of 3,4,5-trinitropyrazole (3,4,5-TNP) were prepared with different nitrogen-rich cation sources such as triazoles, guanidines and imidazoles. All the salts exhibited high energetic performance (23.74-31.9 GPa, 7586-8543 m s^{-1}) and low sensitivities (≥ 35 J) suggesting that they can

find potential applications in energetic materials field. [38] In a slightly different application area, 3,5-dinitropyrazole (3,5-DNP) and 3,4,5-trinitropyazole were used as anions in pyrotechnic formulations containing metal salts. 3,5-DNP and 3,4,5-TNP provide environmentally friendly solutions for producing green pyrotechnics. The resulting materials were found to have low sensitivities, high energetic performances and favourable color properties. [76] As can be seen from the literature, application for nitropyrazole-based energetic materials have been expanded with the studies highlighting their practical uses for different purposes.

1.7 Motivation of the Study

The study described in this thesis has mainly focused on a high-pressure investigation and co-crystal/salt-formation studies of pyrazole-based energetic materials. This group of energetic compounds were chosen to be the subject of this thesis due to their favourable properties and growing interests on them as potential replacements of traditional energetic materials. They also provide numerous opportunities in terms of multicomponent crystallisation studies as they have various synthons that can act as donors and acceptors for different types of non-covalent interactions such as hydrogen bond and π-π stacking. Among this group of compounds, 3,4,5-TNP has been found to be particularly interesting due to its superior detonation performance and low sensitivities to impact, friction and spark. The lack of high-pressure studies of 3,4,5-TNP provided the main motivation for the high-pressure experiments performed in this thesis.

The other important part of this study focused on co-crystallisation and salt formation of nitropyrazole-based energetic materials to correlate the structures of energetic materials to their energetic properties. Therefore, the main motivation of multicomponent crystallisation studies was to establish structure-property relationships using novel co-crystals and salts formed between nitropyrazoles and derivatives of pyridines. This study aims to understand the extent to which co-crystallisation is an applicable method for tailoring the properties of this group of azole compounds. The resulting energetic compounds were characterised in terms of their physicochemical and energetic properties including crystal density, impact sensitivity (for a limited number of them), detonation velocity and pressure (calculated), melting and decomposition points.

1.8 References

1 J. Akhavan, in *RSC publishing*, ed. J. Akhavan, Royal Society of Chemistry, Cambridge, 3rd edn., 2004, pp. 1–181.

2 C. M. Tarver, *High Energy Materials, Propellants, Explosives and Pyrotechnics, Jai Prakash Agrawal*, 2010, vol. 35.

3 W. C. Davis, *Explos. Eff. Appl.*, 1998, 1–22.

4 J. Akhavan, in *Chemistry of Explosives*, ed. J. Akhavan, Royal Society of Chemistry, 3rd edn., 2011, pp. 27–59.

5 J. P. Agrawal, in *High energy materials: Propellants, Explosives and Pyrotechnics*, WILEY-VCH Verlag GmbH & Co. KGaA, weinheim, 2010, pp. 209–330.

6 T. Zeng, R. Yang, J. Li, W. Tang and D. Li, *Combust. Sci. Technol.*, 2021, **193**, 470–484.

7 J. P. Agrawal, in *High Energy Materials*, ed. J. P. Agrawal, WILEY-VCH Verlag GmbH & Co. KGaA, Weinheim, 2010, pp. 331–412.

8 J. P. Agrawal, in *High Energy Materials: Propellants, Explosives and Pyrotechnics.*, ed. J. P. Agrawal, WILEY-VCH Verlag GmbH & Co. KGaA, Weinheim, 2010, pp. 1–67.

9 P. A. Davies, *J. Hazard. Mater.*, 1994, **38**, 75–88.

10 T. M. Klapötke, *Chemistry of High-Energy Materials*, Walter de Grutyer, Munich, 2nd editio., 2012.

11 M. Abd-Elghany and T. M. Klapötke, *Phys. Sci. Rev.*, 2018, **3**, 1–14.

12 G. Bao, R. Y. Abe and Y. Akutsu, *J. Therm. Anal. Calorim.*, 2020, **143**, 3439–3445.

13 L. P. Smirnov, *Usp. Khim.*, 2004, **73**, 1210–1232.

14 P. Ravi, D. M. Badgujar, G. M. Gore, S. P. Tewari and A. K. Sikder, *Propellants, Explos. Pyrotech.*, 2011, **36**, 393–403.

15 J. Akhavan, in *Chemistry of Explosives*, ed. J. Akhavan, Royal Society of Chemistry, London, 3rd edn., 2011, pp. 74–84.

16 D. K. Anand, M. S. Firebaugh, Y. Horie, R. E. Kaczmarek, R. A. Kavetsky, T. M. Klapötke, D. R. Lynch, B. M. Rice and J. M. Short, *Topics in Energetics Research and Development*, calce EPSC Press, southern maryland, 2013.

17 R. N. Rogers, *Thermochim. Acta*, 1975, **11**, 131–139.

18 M. Suceska, in *1st International Symposium on Explosion, Shock Wave and Hypervelocity Phenomena (ESHP)*, 2004, pp. 325–330.

19 C. Zhang, F. Jiao and H. Li, *Cryst. Growth Des.*, 2018, **18**, 5713–5726.

20 Y. Cai, F. P. Zhao, Q. An, H. A. Wu, W. A. Goddard and S. N. Luo, *J. Chem. Phys.*, , DOI:10.1063/1.4825400.

21 A. Tokmakoff, M. D. Fayer and D. D. Dlott, *J. Phys. Chem.*, 1993, **97**, 1901–1913.

22 C. Zhang, X. Wang and H. Huang, *J. Am. Chem. Soc.*, 2008, **130**, 8359–8365.

23 Y. Ma, A. Zhang, C. Zhang, D. Jiang, Y. Zhu and C. Zhang, *Cryst. Growth Des.*, 2014, **14**, 4703–4713.

24 J. S. Murray, M. C. Concha and P. Politzer, *Mol. Phys.*, 2009, **107**, 89–97.

25 A. A. L. Michalchuk, M. Trestman, S. Rudić, P. Portius, P. T. Fincham, C. R. Pulham and C. A. Morrison, *J. Mater. Chem. A*, 2019, **7**, 19539–19553.

26 S. Zeman and M. Jungová, *Propellants, Explos. Pyrotech.*, 2016, **41**, 426–451.

27 A. A. L. Michalchuk, S. Rudić, C. R. Pulham and C. A. Morrison, *Phys. Chem. Chem. Phys.*, 2018, **20**, 29061–29069.

28 A. A. L. Michalchuk, P. T. Fincham, P. Portius, C. R. Pulham and C. A. Morrison, *J. Phys. Chem. C*, 2018, **122**, 19395–19408.

29 C. S. Coffey and E. T. Toton, *J. Chem. Phys.*, 1982, **76**, 949–954.

30 D. D. Dlott and M. D. Fayer, *J. Chem. Phys.*

31 A. A. L. Michalchuk, J. Hemingway and C. A. Morrison, *J. Chem. Phys.*, 2021, **154**, 064105.

32 P. Yin and J. M. Shreeve, *Nitrogen-Rich Azoles as High Density Energy Materials: Reviewing the Energetic Footprints of Heterocycles*, Elsevier Ltd, 2017, vol. 121.

33 I. Dalinger, A. Pivkina, O. Gryzlova, V. Korolev, T. Pivina, Y. Nelyubina, S. Shevelev, N. Muravyev, K. Monogarov and Y. Frolov, *Proc. Int. Pyrotech. Semin.*, 2012, **38th**, 479–493.

34 M. F. Bölter, A. Harter, T. M. Klapötke and J. Stierstorfer, *Chempluschem*, 2018, **83**, 804–811.

35 T. Brinck, *Green Energetic Materials*, WILEY-VCH Verlag GmbH & Co. KGaA, Stockholm, 1st edn., 2014.

36 P. Yin and J. M. Shreeve, *Nitrogen-Rich Azoles as High Density Energy Materials: Reviewing the Energetic Footprints of Heterocycles*, Elsevier Ltd, 2017, vol. 121.

37 A. A. Zaitsev, I. L. Dalinger and S. A. Shevelev, *Russ. Chem. Rev.*, 2009, **78**, 589–627.

38 Y. Zhang, Y. Guo, Y. H. Joo, D. A. Parrish and J. M. Shreeve, *Chem. - A Eur. J.*, 2010, **16**, 10778–10784.

39 V. P. Sinditskii, T. H. Hoang, A. D. Smirnova, V. Y. Egorshev, N. V. Yudin, I. A. Vatsadze and I. L. Dalinger, *Thermochim. Acta*, , DOI:10.1016/j.tca.2018.07.006.

40 X. Zhao, C. Qi, L. Zhang, Y. Wang, S. Li, F. Zhao and S. Pang, *Molecules*, 2014, **19**, 896–910.

41 C. He, J. Zhang, D. A. Parrish and J. M. Shreeve, *J. Mater. Chem. A*, 2013, **1**, 2863–2868.

42 I. L. Dalinger, I. A. Vatsadze, T. K. Shkineva, A. V. Kormanov, M. I. Struchkova, K. Y. Suponitsky, A. A. Bragin, K. A. Monogarov, V. P. Sinditskii and A. B. Sheremetev, *Chem. - An Asian J.*, 2015, **10**, 1987–1996.

43 G. Hervé, C. Roussel and H. Graindorge, *Angew. Chemie - Int. Ed.*, 2010, **49**, 3177–3181.

44 I. L. Dalinger, G. P. Popova, I. A. Vatsadze, T. K. Shkineva and S. A.

Shevelev, *Russ. Chem. Bull.*, 2009, **58**, 2185.

45 H. Gao and J. M. Shreeve, *Chem. Rev.*, 2011, **111**, 7377–7436.

46 P. Ravi and S. P. Tewari, *Catal. Commun.*, 2012, **19**, 37–41.

47 G. R. Desiraju, *Angew. Chemie - Int. Ed.*, 2007, **46**, 8342–8356.

48 F. Jona, G. Shirane and R. Pepinsky, *Phys. Rev.*, 1955, **98**, 903–909.

49 G. M. J. Schmidt, 1971, **27**, 647–628.

50 G. R. Desiraju, *Angew. Chemie Int. Ed. English*, 1995, **34**, 2311–2327.

51 B. Moulton and M. J. Zaworotko, *Chem. Rev.*, 2001, **101**, 1629–1658.

52 E. Arunan, G. R. Desiraju, R. A. Klein, J. Sadlej, S. Scheiner, I. Alkorta, D. C. Clary, R. H. Crabtree, J. J. Dannenber, P. Hobza, H. G. Kjaergaard, A. C. Legon, B. Mennucci and D. J. Nesbitt, *Pure Appl. Chem.*, 2011, **83**, 1637–1641.

53 C. B. Aakeröy and K. R. Seddon, *Chem. Soc. Rev.*, 1993, **22**, 397–407.

54 P. A. Frey, *Low-Barrier Hydrogen Bonds*, Elsevier Inc., 2nd edn., 2013, vol. 2.

55 G. R. Desiraju, P. Shing Ho, L. Kloo, A. C. Legon, R. Marquardt, P. Metrangolo, P. Politzer, G. Resnati and K. Rissanen, *Pure Appl. Chem.*, 2013, **85**, 1711–1713.

56 P. Metrangolo, H. Neukirch, T. Pilati and G. Resnati, *Acc. Chem. Res.*, 2005, **38**, 386–395.

57 J. Chang, G. Zhao, X. Zhao, C. He, S. Pang and J. M. Shreeve, *Acc. Chem. Res.*, 2021, **54**, 332–343.

58 A. Priimagi, M. Saccone, G. Cavallo, A. Shishido, T. Pilati, P. Metrangolo and G. Resnati, 2012, 345–352.

59 A. Priimagi, G. Cavallo, A. Forni, M. G. Leben, M. Kaivola, P. Metrangolo, R. Milani, A. Shishido, T. Pilati, G. Resnati and G. Terraneo, 2012, 2572–2579.

60 C. Janiak, *J. Chem. Soc. Dalt. Trans.*, 2000, **2000**, 3885–3896.

61 S. Aitipamula, R. Banerjee, A. K. Bansal, K. Biradha, M. L. Cheney, A. R. Choudhury, G. R. Desiraju, A. G. Dikundwar, R. Dubey, N. Duggirala, P. P.

Ghogale, S. Ghosh, P. K. Goswami, N. R. Goud, R. R. K. R. Jetti, P. Karpinski, P. Kaushik, D. Kumar, V. Kumar, B. Moulton, A. Mukherjee, G. Mukherjee, A. S. Myerson, V. Puri, A. Ramanan, T. Rajamannar, C. M. Reddy, N. Rodriguez-hornedo, R. D. Rogers, T. N. G. Row, P. Sanphui, N. Shan, G. Shete, A. Singh, C. C. Sun, J. A. Swift, R. Thaimattam, T. S. Thakur, R. K. Thaper, S. P. Thomas, S. Tothadi, V. R. Vangala, N. Variankaval, P. Vishweshwar, D. R. Weyna and M. J. Zaworotko, .

62 A. J. Cruz-Cabeza, *CrystEngComm*, 2012, **14**, 6362–6365.

63 A. R. Thayyil, T. Juturu, S. Nayak and S. Kamath, *Adv. Pharm. Bull.*, 2020, **10**, 203–212.

64 C. B. Aakeröy, T. K. Wijethunga and J. Desper, *Chem. - A Eur. J.*, 2015, **21**, 11029–11037.

65 S. Kennedy and C. R. Pulham, *Co-crystallization of Energetic Materials*, Royal Society of Chemistry, 2018.

66 K. B. Landenberger, O. Bolton and A. J. Matzger, *J. Am. Chem. Soc.*, 2015, **137**, 5074–5079.

67 K. B. Landenberger and A. J. Matzger, *Cryst. Growth Des.*, 2010, **10**, 5341–5347.

68 O. Bolton and A. J. Matzger, *Angew. Chemie - Int. Ed.*, 2011, **50**, 8960–8963.

69 O. Bolton, L. R. Simke, P. F. Pagoria and A. J. Matzger, *Cryst. Growth Des.*, 2012, **12**, 4311–4314.

70 H. Gao and J. M. Shreeve, *Chem. Rev.*, 2011, **111**, 7377–7436.

71 J. Zhang, Q. Zhang, T. T. Vo, D. A. Parrish and J. M. Shreeve, *J. Am. Chem. Soc.*, 2015, **137**, 1697–1704.

72 S. Venkatachalam, G. Santhosh and K. N. Ninan, *Propellants, Explos. Pyrotech.*, 2004, **29**, 178–187.

73 Q. Ma, T. Jiang, Y. Chi, Y. Chen, J. Wang, J. Huang and F. Nie, *New J. Chem.*, 2017, **41**, 4165–4172.

74 J. C. Bennion, Z. R. Siddiqi and A. J. Matzger, *Chem. Commun.*, 2017, **53**, 6065–6068.

75 Y. Zhang, Y. Huang, D. A. Parrish and J. M. Shreeve, *J. Mater. Chem.*, 2011, **21**, 6891–6897.

76 I. E. Drukenmüller, T. M. Klapötke, Y. Morgenstern, M. Rusan and J. Stierstorfer, *Zeitschrift für Anorg. und Allg. Chemie*, 2014, **640**, 2139–2148.

Chapter 2 Experimental and Computational Techniques

2.1 Synthesis of Nitropyrazoles

2.1.1 Materials

The following reagents were purchased and used without further purification. 3-nitro-1-H-pyrazole (Fluorochem), acetic acid (≥99%, Sigma Aldrich), acetic anhydride (≥99%, Sigma Aldrich), benzonitrile (anhydrous, ≥99%, Sigma Aldrich), nitric acid (fuming, ≥90%, Sigma Aldrich), sulfuric acid (95%, Thermo Fisher Scientific), hydrochloric acid (ACS reagent, 37%), diethyl ether (ACS reagent, anhydrous, ≥99%, Sigma Aldrich), magnesium sulfate (anhydrous, ≥99%, Sigma Aldrich), sodium bicarbonate (ACS reagent, ≥99.7%), toluene (≥99%, Thermo Fisher Scientific).

2.1.2 Synthesis reactions

1,3-dinitropyrazole (1,3-DNP), 3,5-dinitropyrazole (3,5-DNP) and 3,4,5-trinitropyrazole (3,4,5-TNP) were prepared from 3-nitro-1-H-pyrazole in a sequence of nitration and thermal rearrangement steps according to relevant literature reports. [1-2] Figure 2.1 shows the overall reaction scheme and experimental conditions.

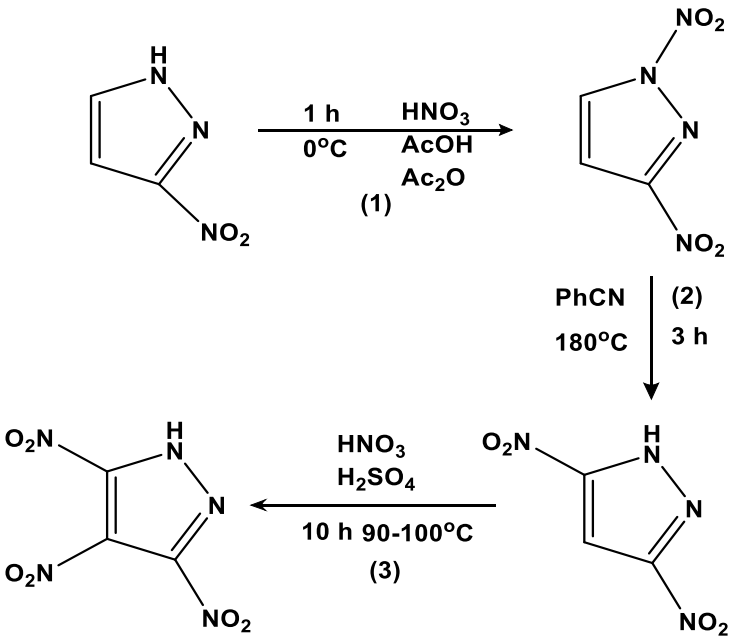

Figure 2.1 Synthetic route for nitropyrazoles

The first step of the synthetic scheme was the nitration of 3-nitro-1-H-pyrazole according to the procedure described in the literature.[3,4,5] Nitration reactions on pyrazole are classified as electrophilic aromatic substitution reactions in which NO_2^+ (nitronium ion) acts as the nitrating agent.

In this step, nitric acid (9.66 ml, d 1.5, ≥90.0%) was added to a cooled solution of 3-nitro-1-H-pyrazole (0.1 mol, 11.3 g) in 30 ml of acetic acid, and cooled in an ice-salt bath. The temperature was monitored during addition and maintained at 0°C. Acetic anhydride (20 ml) was added, and the reaction mixture was allowed to stand for 3 h before pouring onto ice. After being diluted with water, the mixture was neutralised with $NaHCO_3$ and extracted into diethyl ether, which was subsequently dried ($MgSO_4$) and filtered. The ether was removed by evaporation and 1,3-dinitropyrazole collected as a light yellow powder. Using 12.6 g 3-nitro-1-H-pyrazole as starting material, 15.2 g 1,3-dinitropyrazole was obtained representing a yield of 94%.

The second step (Figure 2.1 (2)) was the thermal rearrangement of 1,3-dinitropyrazole which aims to break the N-NO_2 bond at the 1-position via thermolysis and attach the NO_2 group to the 3-position on the pyrazole ring. Thermal rearrangement mechanism of nitropyrazoles is given in Figure 2.2. [6]

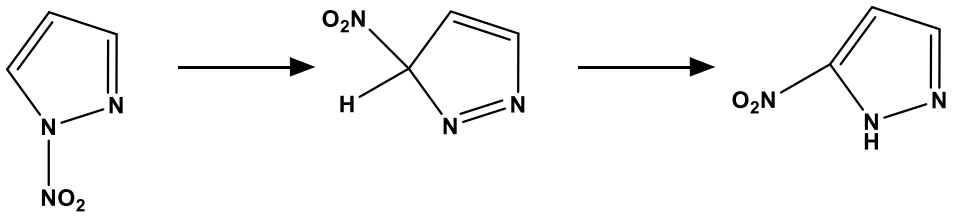

Figure 2.2 Thermal rearrangement mechanism of 1-nitropyrazole

In this step, 3.6 g of 1,3-dinitropyrazole was dissolved in 100 ml benzonitrile and heated for 3 h at 180°C. After cooling to room temperature, aqueous sodium hydroxide (2M, 80 mL) was added and precipitate was collected by filtration. The pH of the precipitate was adjusted to ~1 and extracted into diethyl ether (3 x 200 ml). The organic layer was dried and the solvent removed to yield 3,5-dinitropyrazole (1.5 g, 42%).

The last step was the nitration of 3,5-dinitropyrazole which is described in several reports.[1,2,7] 3,5-dinitropyrazole (3.1 g, 0.02 mol) was dissolved in a mixture of H_2SO_4

(d = 1.824, 31 ml) and HNO_3 (d = 1.51, 12.5 ml). The solution was stirred at 90-100°C for 10 hours. The reaction mixture was extracted with ethyl acetate and the organic layer collected. After drying with $MgSO_4$, the solvent was removed and 3,4,5-TNP was crystallised from toluene. 3.45 g 3,4,5-TNP was synthesised in this way, representing a yield of 85%.

2.2 NMR Spectroscopy

Nuclear magnetic resonance spectroscopy was used to identify reaction products. ^{1}H and ^{13}C NMR spectra were recorded on a Bruker Avance 500 spectrometer operating at 500 MHz. Deuterated dimethylsulfoxide (DMSO-d_6) was used as solvent.

2.3 Preparative Routes to Co-crystals and Salts

One of the most widely used co-crystallisation methods is slow evaporation of solvent. Due to the fact that co-crystal formation is driven by thermodynamic factors, evaporative methods can be easily applied to co-crystallisation. In these methods, co-formers were dissolved in a suitable solvent and the solution allowed to evaporate slowly. However, it is not always easy to identify which co-formers can form intermolecular interactions. There are many factors that affect co-crystal formation such as electron density distribution, aciditiy-basicity, pK_a values and functional groups in molecules. In order to choose suitable pairs of molecules for co-crystallisation and salt formation, supramolecular synthons should be analysed thoroughly. For example, if one of the co-formers is chosen as a hydrogen bond acceptor and the other one as a donor, this match will increase the possibility of co-crystal or salt formation. Likewise, the presence of aromatic groups or halogen atoms often drives the formation of π-π stacking or halogen bonding interactions. These type of strategies have been improved over time to make the co-crystal screening process easier and more reliable, instead of relying on random searches. [8]

Another technique that can be used for co-crystallisation or salt formation is mechanochemical grinding. In this process, co-crystals/salts are produced manually using mechanical force. [9] Although it is a less common technique for co-crystal production, it offers some advantages over evaporative techniques. Due to the

absence (or small amount) of solvent used, it is an economic and environmentally-benign method. The technique features short reaction times and often delivers high yields. The elimination of solvent selectivity for molecules means that it is a promising route for multi-component material production.

Resonance Acoustic Mixing (RAM) developed by ResoDyn Corporation (Battle, MT) is another efficient method to produce novel energetic co-crystals or salts. RAM mixing uses an acoustic energy input into the materials instead of mechanical treatment. It means that there is no contact of energetic materials with fast-moving metal blades, thereby reducing safety concerns. The main principle of RAM is to mix raw materials using oscillation with high amplitude. Then this will create acoustic streaming and particle collisions. The resonater, the most important part of RAM, creates high amplitude oscillation efficiently. Reaching mechanical resonance is an essential condition for transferring the mechanical energy of the mix systems into the material without loss. [10] The technique requires only a minimum amount of solvent and samples in powder forms and provides a time-effective, industrial-scale manufacturing capability for energetic materials. [11] Specific methods used to prepare co-crystals and salts in this study are given in related chapters (Chapter 4, Section 4.2.2 and Chapter 5, Section 5.2.2)

2.4 Single Crystal X-ray Diffraction

X-ray diffraction is one of the most common and desirable techniques used to determine and analyse three dimensional structures of materials. X-rays are electromagnetic waves with a wavelength ranging from about 10 to 10^{-3} nm and are produced by the impact of electrons (Figure 2.3). Monochromatic X-rays then impinge on the sample and are scattered by electrons. The location of atoms in the sample are determined by measuring the angles and amplitude of the scattered X-rays. [8]

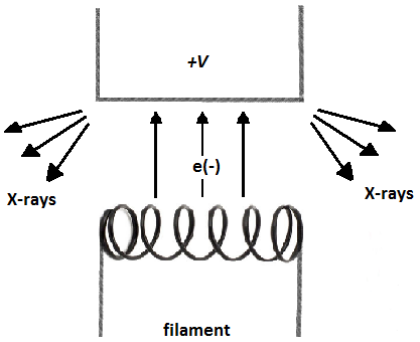

Figure 2.3 Illustration of production of X-rays

The angle (θ) between incident X- rays and scattered from the plane is equal to that between the normal and diffracted beam (Figure 2.4). X-rays which are scattered from different planes have different path lengths to reach the detector, and this causes a path difference. When the path difference is equal to an integer multiple of the wavelength λ, constructive interference occurs and this interference produces detectable diffraction peaks. In the early days of X-ray crystallography, the relationship between the wavelength of the radiation and the path difference was described by Lawrence Bragg and is simply represented as $n\lambda = 2d\,sin\theta$. This equation is known as Bragg's law and forms the basis of X-ray diffraction in terms of reflections of X-rays by lattice planes. These planes are denoted by h, k, l letters and these are known as Miller indices. [12]

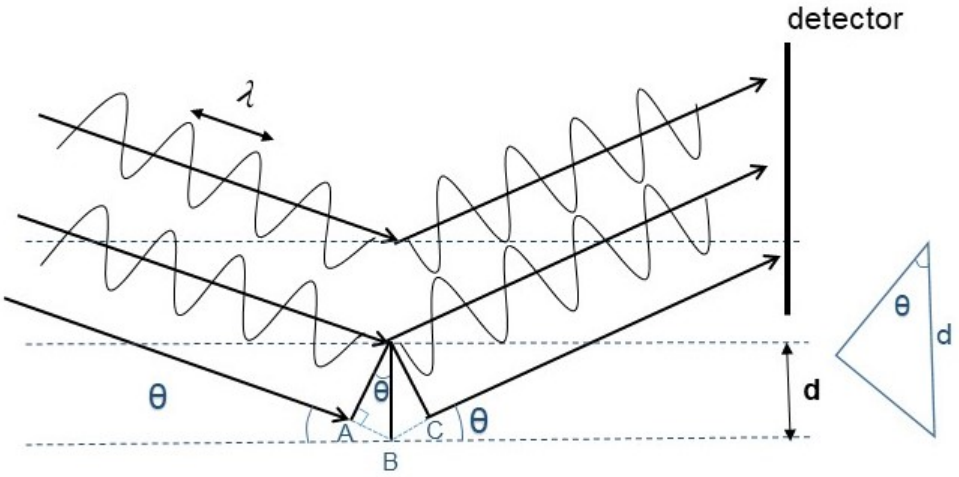

Figure 2.4 Illustration of the geometry of Bragg's law

To image structures of the materials from the diffraction pattern obtained from an X-ray diffraction experiment, the scattered X-rays must be correlated in both amplitude and phase. Whereas the lens systems used with visible light is capable of achieving this, in X-ray diffraction, neither the focusing process nor the measurement of the phase information required can be obtained directly from the experimental data.[13] The information of the phase angle, ϕ_n, cannot be determined from X-ray diffraction experiments, which is called **the phase problem** in crystal structure determination. At this point, a mathematical procedure which is named as "Fourier transformation" is used to explain the relationship between a crystal structure and its diffraction pattern. The crystal structure is the Fourier transform of the structure factors (F_{hkl}) of a wave diffracted from a crystal and is stated in terms of the electron-density ($\rho_{(xyz)}$) distribution located in atoms. [12] The amplitude, $F_{hkl,}$ and intensity, $I_{hkl,}$ of the reflected

X-ray beam can be calculated from the 'structure factor equation', Equation 2.1, by using the atomic positions and atomic scattering factors (f_n). [14]

$$\mathrm{F}_{hkl} = \sum_{n=0}^{n=N} f_n \, exp\, 2\pi i \, (hx_n + ky_n + lz_n) \qquad \text{(Eq. 2.1)}$$

where $2\pi i \, (hx_n + ky_n + lz_n)$ is the phase angle, ϕ_n, of the nth atom in the motif with fractional coordinates (x_n , y_n, z_n). Electron density (ρ) can be calculated using Equation 2.2.

$$\rho(xyz) = \frac{1}{V}\sum_{hkl} | F(hkl) | \exp\, [i\phi(hkl)] \exp[-2\pi i(hx + ky + lz)] \qquad \text{(Eq. 2.2)}$$

In chemical crystallography, two main methods are used to overcome the phase problem and hence determine structures: (i) Direct methods and (ii) Patterson methods. Direct methods are mostly favourable for materials containing light atoms and thus find application areas for organic compounds. In **direct methods**, a complete solution of the crystal structure is attempted to be estimated from the measured X-ray intensities. The derivation of the phases and eventually the electron densities are achieved by using mathematical constraints within the statistical relationship between the set of structure factor. [15]

The second method to overcome the phase problem is the Patterson method. The Patterson synthesis which is given in Equation 2.3, is mostly preferred when there are a few heavy atoms among light atoms and assigns amplitudes with their squares $|F(hkl)|^2$ to deal with the phase problem. The peaks in a Patterson map represent the vectors between pairs of atoms in the structure, thus the relative atomic positions in a structure. The magnitude of the vectors are proportional to the squares of the atomic numbers of the atoms corresponding to this vector. [14]

$$P(uvw) = \frac{1}{\mathrm{V}} \sum_{hkl} | F(hkl) |^2 \, \cos[2\pi(hu + kv + lw)] \qquad \text{(Eq. 2.3)}$$

All ambient pressure single crystal X-ray diffraction experiments for co-crystals and salts were conducted using monochromatic laboratory X-ray sources (MoK_α or CuK_α) in the School of Chemistry (Agilent Technologies Super Nova diffractometer equipped with an Oxford Cryo systems). The crystals were maintained at 120 K during data collection. More experimental details are given in Chapter 4 (Section 4.2.3) and Chapter 5 (Section 5.2.3).

2.5 High-Pressure Single Crystal X-ray diffraction - Diamond Anvil Cell

In order to investigate high-pressure effect on materials, *in situ* experiments, which probe the situation of the sample while it is under pressure, should be performed. The diamond anvil cell (DAC) is a commonly used pressure-generating device, see Figure 2.5, was invented in 1950s at the National Bureau of Standards and is capable of generating sustained static pressures in the multi-megabar range. [16] It has become an important device for conducting high-pressure single crystal X-ray diffraction experiments. Although the DAC has its capability of providing high-pressures, it has some disadvantages related to data collection. Its small and complicated geometrical shape limits the data collection angle (θ) and reduces the amount of data that can be provided from full diffraction pattern.

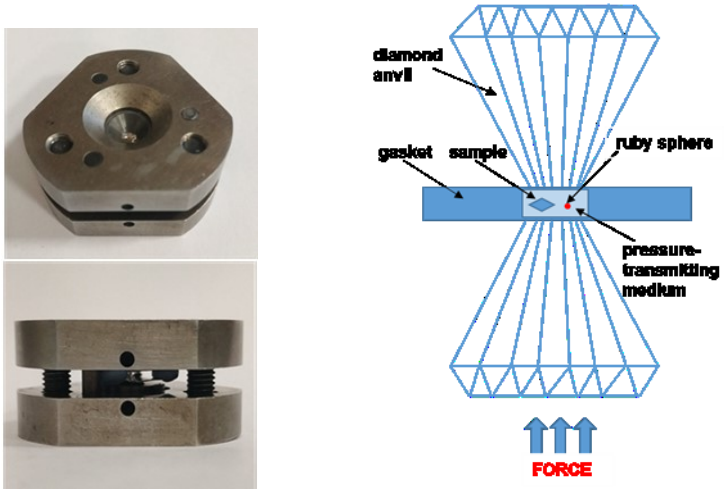

Figure 2.5 Photograph of the Merrill-Bassett DAC used for single crystal high-pressure experiments; and, the schematic representation of the principles of the diamond-anvil cell [17]

In this study, high-pressure single crystal X-ray diffraction measurements were conducted by Dr Xiaojiao Liu from the Pulham group on a Bruker D8 Venture X-ray diffractometer equipped with a CCD detector. More experimental details are provided in Chapter 3 (Section 3.3.4).

2.6 Powder X-ray Diffraction

Powder X-ray diffraction is an efficient non-destructive method for determining different physical and chemical properties of materials. It can be used for determination of the crystallographic unit cell, phase identification, and crystal size.[18] Although the most definitive and widely used X-ray technique is single crystal diffraction, powder diffraction can in favourable cases be used for determination of 3D structures of materials especially when growing single crystals is not possible. There is no significant difference between two methods in terms of application except the form of samples, but interpretation of diffraction patterns is quite different. In powder diffraction, X-ray beams are diffracted by multiple randomly oriented single crystals. In this case, diffracted beams create cones of diffracted X-rays and groups of rings are observed on the detector screen instead of separated single peaks. A good illustration to explain the difference between single crystal and powder X-ray diffraction is given in Figure 2.6 below. [12]

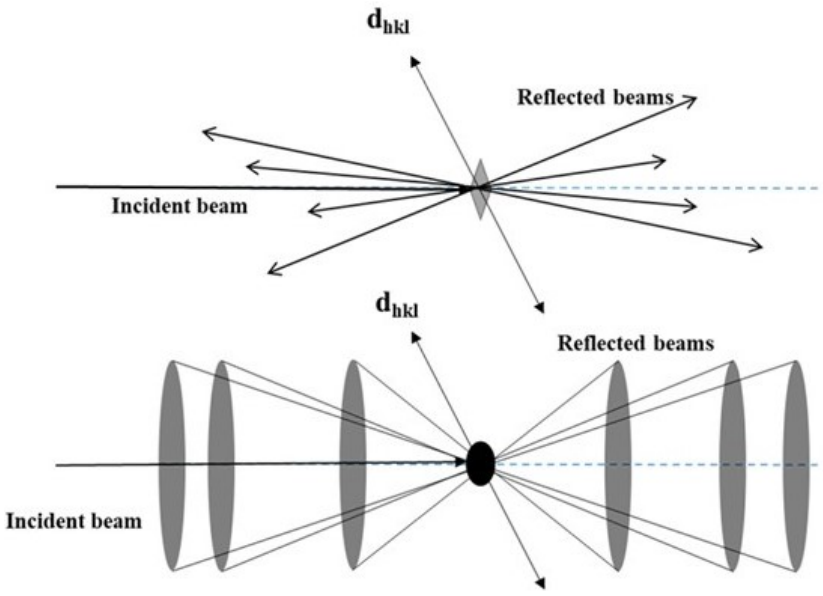

Figure 2.6 Illustration of single (above) and powder (below) X-ray diffraction

In the powder technique it is unavoidable that some information is lost due to the overlapping peaks in the diffraction pattern. Therefore, refinement methods have been developed by H. M. Rietveld to interpret these complicated patterns and extract the maximum amount of data from them. [19] In the later Rietveld refinement procedure, profile intensities are used instead of the integrated quantities which were previously used. [20] By doing so, the difficulties caused by the overlap of independent diffraction peaks can often be overcome.

In this study, powder X-ray diffraction patterns were recorded under ambient-temperature and ambient-pressure conditions using a Bruker D2 PHASER instrument using Cu-K_α radiation (λ=1.54439 Å) and an operating voltage of 40 kV and current of 40 mA. All the data were collected over an angle range of 2θ = 5-50°. This technique was used to characterise bulk samples prior to impact-sensitivity testing and DSC experiments.

2.7 Neutron Diffraction

Neutrons have numerous properties which distinguish them from X-rays. On account of their wave-like properties, they can be used to investigate crystal structures in a manner that is complementary to X-ray diffraction. Neutron diffraction uses the same principles as X-ray diffraction, such as Bragg's law and Fourier transformations, to explain the relationship between a crystal structure and its diffraction pattern. In X-ray diffraction, the radiation is scattered by the electrons located around the nuclei. The position of the nuclei can be determined from an electron density map which is obtained as a result of interaction of X-rays with electron density [8]. In a neutron diffraction experiment, however, neutrons are scattered by the nuclei and thus, nuclear positions can directly be determined. The interaction of a neutron with the nucleus of an atom is weak, and this enhances their penetration ability and allows them to reach the interior of materials, instead of the surface addressed by the other techniques such as X-ray crystallography or electron microscopy.[21] Neutrons are non-destructive tools thanks to their weak interactions. Therefore, they can even be utilised for complex and soft biological materials such as proteins, enzymes or polymeric samples. [22]

The magnitude of interaction does not have a direct relationship with atomic number (Z) in neutron diffraction, whilst X-ray radiation is directly proportional to its atomic

number (Z). Therefore elements with small atomic numbers and different isotopes can be more easily identified with neutron diffraction. Neutrons also allow of determination positions of hydrogen atoms much more accurately than X-rays. They can also be used to determine the anisotropic displacement parameters of hydrogen atoms. Neutron single crystal diffraction becomes an efficient way for investigating the nature of non-covalent interactions in complex molecules and supramolecular structures, involving hydrogen bonds. [22]

2.8 High-pressure Neutron Diffraction – Paris-Edinburgh Cell

Many of the advantages of neutron scattering that described in Section 2.7 also make it a useful tool for investigating materials under extreme conditions such as high pressure or temperature. However, due to the fact that the flux is low compared to that of X-ray sources, a much larger sample volume is required to obtain reasonable counting statistics. [23] Therefore diamond anvil cells with their small size and very limited sample capacity are not appropriate solutions to combine with neutron diffraction experiments. In 1992, a light-weight device called the “Paris–Edinburgh (PE) press” was developed as a result of a collaboration between the Universities of Paris and Edinburgh. [24] The anvils in which the sample is compressed can be made of tungsten-carbide (WC), zirconia-toughened alumina (ZTA) or sintered diamond. Using this press, pressures up to 30 GPa can be generated with sintered diamond anvils over a temperature range 80 - 1400 K with sample volumes in the range 50-100 mm^3. [25]

In this study, high-pressure powder diffraction experiments were conducted on the PEARL instrument at the ISIS Neutron and Muon Source, U.K. [23] The pressure was generated by using Paris−Edinburgh (P−E) cell. Single-toroidal zirconia-toughened alumina (ZTA) and tungsten-carbide (WC) anvils were used. At the ISIS Neutron and Muon Source, neutron beams are produced using spallation technique. The neutron beam produced by spallation is polychromatic which is advantageous for using the full range of neutron wavelengths produced by the source. However, the wavelength (λ) of the radiation is unknown. In order to apply Bragg’s law without λ, time-of-flight technique was developed. In these experiments, the distance between the radiation source and sample is fixed and the time that neutrons spend is measured. Therefore, the data for structure solution can be obtained by combining De Broglie equation (λ =

*h/mv, h:*Planck's constant*, m:*neutron mass*, v:*velocity) and Bragg's law that is explained in Section 2.4. More details are given in Chapter 3.

To interpret high-pressure neutron powder diffraction data, the rigid body technique in Rietveld refinements was implemented. A rigid body is a geometrical constraint which describes a group of atoms as a discrete body allowing all the molecular movements such as translation, rotation without fragmentation. [26] This reduces the number of parameters needed to refine the molecule since atomic positions are provided from the rigid body model. It also prevents chemical irrationality and impossible distortion of the atoms and molecules.

2.9 Equation of States

An "equation of state" (EoS) expresses the relationship that shows how the thermodynamic parameters pressure (P), temperature (T) and volume (V) are interrelated for a specific material. The ideal-gas law (PV = nRT) is as an example of an EoS that is used to explain the behaviour of ideal gases. When the conditions are more relaxed and non-ideal, such as extreme pressure or temperature, more complex models are required to explain energy or geometry transformation in a system. Obtained EoSs are often parameterised by using bulk modulus, $B_0 = -V\,\partial P/\partial V$, and its pressure derivative: $B' = \partial B/\partial P$, which are determined at zero pressure. V_0, the zero-pressure volume is generally refers the unit cell volume at ambient conditions. The parameter B' can be an indicator of trend of mechanical behaviour. For example, a large B' often indicates a rapid stiffening of a material and negative B' can be an indicator of a dynamic stability. In static pressure studies described in this work, temperature is held constant, and isothermal EoS are derived. [16]

$$P = -\left(\frac{\partial F}{\partial V}\right)T,n \qquad \text{(Eq. 2.4)}$$

Equation 2.4 shows the correlation between Helmoltz free energy and volume for an isothermal, closed system. However, Birch expanded the free energy in terms of Eulerian strain. This expansion coupled with Equation 2.5 brought Birch-Murnaghan EoS which has the form:

$$P = \frac{3B_0}{2}\left[\left(\frac{v_0}{v}\right)^{\frac{7}{3}} - \left(\frac{v_0}{v}\right)^{\frac{5}{3}}\right]\left[1 + \frac{3}{4}(B'_0 - 4)\left(\left(\frac{v_0}{v}\right)^{\frac{2}{3}} - 1\right)\right] \quad \text{(Eq. 2.5)}$$

2.10 High-Pressure Raman Spectroscopy

Raman spectroscopy is widely used to provide information on the vibrational, magnetic, electronic, and elastic subsystems by exploiting the observations of the corresponding elementary excitations. It uses inelastic scattering processes with a monochromatic light source which is commonly a laser, for probing elementary excitations in materials. [27] The scattered radiation generates a spectrum that allows finger-printing analysis of the materials, but can also include its composition and state, and insight into molecular vibrations.[28]

Since thermodynamic conditions such as temperature and pressure have significant effects on elementary excitations of molecules, these changes can be observed by *in situ* Raman spectroscopy. These changes can be in the vibrational excitation energies, phase transformations, polymorph changes, chemical properties, and magnetic transitions. The main advantage of Raman spectroscopy is the use of visible light that allows easy access to sample. These factors make Raman spectroscopy a powerful tool for characterisation of materials under extreme pressures. [29]

In this study high-pressure Raman spectra were collected at the University of Edinburgh - Centre for Science at Extreme Conditions. More details are given in Chapter 3 (Section 3.3.2).

2.11 Impact Sensitivity Testing: BAM Fall Hammer

As described in Chapter 1, impact sensitivity represents the ease with which an energetic material can be initiated by a mechanical stimulus. It is very important to determine the sensitivity of energetic materials in order to evaluate safety issues during their use and storage. The impact sensitivity of explosives is usually determined by using the Fall Hammer method. [30] The BAM Fall Hammer impact tester, see Figure 2.7 (a), essentially consists of a large cast steel stand, a round steel anvil, a cylinder attached at the steel block, smoothed guide bars and the drop weight with a device which provides releasing and retaining capability.

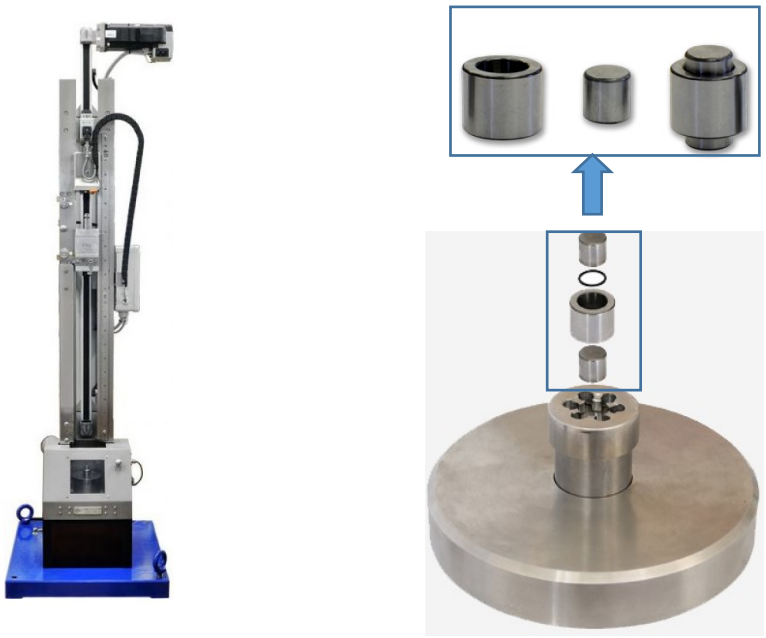

(a) (b)

Figure 2.7 (a) Image of BAM Fall Hammer (BFH-12) impact tester (b) impact device 1, consisting of two coaxial steel cylinders within a guide-ring

All the BAM Fall Hammer impact testing (BFH-12) measurements in this thesis (Chapter 4 and 5) were performed, at the Cavendish Laboratory (Cambridge) on samples of 1,3-DNP.AmClPyr, 3,5-DNP.AmClPyr, 3,5-DNP.BrPyr, 3,5-DNP.Pyr and 3,4,5-TNP.BrPyr. A sample of 40 mm^3 was enclosed in an anvil device comprising two coaxial steel cylinders (Figure 2.6(b)). Anvils were safely disposed of along with the sample after each test. A range of loads (2, 5 and 10 kg) were dropped from varying heights (from 10 to 100 cm) on all samples. The method conducted throughout is the 1 in 6 method. [31] In this method a drop height is determined initially, at which an explosion of the energetic compound could be observed. The impact energy level (height) is decreased step by step until no reaction is observed. Testing is performed up to six trials for that certain energy level. If a reaction is observed (positive result), the procedure is repeated with a lower drop height again. When six trials at a fixed energy level resulted with no reaction (negative), the next higher energy level, where at least one of the six trials resulted in an explosion, is determined as the impact sensitivity value of that compound (also could be called limiting impact energy, J). The impact energy for every height is calculated as a product of the mass, the local gravitational field (9.81 m s^{-2}) and that specific drop height. A positive result for initiation is commonly identified by the presence of a flash of light or noise. However,

in these studies it is also determined by a colour change from initial colour of sample to black or grey, indicating partial initiation.

2.12 Differential Scanning Calorimetry (DSC)

Differential scanning calorimetry is a widely used technique to investigate thermal behaviour of materials. In this technique, the instrument measures the temperature and energy differences that occur when a sample is heated or cooled. One can identify phase transitions (i.e. glass transition, melting, solid-solid transitions or thermal decompositions) and measure their associated enthalpies and the temperatures that phase transitions take place. [32] Heat flow is the main property which is measured by the device as a function of temperature or time. During an exothermic reaction, a certain amount of heat enters the system and decrease the overall heat flow and *vice versa* for endothermic reactions. Therefore, the heat-flow/energy-temperature/time allows determination of whether a reaction is exothermic or endothermic. Energetic materials exhibit exothermic decomposition reactions with a large amount of heat output. The heat of decomposition of an energetic compound can be calculated through integration of its decomposition peak. Similarly, this can be applied to endothermic processes such as melting or other types of phase transitions observed during a DSC measurement. [30]

All the DSC experiments in this thesis (Chapter 4 and 5) were conducted on a NETZSCH STA 449 F1 Differential Scanning Calorimeter. Approximately 2-3 mg of sample was placed in an aluminium pan and the thermal behaviour of the sample was studied under a nitrogen purge (30.0 mL/min) at a heating rate of 10 K/min over the temperature range from 21-350°C. DSC-TGA plots were produced and analysed using Netzsch Proteus – Thermal Analysis software. The diagram of a DSC set-up is shown in Figure 2.8.

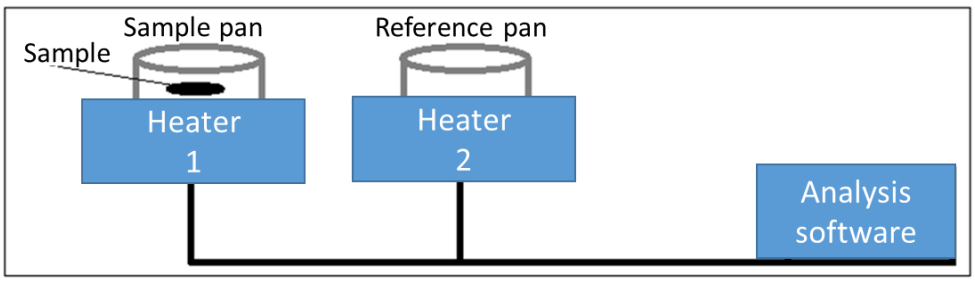

Figure 2.8 DSC-TGA instrument set-up diagram

2.13 Calculations of Detonation Parameters

Detonation parameters are crucial for the assessment of energetic performance of an energetic compound. Since the experiments required to determine these parameters are hard to perform and bring some safety concerns, alternative computational methods are often used. Detonation performance parameters such as detonation temperature, pressure, and velocity, oxygen balance and decomposition products were calculated by using the EXPLO5 V6.03 program which is based on the chemical equilibrium, steady-state model of detonation.

EXPLO5 exploits the Cowan-Fickett's equation of state for solid carbon detonation products and the Becker-Kistiakowsky-Wilson's equation of state (BKW EoS) for gaseous product. It calculates the detonation parameters at the Chapman-Jouguet (C-J) point, which is found from the Hugoniot curve of the system by its first derivative. The main detonation products for the calculations of the energetic parameters were assumed to be N_2, H_2O, and CO_2. In addition, compounds with a positive oxygen balance can produce O_2 as a combustion product.

Based on the Born-Haber energy cycle which is shown in Scheme 2.1, the heats of formation of salts can be calculated by using Equation 2.6.

All calculations of detonation parameters were performed using the program EXPLO-5 V6.03.[33,34] The detonation parameters (including detonation pressure and velocity, and oxygen balance) were determined at the C-J condition point as defined in the steady-state detonation model. An altered Becker-Kistiakowski-Wilson equation of state was used to model the system. The heats of formation, chemical compositions, and experimentally determined crystal densities were used as input data, while N_2, H_2O, and CO_2 were assumed to be the main detonation products.

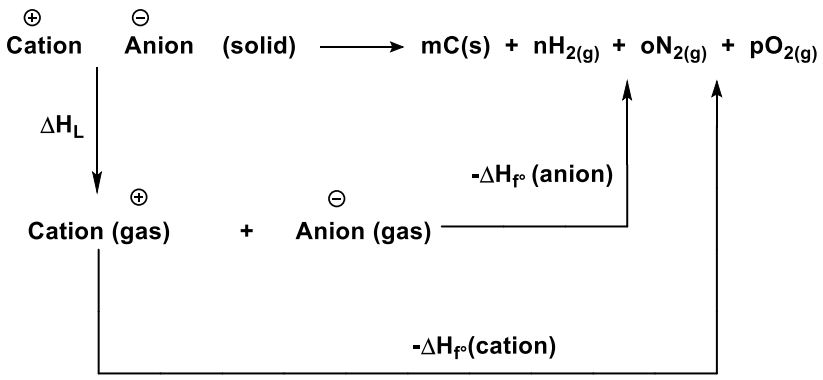

Scheme 2.1 Born-Haber energy cycle

2.14 Heat of Formation Calculations

All the heat of formation calculations in this thesis (Chapter 4 and 5) were performed by Imogen Christopher (PhD student from the Morrison group).The gas-phase heat of formation $\Delta H_f(\mathrm{g})$ for each ion/co-former was calculated directly following geometry optimisation (B3LYP/6-31G*) using a single-point energy calculation using the PM7 semi-empirical method as expressed in Gaussian 16. [35,36]

The heats of formation for solid 1,3-DNP, 3,5-DNP and 3,4,5-TNP were calculated using equation (2.6) and the sublimation enthalpy, ΔH_{sub}, was calculated using the semi-empirical fit equation (2.7),

$$\Delta H_f(s) = \Delta H_f(g) - \Delta H_{sub} \quad \text{(Eq. 2.6)}$$

$$\Delta H_{sub} = a(SA)^2 + b\sqrt{\sigma_{tot}^2 \nu} + c \quad \text{(Eq. 2.7)}$$

where, a, b and c are semi-empirical fitting parameters established by Byrd ***et. al.*** [37], SA is the surface area of the 0.001 electronbohr^{-3} iso-surface describing the molecular electron density, σ_{tot}^2 is the measure of variablity of electronic potential on the surface, and ν is the degree of balance between the positive and negative charges on the isosurface. The latter three parameters were calculated using Multiwfn. [38]

For energetic salts and co-crystals the solid phase heat of formation $\Delta H_f(s)$ was calculated from Equation (2.8). ΔH_L, the lattice enthalpy of the material, was calculated *via* two different apporaches, depending on whether the system was a salt or a co-crystal.

$$\Delta H_f(s) = \Delta H_f(\mathrm{g})\ (cation, coformer1) + \Delta H_f(\mathrm{g})\ (anion, coformer2) - \Delta H_L \quad \text{(Eq. 2.8)}$$

For salt structures, equations (2.9) and (2.10), developed by Jenkins ***et. al***, [39] were used to calculate ΔH_L. It has been demonstrated by Shreeve ***et. al***. [40] that these equations successfully predict the lattice energies of salts.

$$\Delta H_L = U_{pot} + [p(n_m/2 - 2) + q(n_x/2 - 2)]\mathrm{R}T \quad \text{(Eq. 2.9)}$$

In equation 2.9, n_m and n_x are constants that depend on the nature of the ions, and are set to 3 for monoatomic ions, 5 for linear polyatomic ions and 6 for non-linear polyatomic ions. The variables p and q denote the relative charges of the respective ions. The term U_{pot} denotes the lattice potential energy and in turn is defined by equation 2.10,

$$U_{pot} = \alpha V_m{}^{\frac{1}{3}} + \beta \qquad \text{(Eq. 2.10)}$$

where V_m denotes the unit cell volume, in nm^3.The remaining coefficients α and β are fitting terms equal to 117.3 kJ mol nm^{-1} and 51.9 kJ mol^{-1}, respectively, for a 1:1 charge ratio [39]. For co-crystals, $\Delta H_L$was calculated using equation (2.11),

$$\Delta H_L = (E_{cell} - x.E_{co-former1} - y.E_{co-former2})/Z \qquad \text{(Eq. 2.11)}$$

where (E_{cell}) is the lattice energy of the unit cell, calculated via geometry optimisation of the crystal structure, as described in the computational modelling using CASTEP V.16.11. More details of these calculations are given in Section 2.15. x and y are the number of each co-former in the unit cell and Z is the total number of molecules in the unit cell. $E_{co-former}$ is the single-point energy of an isolated co-former, calculated in a super-cell of size equal to the co-crystal unit cell volume, to simulate the gas phase. The same parameters were used for the solid-state and corresponding super-cell calculations to allow for legitimate comparison of the resulting energies.

2.15 Geometry Optimisation and Vibrational Up-pumping Method

All the computational studies in Chapter 3 was performed by Jack Hemingway (PhD student from Morrison group). Geometry optimisation was completed for each 3,4,5-TNP structure using CASTEP V.16.11. [41] The GGA functional PBE combined with the TS dispersion correction scheme was used throughout, alongside 'on-the-fly' pseudopotentials and a plane-wave basis set cut-off of at least 950 eV. [42,43] The electronic structure in the Brillouin zone representation was sampled on Monkhurst Pack grid mesh of 0.05 Å^{-1}. [44] Structures were considered converged when the following criteria were met: residual atomic forces < 0.005 eVÅ^{-1}, atomic

displacements < 0.003 Å, wavefunction self-consistency < 2 x 10^{-6} eV, and lattice vector stresses < 0.005 GPa. Gamma-point phonon calculations were performed for the ambient pressure structure and the structure observed at 5.3 GPa using the DFPT method as implemented in the CASTEP package. [45]

The phonon density of states (PDoS) obtained from the phonon calculations were plotted using a Gaussian smearing width of 5 cm^{-1}. Values for Ω_{max}, denoting the top of the phonon bath, were determined by calculating the centre of mass displacements from the simulated eigenvectors, and noting where the switch-over from large displacements (*i.e.* lattice mode behaviour) to negligible displacements (*i.e*. molecular mode behaviour) occurred. The predicted heat capacities for both polymorphs were calculated by processing the PDoS according to Equation 2.12.

$$C_v = \int \frac{\partial n}{\partial T} \hbar\omega g(\omega) d\omega \qquad \text{(Eq. 2.12)}$$

where n is phonon population, T is temperature (K), ω is frequency, g(ω) is density of states and $\hbar$ is the Planck constant. The integral was evaluated across the entire vibrational spectrum, with the bulk temperature set at 300 K. This process permits the contribution of the low-energy phonon modes to the bulk heat capacity to be obtained; this distinction is important as the low energy phonon modes have a correspondingly lower heat capacity and subsequently superheat following mechanical impact. The ratio of the bulk heat capacity (C_{tot}) to the phonon (C_{ph}) permits a scaling factor to be obtained, from which T_{shock} is calculated (C_{tot}/C_{ph} = 5.00 equates to T_{shock} = 3278 K, from our earlier work). [46] In generating the 2phonDoS the following mode scattering pathways were included: q + q (*i.e*. a phonon bath mode (q) scattering with itself, to create a new state akin to the first overtone state), q + q' (*i.e*. two separate phonon bath modes combining to create a new state akin to a combination mode), and q + Q_D (*i.e*. a phonon mode combining with a low energy molecular 'doorway' vibration (Q_D), located above Ω_{max}).

2.16 References

1 I. L. Dalinger, G. P. Popova, I. A. Vatsadze, T. K. Shkineva and S. A. Shevelev, *Russ. Chem. Bull.*, 2009, **58**, 2185.

2 G. Hervé, C. Roussel and H. Graindorge, *Angew. Chemie - Int. Ed.*, 2010, **49**, 3177–3181.

3 C. L. Habraken and J. W. A. M. Janssen, *J. Org. Chem.*, 1971, **36**, 3081–3084.

4 PCT/IB2008/002535 (87), *J. Org. Chem.*, 2010.

5 R. D. Schmidt, G. S. Lee, P. F. Pagoria, A. R. Mitchell and R. Gilardi, *J. Heterocycl. Chem.*, 2001, **38**, 1227–1230.

6 J. W. A. M. Janssen and C. L. Habraken, *J. Org. Chem.*, 1971, **36**, 3081–3084.

7 Y. Zhang, Y. Guo, Y. H. Joo, D. A. Parrish and J. M. Shreeve, *Chem. - A Eur. J.*, 2010, **16**, 10778–10784.

8 Y. Waseda, E. Matsubara and K. Shinoda, *X-Ray Diffraction Crystallography; Introduction, examples and solved problems*, 2011.

9 P. Baláž, M. Achimovicová, M. Baláž, P. Billik, C. Z. Zara, J. M. Criado, F. Delogu, E. Dutková, E. Gaffet, F. J. Gotor, R. Kumar, I. Mitov, T. Rojac, M. Senna, A. Streletskii and W. C. Krystyna, *Chem. Soc. Rev.*, 2013, **42**, 7571–7637.

10 M. R. Andrews, C. Collet, A. Wolff and C. Hollands, *Propellants, Explos. Pyrotech.*, 2020, **45**, 77–86.

11 K. S. Hope, H. J. Lloyd, D. Ward, A. A. L. Michalchuk and C. R. Pulham, *New Trends Res. Energ. Mater.*, 2015, 134–143.

12 W. Clegg, A. J. Blake, J. M. Cole, J. S. O. Evans, P. Main, S. Parsons and D. J. Watkin, *Crystal Structure Analysis: Principles and Practice*, Oxford Science Publications, Oxford, second., 2009, vol. 9780199219.

13 M. F. C. Ladd and R. A. Palmer, *Structure Determination by X-Ray Crystallography*, 1985.

14 A. J. Blake, W. Clegg, J. M. Cole, J. S. O. Evans, P. Main, S. Parsons and D. J. Watkin, *X-ray crystal structure analysis*, 2nd edn., 2008.

15 Richard J. D. Tlley, *Crystals and crystal structures*, 2006.

16 G. J. P. Eds, *Static Compression of Energetic Materials*, 2008.

17 L. Merrill and W. A. Bassett, *Rev. Sci. Instrum.*, 1974, **45**, 290–294.

18 V. K. Pecharsky and P. Y. Zavalij, *Fundamentals of powder diffraction and structural characterization of materials*, 2005.

19 H. M. Rietveld, *Acta Crystallogr.*, 1967, **22**, 151–152.

20 H. M. Rietveld, *Acta Crystallogr.*, 1966, **20**, 508–513.

21 B. T. M. Willis and C. J. Carlile, *Experimental neutron scattering*, Oxford University Press, Oxford, 2009.

22 R. Pynn, in *Neutron Scattering Applications and Techniques*, ed. L. Liang, Springer Science, Bloomington, 2009, pp. 1–29.

23 C. L. Bull, N. P. Funnell, M. G. Tucker, S. Hull, D. J. Francis and W. G. Marshall, *High Press. Res.*, 2016, **36**, 493–511.

24 J. M. Besson, R. J. Nelmes, G. Hamel, J. S. Loveday, G. Weill and S. Hull, *Phys. B Phys. Condens. Matter*, 1992, **180**–**181**, 907–910.

25 S. Klotz, J. M. Besson, G. Hamel, R. J. Nelmes, J. S. Loveday, W. G. Marshall and R. M. Wilson, *Appl. Phys. Lett.*, 1995, **1735**, 1735.

26 C. H. Lake and B. H. Toby, *Powder Diffr.*, 2011, **26**, S13–S21.

27 K. Nakamoto, *Infrared and Raman Spectra of Inorganic and Coordination Compounds: Part A: Theory and Applications in Inorganic Chemistry: Sixth Edition*, 2008.

28 E. Smith and G. Dent, *Modern Raman Spectroscopy - A Practical Approach*, 2005.

29 A. F. Goncharov, *Int. J. Spectrosc.*, 2012, **2012**, 1–16.

30 T. M. Klapötke, *Chemistry of High-Energy Materials*, Walter de Grutyer, Munich, 2nd editio., 2012.

31 M. S. Gruhne, M. Lommel, M. H. H. Wurzenberger, N. Szimhardt, T. M. Klapötke and J. Stierstorfer, *Propellants, Explos. Pyrotech.*, 2020, **45**, 147–153.

32 P. Gabbott, *Princ. Appl. Therm. Anal.*, 2008, 1–50.

33 M. Suceska, in *1st International Symposium on Explosion, Shock Wave and Hypervelocity Phenomena (ESHP)*, 2004, pp. 325–330.

34 M. Suceska, 2015, 1–120.

35 J. J. P. Stewart, *J. Mol. Model.*, 2013, **19**, 1–32.

36 J. V M. J. Frisch, G. W. Trucks, H. B. Schlegel, G. E. Scuseria, M. A. Robb, J. R. Cheeseman, G. Scalmani, V. Barone, G. A. Petersson, H. Nakatsuji, X. Li, M. Caricato, A. V. Marenich, J. Bloino, B. G. Janesko, R. Gomperts, B. Mennucci, H. P. Hratchian, 2016.

37 E. F. C. Byrd and B. M. Rice, *J. Phys. Chem. A*, 2006, **110**, 1005–1013.

38 T. Lu and F. Chen, *J. Comput. Chem.*, 2012, **33**, 580–592.

39 H. D. B. Jenkins, D. Tudela and L. Glasser, *Inorg. Chem.*, 2002, **41**, 2364–2367.

40 G. H. Tao, Y. Guo, Y. H. Joo, B. Twamley and J. M. Shreeve, *J. Mater. Chem.*, 2008, **18**, 5524–5530.

41 S. J. Clark, M. D. Segall, C. J. Pickard, P. J. Hasnip, M. I. J. Probert, K. Refson and M. C. Payne, *Zeitschrift für Krist.*, 2005, **220**, 567–570.

42 J. P. Perdew, K. Burke and M. Ernzerhof, *Phys. Rev. Lett.*, 1996, **77**, 3865–3868.

43 A. Tkatchenko and M. Scheffler, *Phys. Rev. Lett.*, 2009, **102**, 6–9.

44 H. J. M. James D. Pack, *J. Chem. Inf. Model.*, 1977, **16**, 1748–1749.

45 S. Baroni, S. de Gironcoli and A. Dal Coreso, *Rev. Mod. Phys.*, 2001, **73**, 516–558.

46 A. A. L. Michalchuk, J. Hemingway and C. A. Morrison, *J. Chem. Phys.*, 2021, **154**, 064105.

Chapter 3 High-pressure studies of 3,4,5-Trinitropyrazole (3,4,5-TNP)

3.1 Introduction

The thermomechanical behaviour of energetic materials under extremes of pressure and temperature is crucially important for the development of a full understanding of their performance. Immediately prior to initiation, energetic compounds experience conditions of elevated pressures and temperatures, and it is now well known that both pressure and temperature can cause structural changes. [1] Moreover, high pressure increases the packing density of molecules in materials, which can cause major modifications in non-covalent interactions. [2] Novel polymorphs may also be formed with altered physical and mechanical properties. A novel polymorph formed under extreme conditions may exhibit either inferior or superior energetic properties compared to the form at ambient conditions. In particular, the understanding of crystal structures of energetic materials under extreme conditions is crucial as their energetic performance is strongly governed by structure. [1] The assumption that all energetic compounds exhibit very similar compression behaviour may introduce difficulties in applications. For example, the same explosive might undergo a phase transition at a specific pressure experienced by a munition under operational conditions and become much more sensitive than its ambient-conditions form. Similarly, during the burning process of a rocket propellant, extreme conditions may cause a phase transition and drastically affect burning rates. In summary, the mapping of phase transitions as a function of temperature and pressure is of great importance for both safety and reproducibility of energetic materials.

3,4,5-trinitropyrazole (3,4,5-TNP, see Figure 3.1) is a heavily nitrated aromatic compound that was first synthesised in 2009 by Dalinger *et al.* and has received attention on account of its desirable energetic properties. [3] The first reported crystal structure claimed that the amino hydrogen atom is statically disordered over both aromatic nitrogen sites at ambient temperature. As a consequence, 3,4,5-TNP was reported to crystallise in the monoclinic crystal system with space group *C2/c* (Z'=1.5). [4] More recently, Nelyubina *et al.* suggested that this initial structural model was erroneous on account of overlooked pseudosymmetry. [5] It was instead suggested that the correct space group for 3,4,5-TNP is $P2_1/c$ (Z'=3) under ambient conditions, and

this is the structure that is reported in the Cambridge Structural Database (CSD) with reference code KAHHIM02. [5] Since *C2/c* and *P2₁/c* space groups have similar symmetrical properties, they can often be mistaken. *C2/c* can be considered as a combination of a *c*-centred lattice with *P2/c* or *P2₁/n*. The expanded packing arrangement of 3,4,5-TNP is shown in Figure 3.2 and crystallographic information for the compound is presented in Table 3.1.

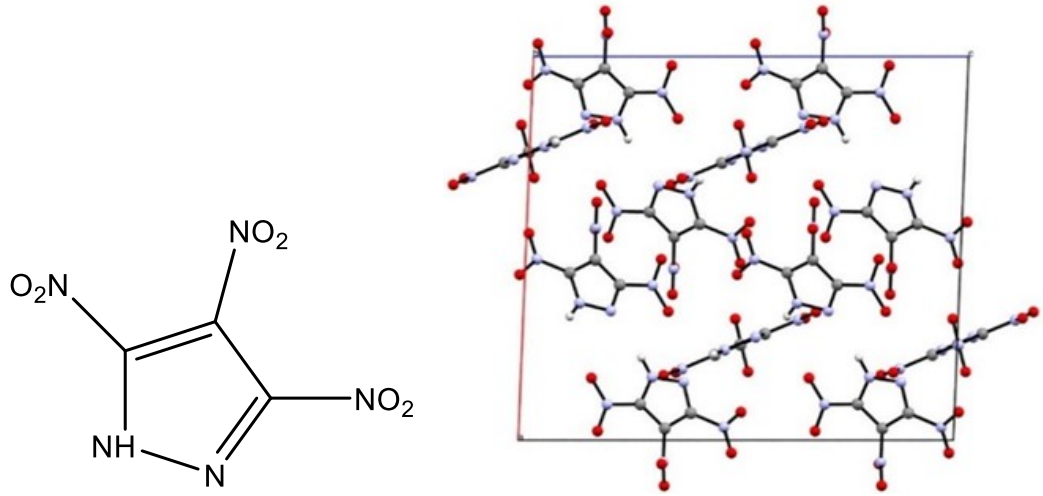

(a) (b)

Figure 3.1 Chemical structure (a) and unit cell of 3,4,5-TNP (b) viewed along the *c*-axis (CSD, reference code: KAHHIM02)

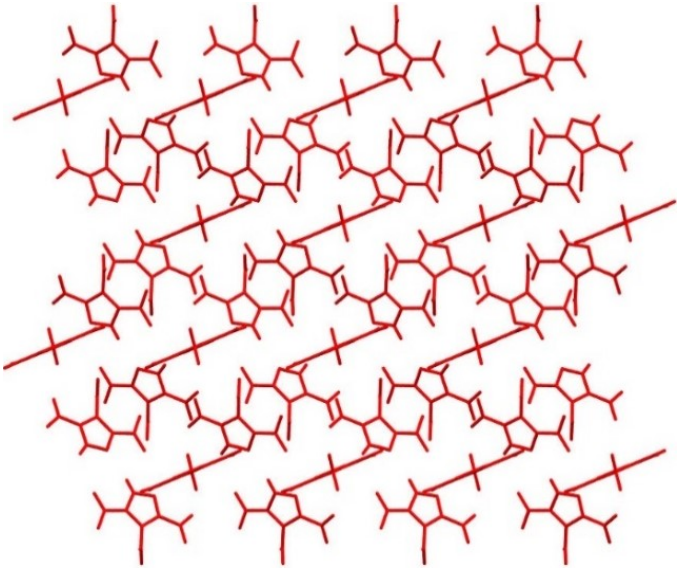

Figure 3.2 Packing arrangement of 3,4,5-TNP viewed along the *c*-axis

Table 3.1 Crystallographic data for 3,4,5-TNP

Compound	3,4,5-TNP
Formula	$C_3HN_5O_6$
Mr (g.mol^{-1})	300.18
Crystal system	Monoclinic
Space group	*P2$_1$/c*
***a*,** ***b*,** ***c* (Å)**	15.1586(13) 8.2781(8) 17.2014(16)
α, **β,** **γ (°)**	90 92.275 90
V (Å^3)	2156.81
ρ (g.cm^{-3})	1.876
R-factor	0.0378
Temperature (K)	Ambient (283-303)

3,4,5-TNP is classed as an insensitive energetic material (impact: 17 J, friction: 92 N, spark: 784 mJ), [6] which exhibits a high energetic performance that is comparable with other powerful energetic materials. Its detonation pressure (38.66 GPa) and detonation velocity (9.253 km/s) are superior to those of TNT (19.5 GPa, 6.9 km/s) and similar to those of HMX (P = 38.7 GPa, D = 9.09 km/s) and RDX (P = 34.8 GPa, D = 8.76 km/s). [7] Both are powerful, but relatively sensitive (impact sensitivity of HMX: 3 J, RDX: 4 J) explosives commonly used for many military applications. [8,4] Beside being a powerful explosive, 3,4,5-TNP is a useful component for rocket propellants. Moreover, it is classified as a green energetic material releasing non-toxic and environmentally benign dinitrogen gas as one of the main detonation products. [9]

The determination of equation of states is a significant aim of this chapter since these equations describe the compression behaviour of materials in a mathematical way. Realistic estimations of high-pressure, high-temperature thermodynamic properties of energetic materials (EM) are necessary to accurately describe their energetic properties. [7] In this study, the equation of state of 3,4,5-TNP was determined experimentally using neutron powder diffraction.

A major aim of this research is to investigate the high-pressure response of 3,4,5-TNP using Raman spectroscopy, neutron powder diffraction and single-crystal X-ray diffraction. Moreover, the prediction of the impact sensitivity of 3,4,5-TNP under-high-pressure condition using vibrational up-pumping model described in Chapter 1 is an additional aim. Understanding the high-pressure behaviour of 3,4,5-TNP will provide additional confidence in the safe use of this material in practical applications.

3.2 Materials

The following compounds were purchased from commercial sources: 3-nitro-1-H-pyrazole (FluoroChem), acetic anhydride (≥99%, Sigma-Aldrich), benzonitrile (anhydrous, ≥99%, Sigma-Aldrich), nitric acid (reagent grade, fuming, >90%, Sigma-Aldrich), sulfuric acid (ACS reagent, 95.0-98.0%, Sigma-Aldrich), D_2O (Sigma-Aldrich), pentane (anhydrous, ≥99%, Sigma-Aldrich) and isopentane (anhydrous, ≥99%, Sigma-Aldrich).

3.3 Experimental and computational methods

3.3.1 Synthesis and Deuteration of Pyrazole-Based Energetic Materials

3,4,5-TNP was synthesised from 3-nitro-1-H-pyrazole using sequential nitration and thermal rearrangement steps according to literature procedures. [3, 6, 10-14] Figure 3.3 shows the reaction scheme and experimental conditions. More details are given in Chapter 2 (Section 2.1.2). Successful syntheses of each of the compounds was verified by ^{1}H NMR and powder X-ray diffraction.

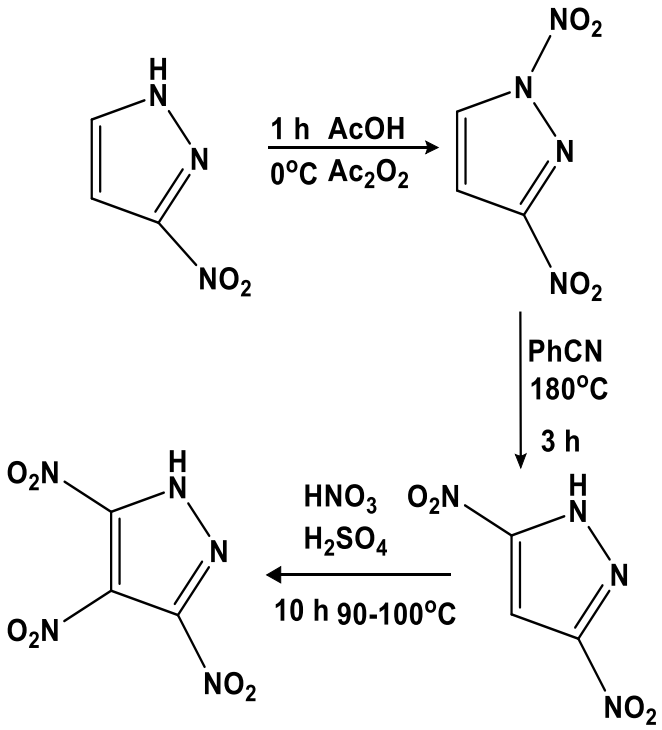

Figure 3.3 Synthetic route to 3,4,5-TNP

Deuteration of 3,4,5-TNP was achieved by recrystallising in deuterium oxide (D_2O) at 50°C three times. The deuterated sample was stored under nitrogen at 4°C until required.

3.3.2 High-Pressure Raman Spectroscopy

In-situ high-pressure Raman spectroscopy experiments were performed at room temperature using a Merrill-Bassett diamond anvil cell (DAC) from Almax EasyLab [half-opening angle of 40°], equipped with 600 μm cut diamonds and a tungsten carbide backing disc. A finely ground sample of 3,4,5-TNP was loaded into a 250 μm sized hole drilled in a pre-indented stainless steel gasket (thickness = 250 μm) was loaded. Small spheres of ruby were loaded in the DAC as a pressure calibrant, with a measurement precision of 0.05 GPa. The experiment was conducted under non-hydrostatic conditions. The pressure within the gasket hole was determined by the ruby fluorescence method [10] using a Jobin-Yvon LabRam 300 spectrometer equipped with a 50 mW He-Ne laser of wavelength 632.8 nm. The pressure was increased in steps of about ~0.5 GPa and Raman spectra measured after a 15 min equilibration time. For each pressure point, Raman spectra were recorded in different regions of the sample, with an exposure time of 60 s.

3.3.3 High-Pressure Neutron Powder Diffraction (NPD)

High-pressure time-of-flight NPD experiments were conducted using the PEARL instrument at the ISIS Neutron and Muon Source, UK.[11] Pressure was generated using a V3 variant Paris−Edinburgh cell (PEC). NPD experiments were performed in two parts. For the first compression experiment (up to a pressure of 4.5 GPa), a ~80 mm^3 of sample was loaded into a single-toroidal zirconia-toughened alumina (ZTA) anvil. For the second experiment, in order to observe very high-pressure behaviour of 3,4,5-TNP, a sample (~80 mm^3) was loaded into a tungsten carbide (WC) anvil for the second experiment. In the second compression, the data collection commenced at 3.9 GPa and reached a pressure of ~5.3 GPa.

In both loadings, a null-scattering TiZr gasket was used to contain the sample, and hydrostatic pressure conditions were achieved by the addition of a mixture of perdeuterated pentane/isopentane as the pressure-transmitting medium. A small pellet of lead foil was included in the sample chamber as a pressure indicator, and

sample pressures were calculated by refining the lattice parameters of lead.[12] A beamline-developed correction for the wavelength and scattering-angle dependence of the neutron attenuation by the anvil (ZTA, WC) and gasket materials were applied to the measured pattern. The data were normalised using MANTID. The MANTID project provides a framework (using Python) which enables data analysis, visualization and manipulation for neutron scattering and muon experiments. [13] The refinements of the data was performed using the GSAS package. [14] Rietveld refinements were performed at each pressure point starting with the data collected at 0.1 GPa, with each of the molecules in the asymmetric unit defined as independent rigid bodies. Constraints were imposed such that thermal vibration parameters were refined collectively for each different atom type. The data were of sufficient quality to allow refinement of the positions of the 3,4,5-TNP molecules in the unit cell. Principal axes with increasing pressure were determined using the program PASCAL. [15]

3.3.4 High-Pressure Single Crystal X-ray Diffraction (SXRD)

High-pressure single crystal X-ray diffraction measurements were conducted by Dr Xiaojiao Liu from the Pulham group on a Bruker D8 Venture X-ray diffractometer equipped with a CCD detector. A crystal of sufficient quality for X-ray diffraction was loaded into a Merrill–Bassett diamond anvil cell (DAC, Figure 3.4) with pentane-isopentane (v:v, 1:1) as a pressure-transmitting medium. Ruby spheres were used for pressure calibration. Data were collected using Mo-K_α radiation at ambient temperature conditions (ca 297 K). The Bruker APEX III software package was used for data reduction and corrections for the Lorentz polarisation and the absorption. Olex2 software was employed for structure determination. The structure was solved with the ShelXT program using Intrinsic Phasing methods. The refinement was performed by ShelXL program using least squares minimisation.

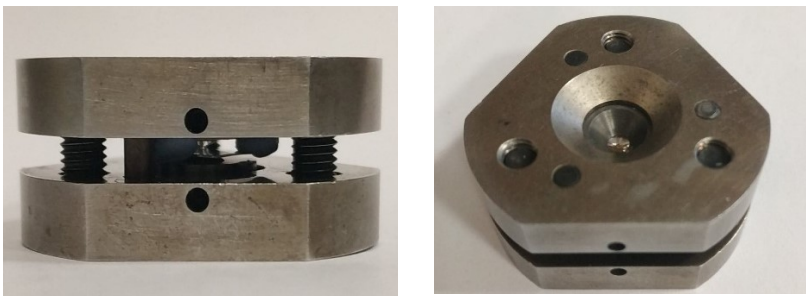

Figure 3.4 Diamond Anvil Cell

3.4 Results and Discussion

3.4.1 Characterisation of Synthetic Energetic Materials (3,4,5-TNP)

In this section, the characterisation of 3,4,5-TNP synthesised in this study is reported. NMR spectroscopy and powder X-ray diffraction (PXRD) results were used to confirm that 3,4,5-TNP had been successfully synthesised.

3,4,5-trinitropyrazole (3,4,5-TNP) was synthesised as the ultimate product of the synthetic route described in Figure 3.3. ^{1}H-NMR and ^{13}C-NMR spectra were recorded; the ^{1}H-NMR spectrum of the compound is shown in Figure 3.5 and exhibits a broad peak at δ = 4.1 ppm corresponding to the exchangeable proton of the NH group. The peak at δ = 2.54 corresponds to the residual protons of the solvent used (DMSO).

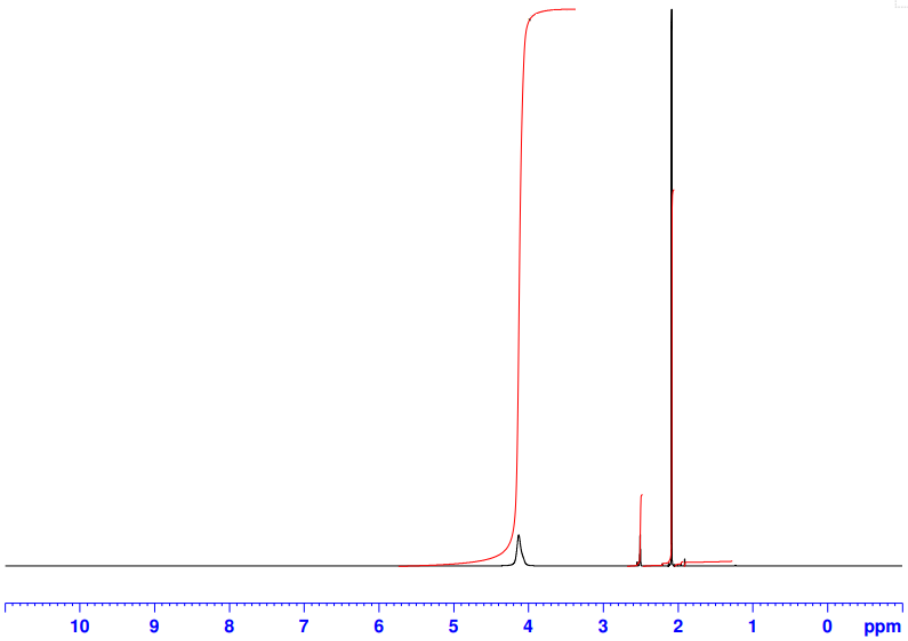

Figure 3.5 ^{1}H-NMR spectrum of 3,4,5-TNP

Figure 3.6 shows the ^{13}C spectrum of 3,4,5-TNP. There are three C atoms in 3,4,5-TNP. The two C atoms adjacent to N atoms are in the same chemical environment. Overall three peaks were observed corresponding to the two different C-atom environments and a peak (δ =40 ppm) corresponding to the NMR solvent used ($CDCl_3$).

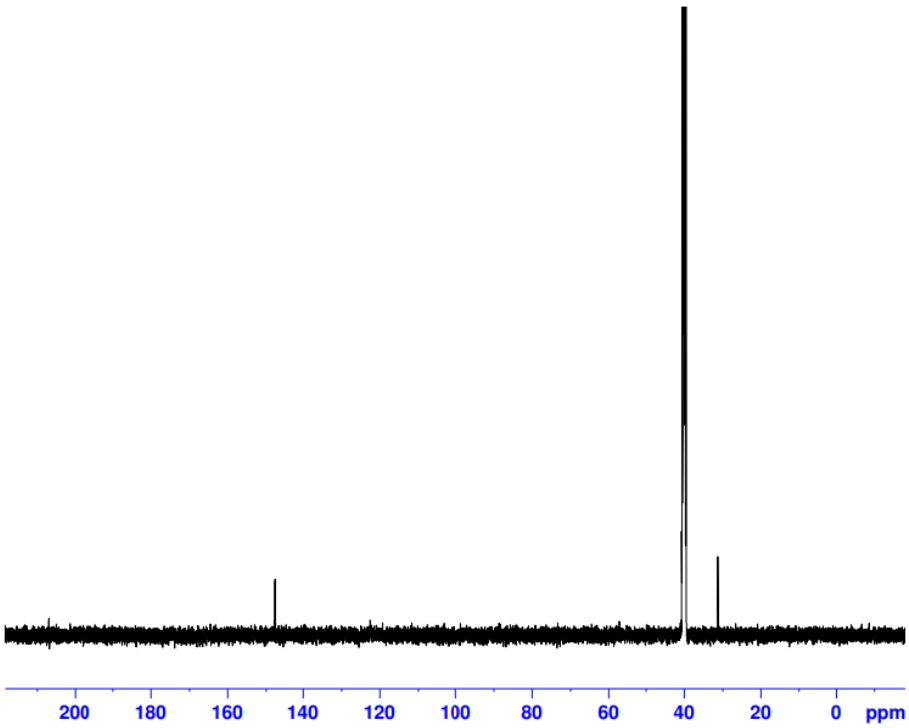

Figure 3.6 ^{13}C-NMR spectrum of 3,4,5-TNP dissolved in $CDCl_3$

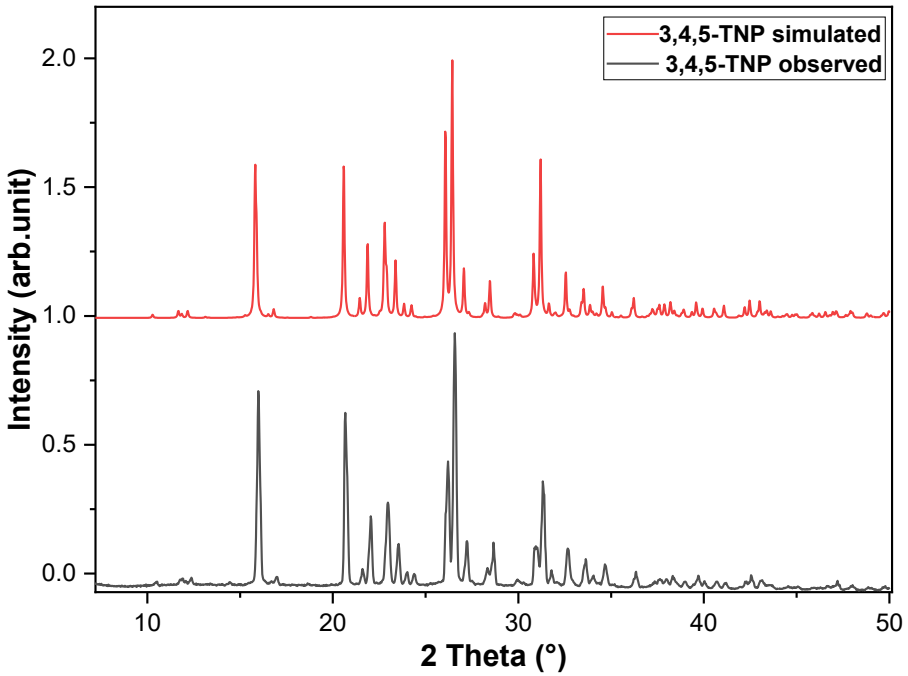

Figure 3.7 Powder X-ray diffraction patterns of 3,4,5-TNP (red line represents the simulated pattern based on the structure deposited in the CSDdata from CSD, black line is experimental data collected using the D2 Phaser instrument.)

^{1}H- and ^{13}C-NMR spectra therefore confirm the successful synthesis of 3,4,5-TNP. In order to check the phase purity of the synthesised 3,4,5-TNP, a powder X-ray diffraction pattern was collected and compared with the pattern simulated from the structure deposited in the CSD (ref. code: KAHHIM02), see Figure 3.7. This showed that the sample was phase-pure and suitable for co-crystallisation and salt formation studies.

3.4.2 High-Pressure Raman Spectroscopy

Raman spectra of 3,4,5-TNP was first collected under hydrostatic conditions. However, any change could not be observed using this data. Raman spectra were collected for a polycrystalline sample of 3,4,5-TNP from ambient pressure to 10.3 GPa under non-hydrostatic conditions, Figure 3.8. After reaching 10.3 GPa, the DAC was released and more measurements were collected during decompression. The gap in the Raman spectra in Figure 3.8 is due to intense scattering from the diamond anvils of the DAC – this very intense peak has not been plotted.

Although there were no major changes observed between pressure points, some subtle changes occurred between patterns at the lower pressure points (0.4-1.1 GPa) and above 4.9 GPa. These are indicated by asterisks in Figure 3.8 (a-b). For example, new peaks between 100-150 cm^{-1} appeared above 0.5 GPa - see Figure 3.8a and are indicated with red asterisks. Peak-shape changes were observed around 1350-1450 cm^{-1} at 0.5 GPa (Figure 3.8b). These spectral changes in the low-pressure range between 0.5-1.1 GPa may imply a structural change of 3,4,5-TNP. After that, the spectra remained consistent with increasing pressure until the sudden appearance of new bands at *ca.* 780 and 800 cm^{-1} at 4.9 GPa. These new bands are in the region associated with ring deformations, in-plane N-H deformations, and NO_2 bending modes. These new vibrational bands suggest a structural phase transition at these elevated pressures. No further changes were observed with increasing pressure to 10.3 GPa. During decompression, all the changes in the Raman spectra were consistent with those observed during compression. The peak at *ca.* 780 cm^{-1} was lost upon decompression below 4.9 GPa. Hence, any structural phase transition observed at elevated pressures appears to be reversible. These preliminary results were then followed up using diffraction techniques.

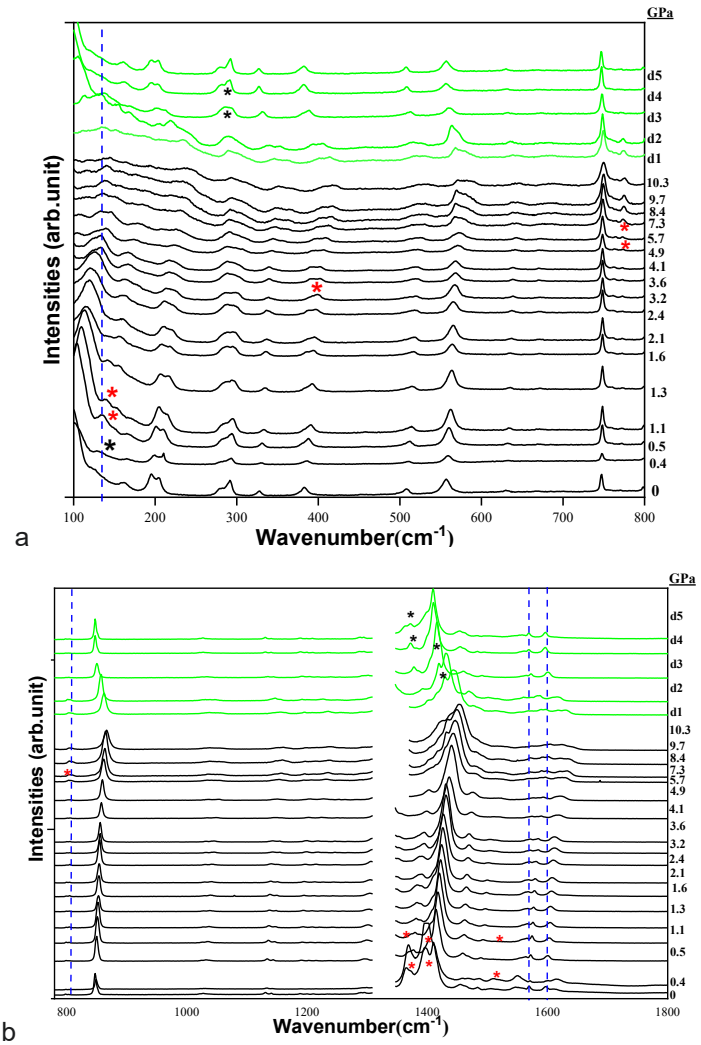

Figure 3.8 (a) Raman spectra showing the range of 100-800 cm^{-1} (b) showing the range of 800-1800 cm^{-1} of 3,4,5-TNP during compression and decompression (Asterisks indicate peaks appearing and disappearing in the spectra. The black colour represents the compression, and the green for decompression.)

3.4.3 High-Pressure Neutron Powder Diffraction

Neutron powder diffraction (NPD) patterns were collected for perdeuterated 3,4,5-TNP over the pressure range 0.1-4.5 GPa using ZTA anvils, and over the pressure range 3.9-5.3 GPa using WC anvils. A Rietveld refinement was performed for the NPD pattern collected immediately after loading at 0.1 GPa (see Figure 3.9a). This confirmed that the sample had not dissolved in the pressure-transmitting medium, and indicated that the sample was fully deuterated, and that the sample was phase-pure. Additional peaks were observed in the powder pattern corresponding to Pb (the pressure calibrant), Al_2O_3 and ZrO_2 (the anvil materials). Up to 4.1 GPa, Rietveld

refinements appear to fit the ambient-pressure structure, albeit with expected changes in the lattice parameters caused by compression, as shown in Figure 3.9b.

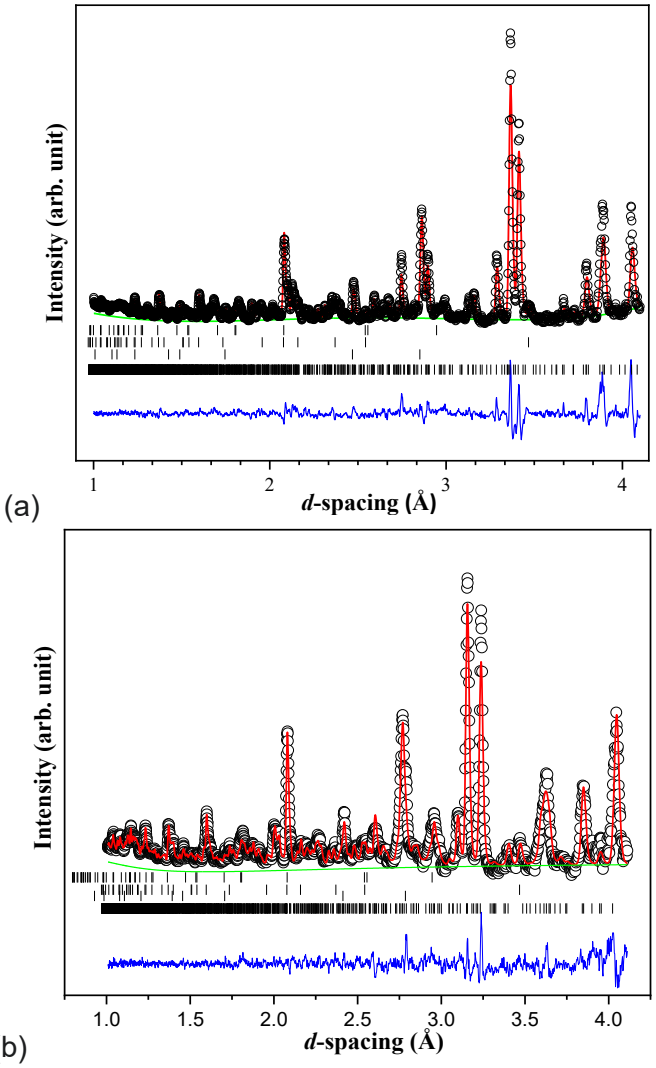

Figure 3.9 (a) Rietveld fit of neutron powder diffraction patterns of perdeuterated 3,4,5-TNP at 0.1 GPa (b) 4.1 GPa (Black circles are observed, red line is calculated 3,4,5-TNP phase, the green line is background, the blue line is the difference. Bragg reflections are shown as tick marks for each phase: from bottom to top 3,4,5-TNP, Pb, Al_2O_3 and ZrO_2.

Figure 3.10 (a) shows the diffraction patterns collected over the pressure range of 0.1 – 4.5 GPa in ~0.2 GPa steps using ZTA anvils. After sitting for ~1 hour at a pressure of 4.5 GPa, the sample violently decomposed resulting in rupture of the gasket and cracking of the anvils (See Figure 3.10 (b)). This abruptly ended the data collection at 4.5 GPa. In Raman spectroscopy, the sample compression was achieved up to 10.3 GPa without a violent decomposition. This difference might be explained with the

different sample and experiment conditions applied for Raman and NPD experiments. While 3,4,5-TNP sample (≈1 g) used for NPD was per-deuterated, Raman spectroscopy was performed on a per-hydrogenated 3,4,5-TNP sample (30-40 mg). Additionally, whereas Raman spectroscopy was conducted under non-hydrostatic conditions, NPD experiments were run under hydrostatic conditions.

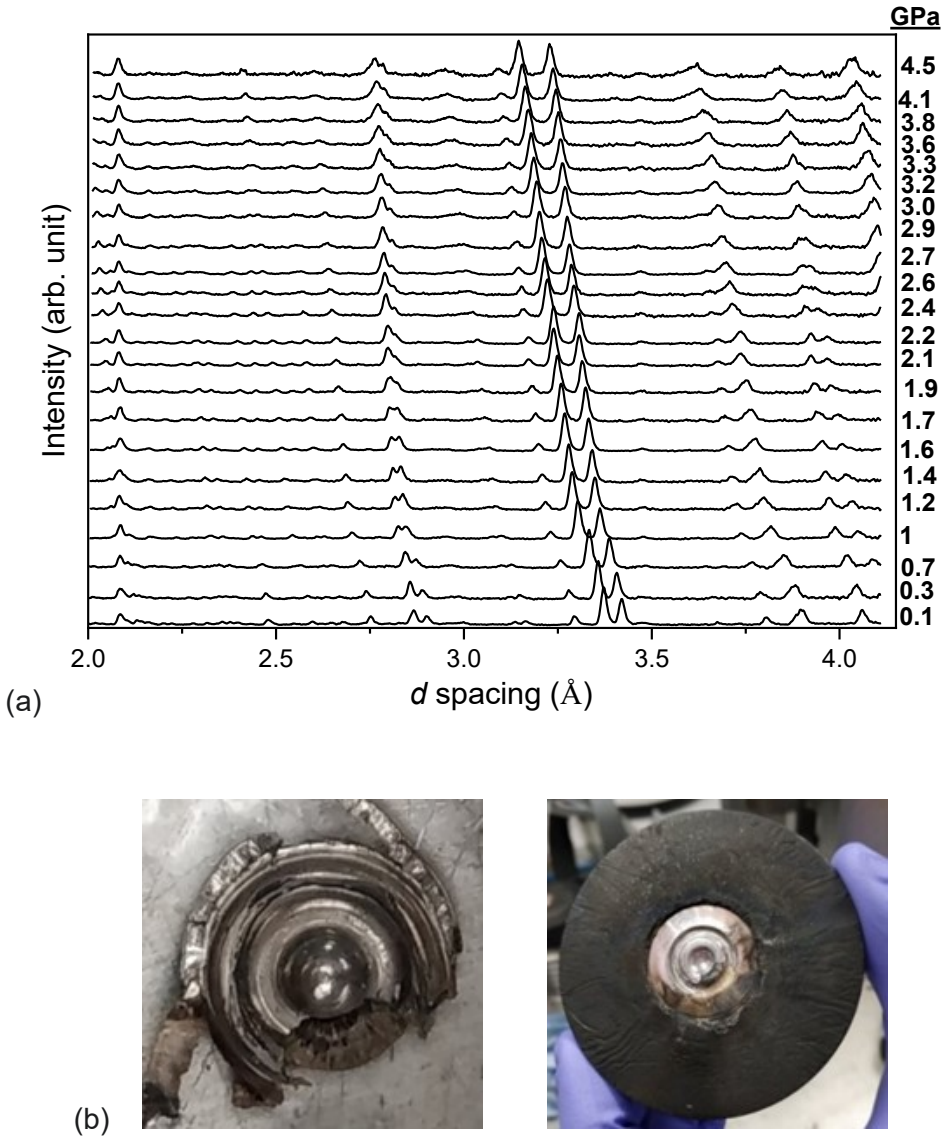

Figure 3.10 (a) Sequence of NPD patterns (rigid body refinements) obtained for perdeuterated 3,4,5-TNP over the pressure range of 0.1-4.5 GPa (b) Damaged ZTA anvil and Ti-Zr gasket

Using the data obtained from the NPD experiments up to 4.1 GPa, unit-cell parameters were refined and plotted against pressure (Figure 3.11). At 0.7 GPa, all of the lattice parameters exhibited a discontinuity in their trends. At 2.2 GPa, slight

discontinuities in the trends of the unit-cell parameters were observed. Also at 2.2 GPa, the downward trend in *β* angle reverses, before increasing again. These changes in the unit-cell parameters at 0.7 and 2.2 GPa were investigated further with single crystal X-ray diffraction (SXRD) and are discussed in section 3.4.4.

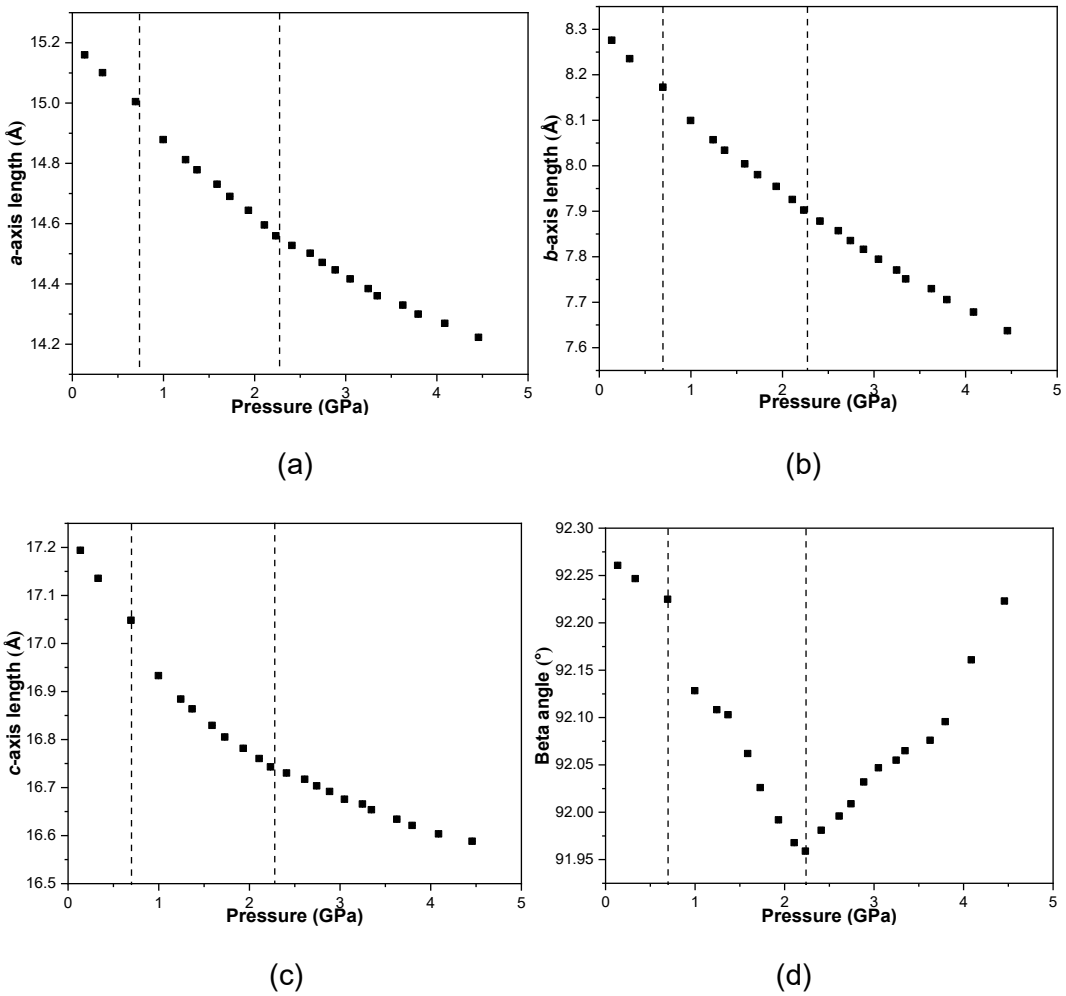

Figure 3.11 Variation in the unit cell parameters of 3,4,5-TNP with the increasing pressure for the first load (a - *a* axis, b - *b* axis, c - *c* axis and d - *β*-angle)

Figure 3.12 illustrates the relative changes in lattice parameters (*a, b, c*) upon compression. It is found that the *c*- axis is the least compressible with a ratio of c/c_0 = 0.965 at 4.1 GPa. The largest compression occurred along the *b*-axis with the ratio of b/b_0 = 0.923 at 4.1 GPa. At 4.1 GPa, the compression ratio of a/a_0 = 0.941 lies between the values for *b*- and *c*-axes. This anisotropic compression of 3,4,5-TNP can be related to void space distribution in the unit cell which is shown in Figure 3.13.

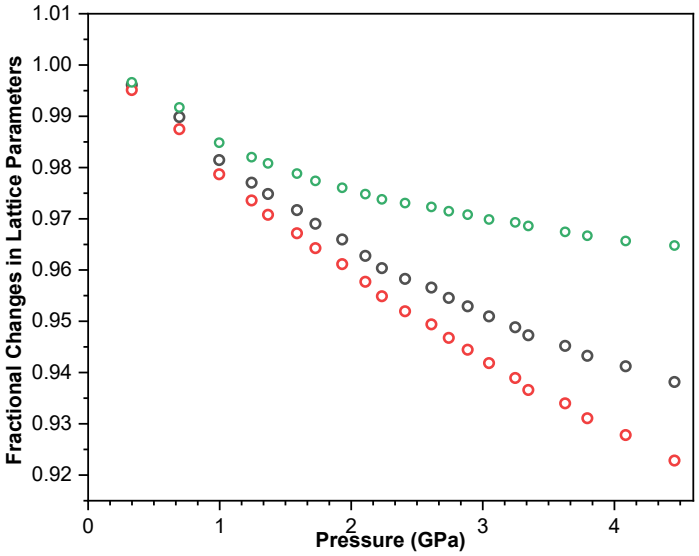

Figure 3.12 Relative compression of lattice parameters of 3,4,5-TNP with increasing pressure (black circles a/a_0, red circles b/b_0, green circles c/c_0)

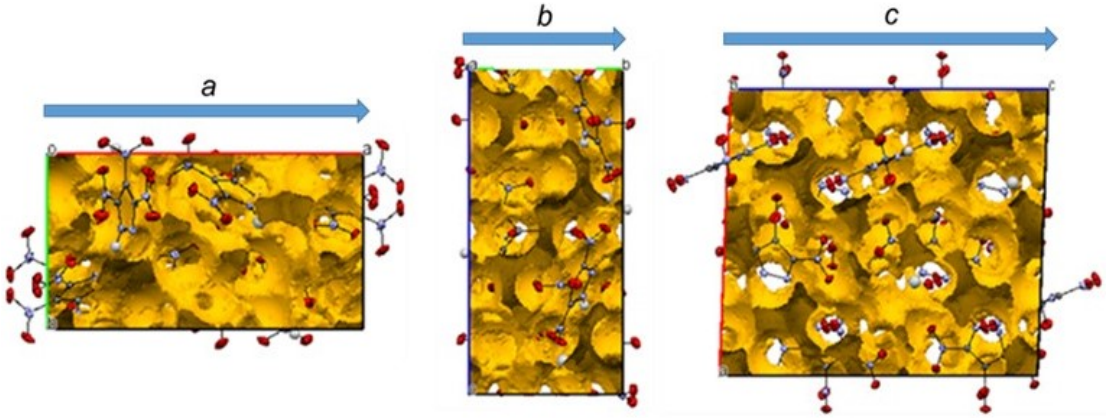

Figure 3.13 Illustration of void space in 3,4,5-TNP unit-cell under ambient conditions through *a*, *b* and *c* axes (Voids spaces are calculated in Mercury 4.3.1 program package. It finds any voids in unit-cell that are the size of a spherical "probe" of 0.2 Å radius.)

In monoclinic and triclinic systems, it is hard to explain the direction of mechanical response by using unit-cell axes since expansion and compressibility depend on the variation in unit-cell geometry determined by cell lengths and angles. Hence, principal axes must be determined as the eigenvectors of the full strain tensor.[15] For the anisotropic compression of 3,4,5-TNP, principal axes were calculated using PASCal, and the changes in the principal axes is given in Figure 3.14(a). Median principle compressibility and directions of the principal axes are given in Figure 3.14(b).

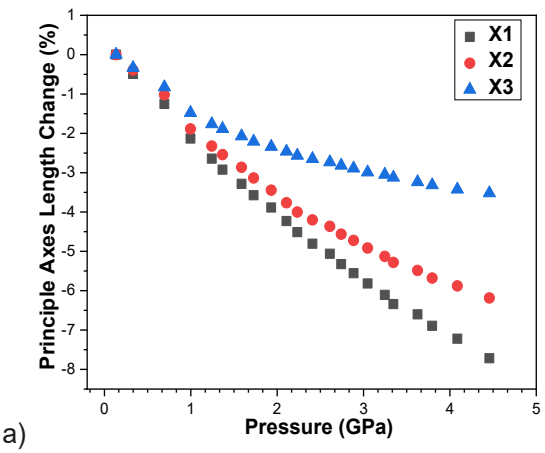

a)

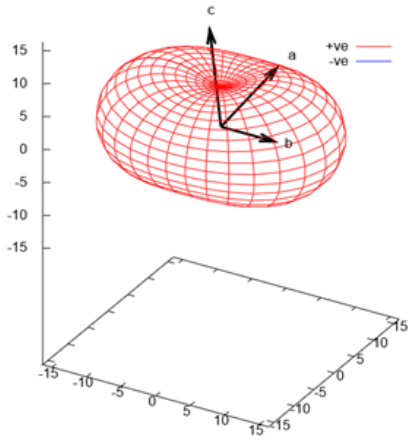

b)

c)

Axes	*K (TPa^{-1})*	a	b	c
X1	16.3(2)	0	1	-0
X2	12.6(2)	0.99	-0	-0.12
X3	6.0(2)	0.20	-0	0.98

Figure 3.14 (a) Principal axes change with increasing pressure (PASCal) (b) compressibility indicatrix of 3,4,5-TNP (c) X_1, X_2, X_3 are principle axes, K represents median compressibility, direction is the projections on the unit cell axes.

The compressibility indicatrix of 3,4,5-TNP was created using PASCal over the pressure range of 0.1-4.5 GPa, and shown in Figure 3.14(b). The compressibility indicatrix is a surface which smoothly varies and is located at the unit-cell origin. [16,17,18,19] Using this indicatrix, the crystallographic directions related to mechanical behaviour of particular interest can be determined and expansivity/compressibility tensors are visualised.

The P-V curves and associated equations of state were fitted using EoSFit7 software and are shown in Figure 3.15. Phases are states of materials characterised by distinct macroscopic properties. These properties of the states change by definition at the phase boundary. When this change is discontinuous 1st order phase transition, if it is continuous 2nd order phase transition is observed. [20] At the first phase transition (From Form I to Form II), the P-V curve shows an obvious discontinuity near 0.7 GPa that represents a first order phase transition to a new phase that will henceforth be termed Form II. This also manifests itself in the behaviour of the lattice parameters (Figure 3.11). A more subtle change is observed in the volume at ~2.2 GPa, perhaps suggesting a second order phase transition. This also manifests itself prominently in the behaviour of the β-angle (see Figure 3.12(d)). Hence, it appears that a phase

transition to a new Form III occurs at ~2.2 GPa. These phase domains are indicated in Figure 3.15.

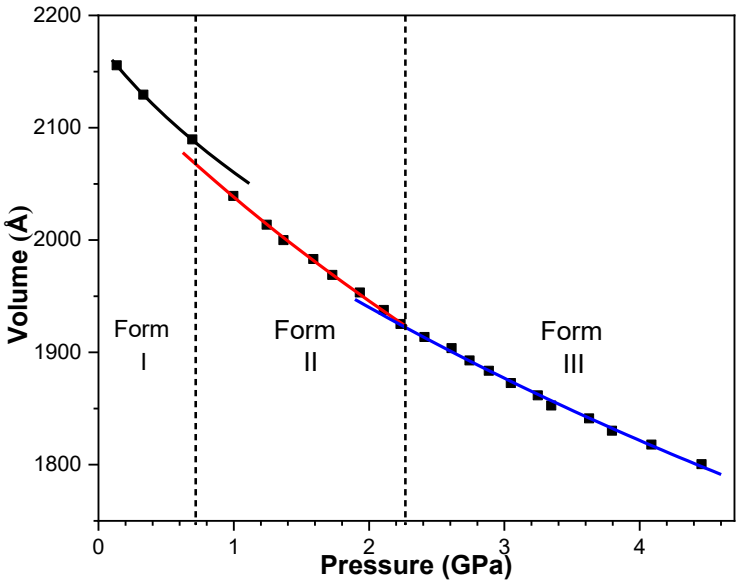

Figure 3.15 Equation of state curve of 3,4,5-TNP (black line:0.1-1 GPa, red line: 1-2.2 GPa, blue line: 2.4-4.5).

Thermodynamic parameters of the EoSs are provided in Table 3.2. It is observed that bulk moduli (B_0) values increase at elevated pressures indicating that the material becomes less compressible. The B_0 values obtained for 3,4,5-TNP are in the range of the values usually obtained for typical organic energetic materials. [21,22] Overall bulk modulus values of 3,4,5-TNP is much lower comparing to inorganic materials or typical ceramics. For instance as a typical ceramic material, γ-Alumina has a bulk modulus of 162±14 GPa which is much higher than the bulk modulus values of 3,4,5-TNP.

Table 3.2 Thermodynamic parameters for equation of states

	V_0(Å^3)	B_0 (GPa)	B'
Birch-Murnaghan 2nd order (0.1-1 GPa)	2175.59	15.57(43)	4
Birch-Murnaghan 2nd order (1-2.2 GPa)	2151.28	16.43(1)	4
Birch-Murnaghan 2nd order (2.4-4.5 GPa)	2116.13	19.6(4)	4

*V_0 values are fixed since both values obtained by fixing V_0 and refining V_0 are very similar.

With the aim of achieving higher pressures and avoiding gasket failure, a second high-pressure experiment was performed using more robust tungsten-carbide anvils (3.8-5.3 GPa). All the patterns for this experiment are shown in Figure 3.16.

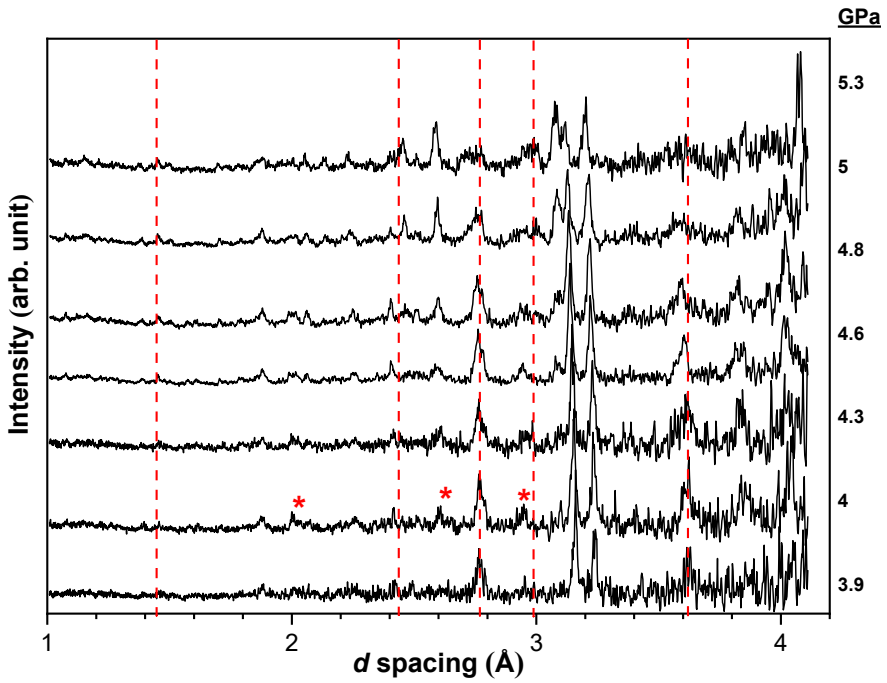

Figure 3.16 Neutron powder diffraction patterns for 3,4,5-TNP with increasing pressure from the second experiment utilising WC anvils (red dashed lines indicate peaks appearing or disappearing.)

During the second compression, a violent decomposition also occurred at 5.3 GPa resulting in loss of sample. Figure 3.16 shows new peaks near 2 Å, 2.6 Å and 3 Å begin to appear at 4 GPa (asterisks) suggesting a sluggish phase transition. More changes in the peaks at higher pressures were observed, and these are highlighted with dashed lines in Figure 3.16. These significant changes between the diffraction patterns strongly suggest a phase transition was occurring gradually over the pressure range 3.9 - 5.3 GPa prior to the initiation of the sample. Based on these results, it can be concluded that Form IV appears above 5.3 GPa via a rather sluggish phase transition. Unfortunately, the quality of the data combined with the restricted *d*-spacing range prevented indexing of these patterns. There are many energetic materials that have been studied using similar techniques up to even higher pressures

without any initiation. [23] For example, RDX, has been investigated using neutron powder diffraction up to 7.9 GPa with no initiation. [24] Since 3,4,5-TNP is known as an insensitive secondary explosive, the initiation of 3,4,5-TNP under hydrostatic compression was unexpected. The unexpected initiation, which coincides with a phase transition to Form IV suggests that Form IV is more sensitive to initiation (friction) than Forms I, II and III. This sudden change in the sensitivity of 3,4,5-TNP should be investigated and correlated with the crystal structure of Form IV as future work. This is discussed further in Section 3.4.6.

3.4.4 High-Pressure Single-Crystal X-Ray Diffraction

In order to obtain the structure of Form IV of 3,4,5-TNP, high-pressure single crystal diffraction experiments were performed. 3,4,5-TNP was compressed from 0.2 to 7.3 GPa in a standard Merrill-Bassett diamond anvil cell (DAC). Data were collected at nine pressure points over this pressure range, and no initiation or violent decomposition was observed. This allowed us to solve the structure of the high-pressure form of 3,4,5-TNP which was named as Form IV. At 5.3 GPa a new unit-cell was obtained with space group *Cc.* The unit-cell dimensions of Forms I to III [Figure 3.17(a)] and Form IV [Figure 3.17 (b)] are shown in Figure 3.17. The structure of Form IV was solved and refined to give an R-factor of 3.99%. Crystallographic information for Form IV along with other forms are given in Table 3.3. It was not possible to refine the positions of the H-atom for each independent molecule and so these were placed in calculated positions for each of the three independent molecules in the asymmetric unit.

A Rietveld refinement was performed using the highest-pressure (5.3 GPa) NPD data from the second load (WC) and CIF file of Form IV obtained from SXRD, by defining each of the independent molecule in the asymmetric unit as rigid bodies. Thermal constraints were applied for the same type atoms and U_{iso} values were refined. The fit is given in Figure 3.18 shows a very acceptable fit (wRp = 0.0413 and Chi^2 = 1.017) confirming that the high-pressure NPD and SXRD results are consistent and that Form IV has been formed in both experiments.

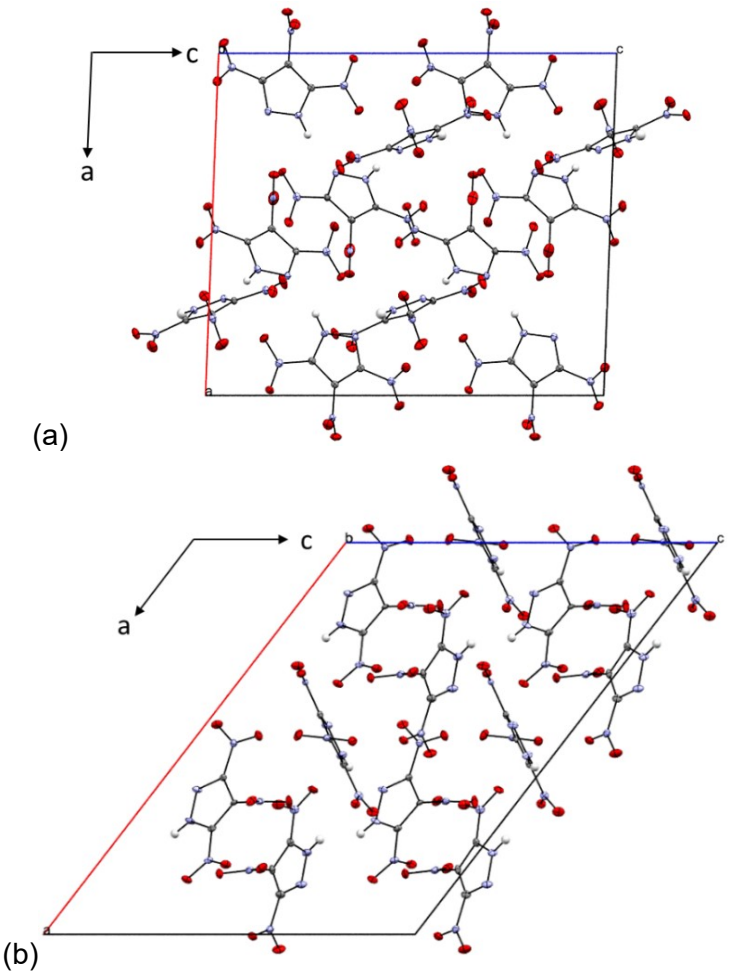

Figure 3.17 (a) Unit cell of 3,4,5-TNP before phase transition, Form III (3.8 GPa) (b) unit cell of Form IV (5.3 GPa).

Table 3.3 Crystallographic information for different phases of 3,4,5-TNP

Compound	**3,4,5-TNP** (Form I, CSD)	**3,4,5-TNP** (Form II)	**3,4,5-TNP** (Form III)	**3,4,5-TNP** (Form IV)
Formula	$C_3HN_5O_6$	$C_3HN_5O_6$	$C_3HN_5O_6$	$C_3HN_5O_6$
Crystal system	Monoclinic	Monoclinic	Monoclinic	Monoclinic
Space group	*P*2$_1$/*c* (14)	*P*2$_1$/*c* (14)	*P*2$_1$/*c* (14)	*Cc* (9)
a, ***b,*** ***c* (Å)**	15.1586(13) 8.2781(8) 17.2014(16)	14.7836(11) 8.0383(8) 16.8670(12)	14.2569(7) 7.6573(6) 16.6118(8)	19.5713(11) 7.6509(8) 14.6982(9)
α, **β,** **γ (o)**	90 92.275(2) 90	90 92.078(4) 90	90 92.197(3) 90	90 127.661(2) 90
Unit cell volume (Å^3)	2156.81	2003.07	1812.17	1742.3
Density (g.cm^{-3})	1.876	2.020	2.233	2.311
R factor	0.0378	0.0488	0.0366	0.0399
Temperature (K)	Ambient	297	297	297
Pressure (GPa)	Ambient	1.1	3.8	5.3

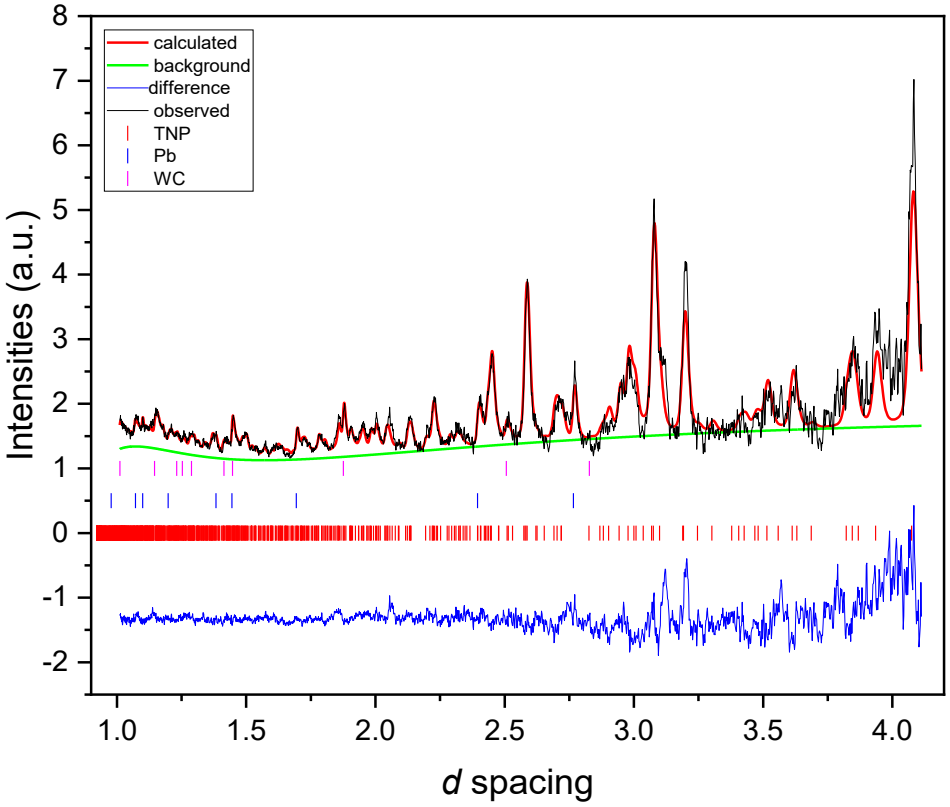

Figure 3.18 Rietveld refinement of 3,4,5-TNP with the highest pressure NPD data and Form IV SXRD data (Red line is calculated from Form IV cif file, black line is NPD data at 5.3 GPa, blue line is difference, green line is background. Vertical lines represent the different phases; red 3,4,5-TNP phase, blue Pb, and magenta WC)

In Form IV, the molecular packing of 3,4,5-TNP became denser and molecules became closer. The H-bonding interactions for Form I and Form IV are illustrated in Figure 3.19. In Form IV the H-bonds in 3,4,5-TNP were reoriented compared to Form I-III. Form IV exhibited a much more extensive H-bonding network than the previous forms, see Figure 3.19(a) and (b). While nitro groups were far from NH group on the pyrazole at low pressures, they became close enough to form new H-bonds with NH groups at high-pressures. Therefore, additional NH···O type of hydrogen bonds were formed in Form IV (Figure 3.19(b)). The appearance of these additional H-bonds may play a significant role in the formation of Form IV.

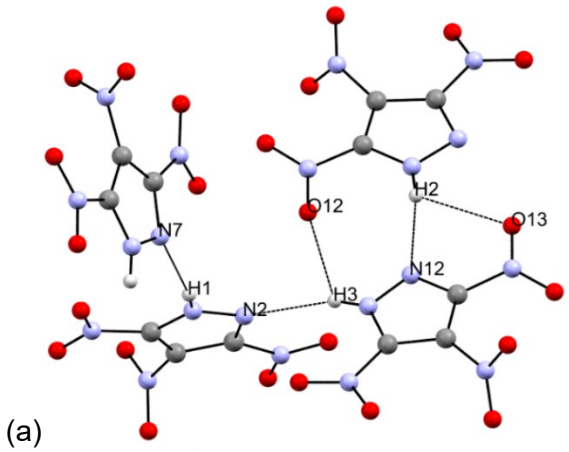

(a)

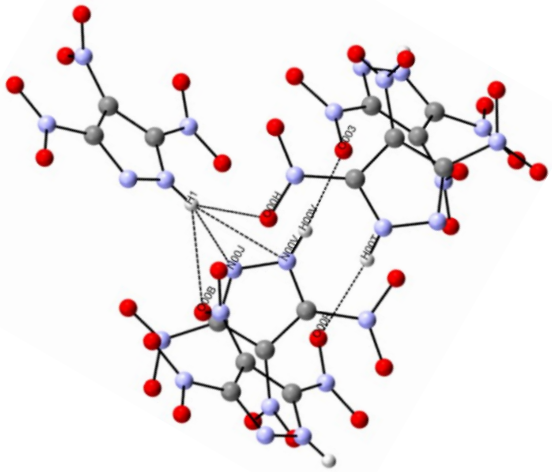

(b)

Figure 3.19 H-bonding in 3,4,5-TNP (a) Form I - III (b) Form IV. (H-bonds are shown with dashed-line. For Form IV, H-atoms were placed in the calculated positions using OLEX2 structure solution program which exploits restrains to place preferred atoms)

In addition to change in the H-bonding network, the transition from Form III to Form IV involves the conformational changes in the NO_2 torsion angles. Changes in the inclination of NO_2 torsion angles obtained from SXRD data are given in Figure 3.20. Significant discontinuities in nitro torsion angle trends were observed in Form IV (Figure 3.20 a,b,c). All the torsion angles in the asymmetric unit of 3,4,5-TNP showed a noticeable discontinuity at 5.3 GPa.

Another change in the torsion angles of 3,4,5-TNP was observed at 2.2 GPa which is the phase change pressure from Form II to Form III. The other implications of this

phase transition including *β*-angle (Figure 3.12d) and EoS (Figure 3.15) changes are explained in Section 3.4.3.

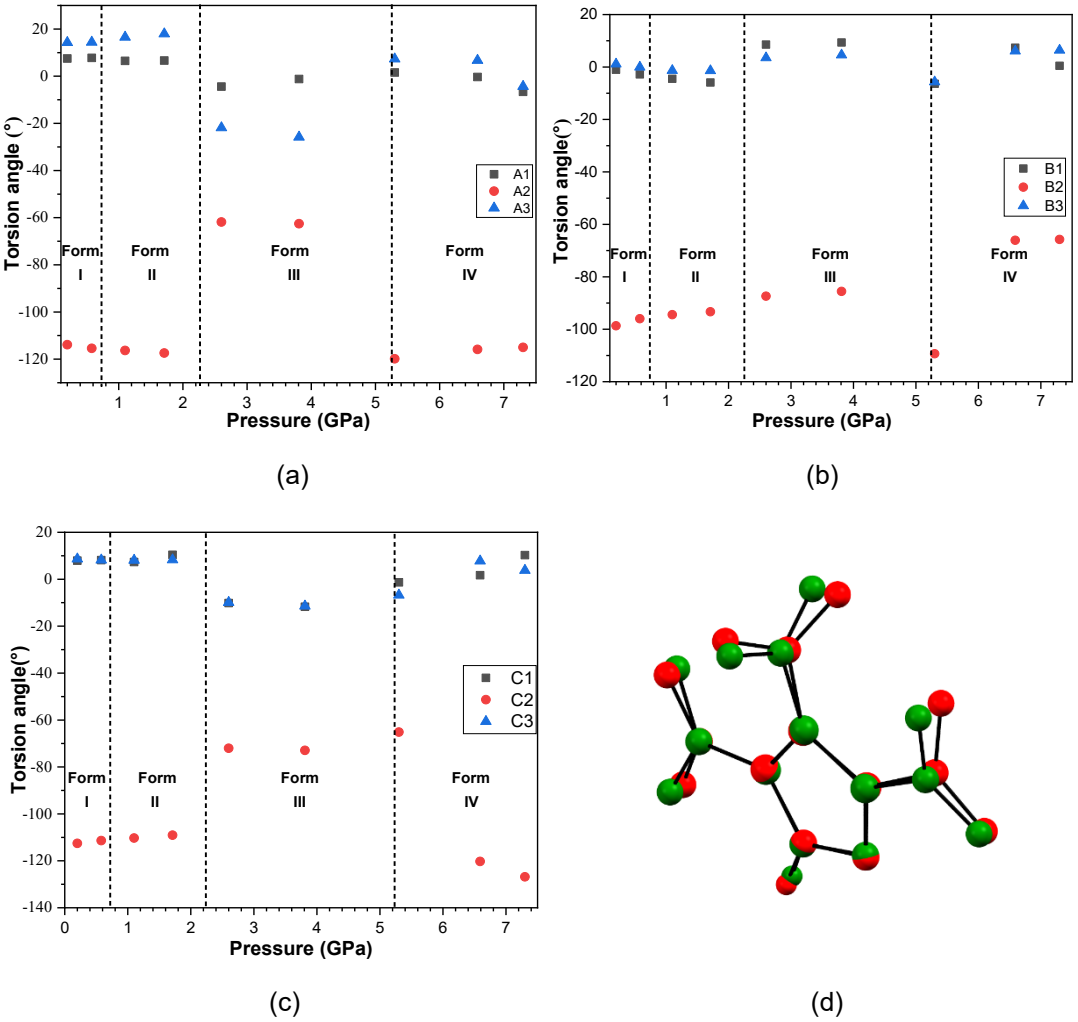

Figure 3.20 (a,b,c) Changes in the inclination of NO_2 torsion angles in the asymmetric unit cell of 3,4,5-TNP, (d) comparison of a 3,4,5-TNP molecule just before and after phase transition (green molecule at 3.8 GPa and red molecule at 5.3 GPa)

3.4.5 Effects of Pressure on Intermolecular Interactions

Since the neutron diffraction experiments were recorded with small pressure steps, this provides useful data to detect small structural changes over the pressure range of 0.1-4.5 GPa. Three dominant hydrogen bonds in 3,4,5-TNP (see Figure 3.21) were identified and their evolution with pressure was explored.

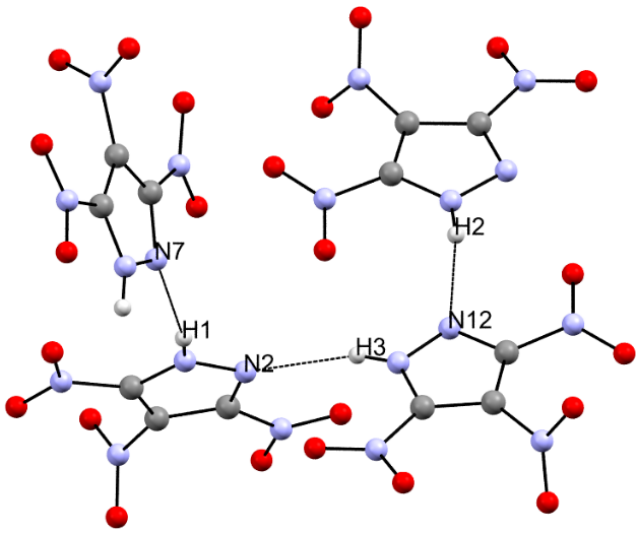

Figure 3.21 Hydrogen bonding in TNP (Form I – III)

Bond lengths (D···A, H···A) for these three H-bonds [N6-H2···N12 (HB1), N11-H3···N2 (HB2) and N1-H1···N7 (HB3)] obtained from neutron experiments are shown in Figure 3.22. Bond angle trends for these H-bonds are given in Figure 3.23. The trends in H-bond lengths showed discontinuities for HB1, HB2 and HB3 between 0.7-1 GPa at the transition pressure from Form I to Form II.

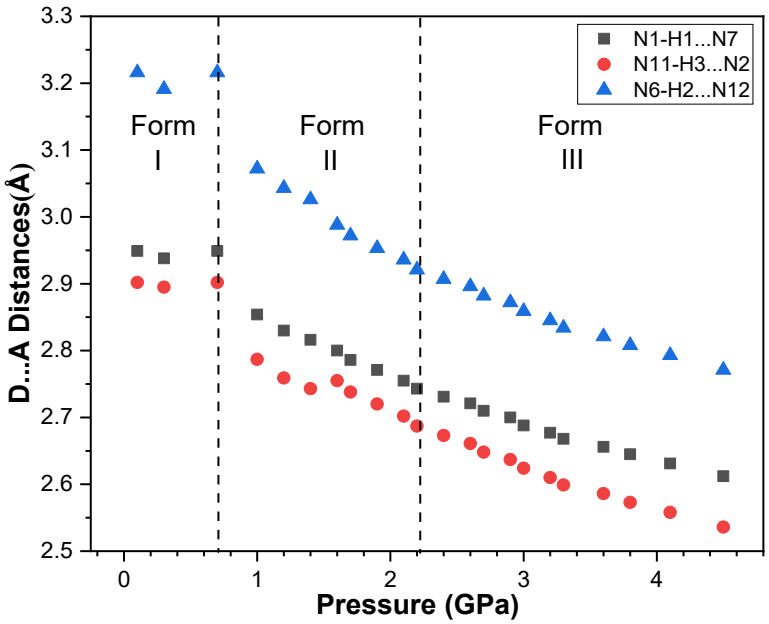

Figure 3.22 Trends of hydrogen bond distances in 3,4,5-TNP (Dashed lines illustrate phase change pressure points.)

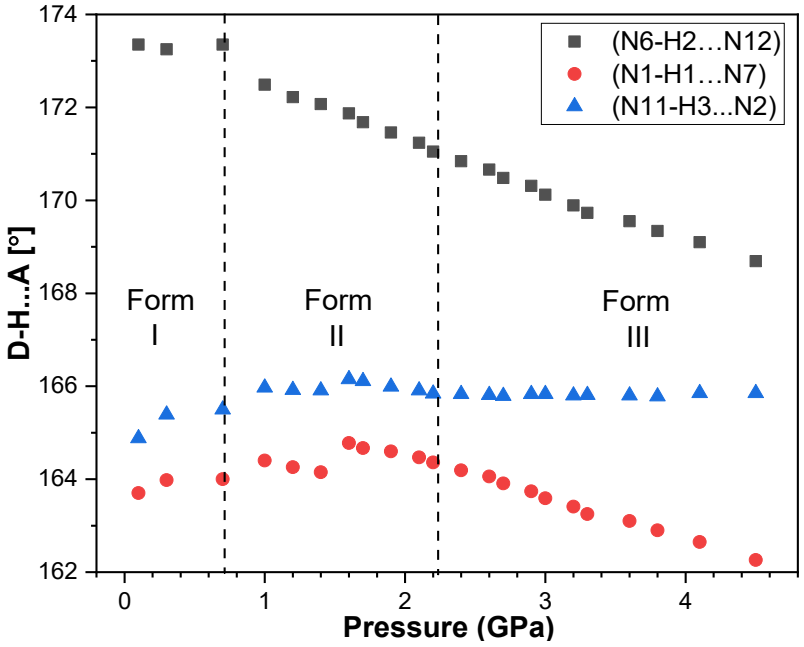

Figure 3.23 Trends in hydrogen bond angles in 3,4,5-TNP (Dashed lines illustrate phase change pressure points.)

3.4.6 Computational studies: Prediction of the sensitivity of Form I and IV

Geometry optimisation

Unit-cell parameters obtained from the geometry optimisation calculations are shown in Table 3.4, from which it can be observed that the simulations are in good agreement with the experimental data.

Form IV appears to be more susceptible to detonation than the ambient pressure structure as mentioned in the previous sections. In an effort to understand why, Prof. Carole Morrison and her research group have applied their recently published impact sensitivity prediction model based-on vibrational up-pumping theory to compare predicted sensitivities for the ambient and high-pressure structures of 3,4,5-TNP. Full details on the theoretical framework, which has demonstrated success for a range of structurally and energetically diverse materials, can be found elsewhere. [25,26,27]

Table 3.4 Experimental and calculated unit cell parameters of 3,4,5-TNP with varying pressure (0-7.3 GPa)

P (GPa)	Experimental							Calculated							
	a (Å)	b (Å)	c (Å)	α (°)	β (°)	γ (°)	V (Å³)	a (Å)	b (Å)	c (Å)	α (°)	β (°)	γ (°)	V (Å³)	Change (%)
0.0	15.16	8.28	17.2	90.0	92.3	90.0	2156.8	15.506(4)	8.367(1)	17.385(6)	90.0	92.179(6)	90.0	2254.0	+4.05
0.2	15.104(1)	8.246(1)	17.141(1)	90.0	92.235(4)	90.0	2133.3	15.404(0)	8.304(9)	17.307(0)	90.0	92.183(5)	90.0	2212.5	+3.71
0.58	14.937(2)	8.134(1)	16.989(2)	90.0	92.2(1)	90.0	2062.7	15.257(5)	8.219(8)	17.187(0)	90.0	92.129(8)	90.0	2153.8	+4.41
1.11	14.784(2)	8.038(1)	16.867(1)	90.0	92.113(8)	90.0	2003.1	15.067(1)	8.124(9)	17.062(2)	90.0	92.018(7)	90.0	2087.4	+4.21
1.71	14.645(1)	7.955(1)	16.795(1)	90.0	92.078(5)	90.0	1955.3	14.885(1)	8.038(0)	16.952(4)	90.0	91.930(5)	90.0	2027.1	+3.67
2.6	14.453(1)	7.818(1)	16.713(1)	90.0	92.015(4)	90.0	1887.3	14.662(5)	7.893(1)	16.876(8)	90.0	92.018(3)	90.0	1952.0	+3.43
3.81	14.257(2)	7.657(0)	16.612(0)	90.0	92.197(3)	90.0	1812.2	14.481(3)	7.728(9)	16.754(7)	90.0	92.460(5)	90.0	1873.5	+3.38
5.3	19.571(1)	7.651(0)	14.698(0)	90.0	127.661(2)	90.0	1742.3	19.664(9)	7.715(4)	14.866(7)	90.0	127.844(7)	90.0	1782.1	+2.28
6.59	19.399(1)	7.596(0)	14.529(2)	90.0	127.637(3)	90.0	1695.3	19.143(4)	7.873(1)	14.399(1)	90.0	126.742(7)	90.0	1739.0	+2.58
7.3	19.319(2)	7.567(1)	14.458(3)	90.0	127.623(5)	90.0	1647.0	19.690(1)	7.423(8)	14.831(2)	90.0	127.804(7)	90.0	1712.9	+2.32

* Form IV data highlighted with the blue colour.

A schematic representation of the vibrational up-pumping model is shown in Figure 3.24. In essence the model, which is based on a vibrational up-pumping process, accounts for the ease with which the vibrational modes of the crystal (the so-called phonon density of states, DoS) can channel the energy from a mechanical impact through the low energy phonon bath modes (marked by ω < Ω_{max} , where Ω_{max} denotes the highest frequency lattice vibration) to reach the molecular vibrations. Following impact, the phonon bath modes superheat and scatter to create a new set of phonons that are termed the two-phonon density of states (2phonDoS). The degree to which the 2phonDoS projects onto the original DoS in the region 1-3Ω_{max} (which is termed the up-pumping window) provides the metric that describes how efficiently the DoS can trap the mechanical energy in the molecular vibrations. Vibrationally exciting the 1-3 Ω_{max} molecular modes induces large amplitude vibrations that distort the molecular structure to the degree that electronic changes occur: band gaps narrow, electrons flow and unstable species emerge all on the timescale of a molecular vibration. [32]

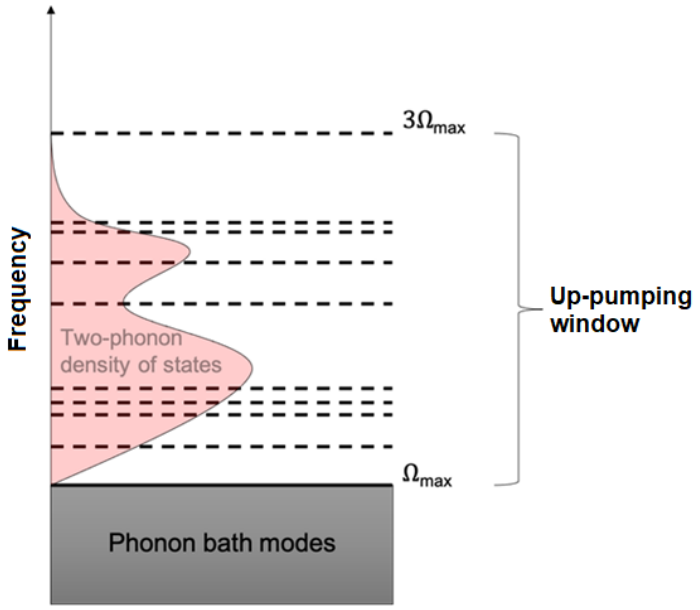

Figure 3.24 Schematic illustration of the vibrational up-pumping model.

The simulated phonon density of states (DoS) for Form I and Form IV are shown in Figure 3.26. The first point to note is that the two plots are notably different. While the number of phonon bath modes (*i.e*. the number of modes shown below the Ω_{max} cut-off) is conserved for both structures, some have 'hardened', shifting upwards by *ca*.

10-20 cm^{-1}, in Form IV. This effect has been previously noted for other molecular crystals. [28] This results in a splitting and spreading out of modes in the phonon bath, such that Ω_{max} rises by 35 cm^{-1} for Form IV and becomes a continuous distribution of modes. Thus Form IV has an expanded phonon bath region compared to Form I. This is a critical observation for the vibrational up-pumping model, for it immediately suggests that Form IV will have a more pronounced 2phonDoS trace, and therefore more likely to produce a notable projection onto the DoS. The phonon bath modes become superheated due to the heat capacity for the phonon bath modes (C_{ph}) being considerably lower compared to the bulk heat capacity (C_{tot}). The ratio C_{tot} / C_{ph} permits a scale factor to be determined, which permits the degree of phonon mode heating, T_{shock}, to be estimated (see Table 3.5). All other modes are vibrationally heated to 300 K. A higher Ω_{max} also defines a broader 1-3 Ω_{max} 'up-pumping' window, where the 2phonDoS envelope (red plots, Figure 3.25) is projected onto the underlying DoS plots. The 2phonDoS plots shown in Figure 3.25 both peak at their respective $2\Omega_{max}$ values, denoting the maximum intensity achieved from the scattering of two phonon states close to upper Ω_{max} limit; the reduced scattering intensity calculated in the 2-3Ω_{max} range arises due to the incorporation of scattering effects that include the so-called doorway modes, which are the low-lying molecular modes found just above Ω_{max}.

Table 3.5 Key computed features in the vibrational structure of TNP polymorphs.

	Form I	**Form IV**
Ω_{max} (cm^{-1})	218	253
C_{ph}/JK^{-1}mol^{-1}	1278	623
C_{tot}/JK^{-1}mol^{-1}	4463	2219
C_{tot} / C_{ph}	3.49	3.56
T_{shock}/K	2288	2334

In comparing the 2phonDoS plots for the ambient and high-pressure polymorphs of 3,4,5-TNP, the reason for the heightened sensitivity observed for the high pressure structure becomes obvious: the broader phonon bath region, the heightened 2phonDoS trace, and the wider 1-3 Ω_{max} up-pumping window results in more of the 2phonDoS successfully projecting onto the underlying DoS. The high pressure DoS itself also contains more split peaks (*i.e*. has a greater ability to 'trap' the 2phonDoS

trace) compared to the ambient pressure DoS. Integrating the overlap between the DoS and the projected 2phonDoS provides the metric for the efficiency of vibrational up-pumping; this is plotted on Figure 3.25, alongside previously reported values for a well-known set of energetic crystals.

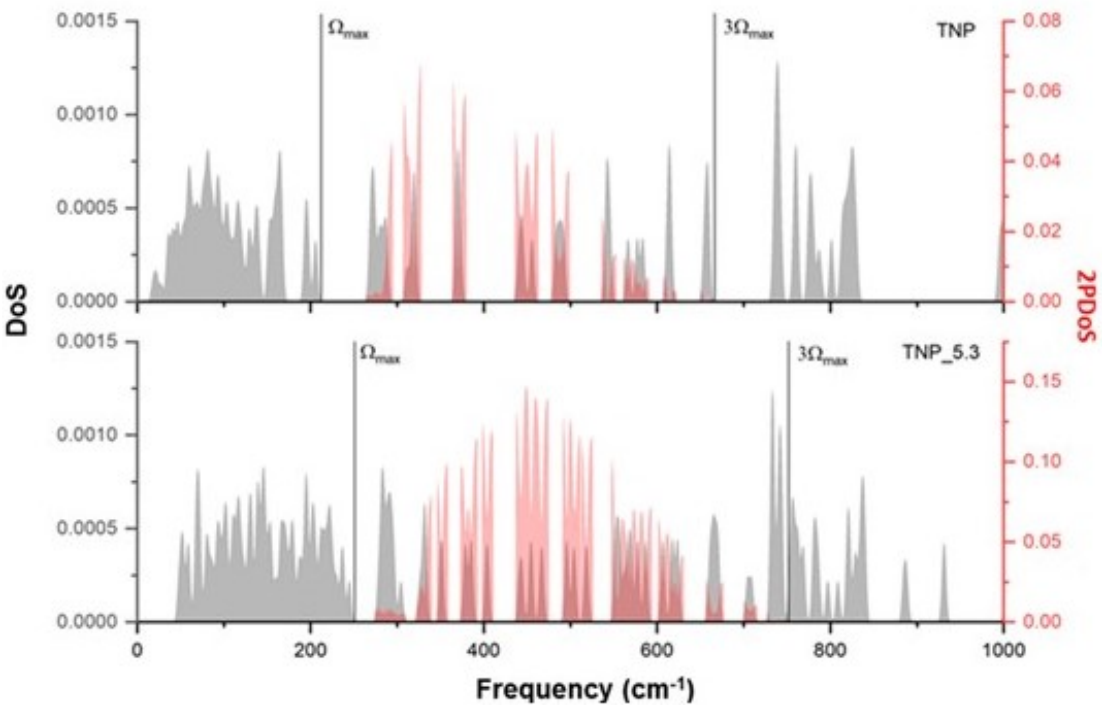

Figure 3.25 Vibrational DoS plots (grey) for Form I and Form IV of 3,4,5-TNP, alongside their corresponding projected 2phonDoS (red)

Two points arise from the data presented in Figure 3.26. Firstly, the predicted impact sensitivity of Form I of 3,4,5-TNP sits more or less on the predicted line (*i.e*. broadly similar to TNT and FOX-7), which further reinforces the success of the vibrational up-pumping model and its application to a broad range of structurally and energetically diverse molecular energetic crystals. Secondly, the model confirms the heightened sensitivity of Form IV of 3,4,5-TNP, with its predicted sensitivity now on a par with CL-20 and HMX. This represents a considerable difference in response, and contrasts with the much smaller predicted variance in impact sensitivity demonstrated for the three different thermally accessible polymorphs of FOX-7. For 3,4,5-TNP, the new polymorph reported in this chapter is only accessible through pressure, and this

results in a more marked change in the DoS, which in turn affects its impact sensitivity response.

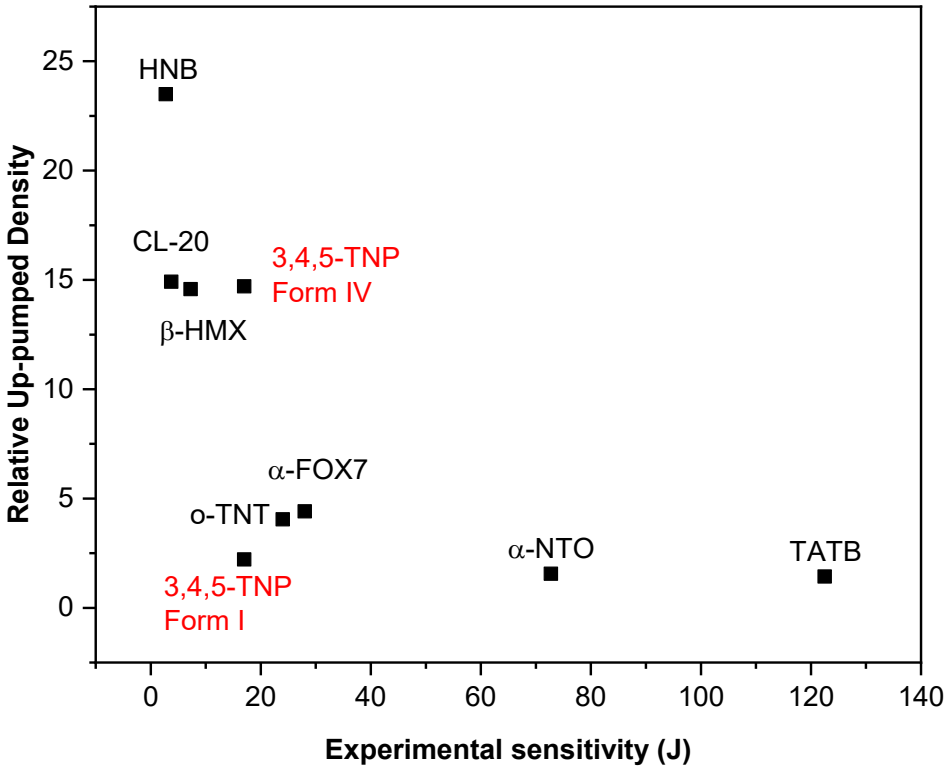

Figure 3.26 Vibrational up-pumped values vs experimental sensitivity for 3,4,5-TNP (ambient - Form I and high pressure – Form IV polymorphs), alongside a range of well-known energetic crystals, taken from ref [26].

As a result of the simulations performed, the gamma-point phonon density of states for the ambient (Form I) and high-pressure (Form IV) polymorphs of 3,4,5-TNP are found to be significantly different from one another. Modes of vibration in the latter have split and shifted to higher wavenumber, resulting in a broader, more continuous phonon bath, which in turn results in an enhanced 2phonDoS response, and heightened projection onto a broadened vibrational up-pumping window. As a result, the impact sensitivity of Form I, which is broadly similar to that of TNT and FOX-7 shifts markedly, to a response more akin to that observed for CL-20 and HMX. This work therefore highlights that pressure-induced polymorphism has a high probability of significantly altering the impact sensitivity of energetic materials.

3.5 Conclusions

This chapter reports the effects of compression on the crystal structure of 3,4,5-TNP, using Raman spectroscopy, neutron powder diffraction (NPD), and single crystal X-ray diffraction techniques. It represents the first example of a high-pressure study of trinitropyrazoles. As a result of the compression of 3,4,5-TNP up to 7.3 GPa, three different high-pressure forms were discovered:

Form I, ambient form of 3,4,5-TNP, is stable up to 0.7 GPa before transforming to Form II, which features abrupt decreases in the N-H···N hydrogen bond lengths. This phase transition is also associated with an abrupt unit-cell volume decrease of 2.4%.

Form II transformed to Form III at ~2.2 GPa. This transition is associated with abrupt changes in all the NO_2 torsional angles of the molecules in the asymmetric unit. Slight discontinuities in unit cell parameters (*a*, *b* and *c* axes lengths) resulting with a subtle change in P-V curve were observed at ~2.2 GPa. Also the downward trend in *β* angle reversed, and started to increase at this pressure.

Form III persisted up to 5.3 GPa, at which point Form IV appeared. The structure of Form IV was solved and refined to give an R-factor of 3.99%. The space group of 3,4,5-TNP has changed from $P2_1/c$ to Cc. Form IV features more extensive H-bonding and possesses additional NH···N bonds. This form appears to be much more sensitive to friction than Form I-III. The possible structural changes that induced third phase transition was explained: abrupt conformational changes in NO_2 torsion angles and non-covalent interaction network movements.

Three different Birch-Murnaghan equations of states (EoSs) for 3,4,5-TNP were determined using NPD data. Thermodynamic parameters for obtained from these EoSs. The average bulk moduli determined for 3,4,5-TNP is similar to other soft energetic materials.

The rationalisation of the increased sensitivity of Form IV compared to Form I using a recently published theoretical model based on vibrational up-pumping has been explored. The theory proposes that mechanical impact induces a compression wave that pass through the crystal, thereby transferring energy into, the lattice acoustic modes of vibration. [27,29,26] Phonon-phonon scattering events then rapidly redistributes this energy across the external acoustic and optical branches, leading to vibrational and thermal excitation across all the lattice modes. This heightened motion induces

changes in the electronic structure which in turn leads to molecular bond breaking and energetic initiation. [29] While the predicted impact sensitivity of Form I sits more or less on the predicted line similar to TNT and FOX-7, the predicted sensitivity of Form IV is closer to the sensitivities of CL-20 and HMX.

3.6 Suggestions for Future Studies

3,4,5-TNP has not yet been studied under combined high-temperature and high-pressure conditions. Hence there is scope for conducting high-pressure crystallographic studies at elevated temperatures in order to explore the P-T phase diagram and map more fully the polymorphism of 3,4,5-TNP. The sensitivities to impact and friction of 3,4,5-TNP should be also investigated at elevated temperatures to explore whether high temperature increases sensitivity to initiation.

So far, structural characterisation of 3,4,5-TNP has only been studied up to 7.3 GPa (in this thesis). It would therefore be of interest to explore the effects of higher pressures on the structure of 3,4,5-TNP.

Exploration of the recovery of Form IV to ambient pressure could be investigated. If it is achieved, dynamic shock experiments can be performed to explore the changes in sensitivity to initiation of Form IV. Moreover, all other energetic and thermal properties of Form IV can be investigated in order to evaluate its practical use as a novel energetic material.

None of the other polymorphs of 3,4,5-TNP is known under ambient conditions. Therefore, an intensive polymorph investigation could be performed to discover novel forms of 3,4,5-TNP.

3.7 References

1 C. R. P. and A. S. C. David I. A. Millar, Helen E. Maynard-Casely, Annette K. Kleppe, William G. Marshall and Received, *CrystEngComm*, 2010, **12**, 2524–2527.

2 K. Wang, J. Liu, K. Yang, B. Liu and B. Zou, *J. Phys. Chem. C*, 2014, **118**, 8122–8127.

3 I. L. Dalinger, G. P. Popova, I. A. Vatsadze, T. K. Shkineva and S. A. Shevelev, *Russ. Chem. Bull.*, 2009, **58**, 2185.

4 G. Hervé, C. Roussel and H. Graindorge, *Angew. Chemie - Int. Ed.*, 2010, **49**, 3177–3181.

5 Y. V. Nelyubina, I. L. Dalinger and K. A. Lyssenko, *Angew. Chemie - Int. Ed.*, 2011, **50**, 2892–2894.

6 United States Patent Office, US 2009/0186931 A1, *United States Pat. Appl. Publ.*, 2009, 56, 1–12.

7 European Patent Office, EP 2155688B1, *Eur. Pat. Specif.*, 2008, 38, 1–19.

8 J. Akhavan, in *RSC publishing*, ed. J. Akhavan, Royal Society of Chemistry, Cambridge, 3rd edn., 2004, pp. 1–181.

9 H. Gao and J. M. Shreeve, *Chem. Rev.*, 2011, **111**, 7377–7436.

10 J. A. Xu, H. K. Mao and P. M. Bell, *Science (80-.).*, 1986, **232**, 1404–1406.

11 C. L. Bull, N. P. Funnell, M. G. Tucker, S. Hull, D. J. Francis and W. G. Marshall, *High Press. Res.*, 2016, **36**, 493–511.

12 J. Hama and K. Suito, *Phys. Lett. A*, 1994, **187**, 346–350.

13 O. Arnold, J. C. Bilheux, J. M. Borreguero, A. Buts, S. I. Campbell, L. Chapon, M. Doucet, N. Draper, R. Ferraz Leal, M. A. Gigg, V. E. Lynch, A. Markvardsen, D. J. Mikkelson, R. L. Mikkelson, R. Miller, K. Palmen, P. Parker, G. Passos, T. G. Perring, P. F. Peterson, S. Ren, M. A. Reuter, A. T. Savici, J. W. Taylor, R. J. Taylor, R. Tolchenov, W. Zhou and J. Zikovsky, *Nucl. Instruments Methods Phys. Res. Sect. A Accel. Spectrometers, Detect. Assoc. Equip.*, 2014, **764**, 156–166.

14 B. H. Toby, *J. Appl. Crystallogr.*, 2001, **34**, 210–213.

15 M. J. Cliffe and A. L. Goodwin, *J. Appl. Crystallogr.*, 2012, **45**, 1321–1329.

16 R. I. Belousov and S. K. Filatov, *Glas. Phys. Chem.*, 2007, **33**, 271–275.

17 K. Durka, A. A. Hoser, R. Kamiński, S. Luliński, J. Serwatowski, W. Koźmiński and K. Woźniak, *Cryst. Growth Des.*, 2011, **11**, 1835–1845.

18 T. I. Krasnenko, L. V. Zolotukhina and L. V. Andrianova, *Inorg. Mater.*, 2000, **36**, 1032–1035.

19 A. D. Vershinin, E. N. Selivanov, R. I. Gulyaeva and N. I. Sel'menskikh, *Inorg. Mater.*, 2005, **41**, 882–887.

20 M. Schwartz, in *Statistical Mechanics*, 2019, pp. 1–17.

21 J. C. Gump, *J. Phys. Conf. Ser.*, 2014, **500**, 1–8.

22 S. Hunter, P. L. Coster, A. J. Davidson, D. I. A. Millar, S. F. Parker, W. G. Marshall, R. I. Smith, C. A. Morrison and C. R. Pulham, *J. Phys. Chem.*, **119**, 2322–2334.

23 D. I. A. Millar, *Energetic Materials at Extreme Conditions*, Springer Theses, Edinburgh, 2011.

24 D. I. A. Millar, W. G. Marshall, I. D. H. Oswald and C. R. Pulham, *Crystallogr. Rev.*, 2010, **16**, 115–132.

25 A. A. L. Michalchuk, P. T. Fincham, P. Portius, C. R. Pulham and C. A. Morrison, *J. Phys. Chem. C*, 2018, **122**, 19395–19408.

26 A. A. L. Michalchuk, M. Trestman, S. Rudić, P. Portius, P. T. Fincham, C. R. Pulham and C. A. Morrison, *J. Mater. Chem. A*, 2019, **7**, 19539–19553.

27 A. A. L. Michalchuk, J. Hemingway and C. A. Morrison, *J. Chem. Phys.*, 2021, **154**, 064105.

28 Steven Hunter, The University of Edinburgh, 2013.

29 A. A. L. Michalchuk, S. Rudić, C. R. Pulham and C. A. Morrison, *Phys. Chem. Chem. Phys.*, 2018, **20**, 29061–29069.

Chapter 4 Structure-Property Studies of Salts Formed between Dinitropyrazoles and Selected Pyridine Derivatives

4.1 Introduction

Nitropyrazole-based energetic materials have been the subject of many salt/co-crystal formation studies, especially in last few decades. The Cambridge Structural Database contains 34 entries for multicomponent DNP-based structures, including salts, co-crystals, hydrates and solvates formed with 1,3-DNP, 3,4-DNP, 3,5-DNP and other substituted DNPs. [1–7] In a study performed by Bolter *et al*., salts of isomers of dinitropyrazoles (3,4-, 1,3- and 3,5-DNP) with potassium, sodium and a group of nitrogen-rich compounds were prepared and investigated.[3] They exhibited high densities (1.59 and 1.99 g cm^{-3}), high detonation velocities (from 6245 to 8610 m s^{-1}) and low impact sensitivities (mostly higher than 40 J). Hence, they can potentially be used as efficient energetic materials for a variety of applications. Different substituents of dinitropyrazoles were also used as co-formers for exploring nitrogen-rich energetic salts due to their favourable energetic properties. For example, 14 energetic salts based on 4-nitramino-3,5-dinitropyrazole were prepared and investigated by Zhang *et al*.[1]. While all the salts exhibited better energetic performance than TNT, together with reasonable impact sensitivities (5 - 40 J), two of them were found to have detonation performances on a par with RDX. In another study, a group of metal salt of 3,5-DNP was prepared. These salts were investigated for applications as pyrotechnics and were found to be thermally stable and insensitive to friction and impact. [6]

Based on these reported structures, it was decided to investigate salts/co-crystals of 1,3-DNP and 3,5-DNP. From the reported studies, it is observed that the acidic H-atom of the pyrazole ring is usually transferred to the co-former. This proton transfer was found to be useful in order to increase the chemical stability of DNPs by eliminating the acidic proton of the pyrazole ring which potentially causes problems in the practical use of DNPs due to its high acidity and tendency to form metal salts.

On the other hand, the key properties affecting co-crystallisation/salt formation such as electron density distribution, ΔpK_a values and π-π stacking, H/halogen bond donor-acceptor characteristics were also considered in order to find successful pairs that can form salts/co-crystals. As a result of this investigation, pyridine, substituted

pyridines and morpholine were found to be suitable co-formers. Moreover, the lone pair of electrons on the N atom of the pyridine ring acted as an effective H-bond acceptor.

In this chapter, the characterisation and property testing (including thermal and energetic properties) of 3,5-DNP salts are reported. Their crystal structures, crystal packing motif and intermolecular interactions are explained in detail. The structure-property relationships of these new explored salts are discussed and rationalised.

4.2 Experimental

4.2.1 Materials

The energetic compound 3,5-DNP was synthesised via the route described in Chapter 2. The following compounds were purchased from commercial sources (Sigma-Aldrich): pyridine (≥99%) (Pyr), 4-aminopyridine (≥99%) (AmPyr), 2-amino-6-picoline (98%) (AmPic), 4-dimethylaminopyridine (≥99.0%) (DMAP) and morpholine (ACS reagent, ≥99.0%) (Morph).

4.2.2 Salt Formation

All the salts were produced using the slow evaporation technique. A solution of the energetic and non-energetic co-formers (1:1 molar ratio) was prepared with a suitable solvent at room temperature in a 2 mL glass vial covered with Parafilm, which was pierced several times to enable gradual evaporation of solvent. 10 mg energetic compound and the molar equivalent amount of non-energetic compound were used to prepare each solution. This process was repeated for every pair of energetic – non-energetic compound. Ethanol was used as a solvent for the salt formation of 3,5-DNP with AmPic, while methanol was used for the other pairs. Crystals that were suitable for single crystal X-ray diffraction were collected after they formed in solution.

In addition to single crystals for structural characterisation, bulk powder samples of the salts (~1 g) were produced using evaporative techniques at larger scales. Heat was applied (up to 50°C) while preparing 3,5-DNP.AmPyr salt since AmPyr was relatively insoluble in methanol at room temperature. A sample of each multicomponent compound with a minimum mass of 1 g was prepared for further

property testing, including impact sensitivity (IS) and thermal studies. Phase purities of the bulk samples were assessed by using powder X-ray diffraction (PXRD). If impurities were detected, the samples were purified by recrystallisation from a suitable solvent.

4.2.3 Single Crystal X-ray Diffraction

All the SXRD data were collected at 120 K, using an Agilent Technologies SuperNova diffractometer equipped with an Oxford Cryosystems N_2 low temperature Cryostream. The total number of runs and images was based on the strategy calculation from the program CrysAlisPro (Rigaku, V1.171.38.46, 2015). The diffraction patterns were indexed and the unit cells were refined using CrysAlisPro (Rigaku, V1.171.38.46, 2015). The diffraction patterns were indexed and the unit cells were refined using CrysAlisPro (Rigaku, V1.171.38.46, 2015). The diffraction patterns were indexed and the unit cells were refined using CrysAlisPro (Rigaku, V1.171.38.46, 2015).

Within the OLEX2 program suite, all the structures except for 3,5-DNP.Pyr were solved with SHELXS using direct methods. [8] 3,5-DNP.Pyr structure was solved with SHELXT using the intrinsic phasing solution method. All the structural models were refined with SHELXL using the least squares minimisation methods. Hydrogen atom positions were identified from a difference Fourier map and freely refined using the riding model.

4.2.4 Powder X-ray Diffraction

Powder X-ray diffraction patterns were recorded under ambient-temperature and ambient-pressure conditions using a Bruker D2 PHASER instrument. Experimental details are provided in Chapter 2 (Section 2.6). This technique was used to characterise bulk samples prior to impact-sensitivity testing and DSC.

4.2.5 Differential Scanning Calorimetry

DSC experiments were conducted on a NETZSCH STA 449 F1 Differential Scanning Calorimeter. Experimental details are given in Chapter 2 (Section 2.12).

4.2.6 BAM Fall Hammer Tests

BAM Fall Hammer impact testing (BFH-12) experiments were performed, at the Cavendish Laboratory (Cambridge). Experimental details and more information about this technique is given in Chapter 2 (Section 2.11).

4.2.7 Calculated Detonation Performance and Heat of Formation Calculations

All calculations of detonation parameters were performed using the program EXPLO-5 V6.03. [9] More details are given in Chapter 2 (Section 2.13). All the heat of formation calculation studies were performed by Imogen Christopher (PhD student from Morrison group). Details of the computational technique are given in Chapter 2 (Section 2.14).

4.3 Results and Discussion

4.3.1 Characterisation of Synthetic Energetic Materials (3,5-DNP)

3,5-DNP was synthesised from the thermal rearrangement of 1,3-DNP. The ^{1}HNMR spectrum of the sample is shown in Figure 4.1. As expected, one peak was observed in the spectrum at δ = 8.01 (500 MHz, DMSO) corresponding to the C-H bond attached to the pyrazole ring, in good agreement with the literature for 3,5-DNP. The broad peak in the middle of the spectrum around δ = 5 corresponds to the NH group of the pyrazole ring. The peak at δ = 2.54 corresponds to the residual protons of the solvent used (DMSO). The ^{1}HNMR spectrum therefore confirms that 3,5-DNP had been successfully prepared.

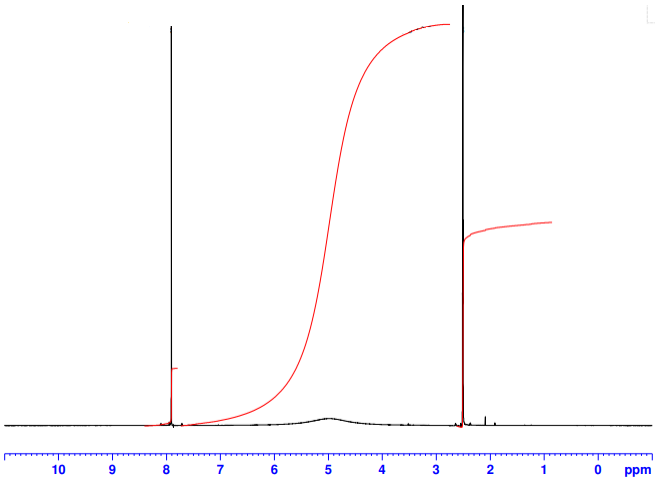

Figure 4.1 ^{1}H-NMR spectrum of 3,5-DNP

Comparison of the experimental powder pattern and the powder pattern simulated from the structure deposited in the CSD (ref. code: RIKNOO) is shown in Figure 4.2 below. It shows that the 3,5-DNP sample was phase-pure and so could be used for co-crystallisation and salt formation studies.

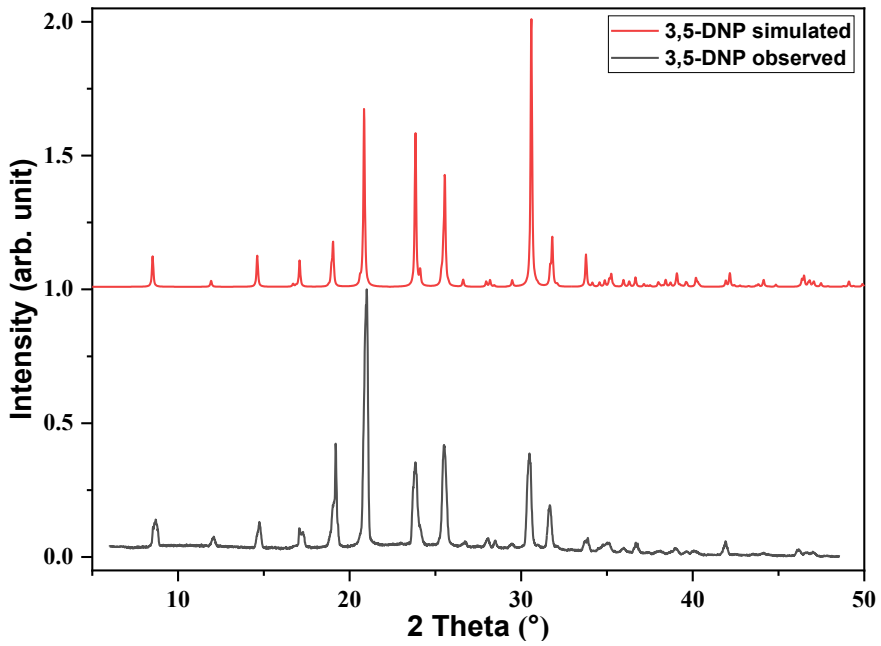

Figure 4.2 Powder X-ray diffraction patterns of 3,5-DNP (red line represent the data from CSD, black line is experimental data observed from D2 phaser.)

4.3.2 Salts Formed with 3,5-DNP and Pyridine Derivatives

A broad range of chemical compound were used to find suitable co-formers for 3,5-DNP. As a result, 5 novel salts of 3,5-DNP were prepared successfully. In this section, characterisation of the salts formed between 3,5-DNP and substituted pyridines is reported. The non-energetic co-formers used are Pyr, AmPyr, AmPic, DMAP and Morph (see Figure 4.3). 3,5-DNP formed salts with this group of non-energetic co-formers. The pK_a value differences (ΔpK_a, Table 4.1) between 3,5-DNP and its co-formers were high enough to cause a proton transfer from 3,5-DNP to substituted-pyridines. These observations are consistend with the ΔpK_a rule, described in Chapter 1.

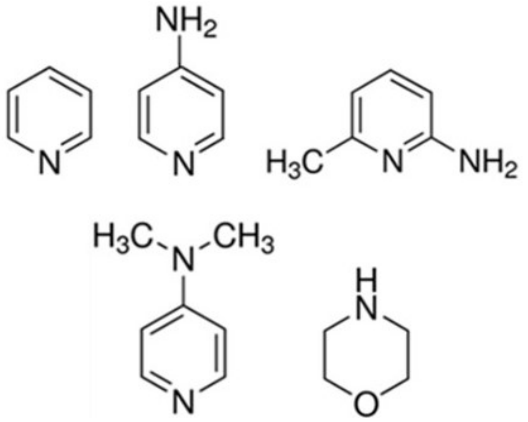

Figure 4.3 Molecular structures of non-energetic co-formers in 3,5-DNP salts (Pyr, AmPyr, AmPic, DMAP and Morph, respectively).

Table 4.1 ΔpK_a values of 3,5-DNP salts

Salt	ΔpK_a	Expected compound (ΔpK_a rule)
3,5-DNP.Pyr	2.09	Salt or co-crystal
3,5-DNP.AmPyr	6.03	Salt
3,5-DNP.AmPic	4.27	Salt
3,5-DNP.DMAP	6.56	Salt
3,5-DNP.Morph	5.35	Salt

Electron density distribution maps of the co-crystals were calculated using TmoleX 4.3.2 software and are shown in Figure 4.4. The maps indicate electron-rich and electron-poor areas of the molecules which are possible synthons for supramolecular motifs. One of the significant factors driving the formation of multicomponent solids, such as salts and co-crystals, is the charge distributions of the constituent molecules. [10] Thus, electron density maps can be exploited to find suitable pairs for co-crystal or salt formation. 4.5 shows the asymmetric units of the salts of 3,5-DNP. Crystallographic data for the structures of 3,5-DNP salts are given in Table 4.2.

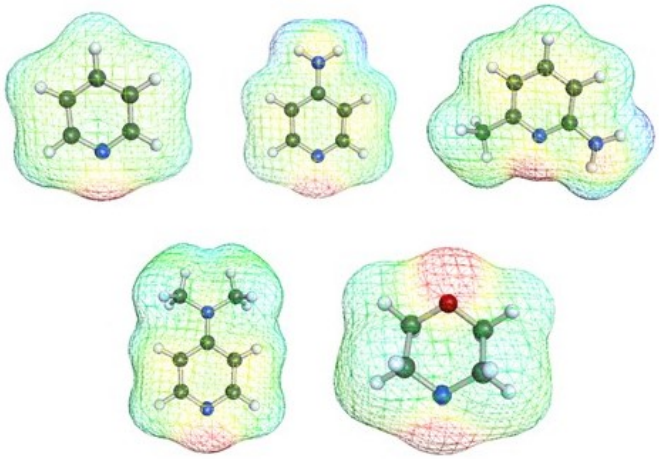

Figure 4.4 Electron density distribution maps of Pyr, AmPyr, AmPic, DMAP and Morph.

Table 4.2 Crystallographic information for 3,5-DNP salts

Compound	**3,5-DNP. Pyr**	**3,5-DNP. AmPyr**	**3,5-DNP. AmPic**	**3,5-DNP. DMAP**	**3,5-DNP. Morph**
Formula	$C_8H_7N_5O_4$	$C_8H_8N_6O_4$	$C_9H_{10}N_6O_4$	$C_{10}H_{12}N_6O_4$	$C_7H_{11}N_5O_5$
M_r (g.mol^{-1})	237.19	252.20	266.23	280.26	245.21
Crystal system	Triclinic	Monoclinic	Monoclinic	Monoclinic	Monoclinic
Space group	*P-1*	*C2/c*	*P2$_1$/c*	*P2$_1$/n*	*P2$_1$/c*
a, b, c (Å)	5.2328(3) 7.4953(3) 12.9286(5)	18.3532(9) 9.7049(5) 12.1944(6)	6.2819(3) 11.5973(5) 16.0396(7)	7.1488(3) 8.1501(3) 21.417(1)	8.9608(3) 9.8046(3) 11.7694(4)
α, β, γ (o)	82.975(3) 79.451(4) 85.531(4)	90 103.406(5) 90	90 99.056(5) 90	90 93.186(4) 90	90 91.671(4) 90
V (Å^3)	493.96(4)	2112.8(2)	1153.97(9)	1245.89(9)	1033.58(7)
Z, Z'	2, 1	4, 1	4, 1	4, 1	4, 1
ρ (g.cm^{-3})	1.595	1.586	1.532	1.494	1.576
Packing coefficient	0.730694	0.725821	0.715398	0.72374	0.731435
R factor	0.0587	0.0549	0.0899	0.0684	0.0526
θ_{min}- θ_{max}	2.332-29.706	3.093-29.687	3.115-29.758	3.093-29.687	3.080-29.609
Radiation	MoKα	MoKα	MoKα	MoKα	MoKα
Wavelength (Å)	0.71073	0.71073	0.71073	0.71073	0.71073

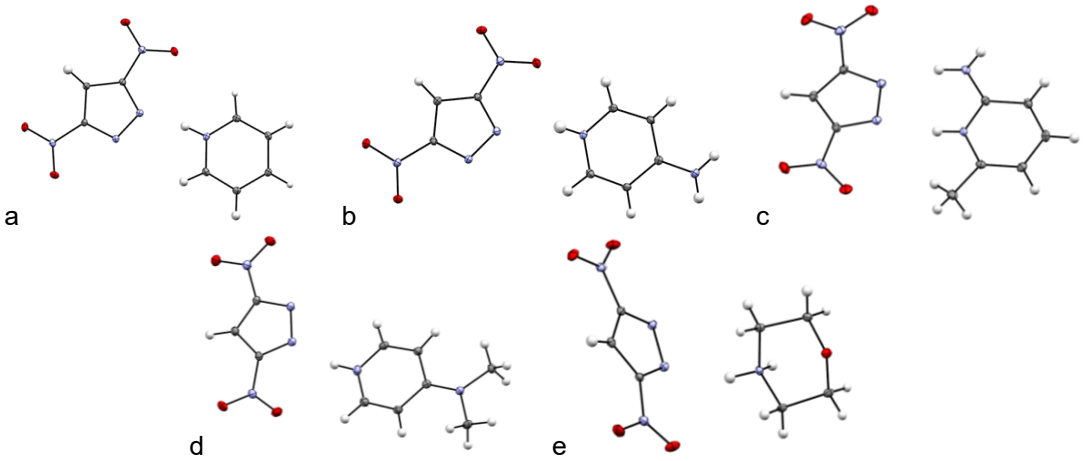

Figure 4.5 Asymmetric units of (a) 3,5-DNP.Pyr, (b) 3,5-DNP.AmPyr, (c) 3,5-DNP.AmPic, (d) 3,5-DNP.DMAP and (e) 3,5-DNP.Morph.

4.3.2.1 Structural Features of 3,5-DNP Salts

In this section, non-covalent interactions including hydrogen bonding, halogen bonding and π-π interactions of 3,5-DNP salts are investigated and compared with the parent energetic compounds. The packing motifs of the novel structures are described in detail. Thus, the effect of co-crystallisation on their crystal structures and

network of non-covalent interaction will be described and discussed. The unit cell and main H-bonding in 3,5-DNP are shown in Figure 4.6. Detailed information about non-covalent bonds in 3,5-DNP and its co-crystals is given in Table 4.3. As can be seen in Figure 4.6, four hydrogen bonds are observed in 3,5-DNP. 3,5-DNP adopts a herring bone style crystal packing motif with extensive H-bonding (Figure 4.7).

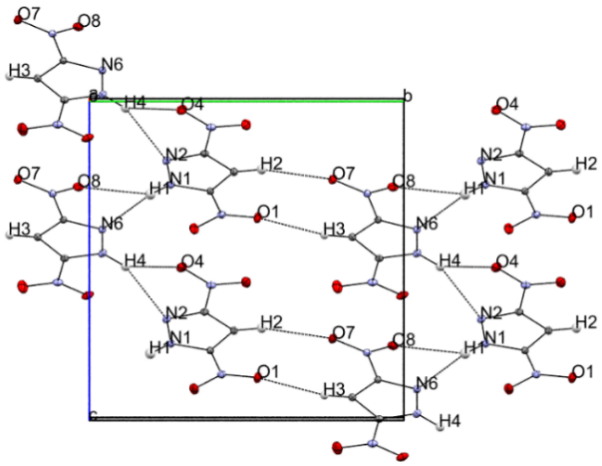

Figure 4.6 H-bonding and C-H···O interactions of 3,5-DNP viewed along *a*-axis within the unit cell (CCDC)

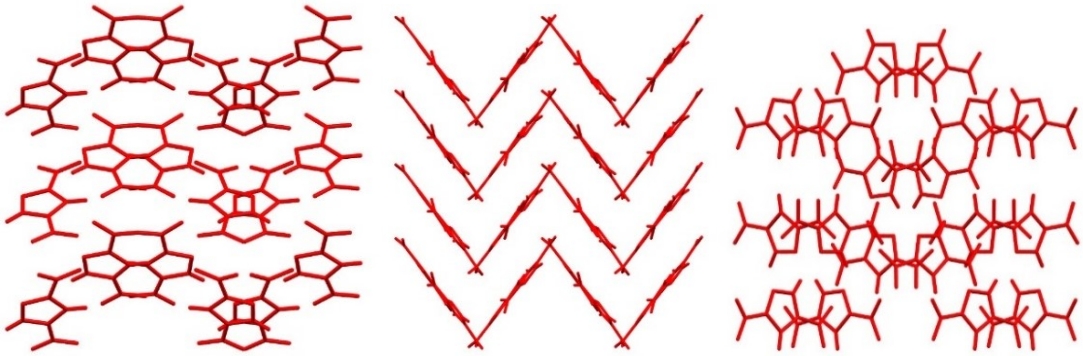

(a) (b) (c)

Figure 4.7 Structural packing arrangement of 3,5-DNP viewed along *a*-axis (a), *b*-axis (b), and *c*-axis (c)

The 3,5-DNP.Pyr salt was formed upon the transfer of the acidic H atom from 3,5-DNP to Pyr to form a hydrogen bond N5-H5···N2 (Figure 4.8). Other hydrogen bonds were observed in N5-H5···N1 and N5-H5···O1 (more details in Table 4.3). The extent of the H-bonding network in 3,5-DNP decreased upon salt formation with Pyr.

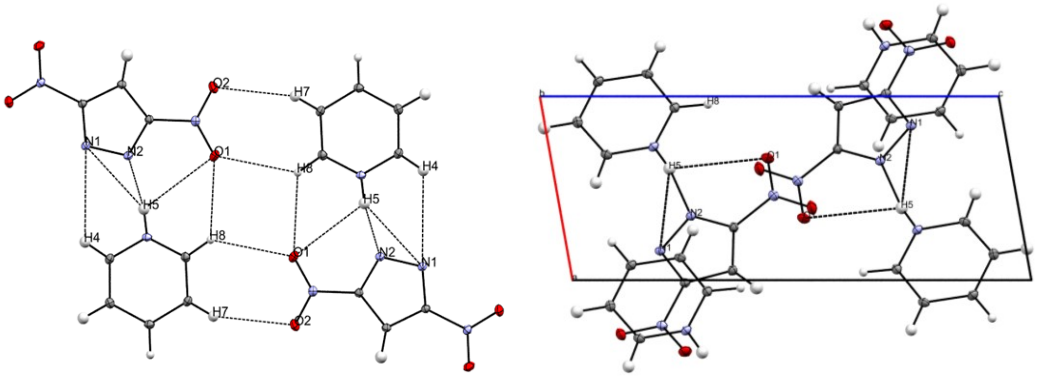

(a) (b)

Figure 4.8 The structure of 3,5-DNP.Pyr, H-bonding interactions along with C-H···O interactions (a) and unit-cell with H-bonding (b)

Crystallisation of 3,5-DNP with Pyr yields a crystal motif consisting of layered arrays (Figure 4.9(c)). The layers formed in 3,5-DNP.Pyr are flatter than in 3,5-DNP, giving rise to 2-D slip planes are formed within 3,5-DNP.Pyr. [11]

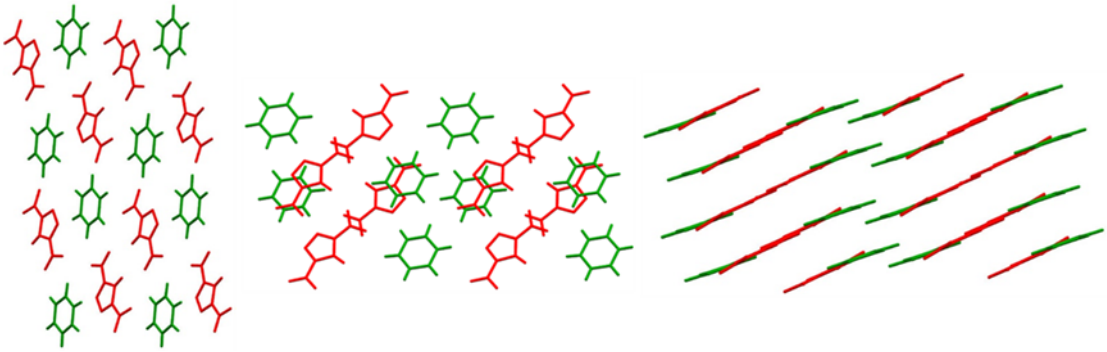

(a) (b) (c)

Figure 4.9 Structural packing arrangement of 3,5-DNP.Pyr viewed along *a*-axis (a), *b*-axis (b) and *c*-axis (c) Red molecules represent 3,5-DNP and green molecules represent to Pyr molecules).

Similar to 3,5-DNP.Pyr, a hydrogen bond is formed involving N5-H5···N1 to give a salt of 3,5-DNP.AmPyr (Figure 4.10). In addition, the amino group on AmPyr formed a H-bond with the oxygen atom on the nitro groups of 3,5-DNP. CH···O type interactions are also appeared in the salt, which were not present for 3,5-DNP. More details of these interactions are given in Table 4.3.

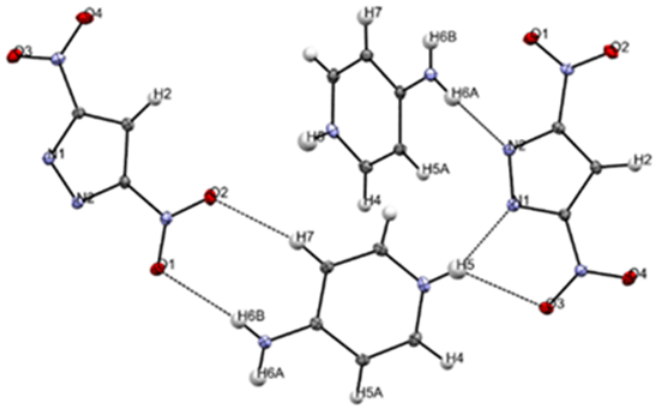

Figure 4.10 The structure of 3,5-DNP.AmPyr and H-bonding interactions along with CH···O interactions

Figure 4.11 illustrates the cage-like packing motif of 3,5-DNP.AmPyr which has larger angle (the angle between the green and red layers, Figure 4.11(a) = 157°) compared to 3,5-DNP (72.5°). 3,5-DNP molecules lie parallel to one another in the salt in an off-set position and the crystal packing is dominated by close N–H···O and N–H···N H-bonds.

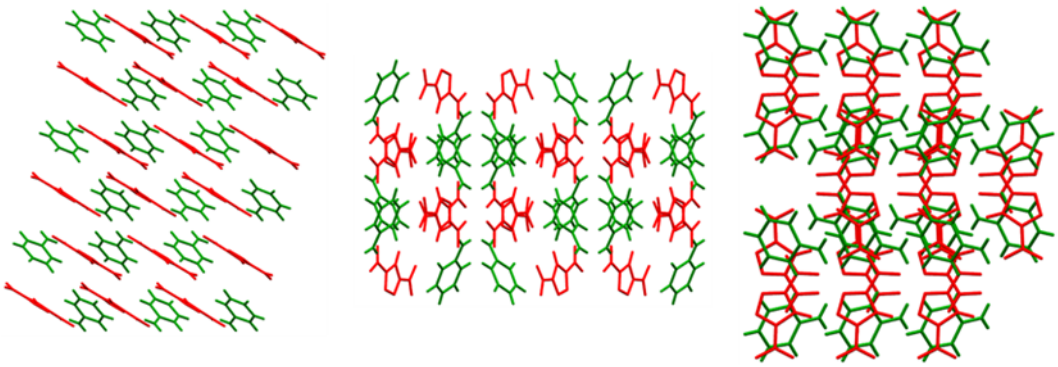

(a) (b) (c)

Figure 4.11 Structural packing arrangement of 3,5-DNP.AmPyr viewed along *a*-axis (a), *b*-axis (b) and *c*-axis (c) (Red molecules represent 3,5-DNP and green ones AmPyr).

Crystallisation of 3,5-DNP and AmPic resulted in salt formation (3,5-DNP.AmPic), which is shown in Figure 4.12. A H-bond is formed upon a proton transfer from 3,5-DNP to AmPic. The amino group on AmPic acted as an efficient H-bond donor for the nitro groups on pyrazole and contributed to the H-bonding in this salt. Two different

types of H-bonds are formed: one with the nitro group (NH···O) and one with the amine group (NH···N) on 3,5-DNP. More details of these interactions are given in Table 4.3.

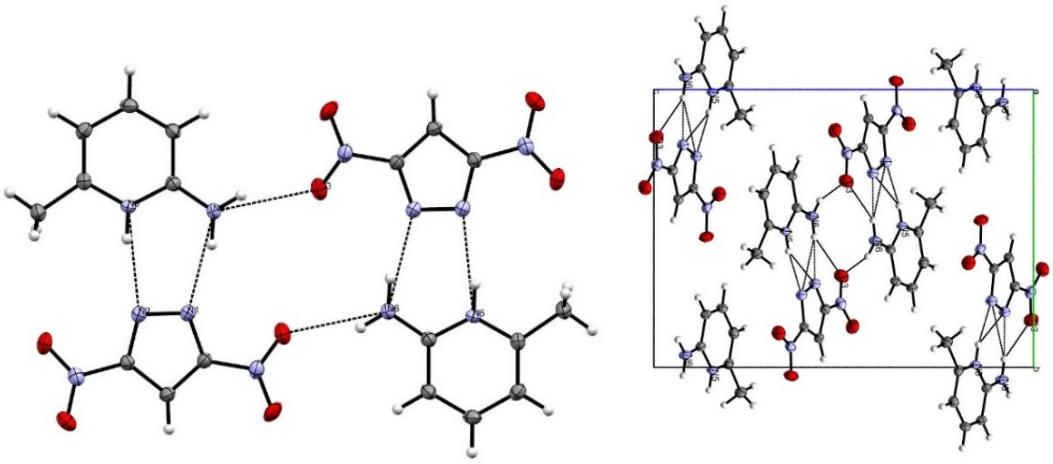

(a) (b)

Figure 4.12 The structure of 3,5-DNP.AmPic and H-bonding interactions (Figure (a) shows repeating interactions in the structure and (b) shows the H-bonding within the unit cell.)

Salt formation between 3,5-DNP and AmPic changed the crystal packing motif from herring-bone (3,5-DNP) to a parallel-layered structure, see Figure 4.13. Although the molecules appear to be aligned, there are some offsets between their centroids which preclude formation of π-π stacking interactions.

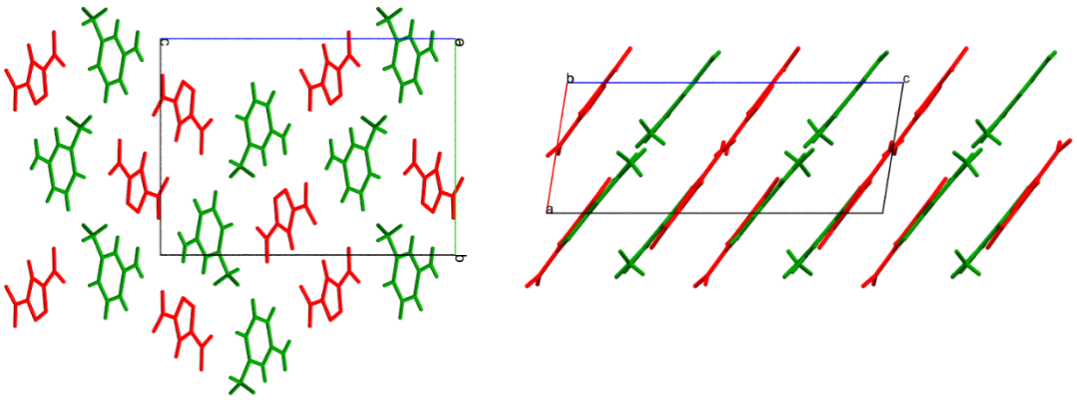

(a) (b)

Figure 4.13 Structural packing arrangement of 3,5-DNP.AmPic viewed along *a*-axis (a) and *b*-axis (b).

Figure 4.14 illustrates the unit cell of the 3,5-DNP.DMAP salt and the associated H-bonding in the structure. Three different H-bonds were observed in this salt. Similar to the other salts a proton transfer from 3,5-DNP to DMAP was observed and a H-bond was formed.

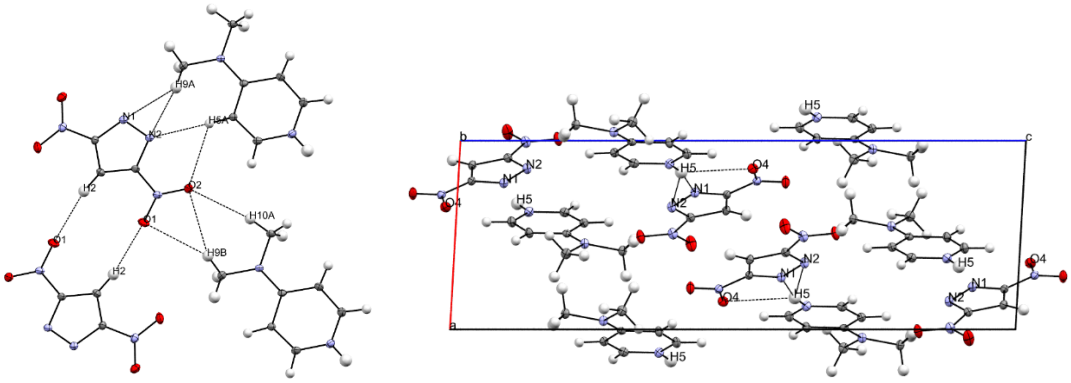

(a) (b)

Figure 4.14 The structure of 3,5-DNP.DMAP with intermolecular interactions (a) and H-bonding interactions within the unit-cell (b)

The 3,5-DNP.DMAP salt adopts a “wine-rack” type of crystal packing motif shown in Figure 4.15. The angle between the layers in the salt (39.5°, see Figure 4.15 (c)) is smaller than the parent energetic compound. The angle between layers is 72.5° in 3,5-DNP.

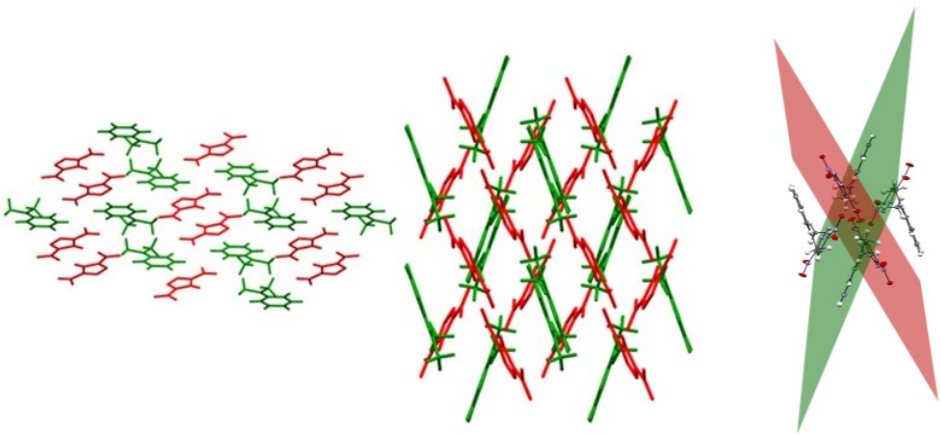

(a) (b) (c)

Figure 4.15 Structural packing arrangement of 3,5-DNP.DMAP viewed along *a*-axis (a), *b*-axis (b) and *c*-axis (c).

The last salt in this chapter was formed between 3,5-DNP and Morph (3,5-DNP.Morph) and shown in Figure 4.16. The salt exhibited an extensive H-bonding network including N-H···N and N-H···O types of H-bonds. The details of these interactions are given in Table 4.3.

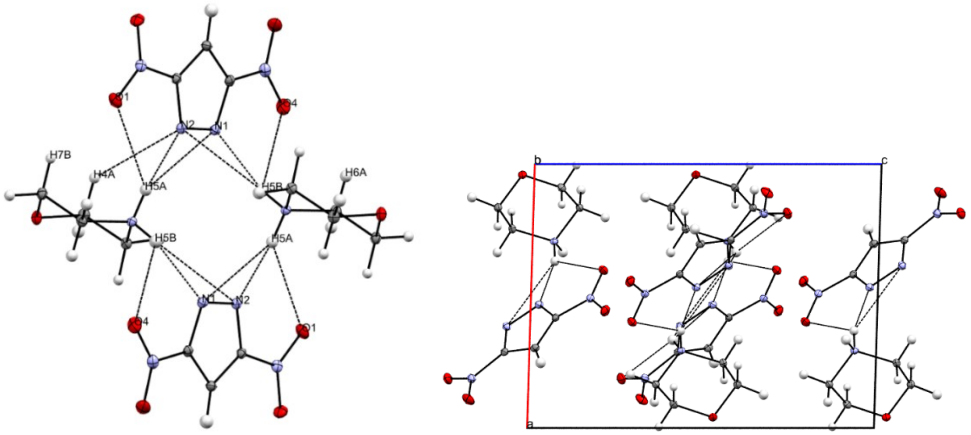

(a) (b)

Figure 4.16 The structure of 3,5-DNP.Morph with repeating H-bond (a) and H-bonding within the unit-cell (b)

The crystal packing of 3,5-DNP.Morph features blocks consisting of pairs of both co-formers (Figure 4.17). The herring-bone type of crystal packing of 3,5-DNP is altered and instead a cage-like structure is observed.

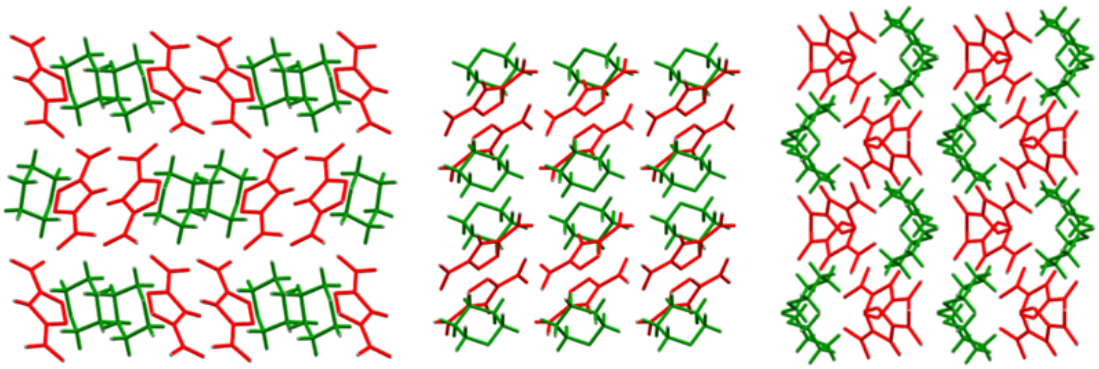

(a) (b) (c)

Figure 4.17 Structural packing arrangement in 3,5-DNP.Morph viewed along *a*-axis (a), *b*-axis (b) and *c*-axis (c)

Table 4.3 Hydrogen bond details of 3,5-DNP and its salts

Salt	D-H···A	D-H [Å]	H···A[Å]	D···A [Å]	D-H···A [°]
3,5-DNP	N1-H1···N6	0.85(3)	2.26(3)	3.103(3)	170(3)
	N1-H1···O8	0.85(3)	2.58(3)	3.112(3)	122(3)
	N5-H4···N2	0.92(3)	2.21(3)	3.029(3)	148(2)
	N5-H4···O4	0.92(3)	2.60(3)	3.400(3)	146(2)
3,5-DNP.Pyr	N5-H5···N2	0.91(2)	1.80(2)	2.698(2)	170(2)
	N5-H5···N1	0.91(2)	2.68(2)	3.461(2)	144(2)
	N5-H5···O1	0.91(2)	2.88(2)	3.466(1)	126(2)
	C7-H7···O2	0.91(2)	2.55(2)	3.391(2)	152(2)
	C2-H2···O2	0.95(2)	2.62(2)	3.516(2)	157(2)
	C8-H8···O1	0.95(2)	2.64(2)	3.383(2)	136(2)
3,5-DNP.AmPyr	N5-H5···O3	0.89(2)	2.43(2)	3.071(2)	129(2)
	N5-H5···N1	0.89(2)	2.04(2)	2.878(2)	155(2)
	N6-H6A···N2	0.89(2)	2.16(2)	3.046(2)	178(2)
	N6-H6B···O1	0.82(2)	2.38(2)	3.184(2)	169(2)
	C7-H7···O2	0.95(2)	2.37(2)	3.286(2)	161(2)
3,5-DNP.AmPic	N5-H2···N2	0.87(2)	2.06(2)	2.916(3)	168(2)
	N6-H6A···N1	0.89(3)	1.96(3)	2.833(3)	165(3)
	N6-H6B···O3[1]	0.85(3)	2.10(3)	2.894(3)	154(3)
3,5-DNP.DMAP	N5-H5···N1	0.91(2)	1.90(3)	2.797(2)	166(2)
	N5-H5···N2	0.91(2)	2.86(2)	3.635(2)	143(2)
	N5-H5···O4	0.91(2)	2.75(2)	3.362(2)	126(2)
	C7-H7…O4	0.94(2)	2.61(2)	3.531(2)	164(20
	C5-H5A…N2	0.95(2)	2.45(2)	3.381(2)	169(2)
	C5-H5A…O2	0.95(2)	2.65(2)	3.244(2)	121(2)
3,5-DNP.Morph	N5-H5B···N1	0.92(2)	2.00(2)	2.840(2)	152(2)
	N5-H5B···O2	0.92(2)	2.51(2)	2.944(2)	109(1)
	N5-H5A···N1	0.91(2)	2.93(2)	3.671(2)	141(1)
	N5-H5A···N2	0.91(2)	1.97(2)	3.479(2)	162(2)
	N5-H5A···O1	0.91(2)	2.75(2)	2.75(2)	162(2)
	N5-H5B···N2	0.92(2)	2.80(2)	3.479(2)	132(1)
	C7-H7B···O3	0.95(2)	2.86(2)	3.541(2)	130(1)

A list of hydrogen bonds of all the salts and 3,5-DNP with geometrical details is given in Table 4.3. In summary, for all the salts of 3,5-DNP, the acidic hydrogen atom of the pyrazole ring acts as an efficient hydrogen bond donor to the N-atom of the substituted pyridine molecules. Other notable H-bond interactions (N-H···O) were observed between amine groups on pyridine rings and adjacent nitro groups of pyrazole molecules. Moreover, amino-nitro interactions appeared as efficient tools to increase the extent of H-bonding networks in nitropyrazole-based energetic salts. The strongest H-bond in each salt involves the interaction between protonated pyridine and deprotonated 3,5-DNP (N-H···N). The shortest (1.80 Å) and therefore strongest H-bond among all the 3,5-DNP salts was observed in 3,5-DNP.Pyr salt (N5-H5···N2).

This salt has the highest packing coefficient and crystal density among the salts (Table 4.2). CH···O interactions also formed in the salts along with these H-bonds. Some CH···O interactions with their almost linear geometries were found to be shorter than some of the H-bonds involving N atoms.

4.3.2.2 Powder X-ray Diffraction Studies

Larger amounts of 3,5-DNP salts were produced for further tests including thermal stability and impact sensitivity tests. Any phase impurities in these salts were checked using powder X-ray diffraction. Comparisons of powder diffraction patterns simulated using SXRD data and experimental powder diffraction data of the structures are given in Figure 4.18, 4.19 and 4.20. As seen from the figures, these powder patterns were generally consistent confirming that the samples could be used for further studies. In some plots, a shift in peak positions and/or intensity differences were observed between observed and simulated powder patterns. The peak shift was observed due to measurement temperature differences. While SXRD data was collected at 120 K, powder patterns were collected at room temperature (298 K). This temperature difference caused an expansion of the unit cell of the structures recorded at 298 K that caused a shift between patterns. The intensity differences between patterns occurs due to preferred orientation exacerbated by the use of flat plate geometry. Importantly, no additional or unassigned peaks were observed in any of the experimental patterns.

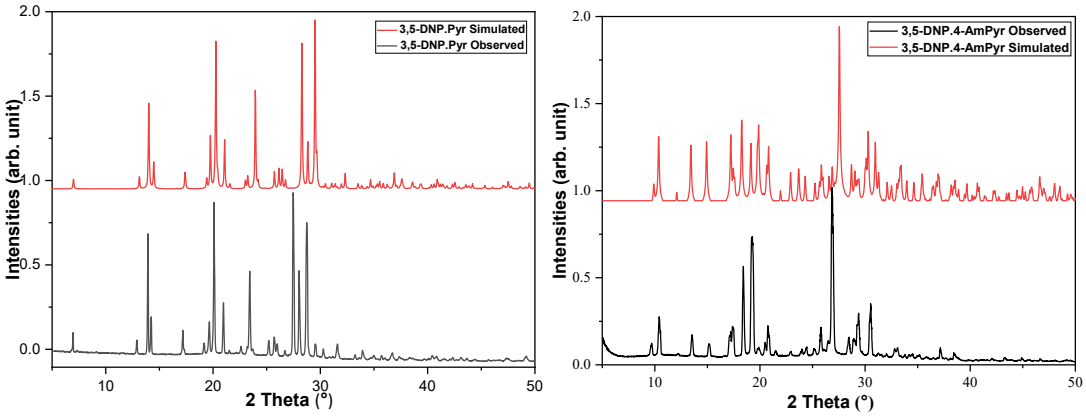

Figure 4.18 Powder X-ray diffraction patterns of 3,5-DNP.Pyr and 3,5-DNP.AmPyr

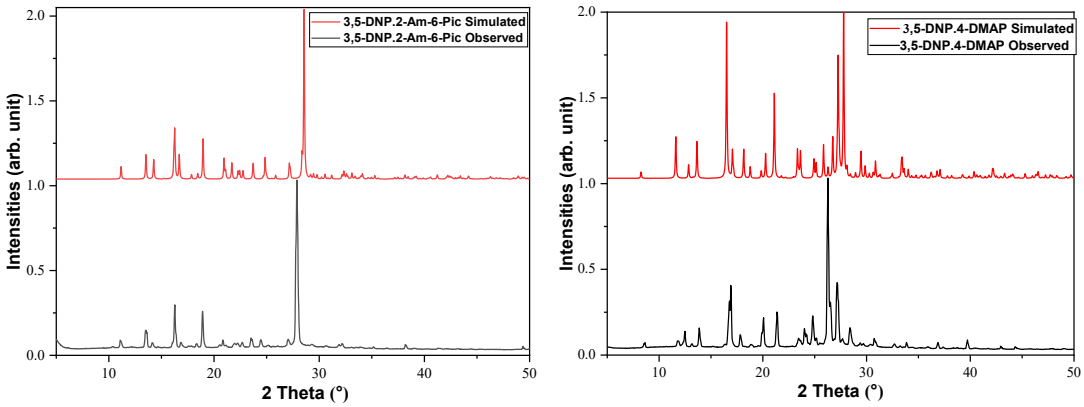

Figure 4.19 Powder X-ray diffraction patterns of 3,5-DNP.AmPic and 3,5-DNP.DMAP

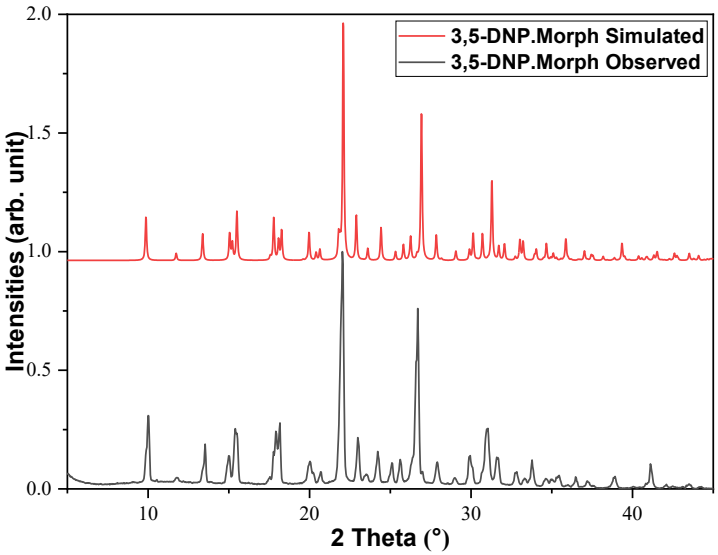

Figure 4.20 Powder X-ray diffraction patterns of 3,5-DNP.Morph

4.3.2.3 Thermal Properties of 3,5-DNP Salts

DSC-TG measurements were performed on DNP salts to obtain data about their thermal stability. Co-crystallisation/salt formation is a process that changes physical properties of materials including melting and decomposition temperature. 3,5-DNP's DSC-TG curve is given in Figure 4.21. Both melting and decomposition points of 3,5-DNP decreased after salt formation with Pyr, see Figure 4.22. Whilst, in principle, the processability of 3,5-DNP could be enhanced by lowering melting point, the energetic performance was reduced by lowering decomposition point through salt formation. Focusing on the TG curve in Figure 4.22, it is seen that mass loss of the compound started slowly just before melting and lasted until decomposition ends. This means

that when the heat is applied slowly on 3,5-DNP.Pyr, a decrease is observed in the amount of 3,5-DNP.Pyr remaining for subsequent decomposition. The second endothermic peak demonstrates that much of the salt evaporated prior to decomposition.

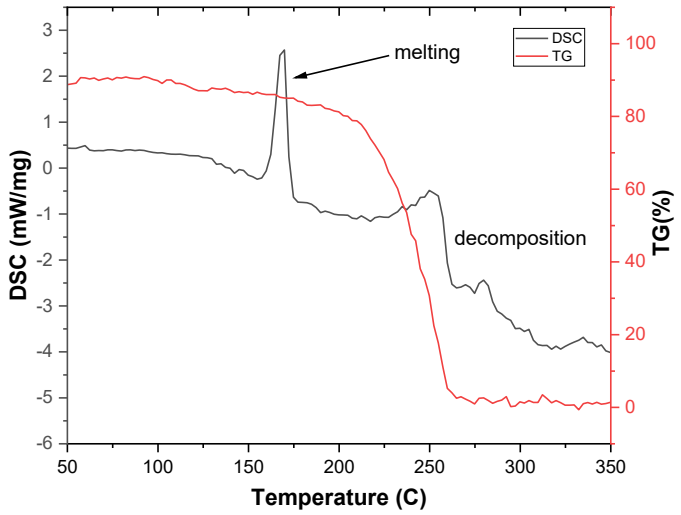

Figure 4.21 DSC and TG traces for the 3,5-DNP (exothermic direction down).

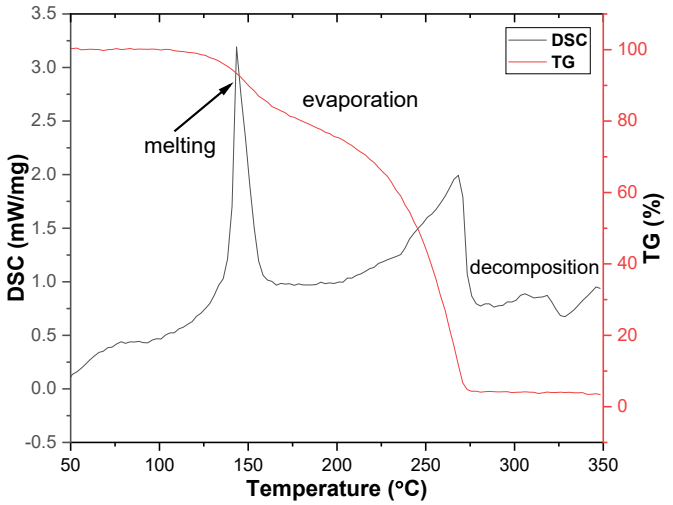

Figure 4.22 DSC and TG traces for the 3,5-DNP.Pyr salt (exothermic direction down).

The melting point of 3,5-DNP increased to 217°C upon salt formation with AmPyr. Decomposition of 3,5-DNP.AmPyr consisted of two exothermic steps starting at 300°C (Figure 4.23). Whereas multistep decomposition is seen as a disadvantage for explosives, it can be desirable for propellants since it increases the reaction time. The TG trace indicates that there is no mass loss observed until decomposition *i.e.* no

evaporation. This means that almost all of the compound was still present at the onset of decomposition, which is a desirable characteristic for an energetic material.

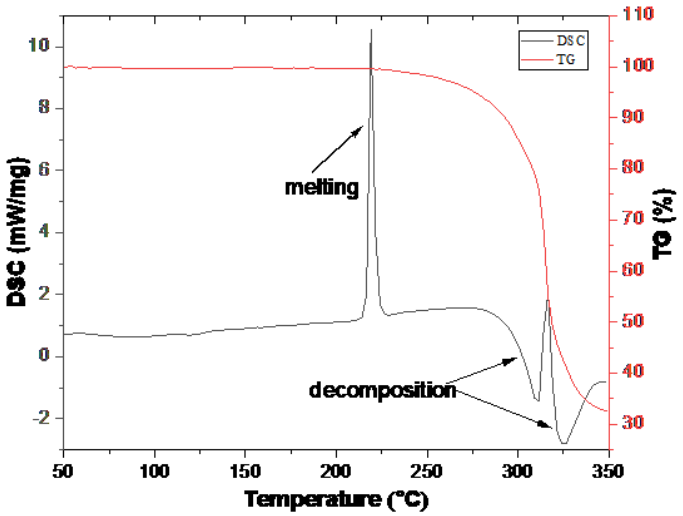

Figure 4.23 DSC and TG thermal traces for the 3,5-DNP.AmPyr salt (exothermic direction down).

The DSC-TG trace for the 3,5-DNP.AmPic salt is shown in Figure 4.24. While the decomposition temperature remained very similar to that of 3,5-DNP, the melting point of the compound has increased from 169°C to 211°C after salt formation. This means that while thermal stability did not change, the potential processability of 3,5-DNP was reduced on salt formation.

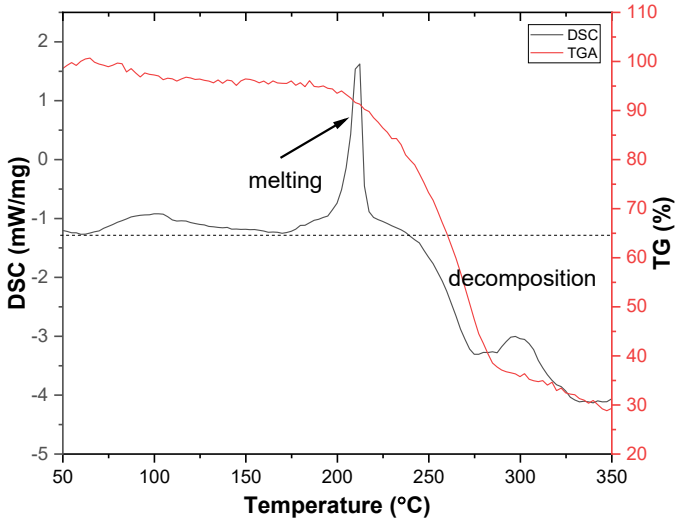

Figure 4.24 DSC and TG thermal traces for the 3,5-DNP.AmPic salt (exothermic direction down).

The DSC-TG thermal trace for 3,5-DNP.DMAP is given in Figure 4.25. The gap between melting and decomposition was slightly lowered after salt formation with DMAP. It exhibited a two-step decomposition starting at 278°C. This multi-step reaction can be considered as advantagous if 3,5-DNP.DMAP were used as a propellant. The salt did not lose any mass until the start of decomposition, thereby retaining the amount of material available for potential detonation or burning processes.

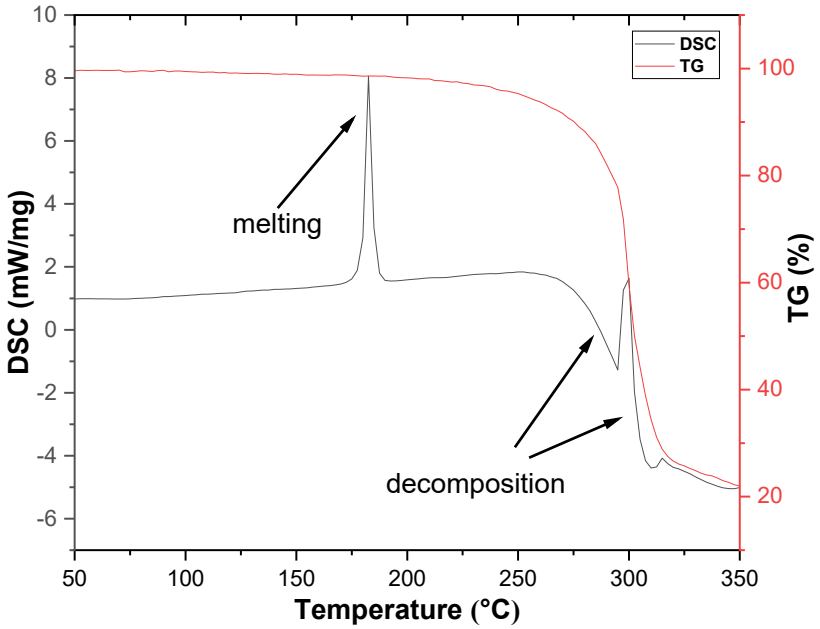

Figure 4.25 DSC and TG thermal traces for the 3,5-DNP.DMAP salt (exothermic direction down). The first endothermic peak shows the melting point and two-step exothermic move is the decomposition of the salt.

The 3,5-DNP.Morph salt has an onset of melting at 216°C (Figure 4.26). As soon as melting completed, a slow decomposition reaction of the salt was observed. While salt formation with Morph increased the melting point, the decomposition temperature decreased compared to 3,5-DNP. A very small temperature gap between melting and decomposition is disadvantageous for melt-castable munitions.

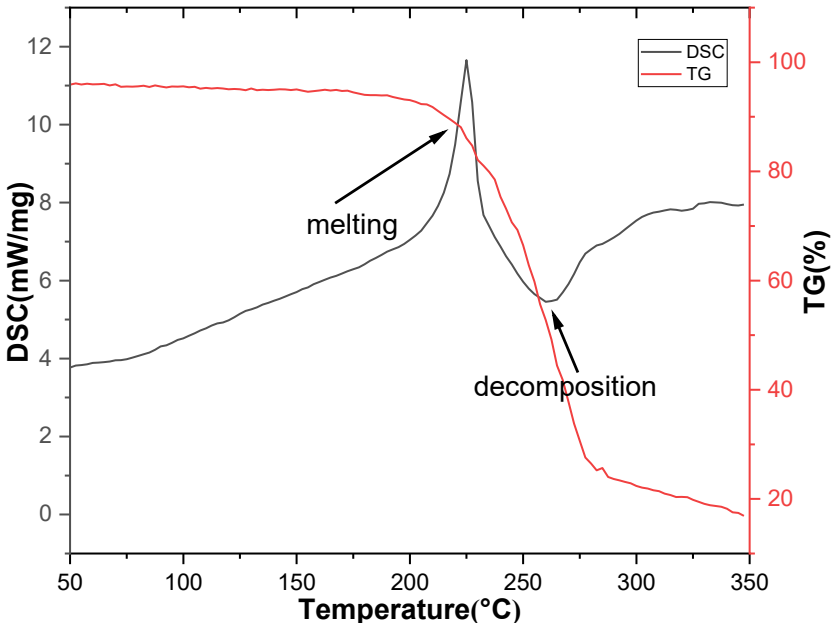

Figure 4.26 DSC and TG thermal traces for the 3,5-DNP.Morph salt (exothermic direction down).

Table 4.4 illustrates the melting and decomposition points and enthalpies of 3,5-DNP and its salts. Due to complicated decomposition patterns, the decomposition enthalpy of 3,5-DNP and 3,5-DNP.Pyr could not be determined. The melting point of 3,5-DNP was increased upon salt formation with all the co-formers except for Pyr. The melting point of materials is highly dependent on their intermolecular and electrostatic interactions. Therefore, this drop in the melting point of 3,5-DNP.Pyr can be attributed to lower intermolecular interaction network in 3,5-DNP.Pyr comparing to 3,5-DNP. The heat required for melting of an energetic material might be of interest for the applications that involve melt-casting process. Therefore, melting enthalpies of 3,5-DNP and its salts are given in Table 4.4.

The decomposition point was found to vary across the series, with lower values recorded for 3,5-DNP.Morph and 3,5-DNP.AmPic, while 3,5-DNP.Pyr, 3,5-DNP.AmPyr and 3,5-DNP.DMAP reported higher values than the parent energetic compound (3,5-DNP). This therefore suggests that salt formation offers significant opportunities to tune the materials properties required for processing and performance of this energetic compound. Decomposition enthalpies, that usually relate to high energetic performance, are given in Table 4.4.

Table 4.4 Melting and decomposition onset temperature values of 3,5-DNP and its salts

Compound	Melting onset temperature (°C)	Melting enthalpy		Decomposition onset temperature(°C)	Decomposition enthalpy	
		J/g	kJ/mol		J/g	kJ/mol
3,5-DNP. Pyr	140	139	11	271	-	
3,5-DNP. AmPyr	217	184	44	314	-390, -416	-98, -105
3,5-DNP. AmPic	211	134	36	250	-	
3,5-DNP. DMAP	180	157	83	298	-	
3,5-DNP. Morph	216	315	59	237	-447	-68
3,5-DNP	169	145	23	256	-	

*****Since 3,5-DNP, 3,5-DNP.Pyr, 3,5-DNP.AmPic and 3,5-DNP.DMAP have gradual complicated decomposition patterns, enthalpies could not be calculated.

4.3.2.4 Calculated Energetic Performance and Impact Sensitivity of 3,5-DNP Salts

Detonation performance parameters were predicted using the EXPLO-5 program [9] and are listed in Table 4.5, along with computed solid-state heat of formation values derived (See section 4.2.7 for more details). In addition, impact sensitivity (IS) of one of the compounds was tested using the BAM Fall Hammer instrument, as described in the experimental section. Detonation pressure and velocity are key parameters that reflect the energetic performance of energetic materials. As can be seen from Table 5.6, the salts all exhibited lower energetic performances compared to 3,5-DNP. This was expected since they have effectively been diluted by combining with a non-energetic component. Oxygen balance, defined as the amount of oxygen needed to ensure complete oxidation of all elements present, is another critical property to monitor in energetic materials. As expected, salt formation with pyridines negatively impacts this metric, indicating that an oxidiser would be required for complete combustion. Among all the salts, 3,5-DNP.Morph has the highest oxygen balance since morpholine includes an oxygen atom. Moreover, morpholine is a known amine compound which is used as an explosive sensitiser (which promotes initiation or detonation). [12]

The volume of gas released upon detonation can be related to the energy released by the energetic compound. The explosive power is defined as the product of the volume of gas released V_0 (STP) and the heat of detonation.[13] Therefore, these two parameters are important to evaluate the performance of an energetic material. The predicted volume of the gas products of 3,5-DNP salts are given in Table 4.5. The largest predicted volume of gas released by 3,5-DNP.Morph which is higher than TNT (740 dm^3/kg).[13] This is expected since it has the highest oxygen balance among the salts.

It is commonly claimed that there is a proportional relationship between crystal density and energetic performance of energetic materials.[14] These trends are plotted for detonation pressure and velocity and given in Figure 4.27 and 4.28. In both plots, it is seen that direct proportional relationship was rationalised except for Morph- and 4-AmPyr-containing compounds. In addition to crystal density, energetic performance depends also on other parameters such as heat of formation and oxygen balance. The exceptional behaviour of 3,5-DNP.Morph can be explained with its high oxygen balance. The reason that 3,5-DNP.AmPyr salt exhibited lower performance relative to its high crystal density should be investigated further as a future work.

Table 4.5 Energetic properties of 3,5-DNP and its salts

	3,5-DNP. Pyr	**3,5-DNP. AmPyr**	**3,5-DNP. AmPic**	**3,5-DNP. DMAP**	**3,5-DNP. Morph**	**3,5-DNP (explo)***
Heat of formation (kJ/mol)	345.5*	170.5*	150.5*	201.7*	-79.6*	136.1*
Heat of detonation (kJ/kg)	-4423	-3551	-3851	-3551	-5083	-5438
Detonation temperature (K)	3012	2585	2640	2585	3145	3945
Detonation pressure (GPa)	17.0	15.0	15.5	14.7	20.5	31.5
Detonation velocity (m/s)	6780	6457	6587	6474	7373	8469
Volume of gas at STP (dm^3/kg)	660	685	692	693	775	702
Oxygen balance (%)	-104.6	-101.5	-114.19	-125.6	-94.6	-30.4
Crystal density ($g.cm^{-3}$)	1.595	1.586	1.532	1.494	1.576	1.820
Impact sensitivity (J)	45	-	-	-		25 [3]

***These detonation parameters were predicted by using the values calculated with computational techniques described in section 4.2.7.

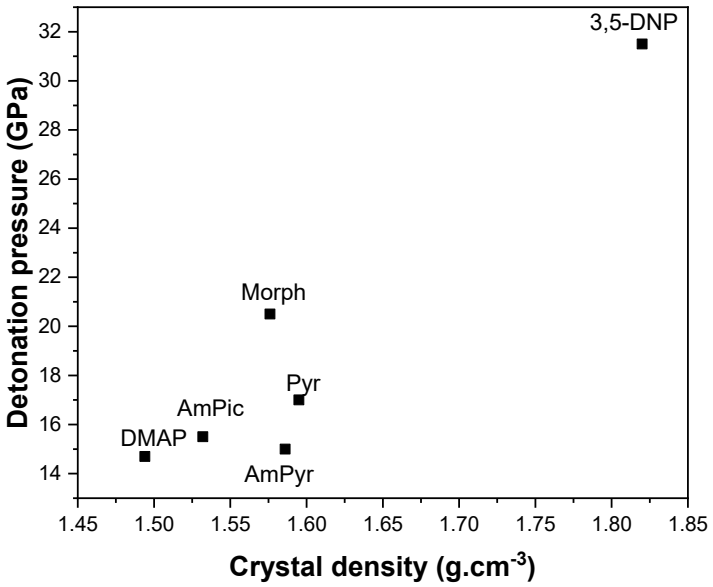

Figure 4.27 Detonation pressure vs crystal density for 3,5-DNP and its salts

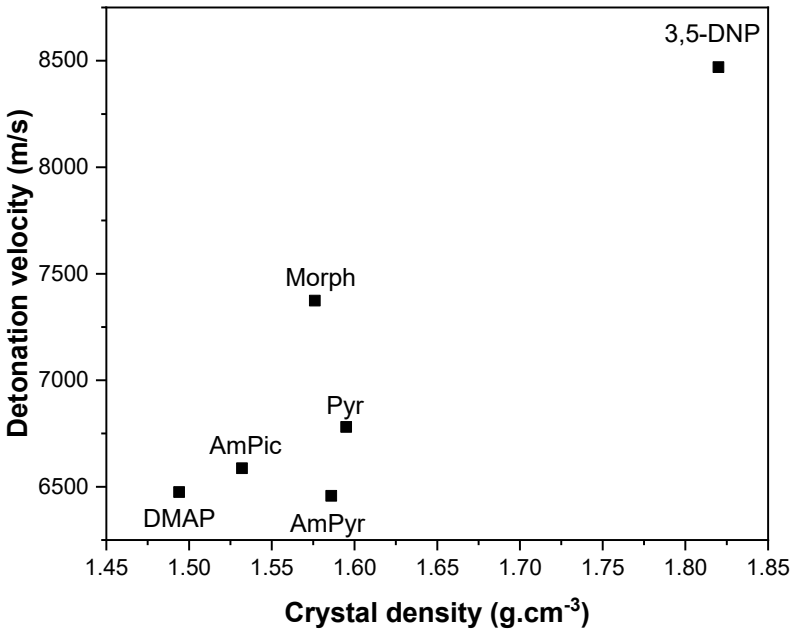

Figure 4.28 Detonation velocity vs crystal density trend in 3,5-DNP and its salts

The composition of the detonation products were also predicted using EXPLO-5 and are given in Table 4.6 and 4.7. The higher oxygen balance a compound has, the higher the predicted molar ratio of oxygen-containing compounds in the detonation products.

Table 4.6 Composition of detonation products of 3,5-DNP and its salts

3,5-DNP.Pyr	Mol (%)	3,5-DNP.4-AmPyr	Mol (%)	3,5-DNP.2-Am-6-Pic	Mol (%)
C(d)	37.7	C(d)	32.9	C(d)	34.5
H_2O	19.9	N_2	20.7	H_2O	19.5
N_2	18.3	H_2O	20.4	N_2	18.1
C(gr)	15.5	C(gr)	17.5	C(gr)	16.5
CO_2	3.3	CO_2	2.6	NH_3	2.8
CH_2O_2	1.4	CH_4	1.7	CH_4	2.1
CH_4	1.2	NH_3	1.5	CO	2.0
NH_3	1.2	CH_2O_2	1.2	H_2	1.6
CO	1	CO	0.8	CH_2O_2	1.2
H_2	0.5	H_2	0.5	CO_2	1.0
C_2H_6	0.2	C_2H_6	0.3	C_2H_6	0.5
C_2H_4	0.009	C_2H_4	0.009	C_2H_4	0.096
HCN	0.005	HCN	0.004	HCN	0.069
CH_3OH	0.001	CH_3OH	0.0015	CH_3OH	0.006
	25.6		**25.0**		23.7

(Oxygen containing compounds are highlighted with the red. *C(gr): graphite C(d): diamond, s: solid)

Table 4.7 Composition of detonation products of 3,5-DNP and its salts

3,5-DNP.4-DMAP	Mol (%)	3,5-DNP.Morph	Mol (%)	3,5-DNP	Mol (%)
C(d)	30.6	C(d)	42.7	N_2	36.6
N_2	20.7	H_2O	27.0	CO_2	17.0
H_2O	20.4	N_2	16.7	C(d)	16.5
C (gr)	19.8	NH_3	3.2	CO	11.6
CO_2	2.5	CO	2.8	CH_2O_2	9.8
CH_4	1.7	CH_2O_2	2.5	H_2O	8.1
NH_3	1.5	H_2	1.9	NH_3	0.1
CH_2O_2	1.2	CH_4	1.4	HCN	0.1
CO	0.8	CO_2	1.05	H_2	0.1
H_2	0.5	C_2H_6	0.38	CH_4	0.008
C_2H_6	0.3	HCN	0.13	NO	0.005
C_2H_4	0.01	C_2H_4	0.12	C_2H_4	0.002
HCN	0.004	CH_3OH	0.008	CNO	0.001
CH_3OH	0.001	N_2H_4	0.002	H	0.0007
	24.9		33.3		36.7

(Oxygen containing compounds are highlighted with the red. *C(gr): graphite C(d): diamond, s: solid)

As a result of BAM Fall hammer impact sensitivity testing, 3,5-DNP.Pyr was found to be much less sensitive (45 J) to mechanical impact than 3,5-DNP (25 J). Precedents in the literature suggest that impact sensitivity correlates with the crystal packing of energetic materials, with layered structures more likely to efficiently dissipate the shock-wave energy than puckered structures. [15,16] The change in crystal packing from the herringbone array in 3,5-DNP (Figure 4.7) to the layered structure in 3,5-DNP.Pyr would support this observation (Figure 4.9).

4.3.3 Trends and Relationships

Figure 4.29 illustrates the density trend exhibited for the salts. The salts studied in this chapter exhibited crystal densities that lie between those of the two co-formers (3,5-DNP and pyridines). This is a common situation that is encountered in similar multicomponent structure studies. For instance, 13 NTO salts/co-crystals with arylamines, different pyridines and aminotolenes were explored by Lloyd and they exhibited crystal densities that were approximately midway between those of NTO and its co-former, with only 2 exceptions that featured compounds halogen-containing. [17]

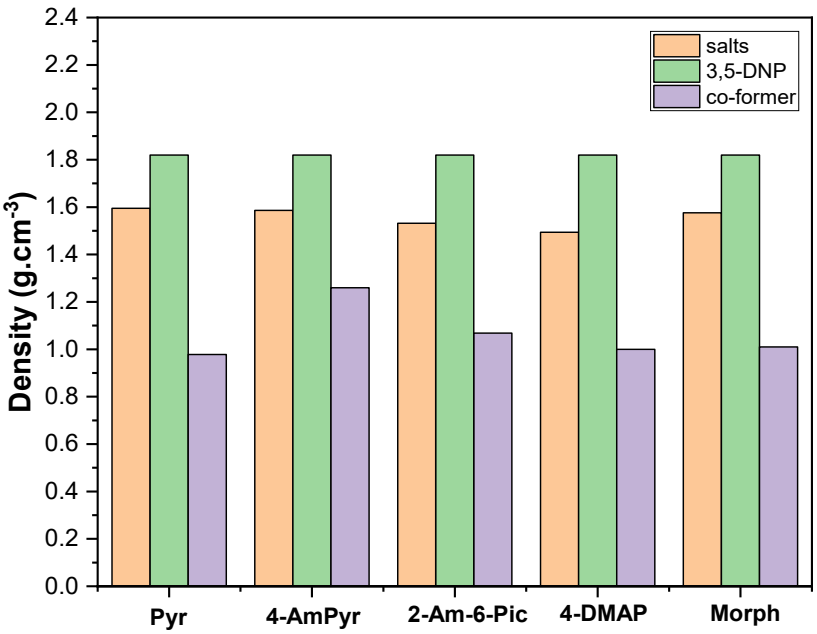

Figure 4.29 Crystal densities of the co-formers (purple), 3,5-DNP (green) and resulting salts (orange)

4.4 Conclusions

As a result of a broad co-former investigation conducted in this study, some strategies were improved to produce dinitropyrazole salts. Weakly basic heterocyclic compounds (pyridine, different pyridine derivatives and morpholine) were suitable co-formers to form salts with 3,5-DNP. Five novel salts between 3,5-DNP and Pyr, AmPyr, DMAP, AmPic and Morph were explored. All the compounds formed with a 1:1 molar ratio. These novel structures were characterised using single crystal and powder X-ray diffraction techniques. The main non-covalent interactions and crystal packing motifs observed in these salts were explained in detail. Nitro and NH groups on dinitropyrazole were found to be efficient tools to form moderate-strength hydrogen bonds with substituted pyridines. Amino containing pyridines appeared as useful co-formers for enhancing non-covalent interaction networks for nitropyrazole-based energetic compounds. Two main types of hydrogen bond interaction were observed across the series of the salts: N-H···N and N-H···O. C-H···O type of interactions were also found to be significant to contribute the non-covalent bond interaction network for nitropyrazole-based energetic materials. All the salts except for 3,5-DNP.Pyr have ΔpK_a values higher than 4, and so obey the ΔpK_a rule described in Chapter 1. The 3,5-DNP.Pyr salt has a ΔpK_a value which places it in an indeterminate region where co-formers may yield as salts or co-crystals.

Energetic performance, thermal behaviour and the impact sensitivities (for one salt) of these energetic materials were determined. Where possible, the important structural features including crystal packing and crystal density were correlated with energetic properties such as thermal stability, impact sensitivity and energetic performance. The thermal properties of 3,5-DNP changed upon salt formation. All the salts exhibited complicated decomposition processes, often comprising multiple exothermic steps. The thermal stability of 3,5-DNP was enhanced upon salt formation with pyridine and its derivatives, except for AmPic. 3,5-DNP.Morph was found to be thermally less stable than the parent energetic compound.

Energetic performance parameters of the salts were predicted using the EXPLO 5 program. The salts with higher densities exhibited higher energetic performance except for two salts formed with AmPyr and Morph. 3,5-DNP.AmPyr exhibited lower energetic performance than expected which should be investigated as future work. Although the crystal density of 3,5-DNP.Morph places it in the middle of the series, it

exhibited the highest predicted detonation pressure and detonation velocity among 3,5-DNP salts. 3,5-DNP.Morph has a detonation pressure of 20.5 GPa and a detonation velocity of 7373 m s^{-1}; this is higher than the commonly used explosive 2,4,6-trinitrotoluene (TNT), (6881 m s^{-1} ,19.5 GPa).[18]

4.5 Suggestions for Future Studies

In the light of the findings of this study, more co-crystals/salts of 3,5-DNP could be produced using co-formers that have similar electronic structures and hydrogen bonding donors/acceptors to pyridines. The more structures explored with these energetic compounds, the more robust will be the correlations between structures and energetic properties. This will open up opportunities to tailor energetic properties of 3,5-DNP for specific aims. On the other hand, more oxygen or nitro containing structures can be used as co-formers in order to enhance the oxygen balance and energetic performance of the resulting salt. This could be exemplified with nitro-substituted pyridines and morpholines.

Due to the COVID-19 pandemic, it was not possible to conduct energetic prorperty testing of some of the salts. Therefore, impact sensitivity tests of 4 DNP salts formed with AmPyr, DMAP, AmPic and Morph should be performed in order to complete the dataset and establish more reliable structure-property relationships for this group energetic material. On the other hand, vibrational up-pumping model calculations which is used for different polymorphs of 3,4,5-TNP (Chapter 3) could be performed on these novel salts to predict their relative impact sensitivities. Furthermore, other types of sensitivities such as spark and friction can be measured in order to explain how salt formation affects these energetic properties.

4.6 References

1 Y. Zhang, Y. Huang, D. A. Parrish and J. M. Shreeve, *J. Mater. Chem.*, 2011, **21**, 6891–6897.

2 P. Yin, L. A. Mitchell, D. A. Parrish and J. M. Shreeve, *Angew. Chemie - Int. Ed.*, 2016, **55**, 14409–14411.

3 M. F. Bölter, A. Harter, T. M. Klapötke and J. Stierstorfer, *Chempluschem*, 2018, **83**, 804–811.

4 Y. V. Nelyubina, I. L. Dalinger and K. A. Lyssenko, *Russ. Chem. Bull.*, 2013, **62**, 1707–1719.

5 M. F. Bölter, T. M. Klapötke, T. Kustermann, T. Lenz and J. Stierstorfer, *Eur. J. Inorg. Chem.*, 2018, **2018**, 4125–4132.

6 I. E. Drukenmüller, T. M. Klapötke, Y. Morgenstern, M. Rusan and J. Stierstorfer, *Zeitschrift für Anorg. und Allg. Chemie*, 2014, **640**, 2139–2148.

7 J. C. Bennion, Z. R. Siddiqi and A. J. Matzger, *Chem. Commun.*, 2017, **53**, 6065–6068.

8 O. V. Dolomanov, L. J. Bourhis, R. J. Gildea, J. A. K. Howard and H. Puschmann, *J. Appl. Crystallogr.*, 2009, **42**, 339–341.

9 M. Suceska, 2015.

10 D. Sun, Y. H. Li, H. J. Hao, F. J. Liu, Y. M. Wen, R. Bin Huang and L. S. Zheng, *Cryst. Growth Des.*, 2011, **11**, 3323–3327.

11 W. Zhang, T. Li, B. Zhang, L. Wang, T. Zhang and J. Zhang, *Inorg. Chem.*, 2019, **58**, 7653–7656.

12 6,007,648, *United States Pat.*, 1999, 3–5.

13 T. M. Klapötke, *Chemistry of High-Energy Materials*, Walter de Grutyer, Munich, 2nd editio., 2012.

14 J. P. Agrawal, in *High Energy Materials: Propellants, Explosives and Pyrotechnics.*, ed. J. P. Agrawal, WILEY-VCH Verlag GmbH & Co. KGaA, Weinheim, 2010, pp. 1–67.

15 Y. Ma, L. Meng, H. Li and C. Zhang, *CrystEngComm*, 2017, **19**, 3145–3155.

16 C. Zhang, F. Jiao and H. Li, *Cryst. Growth Des.*, 2018, **18**, 5713–5726.

17 H. Lloyd, University of Edinburgh, 2016.

18 Y. Zhang, Y. Guo, Y. H. Joo, D. A. Parrish and J. M. Shreeve, *Chem. - A Eur. J.*, 2010, **16**, 10778–10784.

Chapter 5 Structure-Property Studies of Co-Crystals and Salts Formed between Nitropyrazoles and Halogenated Pyridines

5.1 Introduction

As described in Chapter 1, co-crystallisation offers a potential approach for the design of multi-component supramolecular structures with desired characteristics and specific properties. The main tools which govern co-crystallisation and salt formation are the non-covalent interactions such as hydrogen bonds, halogen bonds and π-π stacking. [1] Hence, understanding the nature of non-covalent bonds is of great importance in order to exploit them for desired directions. To date, hydrogen bonding has been at the centre of numerous supramolecular assembly studies and has been investigated thoroughly. However, the focus of co-crystallisation studies has recently been expanded towards less-studied halogen bonding on account of its potential as a crystal-engineering tool. Halogen bonding gains additional importance when molecular components lack H-bond donor or acceptor moieties. Halogen bonding has recently been identified as an important tool in the field of energetic materials. The first example of halogen bond containing energetic co-crystal was DADP/TITNB (diacetone diperoxide and 1,3,5-triiodo-2,4,6-trinitrobenzene) [2], in which iodo-peroxide interactions were the main driving force for co-crystal formation. As a result of co-crystallisation of these explosives, an enhanced, less-sensitive, primary explosive was prepared. In a similar study, two energetic co-crystals of 1,3,5-trinitrobenzene (TNB) were produced with TITNB (1,3,5-triiodo-2,4,6-trinitrobenzene) and TBTNB (1,3,5-tribromo-2,4,6-trinitrobenzene).[3] One of the important potential application areas for halogen-containing energetic materials is as “biocidal energetics”. On initiation they generate X_2 and/or HX as detonation products, both of which are capable of destroying biological weapons and so could be used as an efficient way to mitigate biological agents such as anthrax (*Bacillus anthracis*). [4,5]

Halogen bonding occurs between an electron-rich nucleophile and the σ-hole of a polarized halogen atom.[6] The σ-hole is a region of positive electrostatic potential, whose size and strength increases with the increasing atomic number of a halogen atom (Cl < Br < I). Therefore, the type of halogen atom determines the strength of the halogen bond formed between molecules. In this chapter, the effects of different halogens on the formation of co-crystal and/or salt were explored using halogenated pyridine molecules as co-formers with nitropyrazoles. In particular, the focus was on

exploring structure-property relationships for these salts and co-crystals. Three co-crystals between dinitropyrazoles and halogenated pyridines were obtained and characterised together with three salts formed between 3,4,5-TNP and halogenated pyridines. The effects of halogen substitution and halogen-bond formation in these structures were investigated.

5.2 Experimental

5.2.1 Materials

Energetic compounds 1,3-DNP, 3,5-DNP and 3,4,5-TNP were synthesised by the route described in Chapter 2. The following energetic co-formers were purchased from Sigma Aldrich: pyridine (Pyr), 3-fluoropyridine (FPyr), 3-bromopyridine (BrPyr), 3-iodopyridine (IPyr), 3-amino-2-chloropyridine (AmClPyr).

5.2.2 Co-crystal and Salt Formation

The slow evaporation technique was used to prepare halogenated co-crystals and salts in this chapter. Energetic and non-energetic co-formers were dissolved in suitable solvents in glass vials and covered with parafilm. Methanol proved to be a successful solvent for most of the materials prepared in this section. For 3,4,5-TNP.Pyr, a water-methanol solvent system was used with heating to 50°C to fully dissolve the components. Slow evaporation was achieved by piercing several holes in the parafilm layer. Slow evaporation lasted usually 2-3 days. At the end of this period, single crystals surrounded with a small amount of mother liquor were selected for single crystal X-ray diffraction (SXRD) studies.

In addition to the preparation of single crystals for structural characterisation, bulk powder samples of the co-crystals and salts were prepared using evaporative techniques on a larger scale. Minimum quantities of 1 g of each multicomponent compound were prepared for further physical tests, including impact sensitivity (IS) and thermal studies. The purity of these bulk samples was checked using powder X-ray diffraction. If any impurities were detected, samples were subsequently purified by recrystallisation,

5.2.3 Single Crystal X-ray Diffraction

All the SXRD data for the co-crystals and salts formed with nitropyrazoles and

halogenated pyridines were collected at 120 K using an Agilent Technologies SuperNova diffractometer equipped with an Oxford Cryosystems N_2 low temperature Cryostream. Data for 1,3-DNP.AmClPyr were collected using monochromated Cu-K_α radiation (λ = 1.5418 Å) whilst the data for the remainder of the structures were collected using Mo-K_α (λ= 0.71073 Å). The total number of runs and images was based on the strategy calculation from the program CrysAlisPro (Rigaku, V1.171.38.46, 2015). The diffraction patterns were indexed and the unit cells were refined using CrysAlisPro (Rigaku, V1.171.38.46, 2015).

Within the OLEX2 [7] program suite, the structures of 3,4,5-TNP.FPyr, 3,4,5-TNP.BrPyr and 3,4,5-TNP.IPyr were solved using the intrinsic phasing solution method within the program ShelXT.[8] The structure of 1,3-DNP.AmClPyr was solved by charge flipping methods, 3,5-DNP.AmClPyr by direct methods and 3,5-DNP.BrPyr were solved by Patterson methods using ShelXS.[9] All the structural models were refined with ShelXL using least squares minimisation and refined with anisotropic displacement parameters for all non-H atoms using ShelXS. [10] All non-hydrogen atoms were refined anisotropically. Hydrogen atom positions were located from a difference Fourier map and freely refined using the riding model.

5.2.4 Powder X-ray Diffraction

Powder X-ray diffraction patterns were recorded under ambient-temperature and ambient-pressure conditions using a Bruker D2 PHASER instrument. Experimental details are given in Chapter 2 (Section 2.6).

5.2.5 Differential Scanning Calorimetry

DSC experiments were conducted on a NETZSCH STA 449 F1 Differential Scanning Calorimeter. Experimantal details are given in Chapter 2 (Section 2.12).

5.2.6 BAM Fall Hammer Tests

BAM Fall Hammer impact testing (BFH-12) was performed, at the Cavendish Laboratory (Cambridge) on a sample of 1,3-DNP.AmClPyr, 3,5-DNP.AmClPyr, 3,5-DNP.BrPyr. More details are given in Chapter 2 (Section 2.11).

5.2.7 Detonation Performance and Heat of Formation Calculations

All calculations of detonation parameters were performed using the program EXPLO-5 V6.03. [11,12] More details are given in Chapter 2 (Section 2.13). All the heat of formation $\Delta H_f(\mathrm{g})$ for each ion/co-former was calculated by Imogen Christopher (PhD student from Morrison group). More details are given in Chapter 2 (Section 2.14).

5.3 Results and Discussion

5.3.1 Characterisation of Synthetic Materials (1,3-DNP)

The characterisation of 1,3-DNP is given in this section. Characterisation of the other energetic compounds used in this chapter is given in previous chapters (3,4,5-TNP: Chapter 3, 3,5-DNP: Chapter 4). NMR spectroscopy and powder X-ray diffraction (PXRD) results were used to confirm that 1,3-DNP were synthesised successfully. ^{1}H-NMR spectrum of 1,3-DNP is given in Figure 5.1. As expected, two peaks with the same intensities corresponding to the two hydrogen atoms in the compound were observed in the ^{1}H-NMR spectrum (Figure 5.1). These chemical shifts (δ = 8.49 and δ = 7.17) matched the literature studies for 1,3-DNP. The remainder of the peaks belong to the solvents used during synthesis, recrystallisation and NMR sample preparation steps (δ = 7.28 – $CDCl_3$, δ = 3.5 and δ = 1.22 – diethyl ether, δ = 1.61 – water, δ = 2.17 – acetone used for cleaning the NMR tubes).

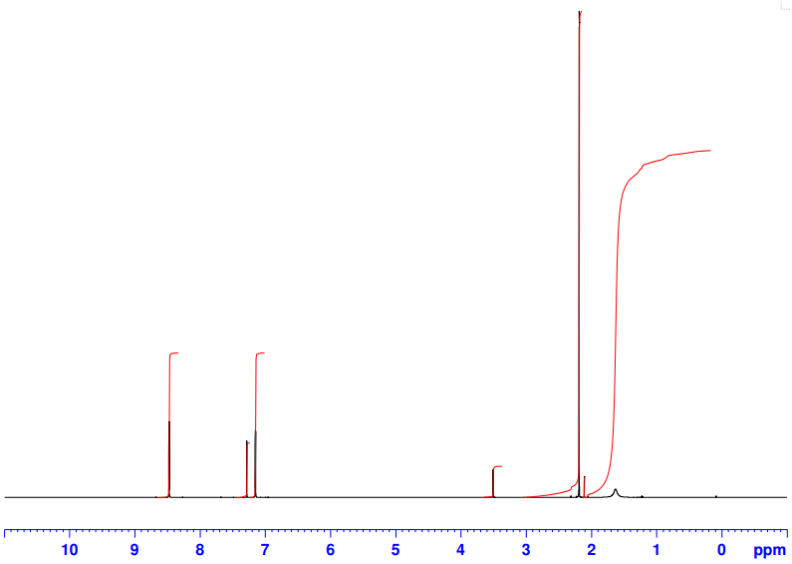

Figure 5.1 ^{1}H-NMR spectrum of 1,3-DNP

In order to check the phase purity of the synthesised 1,3-DNP, a powder X-ray diffraction pattern was collected and compared with the pattern simulated from the structure deposited in the CSD (ref. code: NIPYAZ). This comparison is given in Figure 5.2 and showed that the sample was phase-pure and suitable for co-crystallisation and salt formation studies.

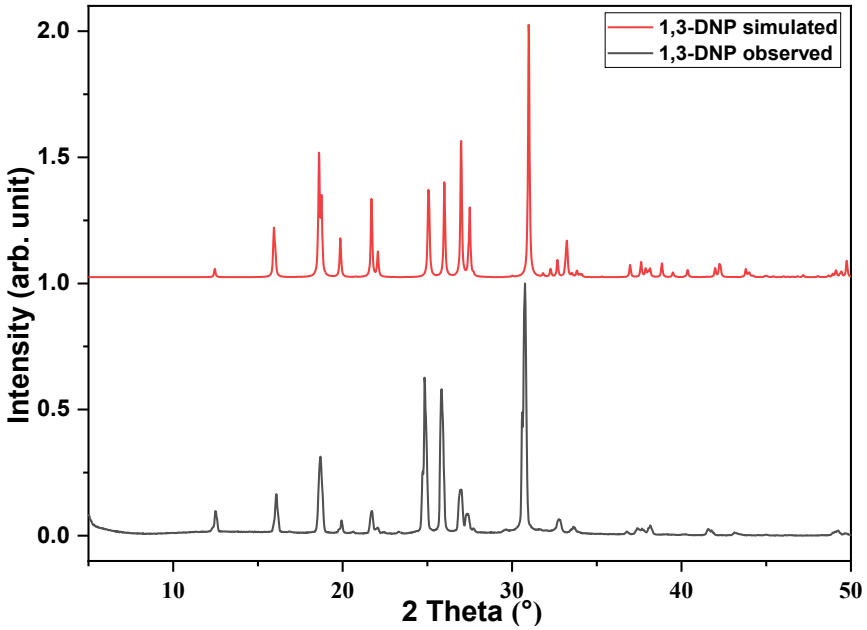

Figure 5.2 Powder X-ray diffraction patterns of 1,3-DNP (red line represent the simulated pattern from the CSD structure, black line is experimental data recorded on the D2 Phaser instrument.)

5.3.2 Co-crystals Formed with Dinitropyrazoles

In this section, characterisation of the co-crystals formed between dinitropyrazoles (DNPs: 1,3- and 3,5-DNP) and halogenated pyridines is reported. The non-energetic co-formers used were AmClPyr and BrPyr, illustrated in Figure 5.3. The structures formed with 1,3-DNP.AmClPyr, 3,5-DNP.AmClPyr and 3,5-DNP.BrPyr were co-crystals without any proton transfer between molecules. This observation can be rationalised from the pK_a rule, described in Chapter 1. The pK_a value difference (ΔpK_a ,-1.18 for 3,5-DNP.AmClPyr and -0.3 for 3,5-DNP.BrPyr) between co-formers was not high enough to cause a proton transfer from H-bond donor to the acceptor.

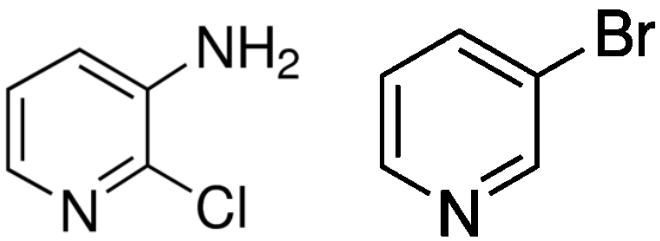

Figure 5.3 Molecular structures of non-energetic co-formers in DNP co-crystals (AmClPyr and BrPyr)

Electron density distribution maps of the co-formers were calculated using TmoleX 4.3.2. and are shown in Figure 5.4. The figures indicate electron-rich and electron-poor areas of the molecules, which are possible synthons for hydrogen or halogen bonding interactions. One of the significant factors driving multicomponent molecule formation of salts and co-crystals is the charge distribution of molecules.[13] Inspection of the electron density distribution maps of both co-formers enables identification of electron-poor and electron-rich areas on substituted pyridine molecules and nitropyrazoles. Therefore, electron density distribution maps in Figure 5.4 were used to make informed predictions to find suitable pairs for co-crystal or salt formation.

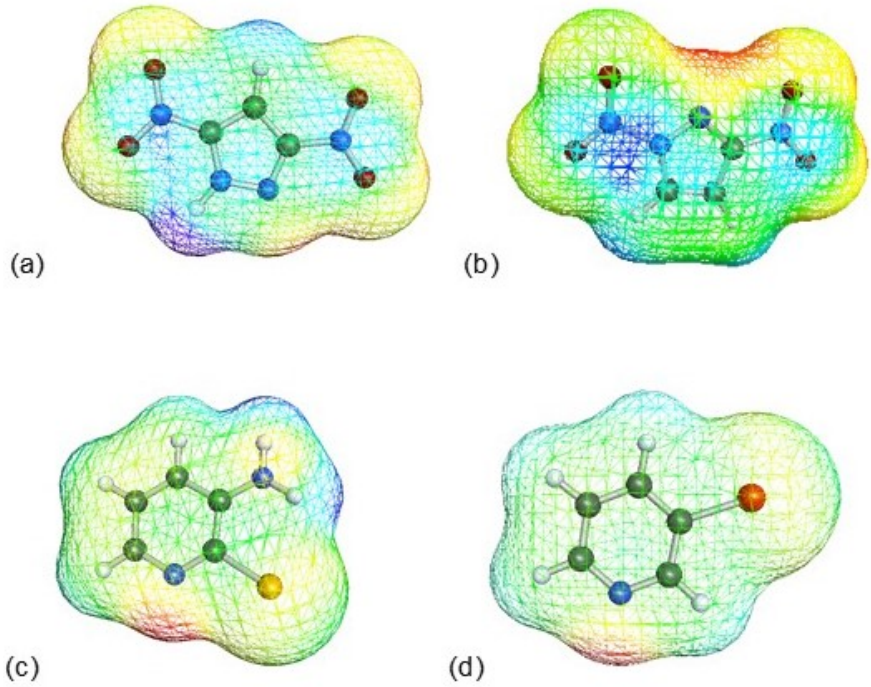

Figure 5.4 Electron density distribution maps of 3,5-DNP (a), 1,3-DNP (b), AmClPyr (c) and BrPyr (d) (The red represents the highest electron density area. The blue/violet represents the lowest e- density area.)

Crystallographic data for the crystal structures of 1,3-DNP and co-crystals are given in Table 5.1. The structure of 1,3-DNP was found to be disordered with C4 and N5 being modelled as interchangeably disordered is shown in Figure 5.5. Figure 5.6 shows the asymmetric units of the co-crystals formed between DNP isomers and substituted pyridines.

Table 5.1 Crystallographic information of the halogenated co-crystals and DNPs

Compound	**1,3-DNP**	**1,3-DNP. AmClPyr**	**3,5-DNP** (CCDC code: 1835062)	**3,5-DNP. AmClPyr**	**3,5-DNP. BrPyr**
Formula	$C_3H_2N_4O_4$	$C_8H_7ClN_6O_4$	$C_3H_2N_4O_4$	$C_8H_7ClN_6O_4$	$C_8H_6BrN_5O_4$
MW ($g.mol^{-1}$)	158.09	286.65	158.09	286.65	316.09
Crystal system	Monoclinic	Triclinic	Orthorhombic	Monoclinic	Triclinic
Space group	$P2_1/c$	P-1	$Pca2_1$	$P2_1/c$	P-1
a, b, c (Å)	5.6944(2) 9.2134(3) 11.2910(4)	6.0564(3) 6.7681(3) 14.2713(6)	10.6055(3) 10.3711(3) 10.4933(3)	11.1308(5) 10.2052(4) 11.3378(6)	6.1034(4) 7.5744(7) 11.7893(7)
α, β, γ (o)	90 103.063(4) 90	84.290(4) 87.528(4) 77.082(4)	90 90 90	90 116.266(6) 90	90.842(6) 92.140(6) 90.158(6)
V ($Å^3$)	577.05(4)	567.22(4)	1154.17	1154.9(1)	544.57(7)
Z, Z'	4, 1	2, 1	8, 0	4, 1	2, 1
ρ ($g.cm^{-3}$)	1.820	1.678	1.820	1.649	1.928
Packing coefficient	0.76	0.73	0.74	0.72	0.73
R factor	0.0506	0.0600		0.0549	0.0661
θ_{min}- θ_{max}	3.673-32.891	2.332-29.706		3.604-29.622	3.176-26.498
Radiation	Mo-Kα	Cu-Kα		Mo-Kα	Mo-Kα
Wavelength(Å)	0.71073	1.54184		0.71073	0.71073

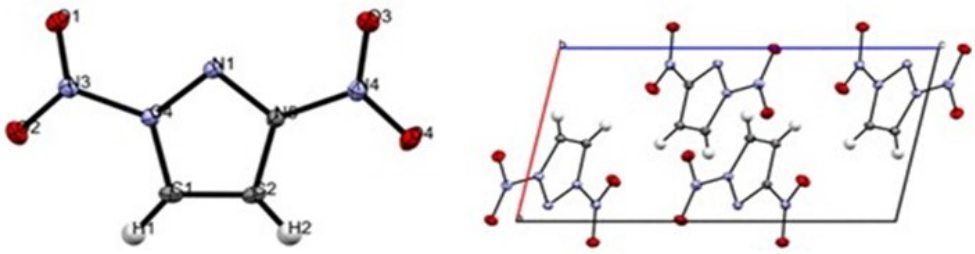

Figure 5.5 Asymmetric unit (left) and unit cell (right) of 1,3-DNP

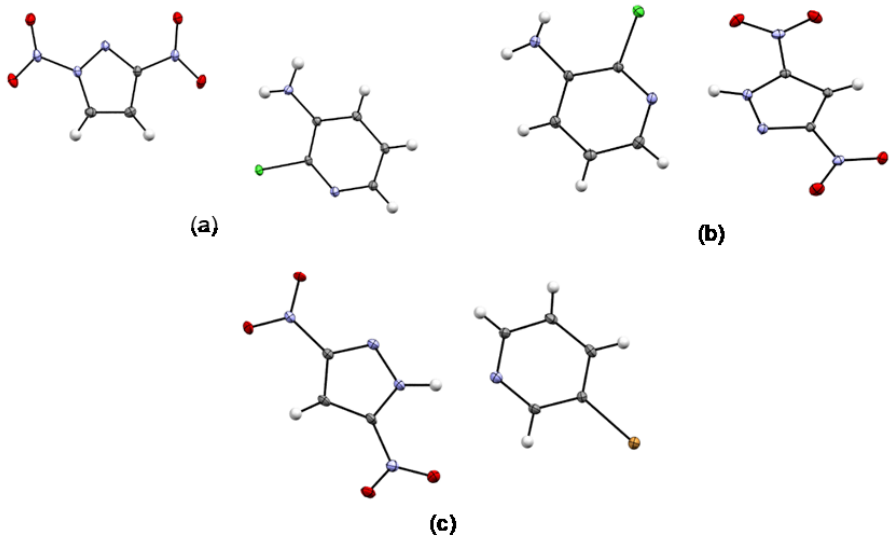

Figure 5.6 Asymmetric unit of (a) 1,3-DNP.AmClPyr, (b) 3,5-DNP.AmClPyr and (c) 3,5-DNP.BrPyr

Among three halogenated co-crystals formed with dinitropyrazoles, only 1,3-DNP.AmClPyr exhibits a disordered structure. The unit cell of 1,3-DNP.AmClPyr is shown in Figure 5.7. Two different views of the unit cell are shown to illustrate the static disorder present in this structure. During structural refinement, C8 and N4 were modelled as substitutionally disordered.

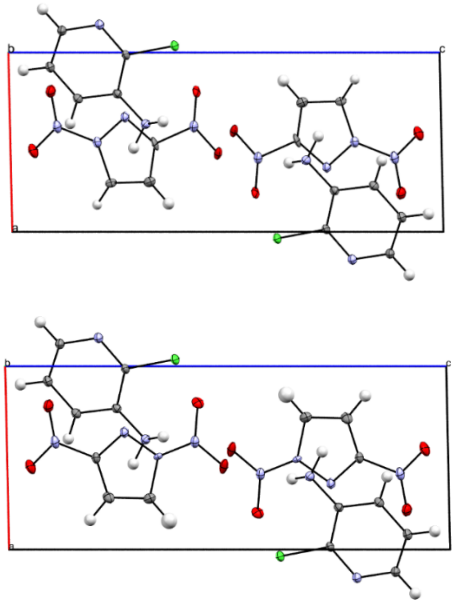

Figure 5.7 Views of packing to show the disorder in the structure of 1,3-DNP.AmClPyr in unit cell

5.3.2.1 Structural Features of DNP Co-crystals

In this section, non-covalent interactions including hydrogen bonding, halogen bonding and π-π interactions with DNP co-crystals are investigated and compared with the parent energetic compounds. The packing motifs of the novel structures are described in detail. The effects of co-crystallisation on their crystal structures and networks of non-covalent interaction will be described and discussed.

The unit cell and associated interactions of 1,3-DNP are shown in Figure 5.6. C-H···O intermolecular interactions were observed in 1,3-DNP and are illustrated in Figure 5.8. While the molecule does not have any H-bond interactions, the ribbons of molecules are linked by C-H···O interactions. Figure 5.9 illustrates the herring bone packing motif of 1,3-DNP.

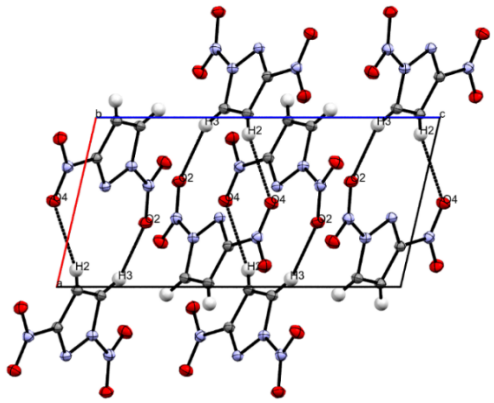

Figure 5.8 The structure of 1,3-DNP as viewed along the *b*-axis showing C-H···O interactions

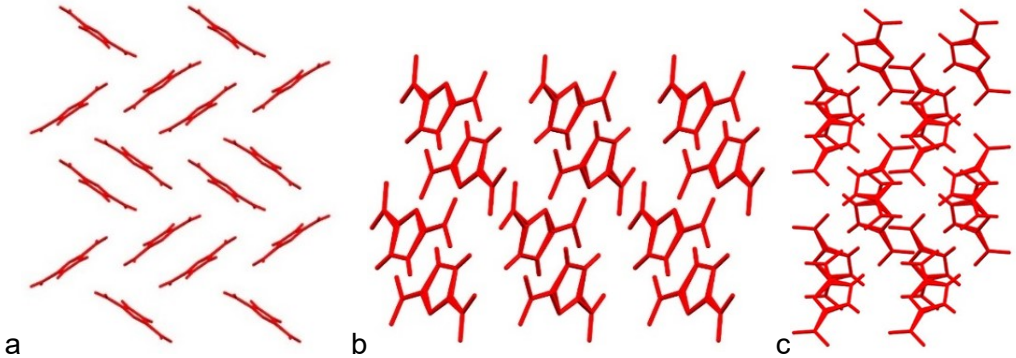

Figure 5.9 Packing motif of 1,3-DNP viewed along *a*-axis (a), *b*-axis (b), and *c*-axis (c)

Figure 5.10 illustrates the intermolecular interactions in 3,5-DNP. Detailed information about non-covalent bonds in 3,5-DNP and its co-crystals is given in Table 5.4. As can

be seen in Figure 5.10, four hydrogen bonds are observed in 3,5-DNP. Two of them are classified as strong H-bonds and two of them have moderate strength. The herring-bone style crystal packing motif of 3,5-DNP is shown in Figure 5.11.

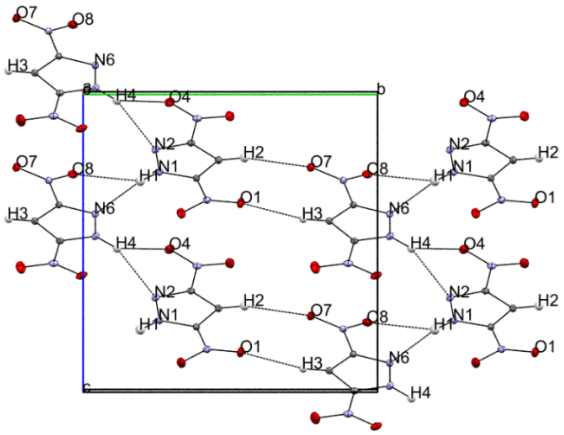

Figure 5.10 H-bonding and C-H···O interactions of 3,5-DNP viewed along *a*-axis within the unit cell (CCDC)

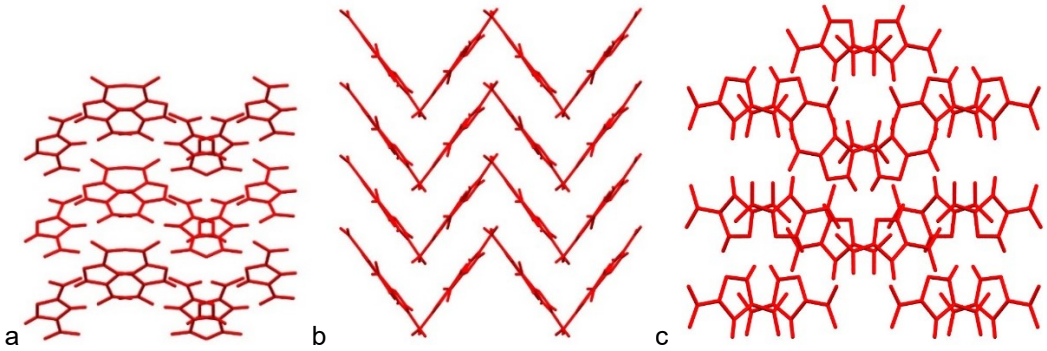

Figure 5.11 Structural packing arrangement of 3,5-DNP viewed along *a*-axis (a), *b*-axis (b), and *c*-axis (c).

Co-crystal of 1,3-DNP

On co-crystallisation of 1,3-DNP with AmClPyr, two hydrogen bonds and a halogen bond were formed, see Figure 5.12(b). Table 5.2 below gives more information about these non-covalent interactions in both 1,3-DNP and its co-crystal with AmClPyr. The number of C-H···O interactions decreased compared to 1,3-DNP due to the presence of AmClPyr molecules that block some. New amino-nitro interactions formed which are stronger compared to C-H···O. In addition, new hydrogen (N-H···N) and halogen (C-Cl···O3) bonds are formed in the novel co-crystal. These halogen and H-bonds are the main interactions in 1,3-DNP.AmClPyr.

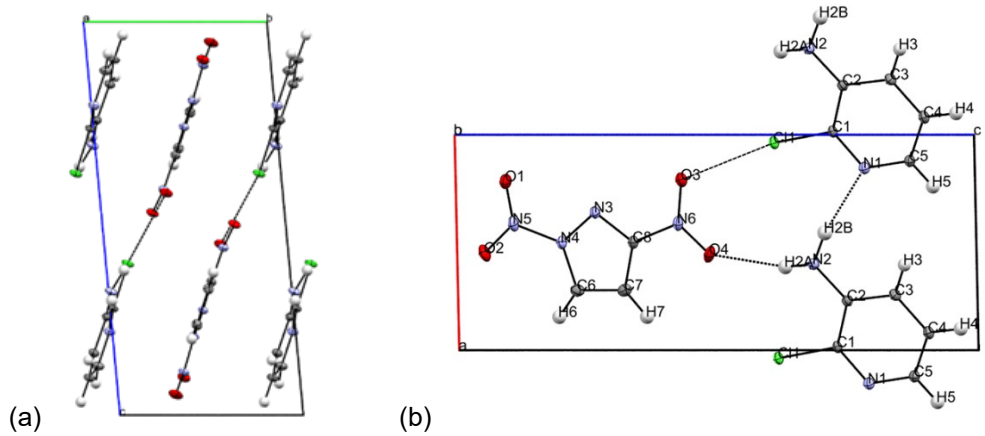

Figure 5.12 Unit cell of 1,3-DNP.AmClPyr including hydrogen and halogen bond interactions as viewed along *a*-axis (a) and *b*-axis (b)

AmClPyr is a heterocyclic compound containing two nitrogen atoms and a chlorine atom. The amino group attached to pyridine acts as a hydrogen-bond donor the nitrogen atom in the pyridine ring to form a hydrogen bond with moderate strength. Another hydrogen bond is formed between the amino and nitro groups attached to pyridine and pyrazole rings. This can be classified as a weak hydrogen bond. In addition, a halogen bond is observed upon involving the chlorine atom and an interaction with an oxygen atom of one of the nitro groups of 1,3-DNP. The crystal structure of 1,3-DNP.AmClPyr has changed drastically compared to the parent compound and adopts a parallel layered structure as shown in Figure 5.13. There is no π-π stacking observed within the co-crystal.

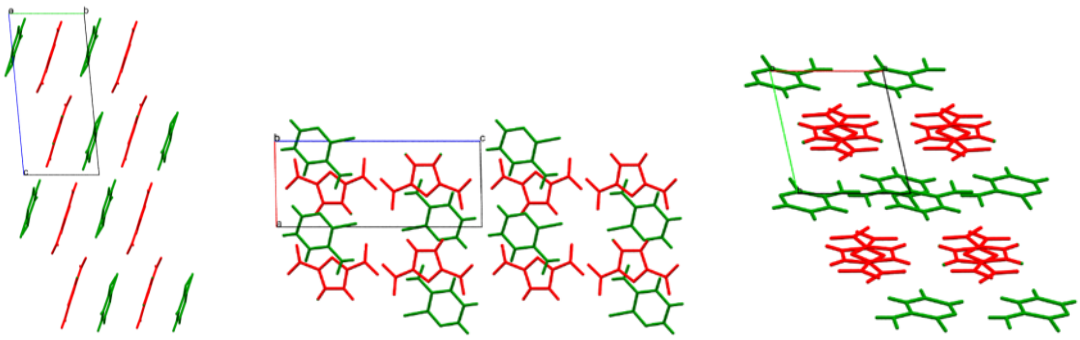

Figure 5.13 Structural packing arrangement in 1,3-DNP.AmClPyr viewed along *a*-axis (a), *b*-axis (b) and *c*-axis (c)

Table 5.2 Hydrogen and halogen bond details of 1,3-DNP and its co-crystal

Co-crystal	**D-H···A** (H-bond) **D-X···A** (Halogen bond)	**D-H [Å]** **D-X [Å]**	**H···A[Å]** **X···A [Å]**	**D···A [Å]** **D···A [Å]**	**D-H···A [°]** **D-X···A [°]**
1,3-DNP	C1-H1···O1 C2-H2···O3	0.93(2) 0.90(2)	2.36(2) 2.43(2)	2.36(2) 3.279(1)	164(1) 158(1)
1,3-DNP. AmClPyr	C6-H6···O1 N2-H2B···N1 N2-H2A···O4 C1-Cl1···O3	0.950(1) 0.93(3) 0.92(3) 1.737(2)	2.682(2) 2.13(3) 2.31(3) 3.181(1)	3.628(2) 3.044(2) 3.205(2) 4.880(2)	174.4(1) 168(2) 165(2) 165.1(2)

Co-crystals of 3,5-DNP

The unit cell of 3,5-DNP.AmClPyr and intermolecular interactions in the structure are illustrated in Figure 5.14 and details are given in Table 5.3. The chlorine atom interestingly blocks some of the possible hydrogen bond donor-acceptor interactions and so reduces the extent of hydrogen bonding. Whereas no π-π stacking is present in 3,5-DNP, two different π-π stacking arrangements occur between neighbouring 3,5-DNP molecules and between neighbouring AmClPyr molecules. These two π-π stacking arrangements are located in intersecting layers, as shown in Figure 5.14(b).

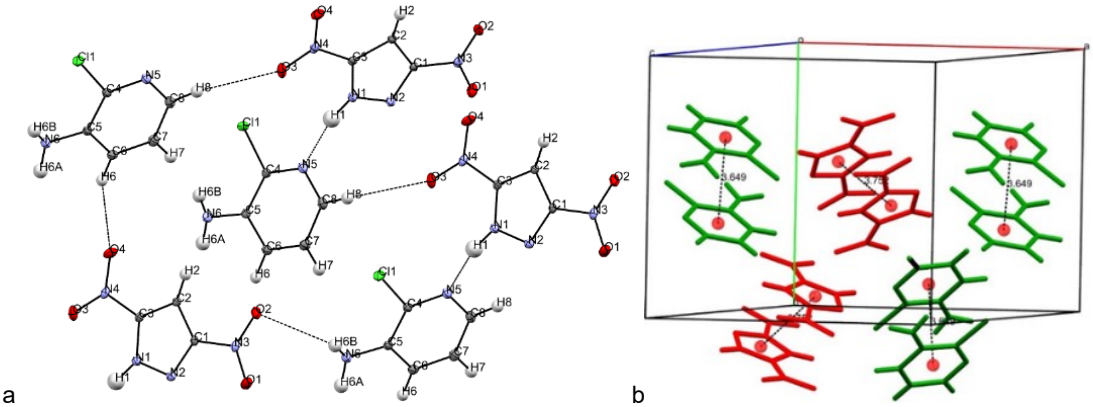

Figure 5.14 H-bond and CH···O interactions (a) and π-π interactions (b) of 3,5-DNP.AmClPyr (3,5-DNP is shown in red, AmClPyr is in green. Red dots represent centroids of molecules. Dashed lines represent non-covalent interactions.)

3,5-DNP adopts a herring-bone style motif with extensive H-bonding (Figure 5.11). However, in 3,5-DNP.AmClPyr the extent of overall hydrogen bonding is reduced and only two H-bond interactions are observed. The N-H···O interactions that are observed in 3,5-DNP are not present in the co-crystal due to AmClPyr molecules surrounding 3,5-DNP and therefore blocking these interactions. AmClPyr molecules and 3,5-DNP molecules are separated into two layers in the crystal packing (Figure 5.15(b-c)).

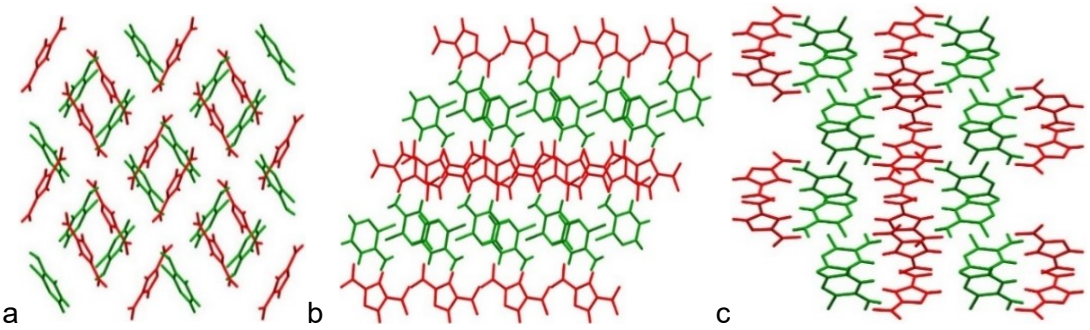

Figure 5.15 Structural packing arrangement of 3,5-DNP.AmClPyr viewed along the *a*-axis (a), *b*-axis (b) and *c*-axis (c)

Figure 5.16 shows the associated intermolecular interactions in 3,5-DNP.BrPyr. Details of these interactions are provided in Table 5.3. Instead of the extensive hydrogen bonding network formed in 3,5-DNP, there is only one hydrogen bond formed in 3,5-DNP.BrPyr between the acidic proton on the 3,5-DNP molecule and the nitrogen atom of AmClPyr. The reason for disruption of some hydrogen bonds is the existence of bulky halogen atoms blocking potential H-bonding interactions. A halogen bond is formed in the co-crystal between C5-Br1···O4. The C5-Br1···O4 halogen bond (3.066 Å) is shorter and therefore stronger than the halogen bond formed in 1,3-DNP.AmClPyr (C1-Cl1···O3, Figure 5.9) due to the higher polarisability of bromine. No π-π interaction are observed in this structure.

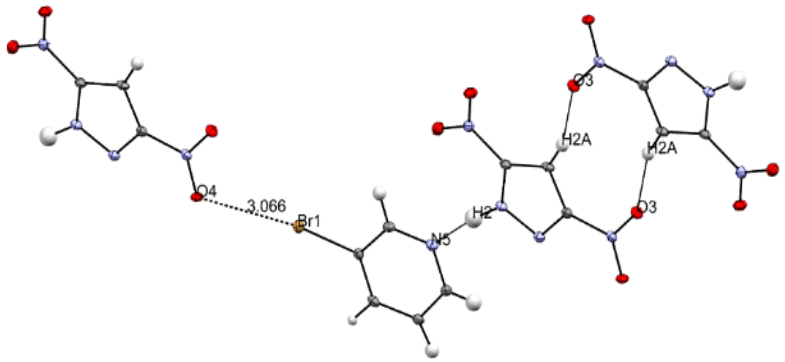

Figure 5.16 H-bonding and halogen bonding in the structure of 3,5-DNP.BrPyr (Dashed lines illustrates intermolecular interactions.)

The combination of these non-covalent interactions results in a packing motif of parallel layers which is shown in Figure 5.17 (c).

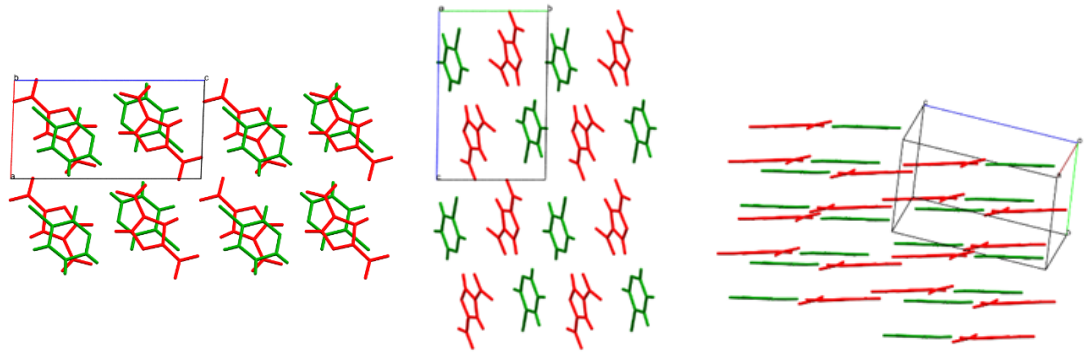

(a) (b) (c)

Figure 5.17 Structural packing arrangement of 3,5-DNP.BrPyr viewed along *a*-axis (a), *b*-axis (b) and (c) from a different angle showing parallel layers

Table 5.3 Intermolecular interaction details of 3,5-DNP and its co-crystals

Co-crystal/ Parent component	**D-H···A** (H-bond)/ **D-X···A** (Halogen bond)	**D-H [Å]/ D-X [Å]**	**H···A[Å]/ X···A [Å]**	**D···A [Å] / D···A [Å]**	**D-H···A [°]/ D-X···A [°]**
3,5-DNP	N1-H1···N6	0.85(3)	2.26(3)	3.103(3)	170(3)
	N1-H1···O8	0.85(3)	2.58(3)	3.112(3)	122(3)
	N5-H4···N2	0.92(3)	2.21(3)	3.029(3)	148(2)
	N5-H4···O4	0.92(3)	2.60(3)	3.400(3)	146(2)
3,5-DNP. AmClPyr	C6-H6···O4	0.91(2)	2.57(2)	3.413(2)	153(2)
	C8-H8···O3	0.90(2)	2.69(2)	3.555(2)	162(2)
	N6-H6B···O2	0.84(2)	2.61(2)	3.176(2)	125(2)
	N1-H1···N5	0.93(2)	1.75(2)	2.665(2)	166(2)
	C8-H8···O3	0.90(2)	2.69(2)	3.555(2)	162(2)
3,5-DNP. BrPyr	N2-H2···N5	1.00(6)	1.70(6)	2.694(5)	171(5)
	C5-Br1···O4	1.885(4)	3.066(3)	4.939(5)	172(1)
	C2-H2A···O3	0.93(5)	2.40(5)	3.297(5)	162(4)

In summary, for all the co-crystals of 1,3-DNP and 3,5-DNP, the acidic hydrogen atom of the pyrazole ring acts as an efficient hydrogen bond donor to the N-atom of the substituted pyridine molecules. Other notable H-bond interactions were observed between N-H groups on pyridine rings and adjacent nitro groups of pyrazole molecules. Among the three halogen containing co-crystals, only 3,5-DNP.AmClPyr compound did not exhibit a halogen bond. Chlorine and bromine both interact with oxygen to form halogen bonds in 3,5-DNP.AmClPyr and 1,3-DNP.BrPyr. This study therefore provides further examples of halogen bonding in multicomponent energetic materials. This supports the idea that halogen bonding is a useful tool to construct multicomponent energetic materials. Moreover, having chlorinated and brominated

compounds, the comparison of halogen bonds formed with different halogens can be evaluated. Finally, the π-π stacking interactions observed in 3,5-DNP.AmClPyr provide an opportunity to observe how π-π stacking affects important properties such as impact sensitivity (IS) for energetic co-crystals.

5.3.2.2 Powder X-ray Diffraction Studies

Larger amounts of 3,5-DNP co-crystals and salts (~1 g) were produced for further tests including thermal stability and impact sensitivity tests. The phase purities of these salts and co-crystals were checked using powder X-ray diffraction. The simulated (from SXRD data) and observed powder X-ray diffraction (PXRD) patterns of 1,3-DNP.AmClPyr, 3,5-DNP.AmClPyr and 3,5-DNP.BrPyr are shown in Figures 5.18 and 5.19. These comparisons show that the patterns are broadly consistent although there are some differences in peak positions and intensities. Simulated patterns were generated from SXRD data recorded at 120 K and observed patterns were collected at room temperature (298 K). This temperature difference causes small shifts between the two patterns since the unit-cell parameters are different. Peaks for the powder shifted to higher d-spacing and hence low 2θ value. The differences in intensities can be explained by the intrinsic preferred orientation of the samples, which is exacerbated by the flat-plate geometry of the sample holder used for PXRD measurement. Overall, these comparisons show that the bulk samples are representative of the single crystal and hence can be used for further analysis *e.g.* differential scanning calorimetry and impact sensitivity testing.

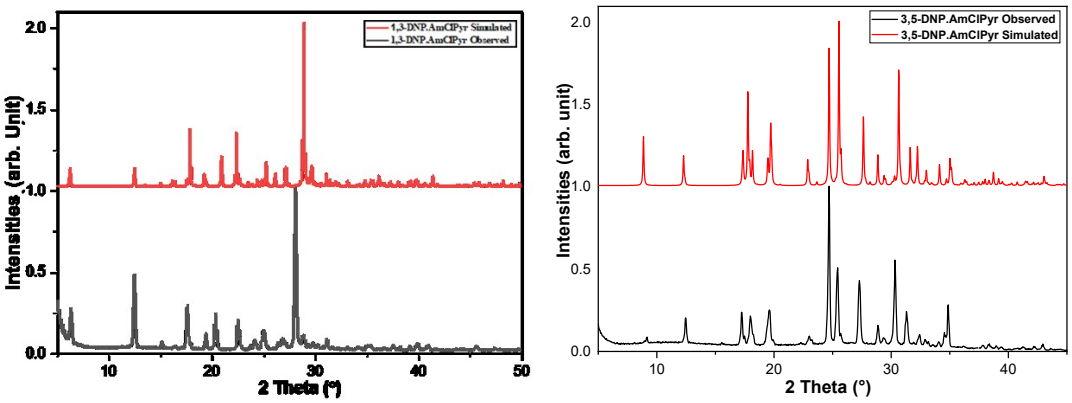

Figure 5.18 Powder X-ray diffraction patterns of 1,3-DNP.AmClPyr and 3,5-DNP.AmClPyr

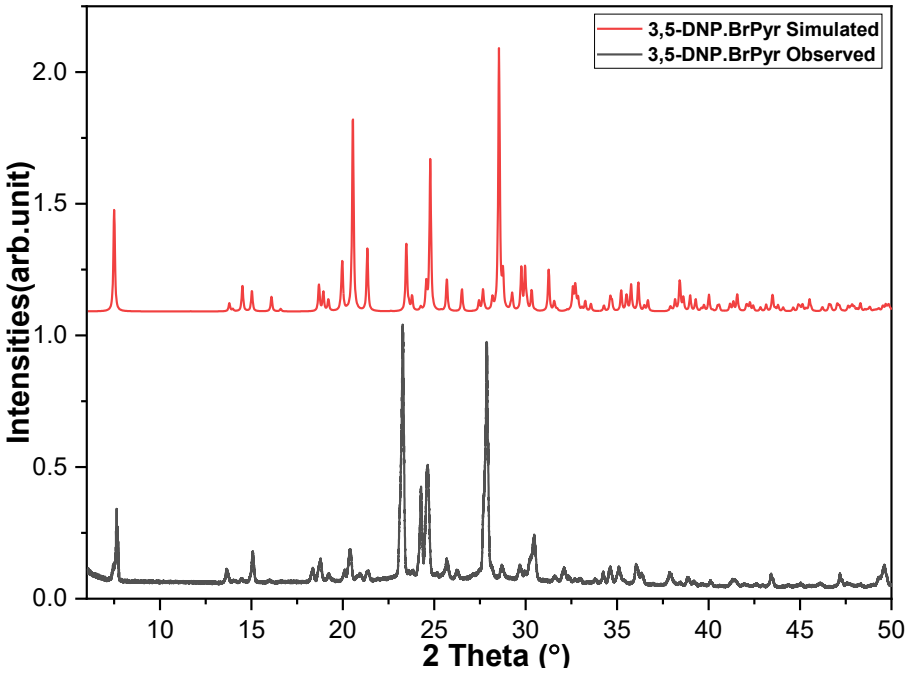

Figure 5.19 Powder X-ray diffraction patterns of 3,5-DNP.BrPyr

5.3.2.3 Thermal Properties of DNP Co-crystals

In this section, the co-crystals formed with dinitropyrazoles were investigated in terms of their thermal properties. Melting and decomposition temperatures (T_m and T_d) are two significant properties that can be manipulated using co-crystallisation.

DSC and TGA thermal traces for 1,3-DNP and 1,3-DNP.AmClPyr are shown in Figure 5.18. Melting of 1,3-DNP.AmClPyr began at 72°C and an exothermic decomposition began at 189°C. Co-crystallisation of 1,3-DNP with AmClPyr therefore slightly increased both the melting and decomposition temperatures compared to 1,3-DNP. 1,3-DNP.AmClPyr exhibited a higher T_d value than 1,3-DNP, thereby suggesting that the thermal stability of 1,3-DNP has been slightly enhanced through co-crystallisation. The observed temperature difference between melting and decomposition points would, in principle, allow this co-crystal to be classed as a melt-castable energetic material. It is also noted that 1,3-DNP does not fully decompose at 210°C: it loses 70% of its mass until 210°C. Afterwards, a gradual loss of mass occurs suggesting that decomposition continues until 350°C. In contrast, decomposition of 1,3-DNP.AmClPyr occurs over a narrow temperature range (190-230°C): it loses 92% of its mass in this temperature range, see Figure 5.20 (b) (The red line represents TG curve).

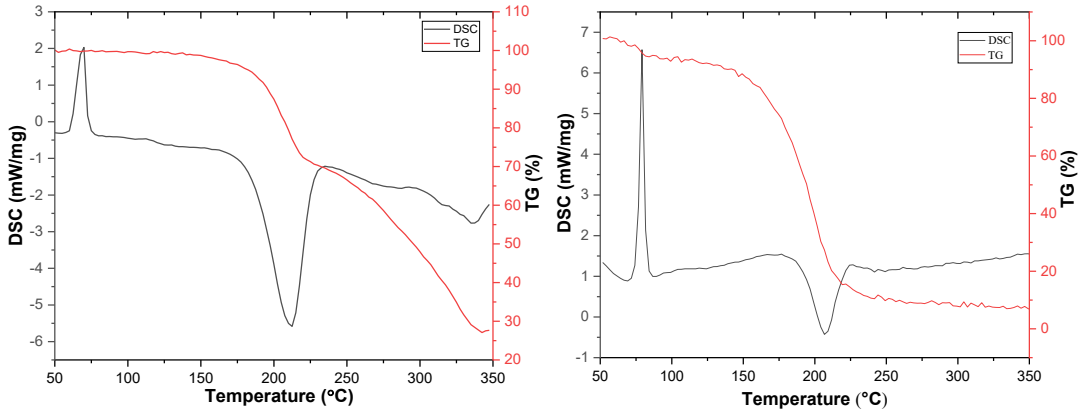

Figure 5.20 DSC-TGA traces for 1,3-DNP (a) and 1,3-DNP.AmClPyr (b) (exothermic direction down).

Figure 5.21 illustrates the DSC and TGA traces for 3,5-DNP.AmClPyr. The onset of melting began at 108.9°C, with the onset of an exothermic decomposition at 259°C. The endothermic peak along with mass loss before decomposition may represent the evaporation of the co-crystal. The co-crystal therefore shows a lower melting and higher decomposition points compared to the parent energetic compound (3,5-DNP). This decrease in melting point compared to 3,5-DNP could be considered as an advantage to enhance processability and could be associated with the reduction in the extent of hydrogen bonding in the co-crystal.

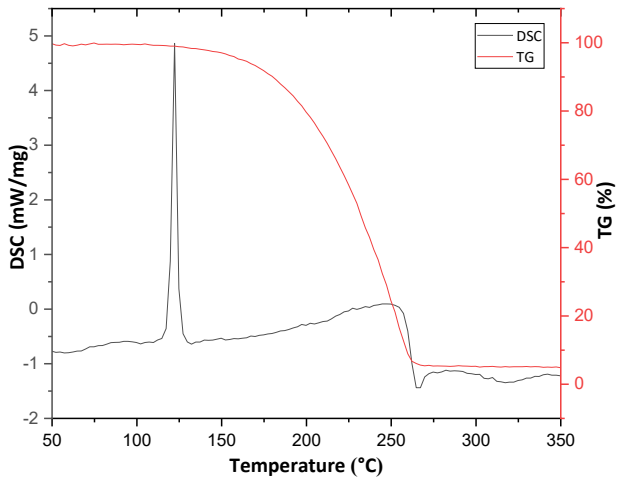

Figure 5.21 DSC-TGA traces for the 3,5-DNP.AmClPyr co-crystal (exothermic direction down).

The onset of melting of 3,5-DNP.BrPyr began at 84°C, see Figure 5.22. The loss of mass from 105°C to 270°C represents evaporation of 3,5-DNP.BrPyr. The exothermic

event at ~270°C corresponds to decomposition. Whilst the decomposition temperature did not change, the melting point has decreased significantly from 163°C to 84°C after co-crystallisation. This could be associated with a reduction in the extent of H-bonding. Although the thermal stability of the compound has not changed, processability has in principle been improved through co-crystallisation. While 3,5-DNP is not categorised as melt-castable energetic material since it has a quite high melting temperature (163ºC), the novel structure has become a melt-castable energetic compound with a large gap between melting and decomposition temperatures. However, it is clear that evaporation of one or both of the components is occurring above the melting point.

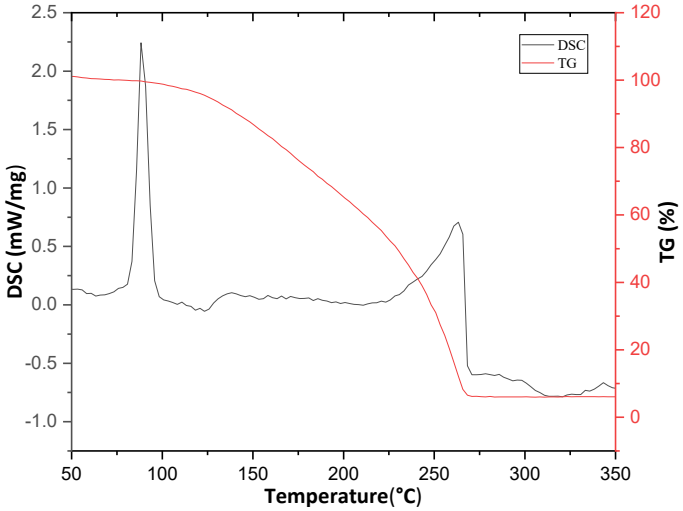

Figure 5.22 DSC-TGA traces for 3,5-DNP.BrPyr co-crystal (exothermic direction down).

Table 5.4 summarises the melting and decomposition points of these materials together with the enthalpies of decomposition and melting. Co-crystals formed with 3,5-DNP exhibited much lower melting points than 3,5-DNP. On the other hand, decomposition temperatures of 3,5-DNP co-crystals were increased. Therefore, the temperature gap between melting and decomposition was increased which, in principle could provide superior/desirable melt-casting characteristics for these compounds. While co-crystallisation has a noticeable positive effects on 3,5-DNP co-crystals, subtle changes were observed on thermal properties of 1,3-DNP co-crystal. All DNP co-crystals exhibited higher decomposition temperatures than the parent energetic compounds implying that thermal stabilities were increased upon co-crystallisation with halogenated pyridines.

Crystal structures and intermolecular interactions are the most significant factors affecting melting points of materials.[21] Therefore, some correlations were explored between H-bonding and melting points of the multicomponent structures formed with nitropyrazoles. The melting point of 1,3-DNP.AmClPyr is found to be lower than 3,5-DNP.AmClPyr. The reason for this could be N-substituted nitro group disrupting some H-bonds. 3,5-DNP has a higher melting point than 1,3-DNP. This can also be explained by the presence of the N-substituted nitro group in 1,3-DNP disrupting some H-bonding that exists in 3,5-DNP. The heat required for melting of an energetic material might be of interest for the applications that involve melt-casting processes. Therefore, melting enthalpies of DNP salts are given in Table 5.4. While 3,5-DNP co-crystals exhibit lower melting enthalpies than 3,5-DNP, 1,3-DNP.AmClPyr possesses higher melting enthalpy than the parent energetic compound.

Table 5.4 Melting and decomposition onset temperature values of DNPs and DNP co-crystals along with enthalpy values

Compound	**Melting onset temperature (°C)**	**Melting enthalpy**		**Decomposition onset temperature (°C) (10K/min)**	**Decomposition enthalpy**	
		J/g	**kJ/mol**		**J/g**	**kJ/mol**
1,3DNP. AmClPyr	72	125	36	189	-197	-56
3,5-DNP. AmClPyr	109	132	38	259	- (*)	
3,5-DNP. BrPyr	84	101	32	270	- (*)	
3,5-DNP	163	141	22	251	- (*)	
1,3-DNP	66	108	17	185	-668	-105

*Due their complicated decomposition patterns, some decomposition enthalpy values could not be derived.

5.3.2.4 Calculated Energetic Performance and Experimental Impact Sensitivity of DNP Co-crystals

Detonation performance parameters were calculated using EXPLO-5 [13] and are listed in Table 5.5, alongside computed solid-state heats of formation (See section 5.2.7 for more details). In addition, impact sensitivities (IS) of some of the compounds were tested using a BAM Fall Hammer, as described in the experimental section. The compositions of the detonation products were also determined using EXPLO-5 and

are given in Table 5.5. Detonation pressure and velocity are key parameters that reflect the energetic performance of energetic materials. As can be seen from Table 5.6, the co-crystals all exhibited lower energetic performances compared to their parent energetic compounds, which was expected since they have effectively been diluted by the presence of the non-energetic component. It should be noted that the literature often states that the energetic performance parameters are closely related to the crystal densities of energetic materials.[22] However, this correlation is not observed for halogen-containing crystal structures, in which the high crystal densities are directly attributable to the heavy, non-energetic halogen atoms. All the DNP co-crystals exhibited similar energetic performances. Oxygen balance is another critical property to monitor in energetic materials. A balance close to zero means that the EM has enough oxygen for complete combustion.[23] A negative value indicates that extra oxygen is needed for complete combustion. Table 5.5 shows that, as expected, co-crystal formation negatively impacted this metric for the DNP co-crystals, indicating that an additional oxidiser would be required for complete combustion.

Table 5.5 Energetic properties of DNPs and DNP co-crystals

	1,3-DNP	**1,3-DNP. AmClPyr**	**3,5-DNP***	**3,5-DNP. AmClPyr***	**3,5-DNP. BrPyr***
Heat of formation (kJ/mol)	189.1	200.67*	136.1*	273.7*	320.6*
Heat of detonation (kJ/kg)	-5676	-3379.39	-5438.6	-3695.72	-2829.87
Detonation temperature(K)	4156	2770.6	3945.35	2886.28	2764.18
Detonation pressure (GPa)	30.3	16.0	31.5	16.5	16.0
Detonation velocity (m/s)	8359	6451	8469	6590	5787
Volume of gas at STP (dm^3/kg)	720	638	702	657	551
Oxygen balance (%)	-30.4	-81.2	-30.4	-83.7	-78.5
Crystal density ($g.cm^{-3}$)	1.76	1.678	1.820	1.649	1.928
Packing coefficient	0.760	0.735	0.744	0.718	0.730
Impact sensitivity (J)	25	5	25	28	25

*****These detonation parameters were predicted by using the values calculated with computational techniques described in section 4.2.7. When the other detonation parameters were calculated, the heat of formation of the co-formers were obtained from the literature.

The volume of gas released upon detonation can be related to the energy released by the energetic compound. The predicted volume of the gas products of DNP co-crystals are given in Table 5.5. The volume of the gas products released by 1,3-DNP.AmClPyr and 3,5-DNP.AmClPyr are (637.61 and 657.267 dm^3/kg) slightly higher than TNT (740 dm^3/kg). 3,5-DNP.BrPyr released the lowest volume of gas among the DNP co-crystals. Predicted decomposition products of DNP co-crystals are given in Table 5.6. Halogen-containing detonation products are highlighted since they are important in terms of biocidal applications and environmental effects.

Table 5.6 Predicted composition of main detonation products of DNP co-crystals

Composition (3,5-DNP. BrPyr)	**Mol (%)**	**Composition (1,3-DNP. AmClPyr)**	**Mol (%)**	**Composition (3,5-DNP. AmClPyr)**	**Mol (%)**
C(s,d)	50.6	**C(gr)**	32.5	**C(s,d)**	30.3
N_2	17.7	**N_2**	23.7	**N_2**	23.0
H_2O	16.7	**C(d)**	14.2	**C**	16.3
Br	5.2	**H_2O**	13.7	**H_2O**	15.7
CO_2	4.3	**HCl**	6.9	**HCl**	6.7
BrH	1.9	**CO_2**	4.7	**CO_2**	3.7
CH_2O_2	1.5	**CO**	1.6	**CO**	1.2
NH_3	0.7	**CH_2O_2**	1.3	**CH_2O_2**	1.2
CO	0.6	**NH_3**	0.6	**NH_3**	0.8
CH_4	0.53	**CH_4**	0.4	**CH_4**	0.6
H_2	0.21	**H_2**	0.3	**H_2**	0.4
C_2H_6	0.056	**C_2H_6**	0.035	**C2H6**	0.07
Br_2	0.052	**HCN**	0.008	**HCN**	0.006
C_2H_4	0.002	**C_2H_4**	0.004	**C_2H_4**	0.005
HCN	0.001	**CH_3OH**	0.0008	**CH_3OH**	0.001
CH_3OH	0.0005	**Cl**	0.0002	**Cl**	0.0001

(Halogenated compounds are highlighted with the red. *C(gr): graphite C(d): diamond, s: solid)

BAM Fall hammer impact-sensitivity (IS) tests for 1,3-DNP.AmClPyr, 3,5-DNP.AmClPyr and 3,5-DNP.BrPyr gave IS values of 5, 28 and 25 J, respectively. The IS of the parent energetic compounds, 1,3-DNP and 3,5-DNP have been reported as 25 J in the literature by using the same method and instrument. [24] The IS can depend on intermolecular interactions and crystal packing motifs of energetic materials, and some correlations between structures and impact sensitivities were explored.

1,3-DNP and 3,5-DNP both exhibit the herring-bone type of crystal packing whereas 1,3-DNP.AmClPyr and 3,5-DNP.BrPyr adopt parallel-layered packing motifs after co-crystallisation (see Figure 5.13 and 5.17). 1,3-DNP.AmClPyr was found to be significantly more sensitive than 1,3-DNP. The other two co-crystals exhibit almost the same impact sensitivities as the parent energetic compound (3,5-DNP). Parallel-layered energetic materials are often observed to display low impact sensitivities, on the basis that they are able to distribute the shock/impact energy within layers. [25] Clearly, this simplistic approach does not apply here – the layered structure of 1,3-DNP.AmClPyr is more sensitive. Other structural factors must therefore play an important role, and the vibrational up-pumping model developed by Michalchuck and Morrison might shed more light on why 1,3-DNP.AmClPyr is more sensitive. [26]

3,5-DNP.AmClPyr shows two different π-π stacking arrangements (Figure 5.14). π-stacking geometry involving conjugated systems often favours low mechanical sensitivities.[27,28] It has been postulated that these structure types act to dissipate the mechanical energy introduced from shock initiation through delocalised phonon vibrations, thus mitigating against the formation of energy hot-spots in the material which lead to explosive decomposition. [29] It was confirmed with BAM Fall Hammer tests that the IS of 3,5-DNP is enhanced through co-crystallisation. Whereas 3,5-DNP itself has an impact sensitivity of 25 J, 3,5-DNP.AmClPyr was found to be marginally less sensitive to impact (28 J). Overall, it is observed that impact sensitivities of dinitropyrazoles could be increased, decreased or retained same after co-crystallisation with non-energetic compounds.

5.3.3 Salts Formed with 3,4,5-TNP

A selection of halogenated pyridines all formed salts with 3,4,5-TNP to give 3,4,5-TNP.FPyr, 3,4,5-TNP.BrPyr and 3,4,5-TNP.IPyr. ClPyr was not used as a co-former on account of its high toxicity. Proton transfer from 3,4,5-TNP to the pyridine ring was observed for all the structures. This can be explained on the basis of the pK_a discussed in Chapter 1 (ΔpK_a values are given in Table 5.7). The co-formers which formed salts with 3,4,5-TNP are FPyr, BrPyr, IPyr, given in Figure 5.23. Although it does not contain a halogen atom, the salt formed between 3,4,5-TNP and Pyr will also be presented in this section.

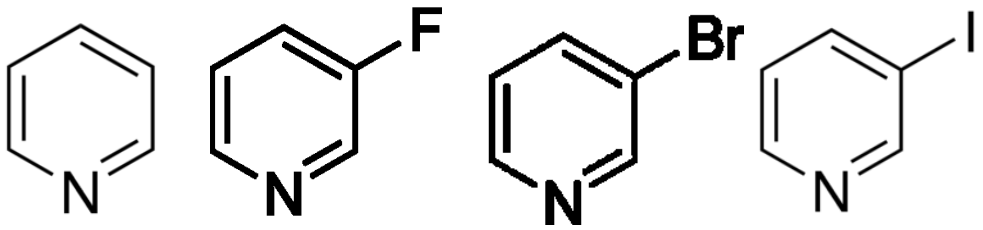

Figure 5.23 Molecular structures of non-energetic co-formers of 3,4,5-TNP salts (Pyr, FPyr, BrPyr, and IPyr, respectively)

Table 5.7 ΔpK_a values for 3,4,5-TNP salts

Salt	ΔpK_a
3,4,5-TNP.Pyr	2.88
3,4,5-TNP.FPyr	0.62
3,4,5-TNP.BrPyr	0.49
3,4,5-TNP.IPyr	0.9

Electron-density distribution maps of the co-crystals were calculated using TmoleX 4.3.2. are given in Figure 5.24. These density maps provide more information to highlight possible intermolecular interaction synthons and identify suitable co-formers.

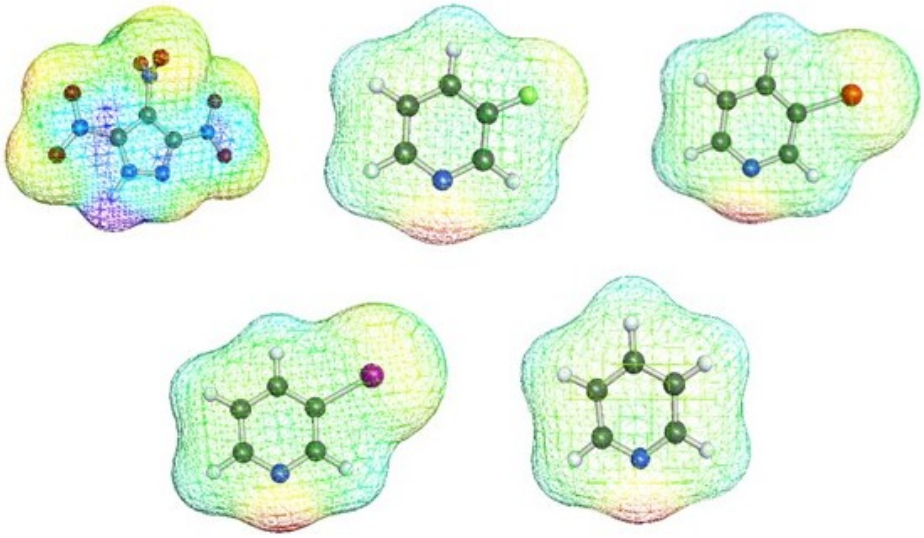

Figure 5.24 Electron density distribution maps of 3,4,5-TNP, FPyr, BrPyr, IPyr and Pyr (The red represents the highest electron density area. The blue/violet represents the lowest e-density area.)

Crystallographic information for the structures of 3,4,5-TNP and its salts are shown in Table 5.8. Figure 5.25 shows the asymmetric units of 3,4,5-TNP and its salts.

Table 5.8 Crystallographic information of the halogenated salts of 3,4,5-TNP

Compound	**3,4,5-TNP**	**3,4,5-TNP.Pyr**	**3,4,5-TNP.FPyr**	**3,4,5-TNP.BrPyr**	**3,4,5-TNP.IPyr**
Formula	$C_3HN_5O_6$	$C_8H_6N_6O_6$	$C_8H_5FN_6O_6$	$C_8H_5BrN_6O_6$	$C_8H_5N_6O_6I$
MW (g.mol^{-1})	203.7	282.19	300.18	361.09	408.08
Crystal system	Monoclinic	Triclinic	Monoclinic	Monoclinic	Triclinic
Space group	$P2_1/c$	*P-1*	*P2/c*	$P2_1/c$	*P*-1
a, **b,** **c (Å)**	15.159(1) 8.2781(8) 17.201(2)	6.6659(5) 8.6913(6) 10.7801(8)	20.1888(7) 10.7216(4) 16.2984(6)	7.7594(2) 21.9256(5) 7.2640(2)	8.9608(3) 9.8046(3) 11.7694(4)
α, **β,** **γ (o)**	90 92.275(2) 90	109.439(6) 92.222(6) 98.207(6)	90 92.806(3) 90	90 103.132(1) 90	91.850(2) 106.540(3) 104.233(2)
V (Å^3)	2156.81	580.42(8)	3523.7(2)	1203.50(5)	675.15(4)
Z, Z'	12, 0	2, 1	12, 3	4, 1	2, 1
ρ (g.cm^{-3})	1.876	1.615	1.698	1.993	2.007
Packing coefficient	0.724	0.700	0.714	0.745	0.674
R factor	0.0378	0.0730	0.0782	0.0218	0.0499
θ_{min}- θ_{max}	2.79-24.19	3.538-29.62	3.293-26.382	1.858 - 28.274	3.080-29.609
Radiation	MoK_α	MoK_α	MoK_α	MoK_α	MoK_α
Wavelenfgth(Å)	0.71073	0.71073	0.71073	0.71073	0.71073

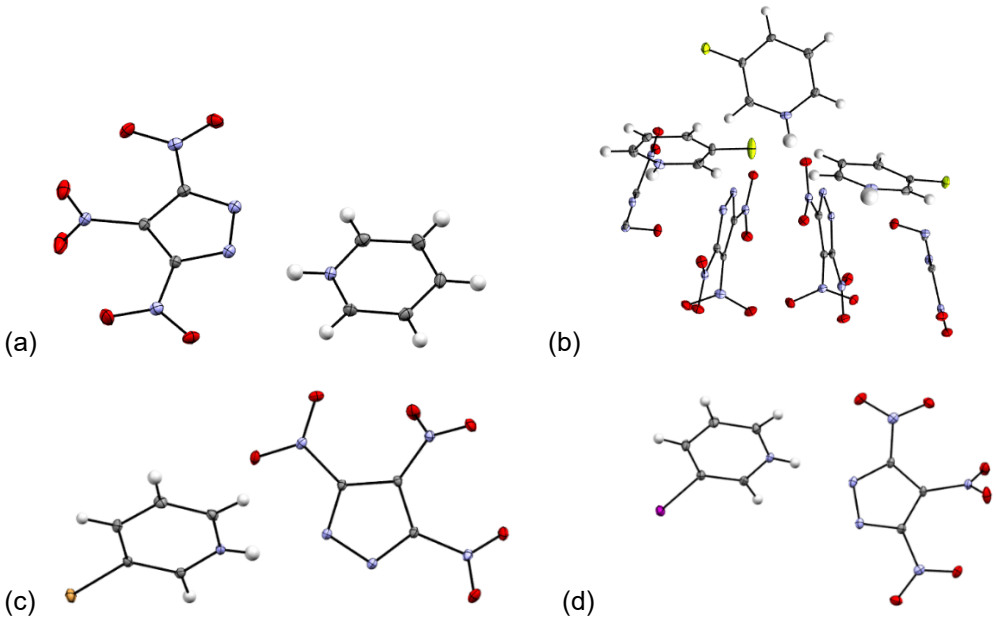

Figure 5.25 Asymmetric units of 3,4,5-TNP.Pyr (a), 3,4,5-TNP.FPyr (b), 3,4,5-TNP.BrPyr (c) and 3,4,5-TNP.IPyr (d)

5.3.3.1 Structural Features of 3,4,5-TNP and Its Salts

The unit-cell and H-bonding network of 3,4,5-TNP is illustrated in Figure 5.26. The data were extracted from the CCDC and the reference code of the structure is KAHHIM02. N-H···N and N-H···O type of hydrogen bonds are formed and shown in Figure 5.26. Table 5.10 gives detailed information about non-covalent interactions in 3,4,5-TNP salts along with 3,4,5-TNP.

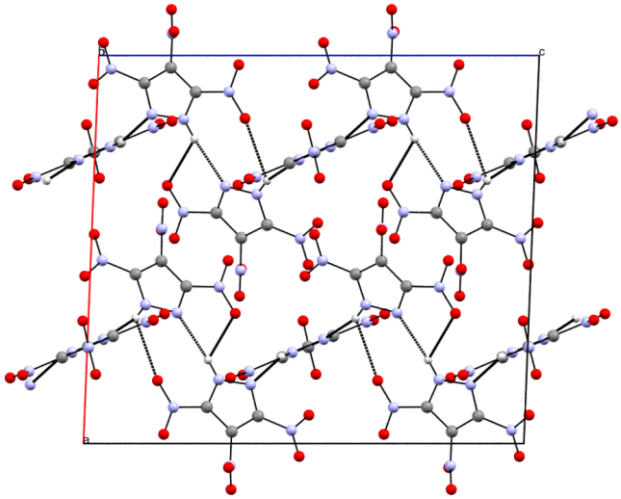

Figure 5.26 Structure of 3,4,5-TNP and hydrogen bonds within a unit cell (Dashed lines represent H bonds.)

The crystal packing motif of 3,4,5-TNP viewed along different axes is given below in Figure 5.27. It displays a T-shaped motif in which some molecules lie parallel to each other and others are intersecting as shown in Figure 5.25 along the *b*-axis.

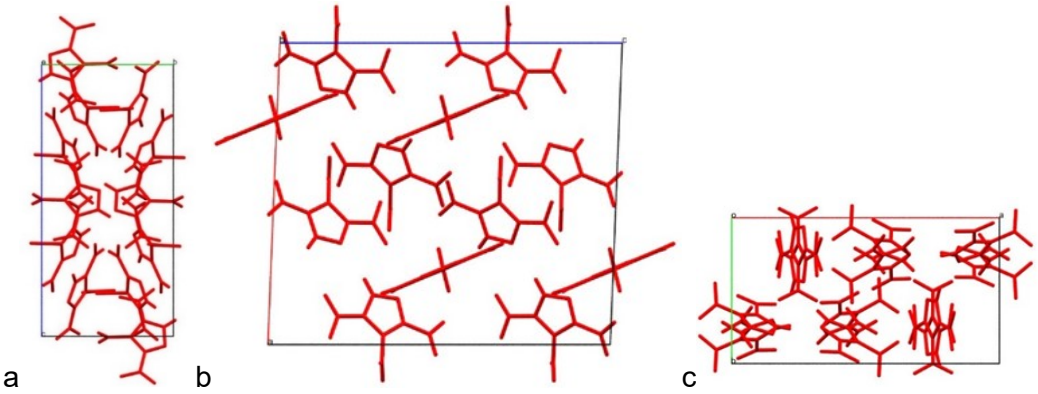

Figure 5.27 Structural packing arrangement in 3,4,5-TNP viewed along the *a*-axis(a), *b*-axis (b) and *c*-axis(c)

Figure 5.28 illustrates a unit-cell of 3,4,5-TNP.Pyr and its hydrogen bonds. Three hydrogen bonds formed in this structure: N6-H6···O6, N6-H6···N1 and N6-H6···N2. More details about these bonds are given in Table 5.10. As shown in Figure 5.28, the acidic proton on the pyrazole ring migrated to the N atom of Pyr. All of the hydrogen bonds in 3,4,5-TNP.Pyr exploited this N-H moiety as a H-bond donor and interacted with nucleophilic areas of the 3,4,5-TNP molecules.

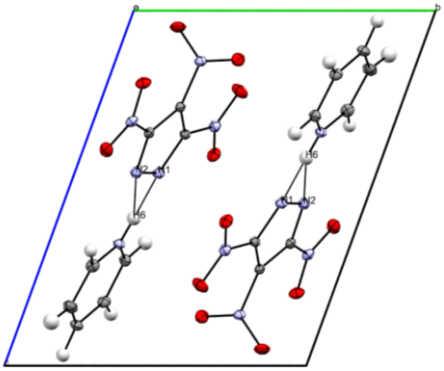

Figure 5.28 Structure of 3,4,5-TNP.Pyr and hydrogen bonds within a unit cell

Figure 5.29 shows the packing motif of 3,4,5-TNP.Pyr from different angles. Compared to 3,4,5-TNP, the novel salt exhibits a flatter pattern in which pyridine molecules lie in parallel layers to each other and 3,4,5-TNP molecules also appear on parallel layers. These two layers are intersect with a small angle (6.7°).

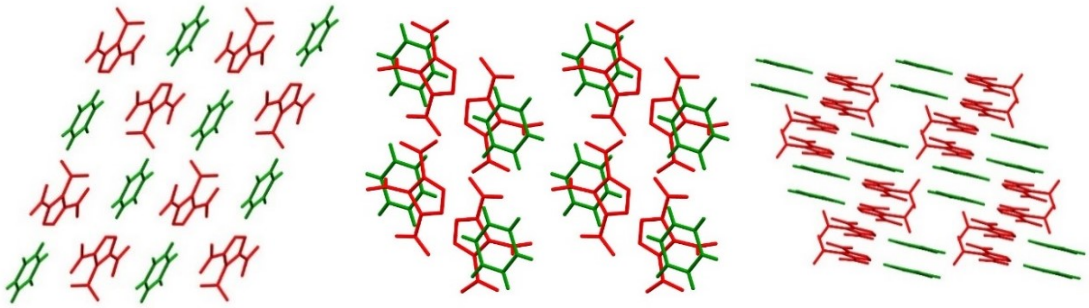

Figure 5.29 Structural packing arrangement in 3,4,5-TNP.Pyr viewed along different directions

The structure and main non-covalent interactions of 3,4,5-TNP.FPyr within a unit cell is shown in Figure 5.30. The H-atom of 3,4,5-TNP transferred to FPyr similar to other 3,4,5-TNP salts. Repeated non-covalent interactions in 3,4,5-TNP.FPyr are shown

more clearly in Figure 5.31. The salt exhibited additional H-bonds, CH···O and CF···H interactions compared to 3,4,5-TNP. More details are given in Table 5.10.

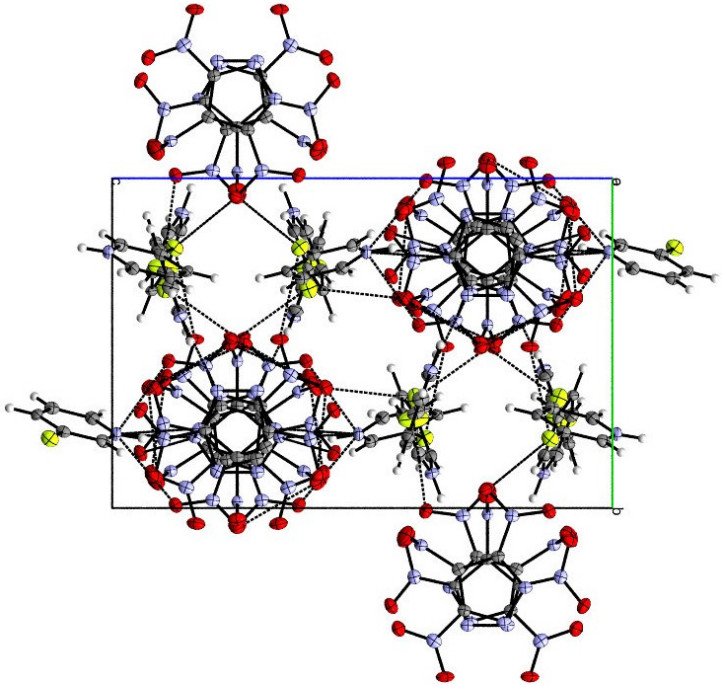

Figure 5.30 Structure of 3,4,5-TNP.FPyr

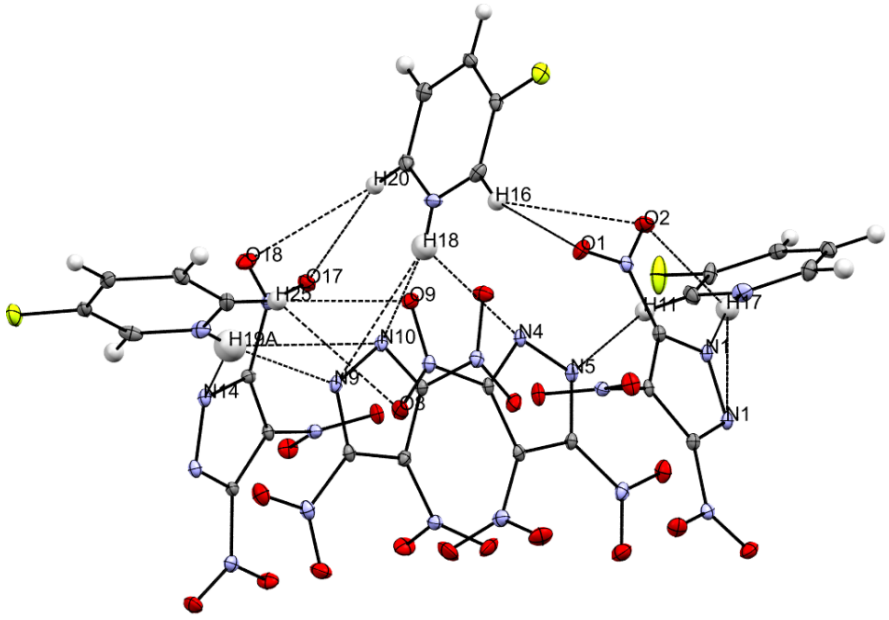

Figure 5.31 H-bonding and C-H…O interactions of 3,4,5-TNP.FPyr (Dashed lines represent non-covalent interactions. CH…F interactions are not shown to reduce the complexity of the image)

Figure 5.32 shows the packing arrangement for 3,4,5-TNP.FPyr. It exhibited a packing motif in which 3,4,5-TNP molecules formed flower-like blocks and FPyr molecules shaped as stars surrounding 3,4,5-TNP blocks. It exhibited an extraordinary symmetry comparing to other halogenated salts.

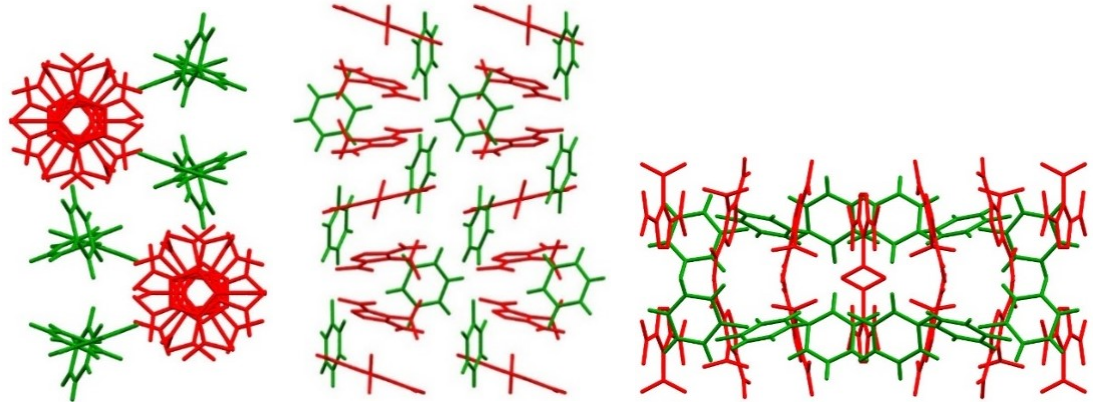

(a) (b) (c)

Figure 5.32 Structural packing arrangement in 3,4,5-TNP.FPyr viewed along *a*-axis (a), *b*-axis (b) and *c*-axis (c).

A proton transfer from 3,4,5-TNP to BrPyr was observed resulting a salt similar to other 3,4,5-TNP salts. Figure 5.33 shows halogen and hydrogen bonds of 3,4,5-TNP.BrPyr salt within the unit cell. 3,4,5-TNP.BrPyr exhibited a quite different non-covalent interaction network compared to 3,4,5-TNP (Figure 5.26). While the number of H-bonds decreased in this salt, a halogen bond was formed between the bromine on BrPyr and the oxygen of the nitro group (C7-Br1···O5).

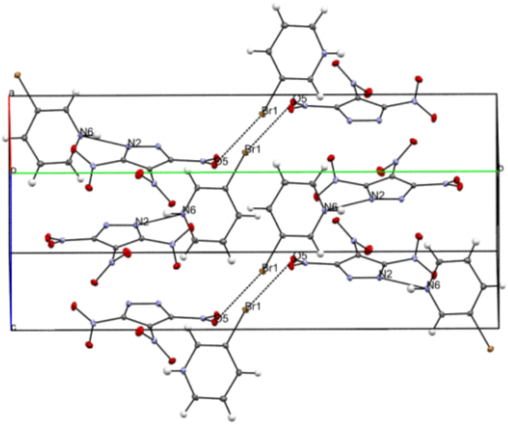

Figure 5.33 Hydrogen and halogen bonding within the unit-cell of 3,4,5-TNP.BrPyr

Figure 5.34 shows the packing arrangement of 3,4,5-TNP.BrPyr. In this motif, 3,4,5-TNP molecules lie parallel to each other, as do BrPyr molecules. However, the angle between different molecules is 69°. 3,4,5-TNP.BrPyr exhibits a wavelike crystal packing motif. In this structure 3,4,5-TNP molecules lie parallel to each other as can be seen clearly in Figure 5.34 (a).

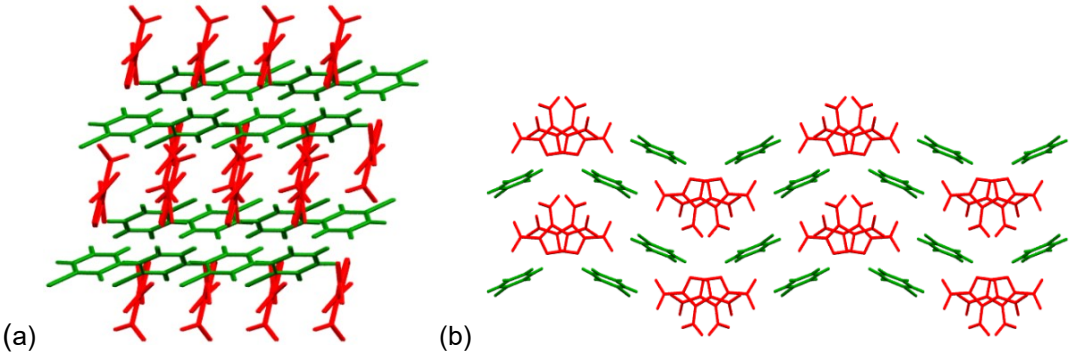

(a) (b)

Figure 5.34 Structural packing arrangement in 3,4,5-TNP.BrPyr viewed along *b*-axis (a) and *c*-axis (b)

3,4,5-TNP formed a salt with IPyr, and its unit-cell and non-covalent interactions are illustrated in Figure 5.35. Iodine is the most polarisable halogen among all the halogen atoms and so tends to favour stronger halogen interactions in structures. A halogen bond is formed here with the nitrogen atom on the pyrazole ring (C5-I1···N1) with a distance of 3.113(2) Å which is slightly stronger than C7-Br1···O5 (3.165 Å) in 3,4,5-TNP.BrPyr. In addition to these halogen and hydrogen bonds, CH···O interactions were formed in 3,4,5-TNP.IPyr which was not observed in 3,4,5-TNP. More details are given in Table 5.9.

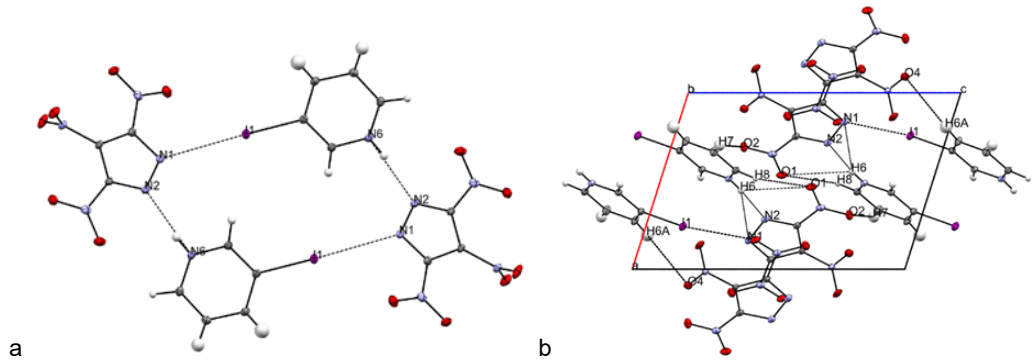

a b

Figure 5.35 (a) Hydrogen and halogen bonding in 3,4,5-TNP.IPyr and (b) shows non-covalent interactions within the unit-cell

The packing arrangement of 3,4,5-TNP.IPyr is shown in Figure 5.36. In this structure, identical molecules are located parallel to each other, whilst 3,4,5-TNP molecules adopt in the same orientation and so are IPyr molecules. However, co-formers lie on the intersecting planes with angle of 38° as illustrated in Figure 5.36(c).

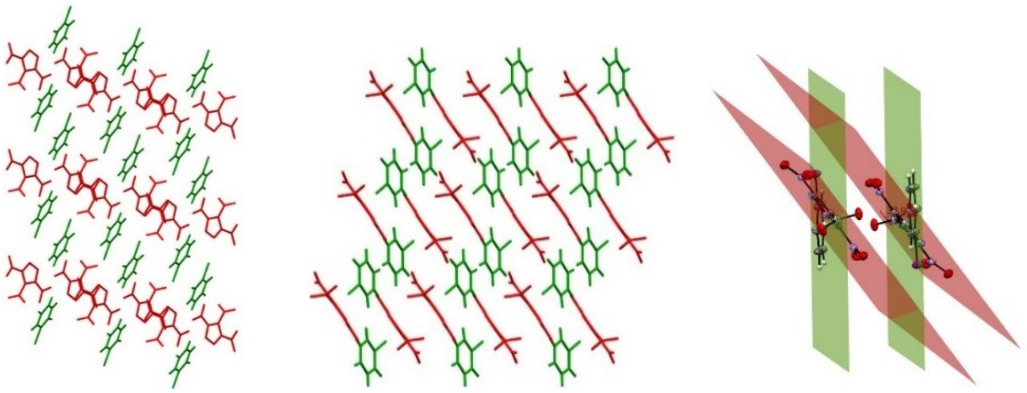

(a) (b) (c)

Figure 5.36 Packing arrangement in 3,4,5-TNP.IPyr (a) viewed along *b*-axis, (b) *c*-axis and (c) shows the calculated planes for each co-former. (Red planes indicate 3,4,5-TNP molecules and green planes indicate IPyr molecules.)

Table 5.9 Details of hydrogen and halogen bonds in 3,4,5-TNP and its salts

Salt	D-H···A	D-H [Å]	H···A[Å]	D···A [Å]	D-H···A [°]
3,4,5-TNP (CCDC, 794560)	N1-H1···N7	0.85(2)	2.25(2)	3.064(2)	163(2)
	N6-H2···N12	0.89(2)	2.21(2)	3.084(2)	168(2)
	N11-H3···N2	0.84(2)	2.25(2)	3.058(2)	162(2)
	N6-H2···O13	0.89(2)	2.47(2)	3.031(2)	121(1)
	N11-H3···O12	0.84(2)	2.60(2)	3.132(2)	122(2)
3,4,5-TNP.Pyr	N6-H6···N1	0.88(2)	1.97(2)	1.97(2)	154(2)
	N6-H6···N2	0.88(2)	2.82(2)	2.82(2)	130(2)
3,4,5-TNP.FPyr	N17-H17···N1	0.90(3)	1.92(3)	2.815(3)	171(3)
	N18-H18···N10	0.88(3)	2.09(3)	2.905(3)	155(3)
	N19-H19A···N9	0.88(4)	2.15(4)	2.919(3)	146(3)
	N19-H19A···N14[6]	0.88(4)	2.45(4)	3.089(3)	130(3)
	C20-H20···O18	1.344(3)	2.460(1)	3.723(2)	155.3(2)
	C12-F1···H24	0.950	2.798	3.604(3)	143.2
	C16-H16···O2	0.950	2.666	3.293(4)	124.0
	C16-H16···O1	0.950	2.464	3.312(3)	148.6
	C17-F2···H15	0.950	2.491	3.502	155.3(2)
3,4,5-TNP.BrPyr	N6-H6···N2	0.83(2)	1.98(2)	2.778(2)	159(2)
	C7-Br1···O5	1.876(2)	3.165(1)	5.005(2)	165.7(6)
3,4,5-TNP.IPyr	N6-H6···N2	0.82(4)	1.97(4)	2.78(3)	173(4)
	N6-H6···N1	0.82(4)	2.87(3)	3.590(3)	149(4)
	C5-I1···N1	2.085(2)	3.113(2)	5.188(3)	172.9(1)
	C6-H6A···O4	0.89(5)	2.70(5)	3.539(3)	158(5)
	C6-H6A···O3	0.89(5)	2.71(6)	3.479(4)	146(5)
	C7-H7···O2	0.92(6)	2.45(6)	3.317(4)	159(2)

5.3.3.2 Powder X-ray Diffraction Studies

Larger amounts of 3,5-DNP co-crystals and salts (~1 g) were produced for further tests including thermal stability and impact sensitivity tests. The phase purities of these salts and co-crystals were checked using powder X-ray diffraction. The simulated (from SXRD data) and observed PXRD patterns of 3,4,5-TNP.Pyr, 3,4,5-TNP.FPyr, 3,4,5-TNP.BrPyr and 3,4,5-TNP.IPyr are shown in Figures 5.37 and 5.38. These comparisons show that the patterns are broadly consistent although there are some differences in peak position and intensity. The simulated patterns were generated from SXRD data recorded at 120 K and observed patterns were collected at room temperature. This temperature difference causes small shifts between two patterns. Differences in intensities can be explained by preferred orientation and the flat-plate geometry of the sample holder used for the PXRD measurements. Overall, these bulk samples are representative of the single crystal and hence could be used for further analysis *e.g.* impact sensitivity testing and DSC measurements.

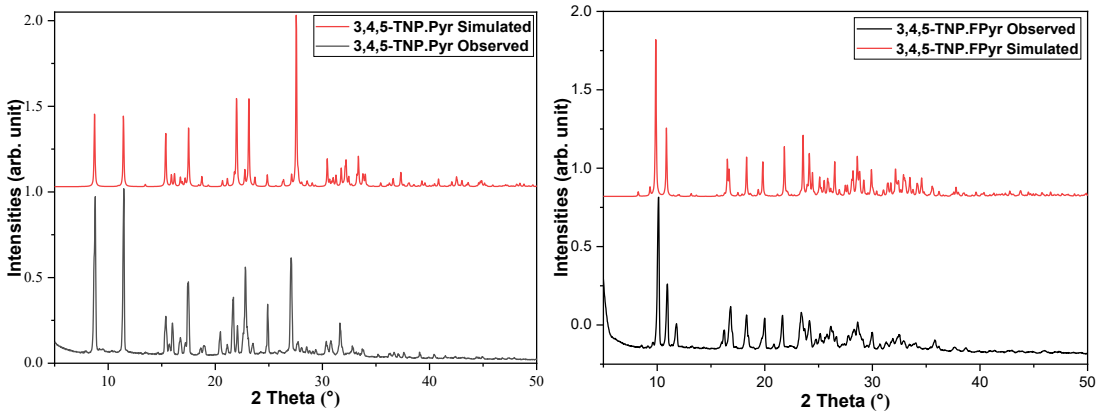

Figure 5.37 Powder X-ray diffraction patterns of 3,4,5-TNP.Pyr and 3,4,5-TNP.FPyr

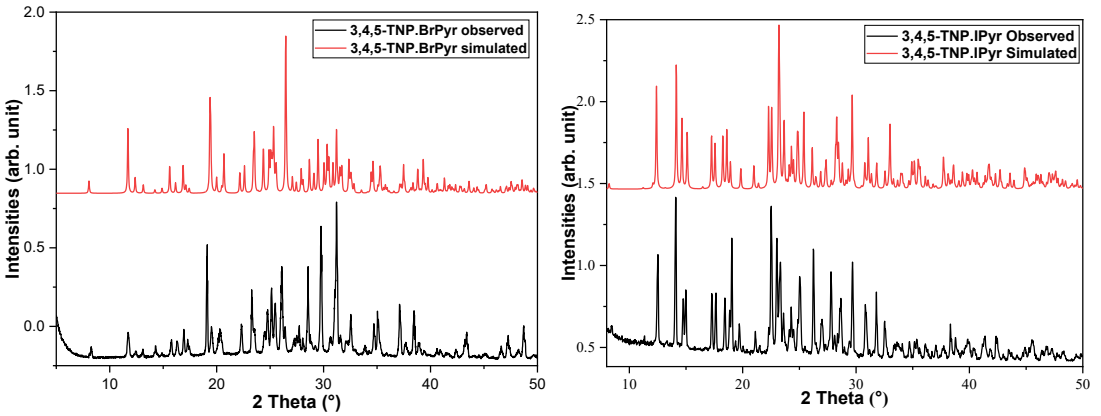

Figure 5.38 Powder X-ray diffraction patterns of 3,4,5-TNP.BrPyr and 3,4,5-TNP.IPyr

5.3.3.3 Thermal Properties of 3,4,5-TNP and Its Salts

The thermal properties of 3,4,5-TNP and its salts were studied using DSC-TGA. DSC-TGA traces of 3,4,5-TNP (Figure 5.39) shows that the onset of melting occurs at 187°C and the onset of decomposition occurs at 245°C. The thermal properties of 3,4,5-TNP were changed as a result of salt formation as described in the following section.

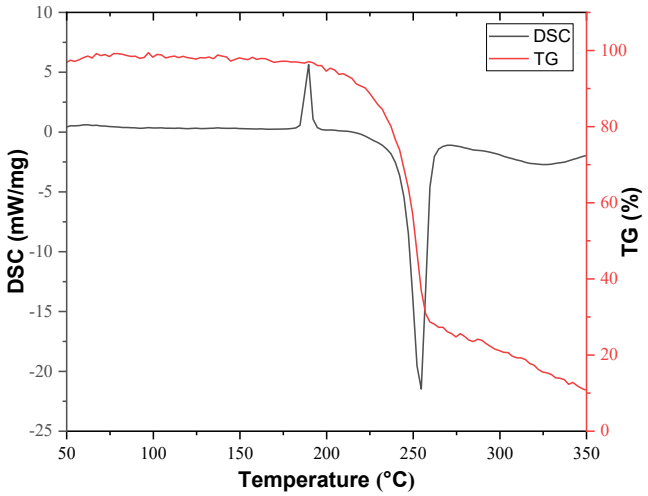

Figure 5.39 DSC-TGA traces for the 3,4,5-TNP (exothermic direction down).

The DSC-TGA traces for 3,4,5-TNP.Pyr are shown in Figure 5.40. A small endothermic peak around 100°C was observed. This perhaps indicates a solid-solid phase transition which should be investigated as future research. The onset of melting occurs at 148°C and the onset of decomposition occurs at 190°C. Decomposition involved three exothermic steps up to 350°C.

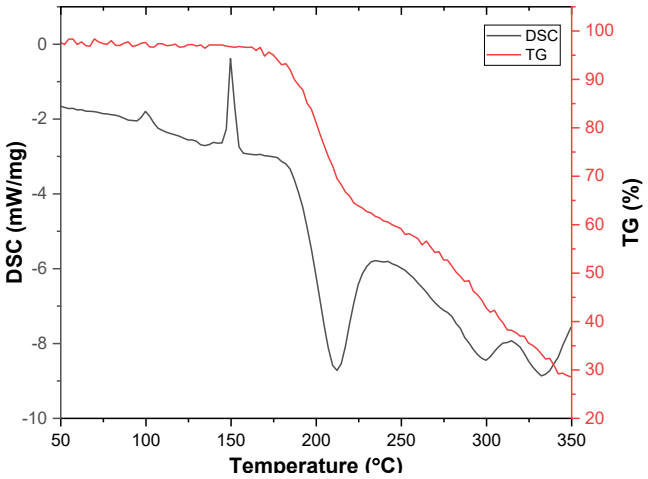

Figure 5.40 DSC-TGA trace for the 3,4,5-TNP.Pyr (exothermic direction down).

Figure 5.41 displays the DSC and TG traces for 3,4,5-TNP.FPyr. Melting occured at 126°C with the onset of decomposition at 182°C. The salt displays the largest exothermic decomposition peak among all of the 3,4,5-TNP salts with a decomposition enthalpy of -2273 J/g. The possible reason for this will be discussed later (Section 5.3.3.4). Melting and decomposition temperatures of 3,4,5-TNP both decreased after salt formation with FPyr. The resulting salt could, in principle, be classified as a melt-castable energetic material with its low melting and high decomposition point.

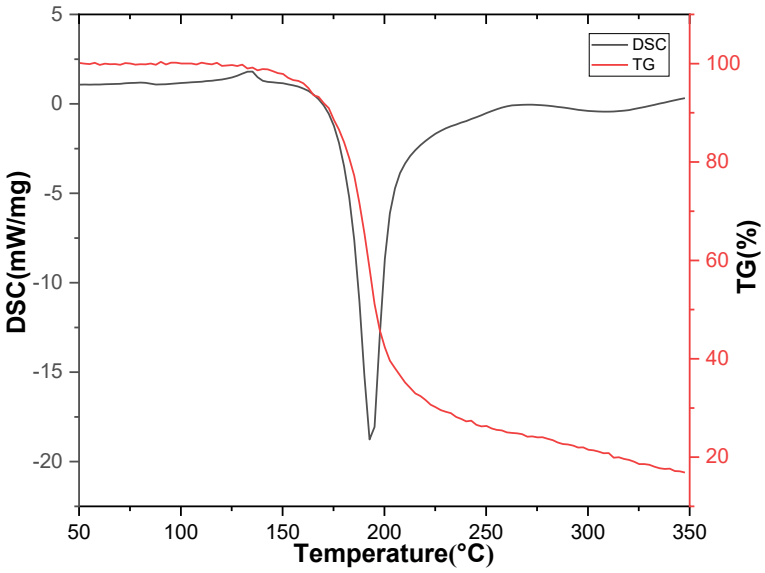

Figure 5.41 DSC-TGA trace for the 3,4,5-TNP.FPyr (exothermic direction down).

The DSC-TGA traces for the 3,4,5-TNP.BrPyr salt are shown in Figure 5.42. 3,4,5-TNP.BrPyr has a melting onset at 138.1°C and an onset of an exothermic decomposition at 177.4°C. The decomposition enthalpy of the salt is -697.2 J/g which is the lowest decomposition enthalpy among all the 3,4,5-TNP salts. Both decomposition and melting points of 3,4,5-TNP decreased and the gap between two thermal processes was narrowed down through salt formation.

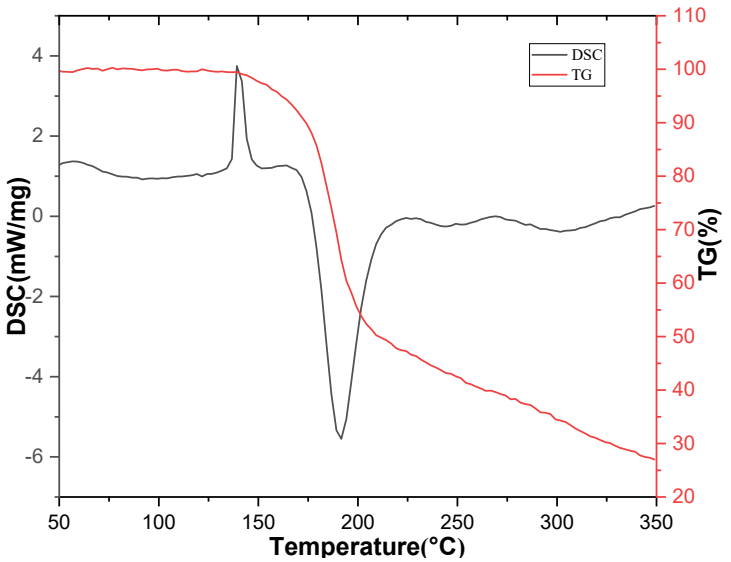

Figure 5.42 DSC-TGA trace for 3,4,5-TNP.BrPyr (exothermic direction down).

The DSC and TGA traces for the 3,4,5-TNP.IPyr salt are shown in Figure 5.43. The onset of melting occurs at 122°C with the onset of decomposition at 178.2°C. The DSC trace shows a large exothermic peak representing decomposition of the salt. Compared to 3,4,5-TNP, the melting and decomposition temperature decreased drastically. However, the gap between these temperatures remained similar after salt formation. Having the decrease in melting point, in principle 3,4,5-TNP.IPyr can be classified as a melt-castable energetic material.

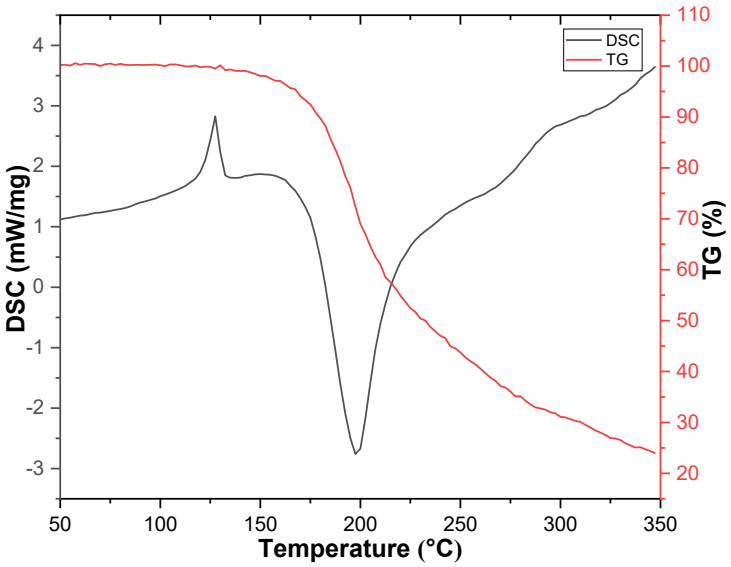

Figure 5.43 DSC-TGA trace for 3,4,5-TNP.IPyr (exothermic direction down).

Table 5.10 Melting and decomposition onset temperatures of 3,4,5-TNP and its halogen containing salts

Salt	Melting onset temperature (°C)	Melting Enthalpy		Decomposition onset temperature (°C)	Decomposition enthalpy	
		J/g	kJ/ mol		J/g	kJ/ mol
3,4,5-TNP.Pyr	148	65	18	190	-510, -108, -202	-231
3,4,5-TNP.FPyr	126	33	10	182	-2273	-682
3,4,5-TNP.BrPyr	138	95	34	177	-697	-252
3,4,5-TNP.IPyr	122	47	19	178	-807	-329
3,4,5-TNP	187	175	71	245	-1344	-273

Table 5.10 illustrates the thermal properties of all the 3,4,5-TNP salts. The decomposition temperature decreased for all the salts compared to 3,4,5-TNP. Similarly, the melting points of all the 3,4,5-TNP salts are lower than for 3,4,5-TNP. On the other hand, decomposition enthalpies were reduced on salt formation, except for 3,4,5-TNP.FPyr. 3,4,5-TNP.FPyr exhibited an exceptionally high decomposition enthalpy which usually relates with high energetic performance. The reason of this high enthalpy is explained in Section 5.3.3.4.

5.3.3.4 Calculated Energetic Performance and Experimental Impact Sensitivity of 3,4,5-TNP Salts

The calculated detonation parameters of 3,4,5-TNP salts were predicted using the EXPLO-5 program and are listed in Table 5.11, alongside computed solid-state heat of formation values and the experimental impact sensitivity (IS) values for 3,4,5-TNP.BrPyr. The estimated composition of detonation products determined on EXPLO-5 is also given in Table 5.12. As expected all the salts exhibited lower energetic performance than 3,4,5-TNP since they were diluted with non-energetic co-formers. 3,4,5-TNP salts formed with halogenated pyridines have high crystal densities due to the high relative molecular masses of the halogen atoms - see Table 5.12. However, EXPLO-5 calculations revealed that their energetic performances are not correspondingly high. Hence, it can be demonstrated that halogen atoms do not

contribute directly to detonation performance. Among all the salts, 3,4,5-TNP.FPyr was found to be the most powerful energetic compound with an estimated detonation pressure of 21.25 GPa and detonation velocity of 7280 m/s. This result was expected since decomposition enthalpy of 3,4,5-TNP.FPyr is the highest among 3,4,5-TNP salts. As expected all of the 3,4,5-TNP salts studied here exhibited lower oxygen balance values compared to 3,4,5-TNP. 3,4,5-TNP.IPyr has the highest oxygen balance (-49.0 %) among all the 3,4,5-TNP salts. The volume of gas products released upon detonation is related to the work performed by energetic material. 3,4,5-TNP.FPyr released the largest amount of gas as decomposition product which is almost same as 3,4,5-TNP itself.

BAM Fall hammer impact-sensitivity test was performed for 3,4,5-TNP.BrPyr and gave an IS value of 20 J. Therefore, 3,4,5-TNP.BrPyr was found to be slightly less sensitive to mechanical impact detonation than 3,4,5-TNP (20 J vs. 17 J, respectively), which may be attributed to the wave-like packing motif of 3,4,5-TNP.BrPyr compared to the more herringbone arrangement in the parent 3,4,5-TNP.

Table 5.11 Detonation parameters and experimental impact sensitivity values

	3,4,5-TNP.Pyr	**3,4,5-TNP. FPyr**	**3,4,5-TNP. BrPyr**	**3,4,5-TNP. IPyr**	**3,4,5-TNP (Explo5)**	**3,4,5-TNP** [30,31]
Heat of formation (kJ/mol)	345.0*	92.7*	329.3*	412.9*	178.8*	142.54
Heat of detonation (kJ/kg)	-4843	-4534	-3455	-3308	-6607	-
Detonation temperature(K)	3484	3432	3206	3457	4884	-
Detonation Pressure (GPa)	19.8	21.2	20.2	18.6	35.4	38.6
Detonation velocity (m/s)	7060	7280	6554	6111	8978	9253
Volume of gas at STP (dm^3/kg)	682.93	687.36	576.63	524.94	703.54	-
Oxygen balance (%)	-73.71	-63.9	-57.60	-49.0	-3.939	-7.88
Crystal density (g/cm^3)	1.615	1.698	1.993	2.007	1.867	1.867
Packing coefficiency	0.700	0.714	0.745	0.674		-
Impact sensitivity (J)			20			17

* These detonation parameters were predicted by using the values calculated with computational techniques described in section 5.2.7. Missing information is not provided by the references.

The composition of the products formed upon detonation can be also predicted using the EXPLO-5 program and are provided in Table 5.12. A potential reason why the 3,4,5-TNP.FPyr salt exhibits the highest decomposition enthalpy among all the salts of 3,4,5-TNP is suggested by the formation of HF as a detonation product. The H-F bond is remarkably strong (562 kJ/mol) and substantially stronger than H-Br (366 kJ/mol) and H-I (299 kJ/mol). Due to the strong H-F bond a high amount of energy (-2273 J/g, -682 kJ/mol) is evolved on decomposition.

Table 5.12 Predicted composition of main detonation products

Composition of detonation products							
3,4,5-TNP.Pyr	**Mol (%)**	**3,4,5-TNP.FPyr**	**Mol (%)**	**3,4,5-TNP.BrPyr**	**Mol (%)**	**3,4,5-TNP.IPyr**	**Mol (%)**
C(s,d)	27.26	**C(s,d)**	39.42	**C(s,d)**	40.96	**C(gr)**	39.33
N_2	22.14	**N_2**	21.00	**N_2**	21.35	**N_2**	21.57
H_2O	16.81	**H_2O**	11.13	**H_2O**	13.63	**H_2O**	13.08
C(s,gr)	15.53	**CO_2**	10.82	**CO_2**	10.10	**CO_2**	8.99
CO_2	8.02	**HF**	7.36	**Br**	6.47	**CO**	6.08
CO	5.26	**CO**	5.82	**CO**	3.13	**I**	4.9
CH_2O_2	3.43	**CH_2O_2**	2.84	**CH_2O_2**	3.03	**CH_2O_2**	3.25
NH_3	0.65	**NH_3**	0.25	**BrH**	0.66	**I_2**	0.95
H_2	0.48	**H_2**	0.24	**NH_3**	0.32	**IH**	0.48
CH_4	0.31	**CH_4**	0.07	**H_2**	0.20	**NH_3**	0.47
HCN	0.05	**HCN**	0.032	**CH_4**	0.11	**H_2**	0.38
C_2H_6	0.03	**C_2H_6**	0.004	**Br_2**	0.02	**C(d)**	0.22
C_2H_4	0.02	**C_2H_4**	0.003	**HCN**	0.01	**CH_4**	0.21
CH_3OH	0.0025	**CF_4**	0.003	**C_2H_6**	0.008	**HCN**	0.053
CH_2O	0.0001	**CH_2F_2**	0.0007	**C_2H_4**	0.003	**C_2H_6**	0.022
H	0.0001	**CH_3OH**	0.0007	**CH_3OH**	0.0007	**C_2H_4**	0.013

(Halogenated compounds are highlighted with the red. *C(gr): graphite C(d): diamond, s: solid)

5.3.4 Trends and Relationships in Co-crystals of DNP and Salts of 3,4,5-TNP

The co-crystals and salts investigated in this chapter exhibited crystal densities lie between those of the two co-formers or higher than both co-formers. Multicomponent materials often possess a crystal density lying between the densities of their co-formers. This is observed for all the 3,5-DNP salts in Chapter 4. Figure 5.44 shows the crystal density trend observed for all the co-crystals and salts in this chapter. The higher crystal density than expected observed in halogen-based materials arises from

the existence of halogen bonding. This is particularly notable for halogen bond containing structures: 3,5-DNP.BrPyr, 3,4,5-TNP.BrPyr and 3,4,5-TNP.IPyr – except for 1,3-DNP.AmClPyr which has the longest and weakest halogen bond among all the halogen bond containing materials. Although 3,5-DNP.AmClPyr and 3,4,5-TNP.FPyr have halogen atoms, they do not exhibit halogen bonding and their crystal densities lie between the crystal densities of the two parent components.

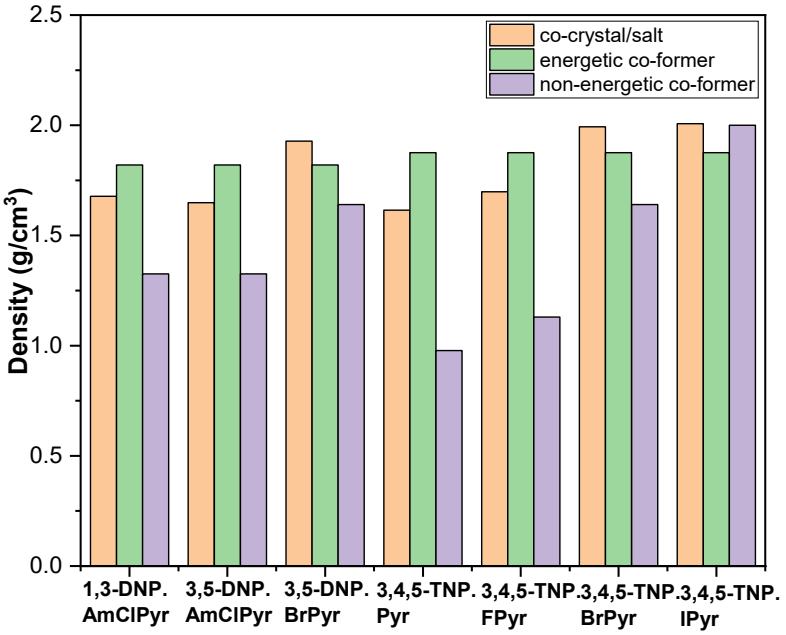

Figure 5.44 Crystal density trend for the co-crystals/salts and their co-formers

5.4 Conclusions

Seven novel multicomponent structures based on nitropyrazoles have been discovered. Three of them comprise co-crystals formed between dinitropyrazoles and halogenated pyridines. The other four structures are salts of 3,4,5-TNP with pyridine and halogenated derivatives of pyridine. All the compounds formed with a 1:1 molar ratio of co-formers. These novel materials were characterised using single crystal and powder X-ray diffraction techniques. Hydrogen bonds with moderate strength were identified together with halogen bonds that were strongest for iodopyridine among 3,4,5-TNP salts. It is demonstrated that halogen bonding contributes to the stability of these multicomponent energetic materials and increase the density of the co-crystals and salts.

Energetic performance, thermal behaviour and impact sensitivities of co-crystals/salts were determined. Attempts were made to correlate important structural features including crystal packing and crystal density with energetic properties such as thermal stability, impact sensitivity and energetic performance. All the co-crystals and salts exhibited slightly lower or equal impact sensitivities to parent energetic compounds except for 1,3-DNP.AmClPyr. This co-crystal has an unexpectedly high impact sensitivity (5 J) highlighting that sensitivity can be dramatically increased by co-crystallisation with even non-energetic co-formers.

The thermal behaviour of the parent energetic materials was altered by co-crystallisation and salt formation. All the salts and co-crystals have large and obvious exothermic peaks representing decomposition process except for the 3,5-DNP co-crystals (AmClPyr and BrPyr). These co-crystals exhibited complicated decomposition patterns; perhaps indicating that the non-energetic component has evaporated prior to decomposition. Whereas the thermal stability of 3,4,5-TNP decreased upon salt formation with substituted pyridines, DNP co-crystals exhibited enhanced thermal stabilities compared to the parent energetic compounds (1,3-DNP and 3,5-DNP).

Energetic performance parameters of the salts and co-crystals were predicted using EXPLO-5 program. Although it has the lowest crystal density among 3,4,5-TNP salts, 3,4,5-TNP.FPyr was found to have the highest energetic performance, with a detonation pressure of 21.2 GPa and velocity of 7280 m s^{-1} among all the co-crystals and salts in this chapter. This is higher than the commonly used explosive 2,4,6-trinitrotoluene, TNT (6881 m s^{-1} , 19.5 GPa). [32] This unexpected result is attributed to the exothermic formation of HF that was formed as a detonation product. A consistent trend could not be observed between crystal densities and detonation velocities of the co-crystals and salts on account of the densities of these materials being dominated by the heavy halogen atoms, but which do not contribute to the energetic output of the materials.

5.5 Suggestions for Future Work

The research conducted in this thesis has revealed some significant aspects that have potential to inform the future design of energetic co-crystals. In particular, the role of

halogen bonding appears important in influencing properties such as thermal stability, density and melting points.

Due to COVID-19 pandemic, it was not possible to conduct energetic property testing of some of the co-crystals and salts. Hence, impact sensitivity tests of 3,4,5-TNP.Pyr, 3,4,5-TNP.FPyr and 3,4,5-TNP.IPyr should be performed in order to expand the dataset of explored energetic materials. This will establish more robustly structure-property correlations in these materials.

Further energetic property testing including sensitivity to spark and friction should be performed on all the salts and co-crystals, in order to establish how these properties are affected. Relative impact sensitivities of these salts and co-crystals can be predicted using vibrational up-pumping model as performed for different forms of 3,4,5-TNP (Chapter 3).

The 3,4,5-TNP.Pyr salt exhibited a small endothermic peak around 100°C on its DSC pattern perhaps indicating a solid-solid phase transition. Therefore, an investigation of this possible phase transition using variable temperature X-ray diffraction should be undertaken. More generally, it would be of interest to explore polymorphism of these materials using temperature and/or pressure. Of particular interest would be a high-pressure crystallographic study to observe the effects of pressure on halogen bonding in materials such as 3,4,5-TNP.IPyr.

Having established the type of compound with which nitropyrazoles form co-crystals and salts, it would be interesting to explore co-crystallisation with energetic co-formers in order to maximize energy output. Examples might include nitrated pyridines.

As mentioned halogen-containing energetic compounds are usually effective biocidal materials. Therefore, the halogen-containing co-crystals and salts should be investigated in terms of their biocidal effects.

5.6 References

1 S. R. Kennedy and C. R. Pulham, in *Co-crystals: Preparation, Characterization and Applications*, eds. C. B. Aakeröy and Sinha S. Abhijeet, Royal Society of Chemistry, Edinburgh, 2018, pp. 231–266.

2 K. B. Landenberger, O. Bolton and A. J. Matzger, *J. Am. Chem. Soc.*, 2015, **137**, 5074–5079.

3 J. C. Bennion, L. Vogt, M. E. Tuckerman and A. J. Matzger, *Cryst. Growth Des.*, 2016, **16**, 4688–4693.

4 O. Mulamba, E. M. Hunt and M. L. Pantoya, *Biotechnol. Bioprocess Eng.*, 2013, **18**, 918–925.

5 C. He, D. A. Parrish and J. M. Shreeve, *Chem. - A Eur. J.*, 2014, **20**, 6699–6706.

6 P. J. Costa, *Phys. Sci. Rev.*, 2019, **2**, 1–16.

7 O. V. Dolomanov, L. J. Bourhis, R. J. Gildea, J. A. K. Howard and H. Puschmann, *J. Appl. Crystallogr.*, 2009, **42**, 339–341.

8 G. M. Sheldrick, *Acta Crystallogr. Sect. C Struct. Chem.*, 2015, **71**, 3–8.

9 R. Shelxl, *User Guid. to Cryst. Struct. refinement with SHELXL*, 2008.

10 G. M. Sheldrick, *Acta Crystallogr. Sect. C Struct. Chem.*, 2015, **71**, 3–8.

11 C. D. Fuh, J. S. Lee and C. M. Liaw, *J. Data Sci.*, 2003, **1**, 83–101.

12 M. Suceska, in *1st International Symposium on Explosion, Shock Wave and Hypervelocity Phenomena (ESHP)*, 2004, pp. 325–330.

13 M. Suceska, 2015, 1–120.

14 J. J. P. Stewart, *J. Mol. Model.*, 2013, **19**, 1–32.

15 J. V M. J. Frisch, G. W. Trucks, H. B. Schlegel, G. E. Scuseria, M. A. Robb, J. R. Cheeseman, G. Scalmani, V. Barone, G. A. Petersson, H. Nakatsuji, X. Li, M. Caricato, A. V. Marenich, J. Bloino, B. G. Janesko, R. Gomperts, B. Mennucci, H. P. Hratchian, 2016.

16 E. F. C. Byrd and B. M. Rice, *J. Phys. Chem. A*, 2006, **110**, 1005–1013.

17 T. Lu and F. Chen, *J. Comput. Chem.*, 2012, **33**, 580–592.

18 H. D. B. Jenkins, D. Tudela and L. Glasser, *Inorg. Chem.*, 2002, **41**, 2364–2367.

19 G. H. Tao, Y. Guo, Y. H. Joo, B. Twamley and J. M. Shreeve, *J. Mater. Chem.*, 2008, **18**, 5524–5530.

20 D. Sun, Y. H. Li, H. J. Hao, F. J. Liu, Y. M. Wen, R. Bin Huang and L. S. Zheng, *Cryst. Growth Des.*, 2011, **11**, 3323–3327.

21 J. H. Wang, C. Shen, Y. C. Liu, J. Luo and Y. Duan, *J. Mol. Struct.*, 2018, **1163**, 54–60.

22 J. P. Agrawal, in *High Energy Materials: Propellants, Explosives and Pyrotechnics.*, ed. J. P. Agrawal, WILEY-VCH Verlag GmbH & Co. KGaA, Weinheim, 2010, pp. 1–67.

23 J. P. Agrawal, *High Energy Materials: Propellants, Explosives and Pyrotechnics. Chapter 6: Explosive and Chemical Safety*, 2010.

24 M. F. Bölter, A. Harter, T. M. Klapötke and J. Stierstorfer, *Chempluschem*, 2018, **83**, 804–811.

25 Y. Ma, L. Meng, H. Li and C. Zhang, *CrystEngComm*, 2017, **19**, 3145–3155.

26 A. A. L. Michalchuk, J. Hemingway and C. A. Morrison, *J. Chem. Phys.*, 2021, **154**, 064105.

27 R. Bu, Y. Xiong and C. Zhang, *Cryst. Growth Des.*, 2020, **20**, 2824–2841.

28 J. Zhang, Q. Zhang, T. T. Vo, D. A. Parrish and J. M. Shreeve, *J. Am. Chem. Soc.*, 2015, **137**, 1697–1704.

29 C. Zhang, X. Wang and H. Huang, *J. Am. Chem. Soc.*, 2008, **130**, 8359–8365.

30 European Patent Office, EP 2155688B1, *Eur. Pat. Specif.*, 2008, 38, 1–19.

31 G. Hervé, C. Roussel and H. Graindorge, *Angew. Chemie - Int. Ed.*, 2010, **49**, 3177–3181.

32 Y. Zhang, Y. Guo, Y. H. Joo, D. A. Parrish and J. M. Shreeve, *Chem. - A Eur. J.*, 2010, **16**, 10778–10784.

Chapter 6 Summary

1,3-DNP, 3,5-DNP and 3,4,5-TNP were synthesised successfully, and used for high-pressure and co-crystallisation/salt formation studies. 3,4,5-TNP was subsequently investigated under high - pressure using a combination of Raman spectroscopy, neutron powder diffraction, and single crystal X-ray diffraction. On compression up to 7.3 GPa, three new high-pressure phases of 3,4,5-TNP were identified and characterised. The ambient form was named as Form I. Form II formed at 0.7 GPa and is characterised by an abrupt shortening of hydrogen-bonding interactions. Form III was observed at 2.2 GPa and is characterised by an abrupt conformational change affecting all of the NO_2 torsional angles in the asymmetric unit of 3,4,5-TNP. Form IV was observed at 5.3 GPa via a single crystal to single crystal transition and by compression of a polycrystalline sample. The structure of Form IV was solved and refined from single crystal X-ray diffraction data – it adopts the monoclinic crystal system with space group *Cc.* The neutron powder diffraction pattern recorded for a polycrystalline sample are consistent with Form IV at pressures above 5.3 GPa. Form IV appears to be more sensitive to initiation as demonstrated by its spontaneous initiation at elevated pressures during both neutron experiments. This increased impact sensitivity of Form IV compared to Form I was rationalised using a computational technique based on a vibrational up-pumping model. This work therefore highlights that pressure-induced polymorphism has a high probability of significantly altering the impact sensitivity of energetic materials. In addition to being the first structural characterisation study of 3,4,5-TNP at high-pressure, it also represents a successful application of sensitivity predictions using vibrational up-pumping theory calculations.

12 novel multicomponent structures including 3 co-crystals with DNPs and 9 salts with 3,5-DNP and 3,4,5-TNP were produced. Thermal behaviour, impact sensitivity and energetic performance of these salts and co-crystals were determined and compared to their energetic co-formers. Energetic performances of all the salts and co-crystals were observed to be lower than the parent energetic compounds. This was expected since all the co-formers were non-energetic compounds. However, impact sensitivity varied substantially upon co-crystallisation/salt formation. All the multicomponent compounds tested exhibited similar or enhanced impact sensitivities (3,5-

DNP.AmClPyr, 3,5-DNP.BrPyr, 3,4,5-TNP.BrPyr and 3,5-DNP.Pyr) as their energetic parent components except for 1,3-DNP.AmClPyr, which was found to be sensitive (5 J). Therefore, it is deducted that combining energetic compounds with non-energetic co-formers does not always reduce their sensitivities. The thermal behaviour of all the multicomponent structures were studied using DSC. While thermal stabilities of three co-crystals were found to be higher than their parent energetic compounds, all nine salts exhibited lower decomposition temperatures after salt formation. This raises the question as to whether co-crystallisation may improve thermal stability compared to salt formation or this was just a coincidence. Since thermal stability relies on more parameters e.g. bond strength, intermolecular interactions, this should be investigated further. In appendix B, table 5 summarises all the structural and physicochemical data of the co-crystals/salts obtained in this thesis. Table 4 (appendix B) exhibits the compounds which were used for co-former investigation of nitropyrazole-based energetic materials including the successful and unsuccessful pairs.

The other important and interesting trend was observed on melting points of the salts and co-crystals. All the halogen containing salts and co-crystals (Chapter 5) except for 1,3-DNP.AmClPyr exhibited much lower melting points (50-85°C) than their energetic compounds, implying that their intermolecular interactions are weakened after multicomponent structure formation. This can be explained by the fact that most H-bonds formation is hindered by the presence of large halogen atoms in salts/co-crystals and formation of relatively weak halogen bonds (Table 5.4 and 5.10). In support of this, since 1,3-DNP has no H-bonds this decrease in its melting point was not observed in 1,3-DNP.AmClPyr. Among these compounds, 3,5-DNP.BrPyr showed low melting point of 85°C that can be associated with the loss of most H-bonds of 3,5-DNP upon co-crystallisation with BrPyr. The non-halogenated salts displayed the opposite trend in their melting points, except for 3,4,5-TNP.Pyr and 3,5-DNP.Pyr. The salts (4 out of 6) have higher (11-50°C) melting temperatures than 3,5-DNP implying the presence of stronger non-covalent interactions than in 3,5-DNP. In the salts, shorter therefore stronger H-bond formations were observed comparing to 3,5-DNP. It is seen that presence of halogen atoms decreased the strength of overall non-covalent interactions and therefore lowered the melting point of the energetic salts. It is also observed that intermolecular interactions have significant effect on melting points of the salts and co-crystals.

Appendix A

Further experimental data of high-pressure studies

Table 1 Unit cell parameters obtained from high-pressure SXRD

GPa	Volume	a (Å)	b (Å)	c (Å)	β-angle(°)
0.2	2133.26	15.104(1)	8.246(1)	17.141(1)	92.235(4)
0.58	2062.67	14.937(2)	8.1341(1)	16.989(2)	92.17(7)
1.1	2016.06	14.815(2)	8.0553(1)	16.905(2)	92.113(8)
1.71	1955.3	14.645(1)	7.9546(7)	16.7946(9)	92.018(4)
2.6	1887.25	14.453(1)	7.8178(8)	16.713(1)	92.015(4)
3.81	1812.17	14.2569(7)	7.6573(6)	16.6118(8)	92.197(3)
5.2	1742.3	19.571(1)	7.6509(8)	14.6982(9)	127.661(2)
6.59	1695.34	19.399(1)	7.5957(8)	14.529(2)	127.637(3)
7.3	1674	19.319(2)	7.567(1)	14.458(3)	127.623(5)

Table 2 Unit cell parameters obtained from high-pressure NPD

GPa	Volume	a (Å)	b (Å)	c (Å)	β-angle(°)
0.135	2155.6(3)	15.1601(0)	8.27607(9)	17.1939(2)	92.261(1)
0.332	2129.4(3)	15.10106	8.23544(8)	17.1355(2)	92.2467(9)
0.694	2089.1(2)	15.0049(1)	8.1728(5)	17.0483(1)	92.225(7)
0.997	2039.2(2)	14.8787(2)	8.09959(8)	16.9330(2)	92.128(1)
1.243	2013.7(2)	14.8121(2)	8.05721(8)	16.8843(2)	92.108(1)
1.368	1999.9(2)	14.7786(2)	8.03408(8)	16.8639(2)	92.10(1)
1.588	1983.0(2)	14.7307(2)	8.00422(8)	16.8295(2)	92.06(1)
1.728	1968.9(2)	14.6904(2)	7.98035(7)	16.8052(2)	92.026(1)
1.932	1953.2(2)	14.6441(2)	7.95454(8)	16.7817(2)	91.99(1)
2.108	1937.8(2)	14.5955(1)	7.92595(8)	16.7606(1)	91.9679(8)
2.233	1925.3(2)	14.5594(2)	7.90267(6)	16.7431(2)	91.96(1)
2.409	1913.7(2)	14.5275(2)	7.87831(7)	16.730(2)	91.98(1)
2.61	1903.7(2)	14.5019(2)	7.85726(8)	16.7174(2)	91.99(1)
2.742	1892.8(2)	14.4711(2)	7.83544(7)	16.7035(2)	92.01(1)
2.885	1883.6(2)	14.4464(2)	7.81632(8)	16.6918(2)	92.03(1)
3.048	1872.7(2)	14.4165(2)	7.7946(8)	16.6757(2)	92.05(1)
3.247	1861.6(2)	14.3842(2)	7.77072(8)	16.6659(2)	92.05(1)
3.346	1852.6(2)	14.3606(2)	7.75135(9)	16.6539(2)	92.06(1)
3.626	1841.2(2)	14.329(2)	7.72976(9)	16.6341(2)	92.08(1)
3.795	1830.3(2)	14.2998(2)	7.7057(1)	16.6212(2)	92.096(1)
4.086	1817.9(3)	14.2691(2)	7.6785(1)	16.6036(2)	92.16(1)
4.457	1800.5(3)	14.2225(3)	7.637(2)	16.5883(3)	92.22(2)

Rietveld refinement plots obtained using NPD data collected for 3,4,5-TNP at every pressure point:

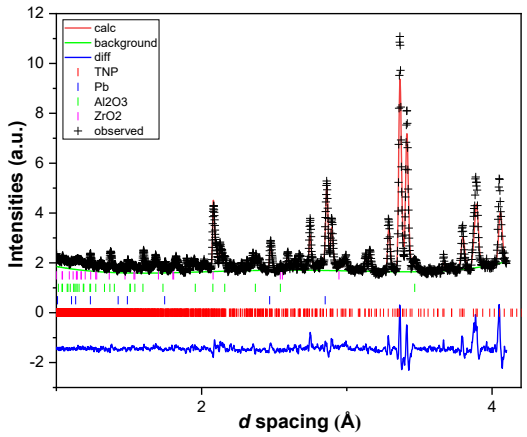

9T (0.1 GPa)

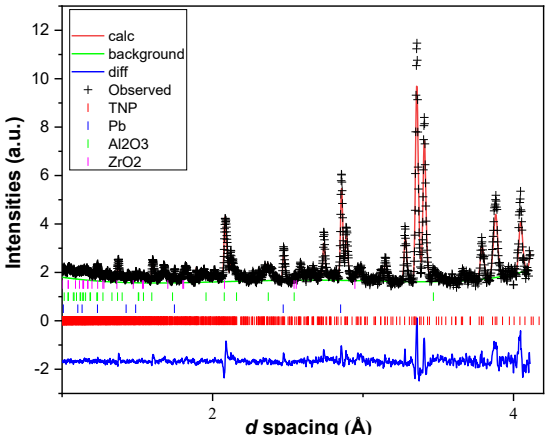

11T (0.3 GPa)

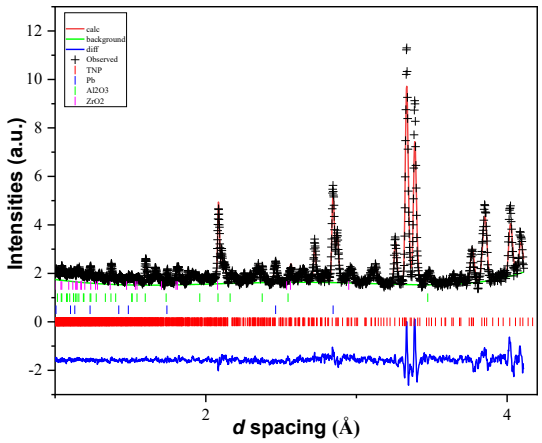

13T (0.7 GPa)

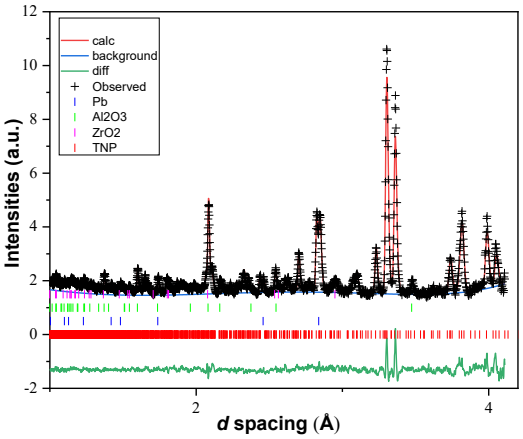

15T (1 GPa)

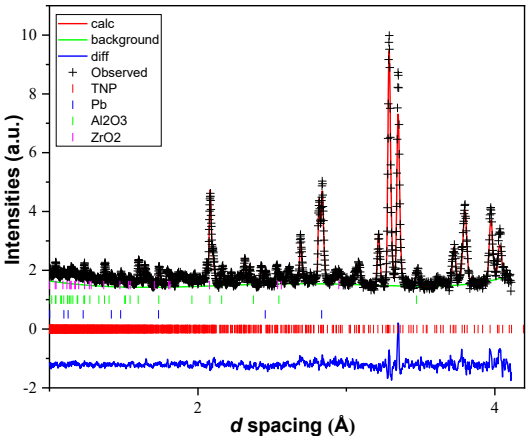

17T (1.2 GPa)

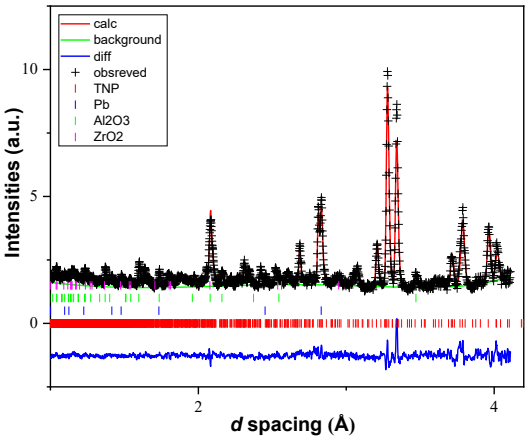

19T (1.4 GPa)

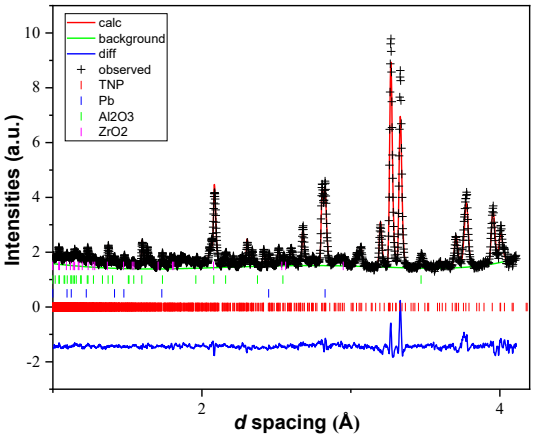

21T (1.6 GPa)

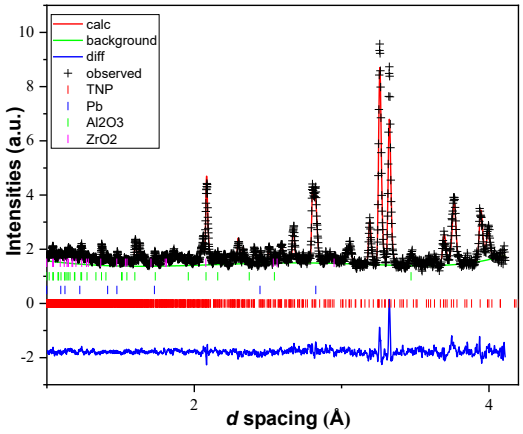

23T (1.7 GPa)

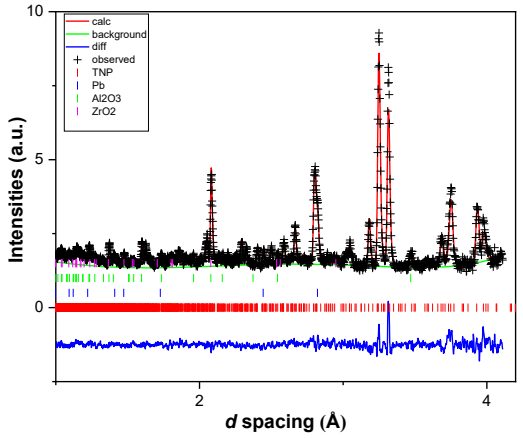

25T (1.9 GPa)

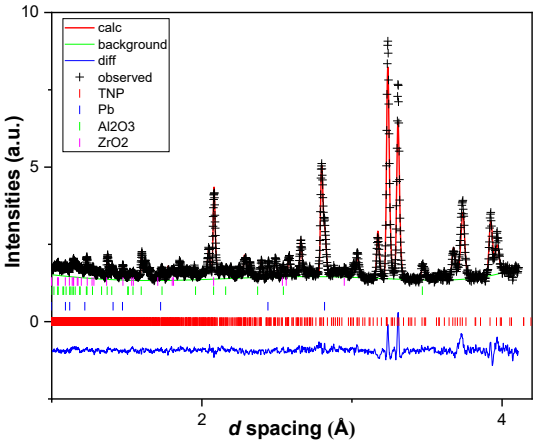

27T (2.1 GPa)

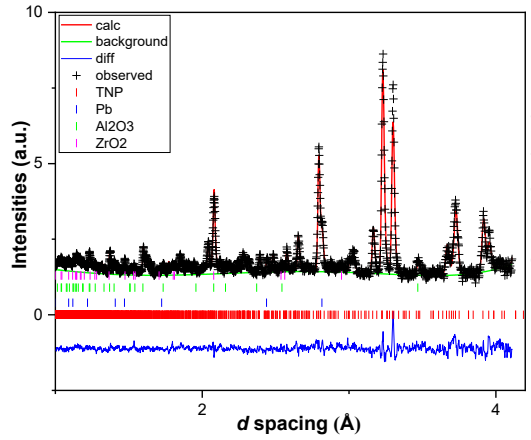

29T (2.2 GPa)

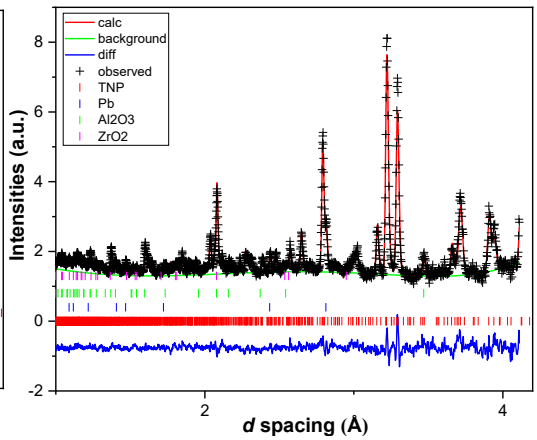

31T (2.4 GPa)

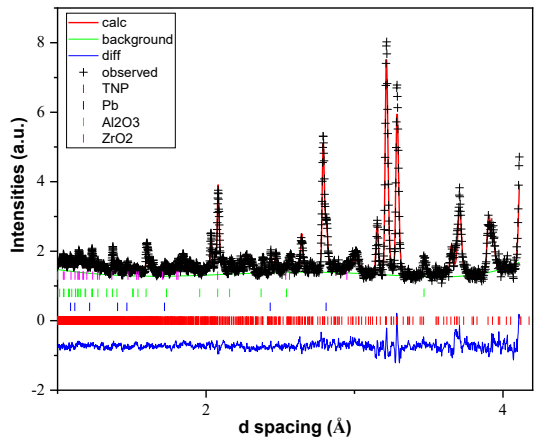

33T (2.6 GPa)

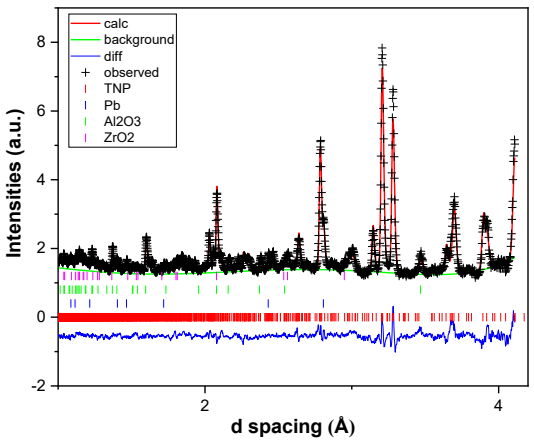

35T (2.7 GPa)

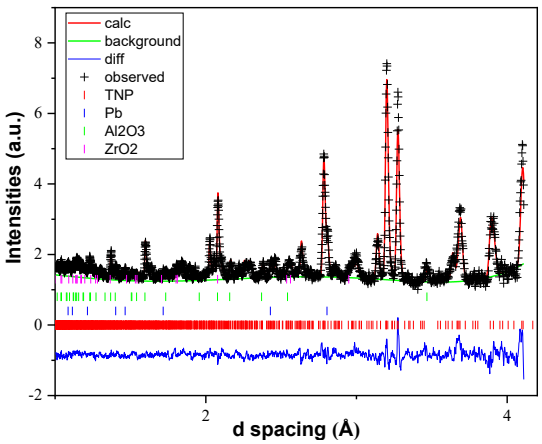

37T (2.9 GPa)

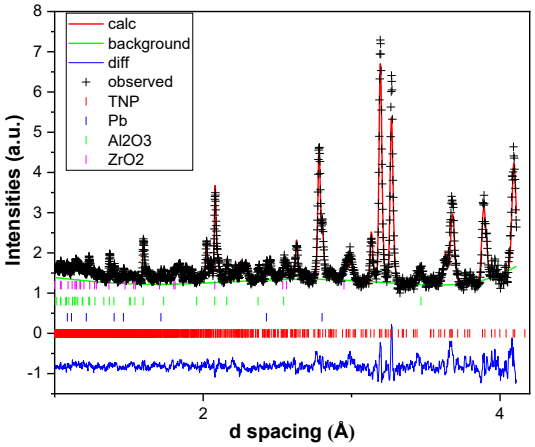

39T (3.0 GPa)

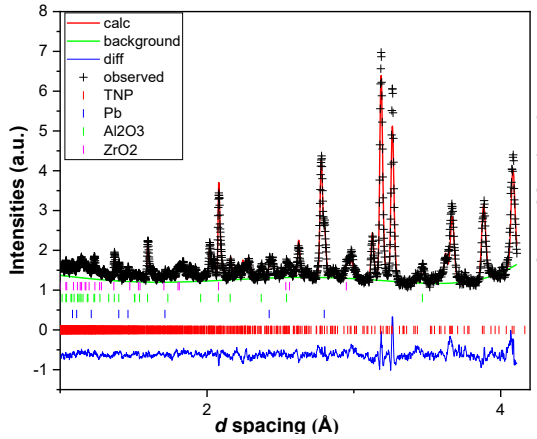

41T (3.2 GPa)

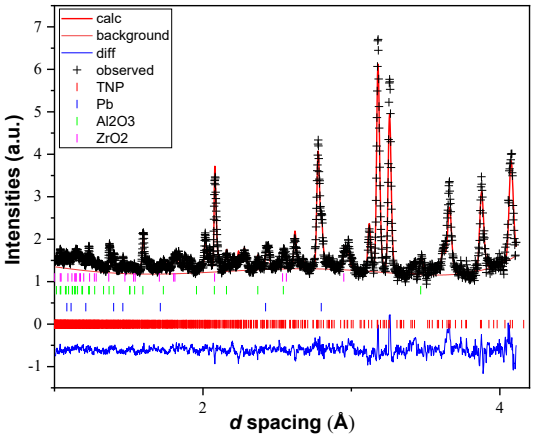

43T (3.3 GPa)

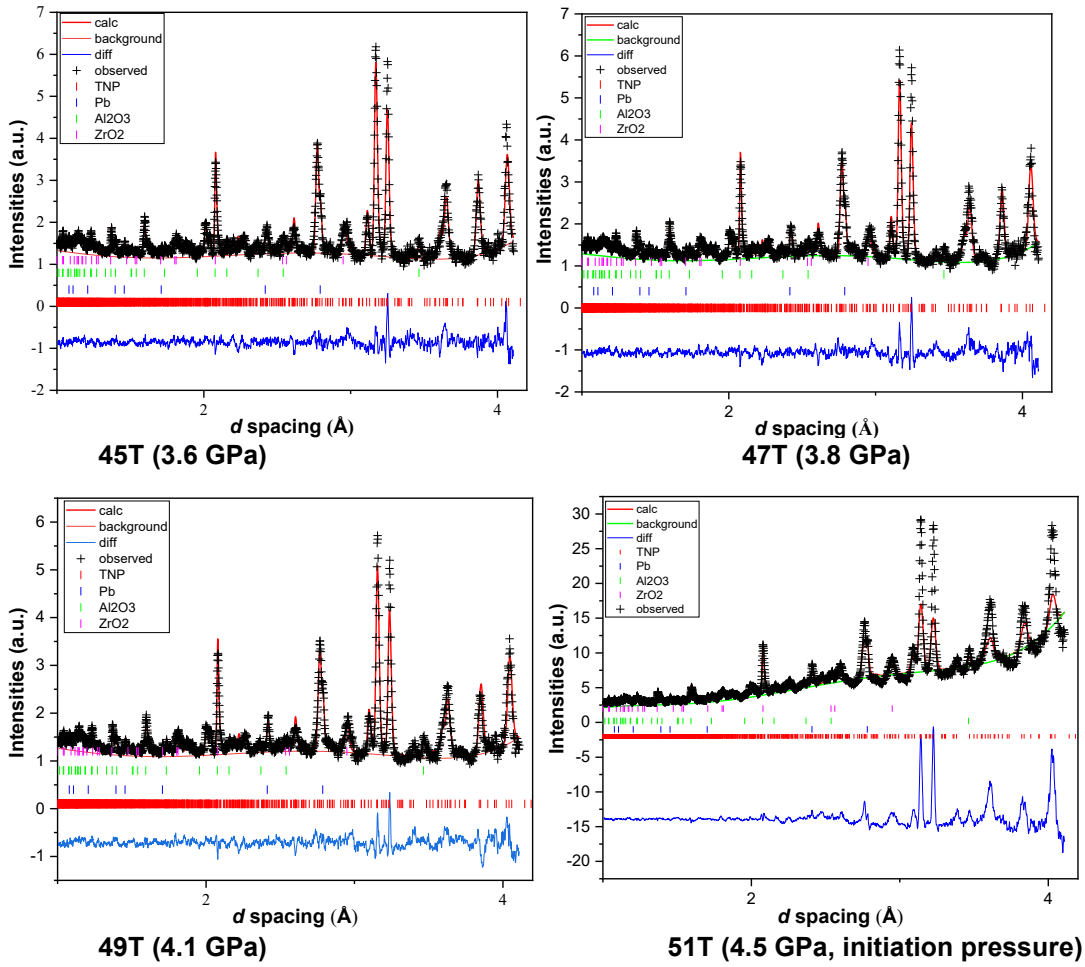

Table 3 Rietveld refinement parameters of NPD data

GPa	Chi2	wRp	Rp
0.135	2.4	3.94	5.04
0.332	1.508	4.44	5.24
0.694	1.041	3.73	4.87
0.997	1.358	3.07	3.78
1.243	0.918	3.61	4.24
1.368	0.9418	3.68	4.35
1.588	2.293	3.09	3.58
1.728	1.017	3.88	4.5
1.932	1.019	3.91	4.43
2.108	1.471	3.35	3.81
2.233	1.023	3.98	4.48
2.409	1.024	3.82	4.42
2.61	1.015	4.01	4.6
2.742	2.322	3.54	4.07
2.885	1.129	4.3	5.01
3.048	1.151	4.39	5.19
3.247	1.837	3.95	4.45
3.346	1.136	4.43	5.12
3.626	1.199	4.61	5.32
3.795	1.287	4.84	5.7
4.086	1.72	4.64	5.52
4.45	7.274	6.09	10.29

Appendix B

Further compounds used to find novel co-crystals and salts with pyrazole-based energetic materials are given in Table 4. All pairs were dissolved in ethanol and methanol.

Table 4 Co-former investigation

Energetic parent compound	Co-former	Result
Pyrazole	3,5-diamino-1,2,4-triazole	Result matched with CCDC
Pyrazole	2,3-dinitroaniline	Result matched with CCDC
Pyrazole	4-nitroaniline	Result matched with CCDC
1-NP	3,5-diamino-1,2,4-triazole	Result matched with CCDC
1-NP	4-aminopyridine	Result matched with CCDC
1-NP	Ammonium chloride	Result matched with CCDC
3-NP	2,4-dinitroaniline	Result matched with CCDC
3-NP	1,3-diaminoguanidine	Result matched with CCDC
3-NP	Nitric acid	Result matched with CCDC
3-NP	1,3-dinitrobenzene	Result matched with CCDC
3-NP	2-aminopyridine	Result matched with CCDC
3-NP	2,4,6-triaminopyrimidine	Result matched with CCDC
3-NP	4-dimethylaminopyridine	Co-crystal
3-NP	2-hydroxy-3-nitropyridine	Result matched with CCDC
3-NP	4-amino-1,2,4-triazole	Result matched with CCDC
3-NP	2-hydroxy-5-nitropyridine	Result matched with CCDC
3-NP	Ammonia	Result matched with CCDC
3-NP	3-amino-1,2,3-triazole	Result matched with CCDC
3-NP	Piperazine	Result matched with CCDC
3-NP	P-phenyl diamine	Result matched with CCDC
3-NP	Ammonium formate	Result matched with CCDC
3-NP	4-methylmphenylene diamine	Result matched with CCDC
3-NP	4-aminopyridine	Result matched with CCDC

3-NP	2-hydroxy-5-iodo-3-nitropyridine	Result matched with CCDC
3-NP	Guanidine hydrochloride	Result matched with CCDC
3-NP	Succinic acid	Result matched with CCDC
3-NP	2-hydroxypyridine	Result matched with CCDC
3-NP	2-hydroxy-3,5-dinitropyridine	Result matched with CCDC
3-NP	2-hydroxy-5-nitropyridine	Result matched with CCDC
3-NP	3-hydroxy-2-nitropyridine	Co-crystal
3-NP	4,4-bipyridine	Co-crystal
1,3-DNP	3-amino-2-chloropyridine	Co-crystal
1,3-DNP	Guanidine hydrochloride	Result matched with CCDC
1,3-DNP	Nitroguanidine	Result matched with CCDC
1,3-DNP	4-aminopyridine	Result matched with CCDC
1,3-DNP	4-dimethylaminopyridine	Result matched with CCDC
1,3-DNP	Hydrazinehydrate	Result matched with CCDC
1,3-DNP	Morpholine	Result matched with CCDC
1,3-DNP	2-ethylpyridine	Result matched with CCDC
1,3-DNP	4-ethylpyridine	Result matched with CCDC
1,3-DNP	Melamine	Result matched with CCDC
1,3-DNP	p-Toluidine	Result matched with CCDC
1,3-DNP	4,7-phenantroline	Result matched with CCDC
3,5-DNP	5-ethyl-2-methylpyridine	Result matched with CCDC
3,5-DNP	Fox-7	Result matched with CCDC
3,5-DNP	Nitroguanidine	Cannot grow single crystal
3,5-DNP	Pyridine	Salt
3,5-DNP	4-aminopyridine	Salt
3,5-DNP	2-amino-6-picoline	Salt
3,5-DNP	4-dimethylaminopyridine	Salt
3,5-DNP	Morpholine	Salt
3,5-DNP	3-amino-2-chloropyridine	Co-crystal
3,5-DNP	3-bromopyridine	Co-crystal
3,4,5-TNP	Nitroguanidine	Cannot grow single crystal
3,4,5-TNP	3-nitro-1,2,4-triazole	Result matched with CCDC
3,4,5-TNP	Fox-7	Result matched with CCDC
3,4,5-TNP	Nitroguanidine (propanol, +heat up to 50°C)	Cannot grow single crystal

		(nitroguanidine is not soluble)
3,4,5-TNP	CL-20	Result matched with CCDC
3,4,5-TNP	3-iodopyridine	Salt
3,4,5-TNP	2-hydroxy-3,5-dinitropyridine	Result matched with CCDC
3,4,5-TNP	3-fluoropyridine	Salt
3,4,5-TNP	Pyridine	Salt
3,4,5-TNP	3-bromopyridine	Salt
3,4,5-TNP	Guanidine nitrate	Result matched with CCDC
3,4,5-TNP	NTO	Result matched with CCDC
3,4,5-TNP	CL-20 (ethtlacetate, ethanol, methanol, acetonitrile)	Result matched with CCDC
1,3-DNP	CL-20 (ethanol, methanol)	Result matched with CCDC
3,5-DNP	Guanidine hydrochloride	Result matched with CCDC

1-NP: 1-nitropyrazole **3-NP:** 3-nitrpyrazole **1,3-DNP:** 1,3-dinitropyrazole
3,5-DNP: 3,5-dinitropyrazole **3,4,5-TNP:** 3,4,5-trinitropyrazole
Energetic co-formers are given in red.

Table 5 A selection of structural features and energetic properties of all the crystals/salts along with nitropyrazoles

Compounds	**Crystal Density (g cm^{-3})**	**Packing coefficient**	**IS (J)**	**Heat of formation (kJ/mol)**	**Detonation Pressure (GPa) / Detonation velocity (m/s) (EXPLO 5)**	**Oxygen balance (EXPLO 5)**	**T_m T_d (°C)**	**Packing motif**
1,3-DNP	1.796	0.749	25	189.1	30.3 9 8359	-30.4	66 171	
3,5-DNP	1.82	0.76	25	136.1 *	31.5 8469	-30.4	163 251	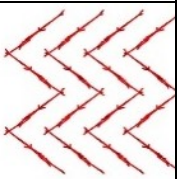
3,4,5-TNP	1.876	0.725	17	179 *	35.4 8978	-3.9	175 245	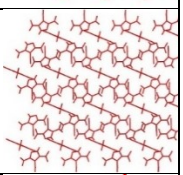
3,5-DNP. Pyr	1.595	0.731	45	345.5 *	17.0 6780	-104.6	140 271	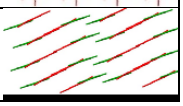

3,5-DNP. AmPyr	1.586	0.726		170.5 *	15 6457	-101.5	217 314	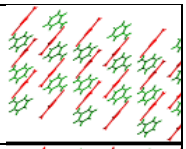
3,5-DNP. AmPic	1.532	0.715		150.5 *	15.5 6587	-114.2	211 250	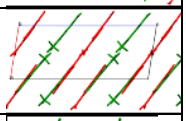
3,5-DNP. DMAP	1.494	0.724		201.7 *	14.7 6474	-125.6	180 298	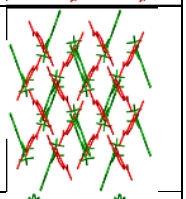
3,5-DNP. Morph	1.576	0.731		-79.6 *	20.5 7373	-94.6	216 237	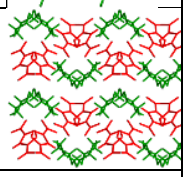
1,3-DNP. AmClPyr	1.678	0.735	5	200.67 *	16 6451	-83.7	72 189	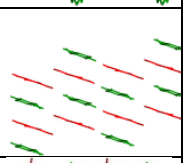
3,5-DNP. AmClPyr	1.649	0.718	28	273.7 *	16.5 6590	-83.7	109 259	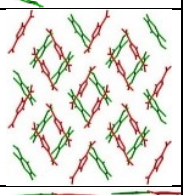
3,5-DNP. BrPyr	1.928	0.73	25	320.6 *	16.0 5787	-79.5	84 270	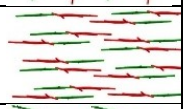
3,4,5-TNP. Pyr	1.615	0.702		345 *	19.8 7060	-73.7	148 190	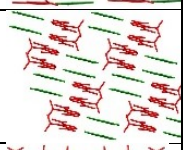
3,4,5-TNP. Fpyr	1.698	0.714		92.7*	21.2 7280	-63.9	126 182	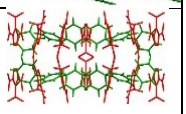
3,4,5-TNP. BrPyr	1.993	0.745	19.9	329.3 *	20.2 6554	-57.6	138 177	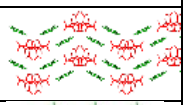
3,4,5-TNP. IPyr	2.007	0.674		412.9 *	18.6 6111	-49.0	122 178	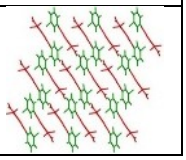

T_m: Melting temperature T_d: Decomposition temperature
*These heat of formation values were calculated using the computational techniques given in Section 2.14.

Appendix C

CONFERENCES – PRESENTATIONS

February - 2018: ISIS Neutron and Muon Source - Neutron Training Course / ISIS Neutron and Muon Source, Science and Technology Facilities Council, Didcot, Oxfordshire, UK./ Poster presentation: “Co-Crystal Engineering of Energetic Materials”

April - 2018: New Trends in Research of Energetic Materials / University of Pardubica, Pardubica, Czech Republic.

June - 2018: Gordon Research Seminars and Conferences on 'Energetic Materials' / Grand Summit Hotel at Sunday River Newry, ME, USA / Poster presentation: “Co-crystallisation of Nitropyrazoles”

May - 2019: Joseph Black Conference / Appleton Tower - University of Edinburgh / Poster presentation: “Co-crystallisation and Structural Studies of Pyrazole-Based Energetic Materials”

June - 2019: The 10th Crystal Forms Meeting / University of Bologna - Italy / Poster presentation: “Co-crystallisation and Structural Studies of Pyrazole-Based Energetic Materials” **(Cryst Eng Comm. – Royal Society of Chemistry - OUTSTANDING POSTER PRESENTATION PRIZE).**

August - 2020: Neutron Scattering Group Early Career Meeting / Science and Technology Facilities Council, Didcot, Oxfordshire, UK. / Oral presentation: “High-Pressure Characterisation of 3,4,5-Trinitropyrazole”

WORKSHOPS/TRAININGS

26.02.18 – 08.03.2018: ISIS neutron and muon source-neutron training course/ Rutherford Appleton Laboratory - Oxfordshire, UK.

06.04.2019 – 14.04.2019: 17th BCA/CCG Intensive Teaching School in X-Ray Structure Analysis/ Durham University - Department of Chemistry, Durham, UK.

PUBLICATIONS

1- **"High-pressure characterization of 3,4,5-trinitropyrazole"** Conference paper, NTREM '20 Seminar on New Trends in Research of Energetic Materials, Czech Republic, 2020 , page 26.

2- Manuscript in preparation: "Exploring the structure-property relationship of TNP at high-pressure"

3- Manuscript in preparation: "Structure - impact sensitivity correlations of energetic novel salts and co-crystals formed with nitropyrazoles"